

## REPORT DOCUMENTATION PAGE

Form Approved  
OMB No. 0704-0188

The public reporting burden for this collection of information is estimated to average 1 hour per response, including the time for reviewing instructions, searching existing data sources, gathering and maintaining the data needed, and completing and reviewing the collection of information. Send comments regarding this burden estimate or any other aspect of this collection (0704-0188), 1215 Jefferson Davis Highway, Suite 1204, Arlington, VA 22202-4302. Respondents should be aware that notwithstanding any other provision of law, no person shall be subject to any penalty for failing to comply with a collection of information if it does not display a currently valid OMB control number.

**PLEASE DO NOT RETURN YOUR FORM TO THE ABOVE ADDRESS.**

1. REPORT DATE (DD-MM-YYYY) 18-OCT-2002	2. REPORT TYPE FINAL	3. DATES COVERED (From - To) 01-SEP-1996 --- 31-AUG-2000		
4. TITLE AND SUBTITLE Advanced Semiconductor Light Emitting Materials		5a. CONTRACT NUMBER Not Applicable		
		5b. GRANT NUMBER N00014-96-1-1240		
		5c. PROGRAM ELEMENT NUMBER Not Applicable		
6. AUTHOR(S) Lapeyre, Gerald J.		5d. PROJECT NUMBER 96PR07849-00		
		5e. TASK NUMBER Not Applicable		
		5f. WORK UNIT NUMBER Not Applicable		
7. PERFORMING ORGANIZATION NAME(S) AND ADDRESS(ES) Physics Department Montana State University-Bozeman PO Box 173840 Bozeman, Montana 59717-3840		8. PERFORMING ORGANIZATION REPORT NUMBER Z1073/429364		
9. SPONSORING/MONITORING AGENCY NAME(S) AND ADDRESS(ES) Office of Grants & Contracts Montana State University-Bozeman PO Box 172470 Bozeman, Montana 59717-2470		10. SPONSOR/MONITOR'S ACRONYM(S) Not Applicable		
		11. SPONSOR/MONITOR'S REPORT NUMBER(S) Not Applicable		
12. DISTRIBUTION/AVAILABILITY STATEMENT Unclassified Unlimited				
13. SUPPLEMENTARY NOTES None				
14. ABSTRACT Photoelectron spectroscopy (PES) methods were developed for investigating interface and bulk properties of crystals for advanced electronic devices and optical devices. These and established PES methods were used to probe and characterize two classes of materials. One is wide-band gap semiconductors (GaN is prototype), which are under development for high frequency and high power electronic devices as well as short wave length light emitters such as bioagent detectors. For CVD hexagonal oriented GaN we measured the bulk electronic structure [bands] and the surface electronic states. The interface formation with Mg adsorption is determined. A unique internal-reference-beam holography method was developed and used to measure surface atomic positions and applied to Mg on GaN. The photoelectron-holographic-imaging technique was also used for ethylene and acetylene site data on the 100 face of silicon. The other material system is insulators doped with rare-earth atoms for optical information devices. For the first time the 4f rare-earth levels were measured with reference to the host (YAG) band gap.				
15. SUBJECT TERMS Light Emitters, Semiconductor, Wide Band Gap, Electron Spectroscopy, Photoemission				
16. SECURITY CLASSIFICATION OF: a. REPORT U b. ABSTRACT U c. THIS PAGE U		17. LIMITATION OF ABSTRACT UU	18. NUMBER OF PAGES	19a. NAME OF RESPONSIBLE PERSON Leslie L. Schmidt
				19b. TELEPHONE NUMBER (Include area code) (406)994-2381

## Manuscripts and Articles Attached

1. "Small cone transform of photoelectron diffraction data for atomic images from arsenic adsorbed on silicon (100) and (111) surfaces", H. Wu, M. Yu, and G.J. Lapeyre. Manuscript.
2. "Spectroscopy: relating localized electron states to host band structure in rare-earth-activated optical materials", C.W. Thiel, H. Cruguel, H. Wu, Y. Sun, G.J. Lapeyre, R.L. Cone, R.W. Equall, and R. M. Macfarlane. OSA OPN, Vol. 12, No. 12, Dec. 2001.
3. "Systematics of 4f electron energies relative to host bands on resonant photoemission of rare-earth ions in aluminum garnets", C.W. Thiel, H. Cruguel, H. Wu, Y. Sun, G.J. Lapeyre, R.C. Cone, R.W. Equall, R.M. Macfarlane. Phys. Rev. B, Vol. 64, 085107.
4. "Systematics of 4f electron energies relative to host bands on resonant photoemission of rare-earth doped optical materials", C.W. Thiel, H. Cruguel, Y. Sun, G.J. Lapeyre, R.M. Macfarlane, R.W. Equall, R.L. Cone. Journal of Luminescence 94-95 (2001) 1-6.
5. "High-resolution photoemission study of acetylene adsorption and reaction with the Si(100)-2-x1 surface", S.H. Xu, Y. Yang, M. Keeffe, G.J. Lapeyre, and E. Rotenberg. Phys. Rev. B, Vol. 60, No. 16, 15 Oct. 1999-II.
6. "Defect formation near GaN surfaces and interfaces", L.J. Brillson, T.M. Levin, G.H. Jessen, A.P. Young, C. Tu, Y. Naoi, F.A. Ponce, Y. Yang, G.J. Lapeyre, J.D. MacKenzie, C.R. Abernathy. Physica B 273-274 (1999) 70-74.
7. "Surface core level shift on GaN(0001) surface", Y. Yang, S.H. Xu, H. Cruguel, G.J. Lapeyre, H.J. Ho, and J.F. Schetzina. Manuscript.
8. "Photoelectron holographic derivative transform for increased range of atomic images", S.H. Xu, H.S. Wu, M. Keeffe, Y. Yang, H. Cruguel, and G.J. Lapeyre, Phys. Rev. B, Vol. 65, 075410 (2002).
9. "Electronic near-surface defect states of bare and metal covered n-GaN films observed by cathodoluminescence spectroscopy", A.P. Young, J. Schafer, L.J. Brillson, Y. Yang, S.H. Xu, H. Cruguel, G.J. Lapeyre, M.A.L. Johnson, and J.F. Schetzina, J. of Electronic Materials, Vol. 28, No. 3, 1999.
10. "Photoemission spectromicroscopy studies on epitaxial lateral overgrowth GaN surfaces", Y. Yang, S. Mishra, F. Cerrina, S.H. Xu, H. Cruguel, G.J. Lapeyre, and J.F. Schetzina, J. Vac. Sci. Technol. B 17(4), Jul/Aug 1999.
11. "A kinetic model for the removal of sulfur from polycrystalline titanium surfaces exposed to oxygen", R. Reibel, S. Schneider, H. Cruguel, J. Lapeyre and R.J. Smith, Surface Review and Letters, Vol. 6, No. 5 (1999) 935-940.
12. "Photoelectron diffraction imaging for C<sub>2</sub>H<sub>2</sub> and C<sub>2</sub>H<sub>4</sub> chemisorbed on Si(100) reveals a new bonding configuration", S.H. Xu, M. Keeffe, Y. Yang, C. Chen, M. Yu, G.J. Lapeyre, E. Rotenberg, J. Denlinger, and J.T. Yates, Phys. Rev. Lett., Vol 84, No. 5, 31 January 2000.
13. "Photoelectron diffraction imaging reveals a new bonding configuration for C<sub>2</sub>H<sub>2</sub> and C<sub>2</sub>H<sub>4</sub> chemisorbed on Si(100)", S.H. Xu, M. Keeffe, Y. Yang, C. Chen, M. Yu, G.J. Lapeyre, Advanced Light Source Activity Report 2000, Berkeley Labs, Surface and Interface Science – Science Highlights.

Small Cone Transform of Photoelectron Diffraction Data  
For Atomic Images from Arsenic Adsorbed on Silicon (100) and (111) Surfaces

Huasheng Wu<sup>1</sup>, Mickey Yu<sup>2</sup>, and G.J. Lapeyre<sup>3</sup>

<sup>1</sup>Physics Department, University of Hong Kong, Hong Kong, China.

<sup>2</sup>IBM Microelectronics, Essex Junction, VT 05452.

<sup>3</sup>Physics Department, Montana State University, Bozeman, MT 59717-0348.

Abstract

The intensity of photoelectron emission from core states of a surface atom exhibits electron diffraction effects due to scattering by atoms neighboring the emitter. The interference oscillations measured by angular-dependent, photon-energy-dependent CIS spectra are inverted to obtain an atomic image of the neighboring scattering atoms. The procedure used to collect and process the data is described. The inversion is based on the holographic principle and consists of an initial transform against (photon energy) wave number yielding a complex field  $\Phi$  and second a transform (summation) against emission directions. Photoelectron holographic image (PHI) based on arsenic 3d emission data directly yield its site symmetry. No model calculations or simulations are used. It is found that As adsorbs as dimers on the (100) surface of silicon and As replaces the first layer Si atoms on the (111) surface. For the (100) case the two As atoms in a dimer sit with different orientations. The inversion yields an image where each of the two inequivalent emitters are at its origin instead of being at two separate locations as in the sample. The image is akin to a "double exposure" photograph and is easily reduced to obtain the physical structure of the adsorption site. The two sites can be chemically equivalent as they are in the present case. Each dimer pair is bonded to four Si atoms which almost form a square but the Si-Si distance parallel to the As dimer bond is about .03 Å shorter. The experimental structure indicates that the surface Si dimer bonds are broken.

In the summation of the  $\Phi$ 's over emission angles, a procedure is found which significantly reduces artifacts in the image. The procedure organizes the various emission directions into collections of angles that are contained in small cones that intersect the emission hemisphere. The summation index is for the directions in a cone. The data for each emission direction used in the experiment are used without bias. In this article a theoretical description is given which illustrates why the small-cone technique emphasizes the effects of interference behavior in the neighborhood of a scatterer and de-emphasizes the effects of interference far from the scatterer so that the strength of artifacts are reduced.

## 1. Introduction

As a direct method for determining the local three-dimensional environment of atoms at surfaces, photoelectron holography imaging (PHI) has undergone many developments in the past few years [1-13]. The dependence of the photoelectron diffraction on photon energy (electron momentum squared) and emission direction is measured and then mathematically inverted using the holographic principle to obtain an atomic image of the atoms neighboring the emitter. The basic properties of photoemission allow for the determination of the emitter's identity and the technique has proved valuable in determining the local geometry of adsorbate atoms. Optimal results are obtained by first transforming a data-set against the magnitude of the electron momentum giving the magnitude and phase of a set of fields  $\Phi(\vec{R})$  and then summing over the momentum directions  $\hat{k}$  to obtain the image function  $U(\vec{R})$  which gives an intensity value for every position in direct space. We introduced a particular procedure in the latter summation, termed the small cone transform, which is effective in controlling artifacts [9, 10].

In this paper, the small cone method of photoelectron holography is successfully employed to experimentally determine the interface structures of arsenic adsorbed on the silicon (111) and (100) surfaces [10, 11]. The determination of an adsorption site has generally been an arduous task, usually employing model dependent tactics where a structure is inferred through an iterative process in which experimental results are compared with calculations from a presumed structure. The holographic imaging technique is a direct technique where (1) a data set is collected, (2) the inversion is carried out giving an intensity value at every position in space  $U(\vec{R})$ , and (3) atoms are assigned to the positions corresponding to the local maxima of  $U(\vec{R})$ . For single site emitters on a mono-element substrate the site position is obtained by inspection. For multi-sites and/or for multi-component substrates the interpretation gives some consideration

to the bulk crystal structure and low-energy electron-diffraction (LEED) pattern data. Such phenomena as non-spherical photoexcited waves, phase shifts in the electron scattering factor, etc., cause artifacts and the small cone method minimizes their strengths.

Arsenic overlayers on silicon surfaces have received considerable attention in the search for an epitaxial compound semiconductor with a direct band gap for the integration of electrical and optical structures. Additionally, As, particularly on the (111) face, passivates the surface; presumably the adsorbate covered surface is left with no dangling bonds to form active "surface chemistry" sites. The atomic images obtained in this work are very clear and the results agree well with those obtained from earlier theoretical calculations and other inferential experimental techniques. The results for the (111) orientation indicate that As atoms replace the first layer Si atoms. Essentially the same method was recently used to study the (111) surface.[14] On the (100) surface, the As atoms form dimer pairs on top of the first-layer Si atoms. The As atoms of the dimer pair occupy inequivalent sites. Strictly speaking, the wave from each of the numerous emitters on the surface forms a holographic image. The reference beams are internally generated by each emitter. Each emitter's signal is incoherent with respect to the other emitters, so the images from each emitter sum by simple addition. The image resulting from each individual emitter, however, has the same origin in the inverted aggregate image. The traditional use of holographic image is for an external reference beam, but since the underlying principal is the same, holographic image is used here. When there are two emitters in inequivalent adsorption sites the resultant image for the pair of atoms is akin to a double-exposed photograph. These images are still easily interpreted. We believe that this is the first multiple surface site experimental image obtained.

A rationale for the success of the small cone method is given in section 3 with a summary of the basic principles of the technique. Experimental considerations and some technical details are discussed in section 2. The experimentally obtained images are presented and discussed in sections 4 and 5.

## 2. Experiments and Data Analysis

The dependence of the photoelectron diffraction from the As 3d core level on the magnitude of the momentum,  $\hbar k$ , and the emission direction,  $\hat{k}$ , was measured. It is the basic angle-resolved photoemission experiment where the photon energy is scanned. The continuum property of synchrotron radiation is used. Essentially the photoelectron waves emitted by an As atom into a given direction were measured. The emission  $I_{\hat{k}}(k)$  is measured as a function of the wave number  $k$  (photon energy) and at a uniformly spaced set of emission direction  $\hat{k}$ . Measurement of the emission over suitable portions of the emission hemisphere, the  $\hat{k}$ -dependence, is achieved by rotations of both the sample and the electron energy analyzer.

From the experimental point of view it is important to first measure the emission as a function of photon energy, i.e. the wave number  $k$ . An overview spectrum containing the As 3d emission peak is shown in Fig. 1. The radiation is dispersed by a grazing incidence monochromator in the Iowa State/Montana State beam line at the Wisconsin Synchrotron Radiation Center (SRC). The diffraction experiments use the 2 m configuration of the extended-range-grasshopper (ERG) monochromator.[15] An electrostatic energy analyzer using hemispherical elements (VSW model HA 50) was mounted on a double axis goniometer. The analyzer's collection aperture was enlarged to obtain a collection angle of about  $\pm 1.5^\circ$ . The angularly resolved emission intensity from the As 3d core level was measured for wave numbers

in a range of approximately 3 to 7  $\text{\AA}^{-1}$  in increments,  $\Delta k$ , of 0.15  $\text{\AA}^{-1}$  by scanning the photon energy from approximately 80 to 240 eV. At each photon energy, an electron-energy-distribution curve (EDC) of the As 3d core-level emission peak was recorded. The intensity for each peak then forms the wave-number dependent spectrum. Since the binding energy of an electronic core level is a constant, the spectra are termed Constant Initial-energy Spectra (CIS). [16] Sample spectra are shown in Fig. 2 where each data point represents the intensity of the As peak as exemplified in the EDC of Fig. 1.

In order to measure in a timely manner the dependence of the photoelectron diffraction on the emission direction, the spectra were measured for a set of angles distributed over an irreducible symmetry element on the sample's emission hemisphere. Since Si(111)1x1 - As has a 3-fold rotation axis (the Z-axis) and three vertical mirror planes, the angular region used for data collection was polar angle  $\theta = 0 - 82.5^\circ$  and azimuthal angle  $\phi = 0 - 60^\circ$ . The normal to the surface corresponds to the zero in polar angle and the zero in the azimuthal angle corresponds to a mirror plane. The Si(100)1x2 - As has a 2-fold rotation axis and two vertical mirror planes, and in accordance with the sample symmetry, a data set was collected over the azimuthal range  $\phi=0 - 90^\circ$ . Low-energy electron diffraction (LEED) was used to establish the major crystallographic directions for each face. The angular step,  $\Delta\theta$ , was chosen to be  $5^\circ$  for the Si(111)1x1-As and  $7.5^\circ$  for the Si(100)1x2-As. For a given polar angle, the azimuthal step size was determined in accordance with  $\Delta\phi=\Delta\theta/\sin\theta$  which gives the same solid angle interval for each emission direction. The polar angle was varied mechanically by rotating the electron analyzer in the laboratory's horizontal plane which contains the photon polarization vector, the propagation vector, and the sample normal. The azimuthal angle was varied by rotating the

sample around its normal. A total of 95 emission directions were measured for each sample orientation.

For a given emission direction  $\hat{k}$ , the intensity and the position of the peak in each EDC form a Constant Initial-energy Spectra (CIS),  $I_{\hat{k}}(k)$ . The EDC data set used for an individual CIS was obtained with fixed monochromator slits resulting in a change in the energy resolution from approximately 0.8 eV to 3.0 eV over the spectral range. The EDC scan range was adjusted to obtain sufficient wings on each side of the peak for good background determination. For data reduction, each As 3d EDC was fit with a Gaussian peak with a linear background. (For efficient data reduction the number of data point in each EDC was kept constant and only the size of the energy step was adjusted.) The procedure works very well when the As peak steps through the Auger edge which occurs about 90 eV for Si. Use of the Gaussian area works well for the intensity determination since it avoids the problem of properly accounting for the signal in the “wings” of a peak. If direct numerical intergration of the peak area is used to represent the intensity, it has a considerable dependence on the algorithm used to fit the background because the “wings” of the peak make a sizable contribution to the peak’s area. The Gaussian fit also resulted in an average taken over a large number of data points yielding better signal-to-noise performance. The spectral and time-dependent properties of the photon beam were monitored using the photo-current produced by a high-transmission tungsten mesh placed just ahead of the sample. The electron yield of the tungsten mesh was a smooth, weak function of photon energy. After obtaining each EDC, a photon-flux mesh current was recorded to use for relative normalization of the EDC spectra. The normalization procedure is very important for the technique and, for the monochromator system we have used, it worked well. If technical

problems (e.g. jump in flux) occur, one can still process the data with the method reported by T.-C. Chaing's group. [14]

To extract the diffraction effects, a non-diffractive curve  $I_{\hat{k}0}(k)$  was then found by using a spline routine [17] to obtain a smooth average for each CIS, which takes account of the  $k$ -dependent photo-excitation cross section of the core, the mesh-emission flux, and the transmittance of the electron energy analyzer. Initially a number of different algorithms were explored to identify an  $I_{\hat{k}0}(k)$ . The results showed that the positions of the local maximums in the image function  $U(\vec{R})$  were not affected. Normalized diffraction curves were then calculated using

$$\chi_{\hat{k}}(k) = \frac{I_{\hat{k}}(k) - I_{\hat{k}0}(k)}{I_{\hat{k}0}(k)} \quad (1)$$

The Si(111) wafer is cut on axis while the Si(100) wafer is a  $4^\circ$  vicinal cut. After outgassing at about  $500^\circ\text{C}$ , the Si wafer was heated to  $1150^\circ\text{C}$  for about 10 seconds while maintaining the chamber pressure in the  $10^{-10}$  Torr range. Then it was quickly lowered down to about  $850^\circ\text{C}$  and then slowly cooled down to  $500^\circ\text{C}$ . The up and down temperature cycle was repeated two or three times and then the wafer was cooled down to room temperature. This procedure resulted in a good  $7 \times 7$  LEED pattern for a Si(111) face or a single domain  $2 \times 1$  LEED pattern for the Si(100) vicinal surface. The samples were exposed to about a  $10^{-5}$  Torr arsenic flux obtained by thermal evaporation of As from a tungsten basket in an attached preparation chamber. The Si(111) sample was post-annealed at  $350 - 400^\circ\text{C}$  for 3 minutes which resulted in a sharp  $1 \times 1$  LEED pattern. The Si(100) vicinal surface was heated from room temperature to  $700^\circ\text{C}$  over a time period of 2 minutes, kept at  $700^\circ\text{C}$  about 3 minutes, and then slowly cooled down to room temperature in the presence of an arsenic flux. The As exposed sample exhibited

a sharp single domain 1x2 LEED pattern in contrast to the single domain 2x1 pattern exhibited from the clean sample.[18] A complete data set was obtained over about a period of 24 hours. Sample cleanliness was monitored at appropriate intervals by examining the shape of high-resolution core level emission. The carbon and oxygen 1s levels were also measured.

### 3. Comments on the Rationale of the Method

This section gives a rationale for the success of the small-cone method preceded by a summary of the basic principles of internal-reference-wave photoelectron holography. In the photoemission process a core level in the emitter is excited which gives a monochromatic outgoing beam with point source properties, a requirement of the holographic phenomena. When a photoelectron with momentum  $\hbar\hat{\mathbf{k}}$  is generated from an emitter, part of the electron wave propagates to the detector in the direction  $\hat{\mathbf{k}}$  and other parts are scattered by neighboring atoms located at positions  $\vec{r}_i$  before propagating to the detector, where the interference is measured in the far field by an angle-resolved electron detector. Coherence of the reference and scattered waves, the other requirement of the holographic principle, is a natural property of the photoemission process.

#### 3. A. Elements of the Inversion

The experimentally obtained data must undergo two mathematical transforms to produce an image function; one transform is over the wave number  $k$  and the other is over the emission directions  $\hat{\mathbf{k}}$ . We term the algorithm by which one determines the image function from the data

the inversion process. The interference effects in each CIS  $\chi_{\hat{k}}(k)$  are transformed to obtain the CIS transform field  $\Phi_{\hat{k}}(\vec{R})$  using

$$\Phi_{\hat{k}}(\vec{R}) = \int_{k_{\min}}^{k_{\max}} \chi_{\hat{k}}(k) e^{-ik\vec{R}(1-\hat{k}\cdot\hat{R})} g(k) dk . \quad (2)$$

where  $\vec{R}$  is a three dimensional variable in direct space with origin at the emitter atom. Tong, Hong and Wu (THW) first wrote down the transform and emphasized the importance of doing this transform first. [5] The first experimental verification was done by H. Wu et al. [ 8, 10, 19] As discussed in the Appendix, an energy window  $g(k)$  is used to avoid termination errors in the computation since the experimental  $\chi(\theta, \phi, k)$  has the finite range of the CIS data. Also discussed in the Appendix is the correction made to the normalized function  $\chi_{\hat{k}}(k)$  due to the inner potential of the crystal. The contribution from each emitter is incoherent and in effect each emitter forms a "hologram". The origin of the field is the emitter's position. As a result, all sites, including inequivalent sites, form an image with the same origin. Hence, for two inequivalent sites the net image is akin to a double exposed photograph.

The properties of the above field,  $\Phi_{\hat{k}}(\vec{R})$ , are examined by using a model form of  $\chi$ . For first order scattering the function can be written phenomenologically as [5, 11]:

$$\chi_{\hat{k}}(k) = \sum_j [A_{\hat{k}}(k, \vec{r}_j) e^{ik\vec{r}_j(1-\hat{k}\cdot\hat{r}_j)} + A_{\hat{k}}^*(k, \vec{r}_j) e^{-ik\vec{r}_j(1-\hat{k}\cdot\hat{r}_j)}] . \quad (3)$$

The factor  $A_{\hat{k}}(k, \vec{r}_j)$ , an effective scattering term, represents a combination of the atomic scattering factor and photon-excitation matrix elements and is discussed later. The index  $j$  is for each scattering atom. Upon combining Eqs. (2) and (3), it is clear that the first term in Eq. (3) gives  $\Phi_{\hat{k}}(\vec{R})$  a maximum intensity at those positions for which the phase factor is zero:

$$R(1 - \hat{k} \cdot \hat{R}) - r_j(1 - \hat{k} \cdot \hat{r}_j) = 0 \quad (4)$$

This equation describes a parabolic surface of revolution where the axis of revolution is the line connecting the emitter and the detector,  $\hat{k}$ . The complex value on each parabolic surface is a constant and can be written as:

$$\Phi_{\hat{k}}^{\max} = \Phi_{\hat{k}}(\vec{r}_j) \equiv \overline{A_{\hat{k}}(\vec{r}_j)}(k_{\max} - k_{\min}) \quad (5)$$

From (Eq. 5), it is observed that the parabolic surfaces formed by each CIS of direction  $\hat{k}$  pass through the positions of the scattering-atoms,  $\vec{R} = \vec{r}_j$ . So, if all of the CIS inversions  $\Phi_{\hat{k}}(\vec{R})$  are in phase at  $\vec{R} = \vec{r}_j$ , the summation over all emission directions would give rise to a large intensity at  $\vec{R} = \vec{r}_j$ . This leads to the second step of the inversion process:

$$U(\vec{R}) = \left| \sum_{\text{all } \hat{k}} \Phi_{\hat{k}}(\vec{R}) \right|^2 \quad (6)$$

The sum over directions may be performed in different ways. We use the term full hemisphere when the sum is simply over all possible directions. This procedure was first articulated by Tong et al. [5]. However, CIS inversion fields for different emission directions  $\hat{k}$  may not be in phase at  $\vec{R} = \vec{r}_j$ . Actually, on the emission hemisphere, there exists a limited angular window where the phases are uniform. The center of the window region is given by the emitter-scatterer axis. For emission directions which lie within the window, the fields  $\Phi_{\hat{k}}(\vec{r}_j)$  have a fairly constant phase and a larger magnitude; while for emission directions beyond the window the fields  $\Phi_{\hat{k}}(\vec{r}_j)$  have a rapidly changing phase and a smaller magnitude. When the sum in Eq. (6) is over all directions, those CIS inversions corresponding to the emission directions inside the small window build up intensity at  $\vec{R} = \vec{r}_j$ . Those CIS inversions corresponding to the emission

directions outside the small window may not build up intensity at  $\vec{R} = \vec{r}_j$ , but may actually build up intensity somewhere else in space thus forming artifacts. To take advantage of this property and to reduce artifacts, we introduced a modified summation method, where for each spatial point the angular sum is taken over a small cone. The second step of the inversion process is then as follows [9, 10, 11, 19]:

$$U(\vec{R}) = \left| \sum_{\hat{k} \in \text{Cone}(-\hat{R}, w)} \Phi_{\hat{k}}(\vec{R}) \right|^2. \quad (7)$$

The axis of the small cone is  $\hat{k} = \hat{R}$  and the half angle  $w$  is a free parameter whose value is justified by examining the experimentally obtained  $\Phi$ 's. In calculating the sum for each point in space, all of the CIS data are systematically used as the small-cone axis (so to speak) moves over the emission hemisphere. The image function  $U(\vec{R})$ , is interpreted by assigning atoms to the "peaks" in the image. The peak's centroid is used for the position.

The above properties of  $\Phi_{\hat{k}}(\vec{R})$ , the CIS transform field, can be observed by examining the properties of an experimentally obtained set of  $\Phi$ 's. Two important and useful constructions can be formed from the experimentally determined CIS fields. One is to fix the emission direction and show the amplitude as a function of direct space position,  $\vec{R}$ . The result exemplifies the parabola of constant phase factor for the integrand of the THW transform. Figure 3 shows the amplitude of  $\Phi_{\hat{k}}(\vec{R})$  for a given  $\hat{k}$ . The other construction is to fix  $\vec{R}$  at the position of a scatterer and to show the magnitude and phase of  $\Phi$  as a function of emission direction  $\hat{k}$ , i.e.,  $\theta$  and  $\phi$ . Results for a Si nearest-neighbor of the As emitter for the (111) face is shown in Fig. 4(a) and 4(b) and that for the (100) face is shown in 4(c) and 4(d). At  $\vec{R} = \vec{r}_j$ , each contribution adds to the total (see Fig. 3), so any experimental error in normalizing an

individual EDC spectrum within a  $\chi_k(k)$  and, hence within a set of  $\chi$ 's, has a minimal effect. That is, if a particular  $\Pi$  is larger or smaller than it should be, there is minimal adverse effect. This is a reason that contributes to the importance of first measuring the photon energy (wave number) dependence and transforming the spectra.

Another perspective can be taken for the small cone method. The cone used in processing the data is equivalent to a cone in direct space with the same half angle  $w$ . Only those portions of the  $\Phi$  field within  $w$  contribute when summing over the directions. That is, in Fig. 3 only the results for  $-w < \theta < w$  contribute to the sum in Eq. (7). The sum is then equivalent to summing only those pieces of the parabolic surfaces that lie within an angular window  $w$  for each  $\vec{R}$  direction, thus suppressing the contribution of regions far from the point of interest.

The value of  $w$ , usually  $15^\circ - 30^\circ$ , is the only free parameter in the inversion process and can be easily obtained from the experimental values as shown in Fig. 4. As a logical procedure for obtaining an unknown structure, a small value of  $w$ , say  $10^\circ - 15^\circ$ , is used first to obtain a preliminary image function  $U(\vec{R})$ . Then at the positions of the maximum intensity points of the function (atomic images), the experimental curves of the phase and the magnitude of the CIS inversion as a function of emission direction are calculated using the formula above; the half angle width  $w$  found from the curves is used in the final inversion. The results of the discrete transformations for the image function  $U(\vec{R})$  were then interpolated with MATHEMATICA [20] to form a continuous image function  $U(X, Y, Z)$  (or a continuous  $U(\vec{R})$ ), from which any form of display could be extracted. Experience shows that while the value of  $w$  has little effect on image positions, larger values of  $w$  may give some reduction in the width of the image peaks. Sometimes examining the images obtained with several different values of  $w$  helps to

differentiate weak image peaks from artifacts. The small-cone transform emphasizes the most important portion of the diffraction information while reducing the artifacts dramatically [9, 19].

### 3. B. Atomic Model for an Effective Scattering Factor

The relationship  $\vec{k} = -\vec{R}$  is very important in photoelectron diffraction and illustrates the success of the small cone method. For an emitter, located at the origin, and a particular scatterer at  $\vec{r}$  the angle-resolved signal intensity using atomic orbitals can be written in the general form

$$I_k(\hat{k}) = \sum_m \left| \sum_{l=l_0-1}^{l_0+1} c_l [Y_{lm}(\vec{k}) + Y_{lm}(\vec{r}) f(\hat{r} \cdot \hat{k}) e^{ikr(1-\hat{k} \cdot \hat{r})}] \right|^2. \quad (8)$$

The first term in the bracket describes the photoexcitation of state  $l_0$  and the function  $f$  is the atomic scattering factor. The expansion is in terms of atomic orbitals and the coefficients  $c_l$  are functions of  $k$ , only. [21] The final-state plane wave has been expanded in spherical harmonics, the  $Y_{lm}$ , which have a polar angle referenced relative to the polarization direction  $\hat{A}$  of the photon flux. As above the emitter is placed at the origin and the scatterer is at the position described by  $\vec{r}$ . The above expression when expanded has four terms where the two relevant terms are,

$$I_k(\hat{k}) = \sum_m \sum_l \sum_{l'} c_l c_{l'}^* Y_l(\vec{k}) Y_{l'm}^*(\vec{k}) + \sum_m \sum_l \sum_{l'} c_l c_{l'}^* Y_l(\vec{k}) Y_{l'm}^*(\vec{r}) f^*(\hat{r} \cdot \hat{k}) e^{-ikr(1-\hat{k} \cdot \hat{r})} + c.c. + \dots \quad (9)$$

The first summation term represents a background function  $I_0$  and the next two cross terms are the interference effects. (The third term is the complex conjugate of the second term.) The fourth term is not shown because it contains the factor  $f^2$  which typically is very small. The normalized intensity function is expressed by

$$\chi_{\hat{k}}(k) \equiv \frac{I_{\hat{k}}(k) - I_{\hat{k}0}(k)}{I_{\hat{k}0}(k)} = A_{\hat{k}}(k, \vec{r}) e^{-ikr(1-\hat{k} \cdot \hat{r})} + A_{\hat{k}}^*(k, \vec{r}) e^{ikr(1-\hat{k} \cdot \hat{r})}. \quad (10)$$

with [21]

$$A_{\hat{k}}(k, \vec{r}) = \frac{\sum_m \sum_l \sum_{l'} c_l c_{l'}^* Y_{lm}(\vec{k}) Y_{l'm}^*(\vec{r})}{\sum_m \sum_l \sum_{l'} c_l c_{l'}^* Y_{lm}(\vec{k}) Y_{l'm}^*(\vec{k})} f^*(\hat{r} \cdot \hat{k}). \quad (11)$$

When  $\hat{k} = -\hat{r}$ , use of the spherical harmonic property  $Y_{lm}(k) = Y_{lm}(-r) = (-1)^l Y_{lm}(r)$ , reduces Eq. (11) to

$$A_{\hat{k}}(k, \vec{r}) = (-1)^{l_0+1} f^*(\hat{r} \cdot \hat{k}). \quad (12)$$

The complicated ratio of sums in Eq. (11) becomes essentially one. This condition,  $\hat{k} = -\hat{r}$ , is the backscattering condition where the atomic scattering factor has a large value. Thus, when  $\vec{R}$  is near  $\vec{r}$  the effective scattering factor A is large due to the backscattering peak in the atomic scattering factor and the transform against  $k$  yields a large intensity in  $U(\vec{R})$ . The importance of the effect of the backscattering peak in the atomic scattering factor is also pointed out by Dippel et.al. in their analysis of CIS data which they term scanned-energy-mode data. [6]

A remaining issue of concern is the phase factor in the atomic scattering factor, which has the effect of shifting the position of an atom in an image away from that atom's true position. Because the small-cone method emphasizes back scattering, an approximate correction for the shift is obtained by expressing the phase factor of the scattering function by the first order term in the Taylor expansion of  $k$ . The transformation against  $k$  by Eq. (2) then becomes:

$$\Phi_{\hat{k}}(\vec{R}) = \int_{k_{\min}}^{k_{\max}} \chi_{\hat{k}}(k) e^{-ik[R(1-\hat{k} \cdot \hat{R}) + S(\pi)]} g(k) dk \quad (13)$$

where  $S(\pi)$  is the coefficient of the first order term (a slope) evaluated at the back-scattering angle. For Si the value of  $S(\pi)$  is  $-0.18 \text{ \AA}$  and inclusion of the correction term in the inversion increases the bond-length values by about  $0.1\text{--}0.2 \text{ \AA}$ . [9] The small cone method makes this correction possible.

#### 4. Results of Si(111)As-1x1

Both the small-cone and full hemisphere method of inverting the photo electron data from the Si(111)1x1-As system are presented. A diagram for the Si(111) surface structure is shown in Fig. 5a. Various representations of the photoemission holographic image (PHI) obtained are shown in Figure 6. Parts a, b, and c are from the small-cone method. The image function  $U(\vec{R})$  was adapted to a coordinate system such that  $U(\vec{R}) = U(X, Y, Z)$  where the sample normal and the polar axis are parallel to the Z-direction. The origin of this coordinate system remains at the emitter atom. The X-Y axes are determined from the LEED pattern. The image function  $U(X, Y, Z)$  is examined and particular atomic species are assigned to those positions where the function has local maxima.

The image is a three dimensional object which can be displayed and presented in a number of ways. Fig. 6(a) shows iso-intensity surfaces in 3-D perspective. [19] In this representation, the intensity value of the iso-intensity surface was chosen to be 60% of the value of the local maximum. Note that the "balls" formed by the iso-intensity surfaces are quite isotropic and show only a slight elongation in the vertical direction. The position of the local maxima, the scattering atom, would then be at the center of each "ball." Since the emitter does not "see itself" it is represented by a spherical surface. When initially evaluating an image  $U(X, Y, Z)$ , 2-D planar cuts with the intensity indicated in the third dimension are used. The horizontal cut through the first layer of Si atoms ( $Z = -1.0 \text{ \AA}$ ) is shown in Fig 6(b) where the plane of the cut is noted in Fig. 6(a). The X-Z cut for  $Y=0$  is shown in Fig. 6(c). In this last cut the emitter is represented with a "+" sign. The actual coordinates of the scattering atoms, used

to calculate bond lengths, etc., are taken as the positions of the centroid for the local maxima in  $U(X, Y, Z)$ .

By comparing the structure in the image in Fig. 6(c) with the structure of the unreconstructed Si(111) surface (Fig. 5a) and considering the sharp 1x1 LEED pattern, we can conclude that in the system Si(111)1x1-As, the As atoms replace the top layer silicon atoms. The observed image does not relate to any of the high-symmetry adatom sites. Each As atom is bonded to three Si atoms on the next layer down. This structure agrees with that preferred by the fitting of experimental and theoretical energy-bands by Uhrberg et al. [18] The Z coordinate of the atom D obtained from this method is  $-1.0 \text{ \AA}$ , which agrees well with the calculated value of  $-0.97 \text{ \AA}$  [18] and the value of  $-0.95 \text{ \AA}$  obtained from an x-ray standing wave measurement. [22] From the small-cone image the X-coordinate of atom D was determined to be  $2.3 \text{ \AA}$ . For the unreconstructed Si(111) surface this value is  $2.2 \text{ \AA}$ . A similar holographic result has recently been reported, which agrees with this measurement [14].

The As 3d data was inverted to obtain a preliminary image function which contained a local maximum at the position of atom D. The phase and magnitude of the CIS transfer field  $\Phi_{\vec{k}}(\vec{R})$  at this position are shown in Fig. 4(a) and (b). The curves clearly show the small angular window behavior with the window centered at  $(\theta, \phi) = (70^\circ, 180^\circ)$ . The half-angle of the window gives the half-angle of the small-cone, in this case roughly  $30^\circ$ . This value was then used in the angular transform, Eq. (7), to obtain the image shown in Fig. 6 (a), (b), and (c).

The As/Si(111) data was also inverted with the full window summation, Eq. (6). The vertical planar cut for the image obtained is shown in Fig. 6(d). The large intensity at the real atomic position, D, is evident, but significant intensity is seen at other positions. Such artifacts make the determination of atomic position rather problematic but are essentially absent in the

image shown in Fig. 5(c) obtained with the small cone summation. The reduction in artifacts is clearly seen.

## 5. Results of Si(100)1x2-As

First a note on the reconstruction of the Si(100) surface, where neighboring atoms hybridize to form dimers. See Fig 5(b) for the surface structure. The dimers are aligned in rows which can be found in two orthogonal directions, i.e., two domains exist. It is well established that vicinal surfaces of about  $3.5^\circ$  form single domain 2x1 LEED patterns with the dimer bonds oriented parallel to the steps; the dimers form rows perpendicular to the steps. In this work, the X-Y plane is chosen to be parallel to the terrace with the X-direction parallel to the step (dimers) and the Y-direction perpendicular to the step. The step direction, and therefore the X- and Y-directions, were determined from a LEED pattern.

The deposition of As produced a surface with a LEED pattern of 1x2, in contrast to the 2x1 pattern obtained for the clean surface. This change in the two-by orientation indicates that the As atoms form dimers with bond directions perpendicular to the step edges. The two As atoms composing the dimer are inequivalent, since the As atoms are in different structural orientations, so they appear as two different "kinds" of emitters. This leads to a bit of complication in assigning atoms to the spots in the image.

The As 3d data were inverted to obtain a preliminary image which contains a local-maximum-intensity spot, called A, at  $(-1.8, -0.5, -1.5)\text{\AA}$  for a first layer Si atom. The phase and magnitude of the CIS transfer field  $\Phi_{\hat{k}}(\vec{R})$  is shown in Fig. 4(c) and (d) plotted as a function of the emission polar angle,  $\theta$ , at the azimuth emission angle,  $\phi=15^\circ$ . The curves clearly show

the small angular window behavior, just as found for As on the (111) surface. The window is centered at  $(\theta, \phi) = (60^\circ, 15^\circ)$  with a window half-angle of about  $30^\circ$ .

Figure 7(a) shows the resulting local site symmetry. The two inequivalent As emitters are represented by the addition of two spheres P and Q. The first layer Si atoms A,B,C,D are iso-intensity surfaces from the experimentally obtained image. The intensity is about 70% of the maximum intensity. This figure is partially a construction since the two inequivalent As emitters are BOTH at the origin of the inversion image field. The inversion-obtained image is obtained by sliding the two spheres P and Q together so that they are at the same point (all emitters are at the origin); if P and Q were shifted to the same point then the construction shown in panel (a) would correspond to the image construction in part (b). Two planar cuts of the inversion image are shown in part (c) and (d) of Fig. 7.

To clearly distinguish the contributions from the two different As emitters, a two-letter symbol A/B is used which denotes the image of the scatterer A viewed from an emitter B. Figure 6(c) shows a horizontal planar cut passing through the first layer of Si atoms at  $Z = -1.5$  Å, which shows four Si atoms as doublets at  $X = \pm 1.8$  Å. The separation between A/P and D/P along the X-axis is the actual separation between the Si atoms A and D, since the two spots are viewed from the same emitter P. Similarly, emitter Q makes the images B and C. However, the separation between the spots A/P and B/Q is not the actual separation between the Si atoms A and B, since these two peaks are viewed from the two different emitters P and Q, respectively, but the image has both at its origin as noted above. The separation between the spots is the difference between the separation of the Si atoms A and B and the separation of the As atoms P and Q. Figure 6(d) shows a Y-Z vertical planar cut at  $X = -1.8$  Å, which gives the separation of the doublet and the depth of the first-layer Si atoms. The image function as shown in Fig. 6(c)

and (d) is akin to a double-exposed photograph. The real-space structure is achieved by separating the doublets (i.e., D/P and C/Q as well as A/P and B/Q) by the As-As dimer length and results in the 3-D construction shown in Fig. 7(a). Now that the site symmetry has been established the image can be further examined to determine the value of the As-As dimer length.

A good way to find a value for the As-As dimer length would be to observe an As emitter scattering from an As scatterer, say P scattering from Q or vice-versa. Figure 8(a) shows a planar cut at  $Z = 0 \text{ \AA}$ . The As dimer formation and its site-position observation do not depend on this cut. The intensity is enhanced considerably compared to that of Fig 6(d) whose peak intensity is greater than that of 8(A). Two weak but well localized spots are seen in the image. One test for an artifact in an image cut is whether the spot in the 2-D cut is really a 3-D spot and not a slice through a "tube" of intensity. Assuming that these spots are due to the As atoms, seen as scatterers, a value of about  $2.3 \text{ \AA}$  is obtained for the As-As dimer bond length. This gives an A-B (C-D) spacing of about  $3.3 \text{ \AA}$  while A-D (B-C) spacing is about  $3.6 \text{ \AA}$ . The four first-layer Si atoms A, B, C, and D are at the corners of a rectangle, not a square. The difference in side lengths is noted as  $\delta$  in the table. The A-D (B-C) spacing of  $3.6 \text{ \AA}$  is greater than the Si-Si dimer length of  $2.3 \text{ \AA}$  indicating that the Si-Si dimers are broken.

The planar cut through the image containing the emitter, Fig. 8(a) also shows two very strong spots on the X-axis. These are attributed to artifacts which are due to the spatial relationship of the atoms and the "incidental" bunching or overlapping of the parabolic surfaces which pass through the first-layer Si atoms. To illustrate the behavior consider the construction in fig. 8(b) which shows an effective local structure for  $\text{Si}(100)1\times2\text{-As}$  as seen by the emission from the inequivalent As emitters. The construction has a representative small angular cone which points from the emitter to the "atom" D/P. There are five sticks in the small cone

representing five typical emission directions: four on the edge of the cone and one on the cone axis. Omitted from the figure for clearness are five more such angular cones, which point from the emitter to the “atoms” A/P, B/Q, C/Q, P/Q and Q/P, respectively. The six small cone containing 5 sticks represent a total of 30 emission directions. The CIS for each direction gives a parabolic surface, whose axis is that direction, passing through the scatterer atom. Figure 8(c) shows the curves formed by the 30 parabolic surfaces, intersecting the plane formed by the As atoms ( $Z = 0 \text{ \AA}$ ). The two points on the Y-axis intersected by three parabolic surfaces correspond to the As emitters P and Q. There are, however, many more parabolic surfaces passing the X-axis in the region of  $-3\text{--}2 \text{ \AA}$  and  $2\text{--}3 \text{ \AA}$ , which form the large intensity spots on the X-axis shown in Fig. 8(a). This illustrates the idea of artifact formation by incidental bunching.

Table 1 gives a comparison between the results of this work and several other studies of this adsorption system. Northrup et al. calculated the structure [23], Zegenhegen et al. measured the vertical distance between the As layer and the first Si layer using the x-ray standing wave technique (XSW) [24], and Jedrecy et al. measured the As dimer bond length by the grazing incidence x-ray diffraction technique (GIXD)[25]. The maximum discrepancy is about  $0.2 \text{ \AA}$  or better, a value which is reasonable for the methods involved. The four surface Si atoms bonded to an As dimer do not form a square. The difference between the first layer Si-Si spacings, that is the difference between the A-D spacing as compared to the A-B spacing, is denoted as  $\delta$ . The theory value agrees with the measurement.

Table 1. Comparison of atomic positions for Si(100)1x2-As obtained from this work, XSW, GIXD and theoretical calculation (Coordinate Unit Å). The coordinates of the spot representing atom A is listed and the nearest neighbor distances for spots A to P and P to Q. See text for  $\delta$ .

Å Units	A <sub>x</sub>	A <sub>y</sub>	A <sub>z</sub>	PA	PQ	$\delta$
This method	-1.8	-0.5	-1.5	2.4	2.3	0.3
*XSW, **GIXD			*-1.26		**2.55	
Calculation	-1.92	-0.52	-1.41	2.44	2.55	0.25

## 6. Summary

The small-cone photoemission-imaging method based on the holographic principle is used to experimentally determine the local site structure of As on the (111) and (100) faces of Si. Experimental data was inverted to obtain an image function  $U(\vec{R})$ . The local site symmetry was obtained by inspecting each image without using simulations or model calculations. Numerical values obtained for interatomic spacings are good to within 0.1 to 0.2 Å.

The data were used to obtain an effective scattering factor which exhibits the small-window behavior needed for the small-cone method. A theoretical construct was presented which suggests why the small-cone method is effective in reducing artifacts. It substantiates the use of the relation of  $\hat{k} = -\hat{R}$  used in the small-cone method. Similar small-cone behavior has been analyzed for Al and Ga on the (111) surfaces of Si which have the root three reconstruction [9, 19]. Site symmetry has been determined for ethylene and acetylene on Si(100). [26]

On the (100) surface, the As atoms form dimer pairs each of which are bonded to four Si surface atoms. The investigation is an example of the complexity resulting from multiple sites. Since the Si-Si distance in the first layer under the As layer is much larger than the Si-Si dimer

distance, one may conclude that the Si dimer bonds were broken. Within the Si-Si first layer, the separation between Si atoms in the direction perpendicular to the As-As dimer-bond orientation is 3.6 Å. The value for bulk Si is 3.84 Å, which is in reasonable agreement considering the atomic-scattering-factor phase-shift distortion of interatomic-distance values. The separation distance between Si atoms in the direction parallel to the As-bond orientation is about 3.3 Å. Thus, the As-As dimer induced "distortion" is about 0.3 Å while theory gives 0.25 Å. The good numerical agreement may be fortuitous. Additionally, the case of As on Si(100) serves as an example of how the geometry of the  $\Phi$  field parabolic surfaces can be used to interpret image features as artifacts.

On the (111) surface As atoms are in a single site where they replace the first layer Si atoms forming a 1x1 surface net. The same local structure with similar data has recently been published [14]. The numerical values are essentially the same.

The interpretation of a mathematical image may be "tricky" since second-nearest-neighbor scatterers are infrequently obtained and third-nearest-neighbor scatterers are rarely obtained. Sometimes the latter are in the image but not stronger than most artifacts. Most importantly, a proper site position can only be made with dominant image spots, as in this investigation. Thereafter, weaker features can be invoked for more details. The bulk-crystal structure, electron diffraction pattern, and scanning-probe spots can be important ingredients for assignment of atoms to image spots. The ability to "see under" the emitter is a power of the imaging technique. If a larger sphere was sampled, containing second- and third-scattering-neighbors then the site would be determined by inspection and essentially no interpretation would be needed.

The graphical properties of the complex field obtained by transformation of photon-energy scanned CIS data are shown to be useful for analyzing the results.

The results exemplify the effectiveness of the small cone method for determining the site structure of atoms on surfaces. It reduces artifacts and eliminates split images. [9] While, so far, other methods require a trial and error comparison between experimentally-obtained data and model calculations. Knowledge of the local-site-symmetry structure combined with numerical values of interatomic spacings, usually good to within 0.2 Å, is enough to answer many questions. More precise distance values may be obtained with trial and error comparisons of measured and simulated CIS data.

The method is well established for non-embedded emitters. For embedded and bulk emitters the utility of photoelectron diffraction is pretty much an open question. The electron scattering phenomena in these cases also have the forward scattering lobe which can be very strong. Effective methods to treat the phenomena for imaging are still needed.

### Acknowledgments

We are grateful for the help and support from Jim Anderson, Cliff Olson and the Synchrotron Radiation Center (SRC) staff. Discussion with Shihong Xu, Yi Yang and Herve Cruguel were very helpful. We are most appreciative of the support by NSF under Grant No. DMR-9107854 and ONR DEPSCoR. SRC is supported by NSF.

### Appendix

The discrete set of CIS taken in the irreducible angular range were used to form an inner-potential-corrected continuous function  $\chi(\theta, \phi, k)$  using a spline fit and extended to the whole-emission hemisphere according to the symmetry of the sample. The inner potential correction changes the three dimensional electron momentum from its external values,  $(\theta_0, \phi_0, k_0)$ , to its internal values,  $(\theta, \phi, k)$ , according to

$$\frac{\hbar^2 k^2}{2m} = \frac{\hbar^2 k_0^2}{2m} + \square V_0 \quad (A.1)$$

with  $\sin(\theta)k = \sin(\theta_0)k_0$  (A.1)

and  $\phi = \phi_0$ .

In this work the inner potential  $V_0$  was taken to be 10 eV, a typical value used in most dynamical LEED analysis. The value of  $V_0$  affects the numerical values obtained from an image but does not affect the local geometry present in the image.

The experimental  $\chi(\theta, \phi, k)$  has the finite range of the CIS data and an energy window function,  $g(k)$ , is used to avoid termination errors in the inversion computation. The Hanning function [25] is used with a Hanning fraction  $h = 0.25$ ,

$$\begin{aligned}
g(k) &= \sin^2\left(\frac{\pi(k-k_{\min})}{2(k_2-k_{\min})}\right) \quad \text{for } k_{\min} < k < k_2 \\
&= 1 \quad \quad \quad \text{for } k_2 < k < k_3 \\
&= \cos^2\left(\frac{\pi(k-k_3)}{2(k_{\max}-k_3)}\right) \quad \text{for } k_3 < k < k_{\max}
\end{aligned} \tag{A.2}$$

where

$$\begin{aligned}
k_2 &= k_{\min} + h(k_{\max} - k_{\min})/2 \\
k_3 &= k_{\max} - h(k_{\max} - k_{\min})/2.
\end{aligned}$$

Additionally, a window function in the angular transform may be used but was not used for these data. [12,13]

## References

1. J. J. Barton, Phys. Rev. Lett. **61**, 1356 (1988); J. J. Barton, Phys. Rev. Lett. **67**, 3106 (1991).
2. G. R. Harp, D. K. Saldin, and B. P. Tonner, Phys. Rev. Lett. **65**, 1012 (1990).
3. S. Y. Tong, C. M. Wei, T. C. Zhao, H. Huang, and Hua Li, Phys. Rev. Lett. **66**, 60 (1991).
4. G. S. Herman, S. Thevathasan, T. T. Tran, Y. J. Kim, and C. S. Fadley, Phys. Rev. Lett. **68**, 650 (1992). S. Thevathasan, R. X. Ynzunza, E. D. Tober, C. S. Fadley, A. P. Kaduwela, and M. A. Van Hove, Phys. Rev. Lett. **70**, 5 (1993).
5. S. Y. Tong, H. Huang, and C. M. Wei, Phys. Rev. B **46**, 2452 (1992).
6. R. Dippel, D.P. Woodruff, X.-U. Hu, M.C. Asensio, A.W. Robinson, K.M. Schindler, K.-U. Weiss, P. Gardner, and A.M. Bradshaw, Phys. Rev. Lett. **68**, 1543 (1992). D.P. Woodruff and A.M. Bradshaw, Rep. Progr. Phys. **57**, 1029 (1994).
7. L. J. Terminello, J. J. Barton, and D. A. Lapiano-Smith, Phys. Rev. Lett. **70**, 599 (1993).
8. H. Wu, G. J. Lapeyre, H. Huang, and S. Y. Tong, Phys. Rev. Lett. **71**, 251 (1993).
9. Huasheng Wu and G. J. Lapeyre, Phys. Rev. B **51**, 14549 (1995).
10. G. J. Lapeyre, Bulletin of the American Physical Society **39**, 167 (1994). The small-cone concept was independently reported by S.Y. Tong at the same meeting.
11. S. Y. Tong, H. Li, and H. Huang, Surface Review and Lett. **1**, 303 (1984).
12. D. Tarnowski, Science and Vie, No. **912** 56 (1993).
13. P. M. Len, J. D. Denlinger, E. Rotenberg, S. D. Kevan, B. P. Tonner, Y. Chen, M. A. Van Hove, and C. S. Fadley, Phys. Rev. B **59**, 5857 (1999).
14. D. A. Luh, T. Miller, and T. C. Chiang, Phys. Rev. Lett. **81**, 4160 (1998).
15. C. G. Olsen, Nuclear Instruments and Methods in Physics Research A **266**, 205 (1988).
16. G. J. Lapeyre, et al., Solid State Communications **15**, 1601 (1974).

17. Software GENPLOT from Computer Graphic Service, 52 Genung Circle, Ithaca, NY 14850; Software IGOR Pro from Wavemetrics, Inc., P.O. Box 2088, Lake Oswego, OR 97035.
18. R. I. G. Uhrberg, R. D. Bringans, Marjorie A. Olmstead, and R. I. Bachrach, Phys. Rev. B **35**, 3945 (1987).
19. Huasheng Wu, PHD Thesis, Montana State University, (1994), unpublished.
20. Software MATHEMATICA, Wolfram Research Inc., 100 Trade Venter Drive, Champaign, IL 61820.
21. Huasheng Wu and G.J. Lapeyre, to be published.
22. J. R. Patel, J. A. Golovchenko, P. E. Freeland, and H. J. Gossman, Phys. Rev. B **36**, 7715 (1987).
23. R. I. G. Uhrberg, R. D. Bringans, R. Z. Bachrach, and John E. Northrup, Phys. Rev. Lett. **56**, 520 (1986).
24. Zegenhagen et al., Appl. Phys. Lett. **53**, 252 (1988). Check et al
25. N. Jedrecy, M. Sauvage - Simkin, R. Pinchaux, J. Massies, N. Greiser, and V. H. Etgens, Surface Science, 230(1990).
26. D. E. Sayers and B. A. Bunker, in X-Ray Absorption, edited by D. C. Koningsberger and R. Prins, p232, (John Wiley & Sons, 1988).
27. S.H. Xu et al., Phys. Rev. Lett, **84**, 939 (2000).
28. M. T. Sieger, J. M. Roesler, D. S. Lin, T. Miller, and T. C. Chiang, Phys. Rev. Lett. **73**, 3117 (1994).

## Figure Captions

**Figure 1.** Wide-scan Energy Distribution Curve (EDC) from Si(111)1x1-As. Incident photon energy was 150 eV. The As 3d core level was used to obtain the images presented in this study. The insert shows the formation of electron diffraction beam where the square is the emitter and the circle is a scatterer.

**Figure 2.** Representative experimental curves  $I_{\hat{k}}(k)$  (CIS) (circles and solid lines) (a) from As 3d core emission from Si(111)1x1-As. (b) from As 3d core emission from Si(100)1x2-As. Computer-chosen backgrounds  $I_{\hat{k}0}(k)$  are dashed line. The short bars close to the left axis are the baselines for the corresponding curves. The polar angle  $\theta$  and the azimuthal angle  $\varphi$  are indicated.

**Figure 3.** The Si(111)1x1-As CIS transform field,  $\Phi(X, Z)$ , for one emission direction  $\hat{k}$  given by the shown line. The plot is in the  $Y = 0$  plane and the intensity of the field is indicated with a gray scale.

**Figure 4.** Phase (a) and magnitude (b) of the CIS transform  $\Phi_{\hat{k}}$  at the position of the neighboring Si atom D plotted as a function of polar angle from Si(111)1x1-As. The negative angular value denotes that the azimuthal angle is  $180^\circ$ . Phase (c) and magnitude (d) of the CIS transform  $\Phi_{\hat{k}}$  at the position of the Si atom A plotted as a function of polar angle at the azimuthal angle of  $15^\circ$  from Si(100)1x2-As.

**Figure 5.** a) Sketches of the unreconstructed Si(111) surface showing the first two layers of atoms (bilayer). The squares show the four high-symmetry adatom sites with conventional labels.

b) Sketch of the reconstructed Si(100) surface. The open circles are the Si-Si dimer with dangling bonds indicated. The second and third Si layers are indicated by large and small dots, respectively. The dimer direction is assigned the x axis.

**Figure 6.** Atomic image of Si atoms for the structure Si(111)1x1-As, coordinate unit: Å. (a) Three-dimensional surface of constant-intensity plot with a sphere A shown to represent the As emitter. The iso-intensity surfaces of the three Si atoms D, F, G are plotted at 60% of the local maximum intensity value of the corresponding image spot. (b) X-Y planar cut passing through the first layer Si atoms at  $Z = -1.0$  Å, obtained from the small-cone-transform image where the third dimension is the image intensity. (c) Vertical X-Z planar cut obtained from the small-cone-transform image. (d) Vertical X-Z planar cut obtained from the full-hemisphere-transform image,

**Figure 7.** Atomic image of Si atoms for the Si(100)1x2-As structure, obtained from the small-cone-transform-image, coordinate unit: Å. (a) Three-dimensional surface of constant intensity plot arranged in a ball and stick construction of the atomic structures with spheres P and Q added to represent the As emitters. A ball and stick construction of the image is shown in panel (b) with the emitters shown by a sphere at the origin. The atomic structure of panel (a) is obtained by separating the two As emitters in the image along the dimer direction (x axis) by the dimer length. The value of the iso-intensity surfaces are 70% of the local maximum value of the corresponding image spots, A, B, C, and D. (c) The X-Y planar cut at  $Z = -1.5$  Å of the image

function  $U(X,Y,Z)$ , whose intensity is the third dimension. Peaks A/P and D/P are images for the Si atoms A and D as "seen" by emitter P and the peaks B/Q and C/Q have analogous meanings. (d) Y-Z planar cut at  $X = -1.8 \text{ \AA}$ . The image intensity is shown by a gray scale and the spots A/P and B/Q are due to Si atoms.

**Figure 8.** Si(100)1x2-As image cut in the As plane showing As-As scattering. The two different As emitters are both at the origin. The symbol P/Q denotes the image of scatterer atom P "viewed" by the emitter Q and Q/P represents the image of Q as "viewed" by P. (a) X-Y planar cut at  $Z = 0 \text{ \AA}$  and the two spots along the Y-axis are the As atoms as scatterers. (b) A ball and stick construction corresponding to the image generated by inversion with a small-cone which points from the emitters to the Si "atom" D/P. Five typical emission directions are shown by sticks, the axis and four on the conical surface. (c) Curves formed by 30 parabolic surfaces intersecting the plane of the As atoms at  $Z = 0 \text{ \AA}$ . The 30 parabolic surfaces are five p from each of the from the six small cones pointing away from the "atoms" A/P, B/Q, C/Q, D/P, P/Q and Q/P through to the emitter (only one is shown in (b)). The incidental accumulation of the parabolic surfaces around the X-axis in the neighborhood of 2-3  $\text{\AA}$  is taken to be the source of the extensive intensity patches about the x axis. The intensities are small compared to those in Fig. 7.

OSA®

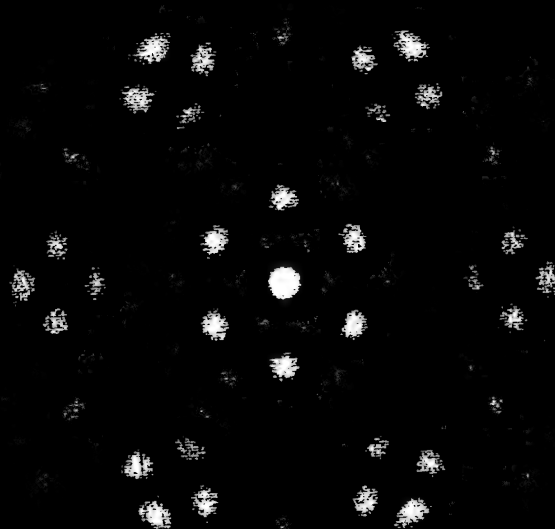
December 2001 Vol. 12 No. 12 \$3.25

OPN

Optics & Photonics News

Optics in  
2001

# Optics in 2001



**Guest Editor: Bob D. Guenther**  
**Physics Department, Duke University**

Every December, *Optics & Photonics News* (OPN) highlights the year's most exciting developments in the fast-paced world of optics. Our special December issue, "Optics in 2001," presents key research in the form of summaries of articles that have appeared in peer-reviewed journals over the course of the past 12 months.

The overwhelming number of submissions received in 2001 signals another groundbreaking year for the world of optics. The increase in the number of submissions—almost twice as many were received this year as last—is vibrant testimony to the vitality of the optics community and to the importance of the work being carried out by optics researchers all over the world. The 58 summaries that compose this year's issue represent the work of nearly 200 scientists.

Submissions included in "Optics in 2001" are judged according to the following selection criteria:

- the accomplishments described must have been published in a refereed journal in the year prior to publication in OPN;

- the work must be illustrated in a clear, concise manner, comprehensible to the at-large optics community;
- the topical area as a whole must be described, and the importance of the research must be detailed.

Although we make every effort to insure that progress in all optics subfields is recognized, there are no requirements in the selection process for inclusion of specific topical areas. When a large number of submissions are received for a specific area, this is taken as evidence that the topic has been fertile ground for activity and research over the course of the preceding year. OPN strives to ensure that engineering, science, and technology are all represented. The number of papers accepted overall is limited by space. This year, a significant increase in submissions in the field of bio-optics reflects the rapid growth registered in this area of research.

OPN and OSA would like to thank the hundreds of researchers from all over the world who submitted summaries to "Optics in 2001."

# SPECTROSCOPY

## Relating Localized Electronic States to Host Band Structure In Rare-Earth-Activated Optical Materials

Charles W. Thiel, Herve Cruguel, Huasheng Wu, Yongchen Sun, Gerald J. Lapeyre, Rufus L. Cone, Randy W. Equall, and Roger M. Macfarlane

Rare-earth ions have a multitude of technological applications as optically active impurities in insulators and semiconductors. Understanding the properties and performance of these optical materials often requires knowledge of the energies of the host crystal's electronic band states relative to the  $4f^N$  or  $4f^{N-1}5d^1$  states responsible for the ion's optical transitions. This knowledge is important because energy and electron transfer between these states can influence the optical material's efficiency and stability.<sup>1</sup> Although little is known about the relationships between these states, the motivation to explore these properties is growing. Better understanding of these properties could accelerate the development of ultraviolet laser materials,

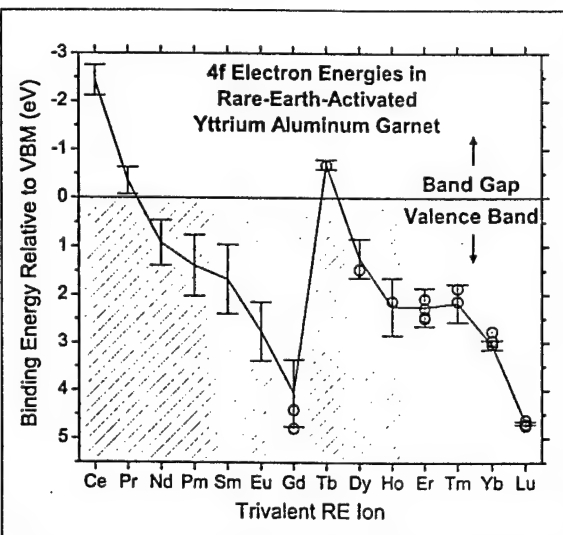


**Figure 1.** Relating localized electronic states to host band structure. Circles represent measured  $4f$  electron binding energies relative to the valence band maximum (VBM). Negative binding energies are within the bandgap of the host, and positive energies are below the VBM. The solid line is the model's fit to our measured values. The error bars on the model are due to uncertainty in the input parameters and can be improved with further measurements on more materials. Note that the bottom of the conduction band lies at about  $-6.5$  eV.

phosphors for applications such as plasma displays and mercury-free lamps, scintillator materials for medical imaging, and optical data processing and storage technologies based on photorefractivity or photogated photoionization holeburning. In order to fully understand the properties of current optical materials and logically develop new materials, knowledge of the systematic trends and behavior of rare-earth energies will be required.

We have recently initiated a systematic study of the energies of the rare-earth ions' electronic states relative to the host band states in optical materials using resonant electron photoemission spectroscopy (REPS).<sup>2,3</sup> REPS directly determines the energies of all occupied electronic states relative to a common energy reference and can unambiguously separate and assign spectral features to a particular electronic state.<sup>4</sup> Figure 1 presents results for yttrium aluminum garnet (YAG), the most important host crystal for solid-state lasers. Circles

represent measured binding energies of the rare-earth  $4f^N$  ground state relative to the valence band maximum (the host's highest energy occupied state).

These results have led to an empirical model that successfully describes the rare-earth binding energies in optical materials with two parameters: one describes a constant shift experienced by all rare-earth ions, and the second describes a smaller dependence on the ionic radius of the rare-earth ion. These empirical parameters may be determined from measurements on just two different rare-earth ions, or in certain cases, simply from measurements on the host crystal itself. With parameters determined from our measured data, the model predicts the energies of the remaining ions, as shown in Fig. 1.

This information is directly relevant to understanding and predicting properties critical for many technological applications. These properties include excited-state absorption energies to the conduction band and relaxation pathways involving ionization. For example, the results for YAG predict that the ionization of  $Nd^{3+}$  occurs at energy larger than the band gap and that ionization from  $1.064\text{ }\mu\text{m}$  laser photons requires a very low probability five-photon absorption from the upper laser level. In contrast, the results for  $Ce^{3+}$  predict that excited-state absorption to the conduction band would overlap emission wavelengths from the  $5d^1$  to  $4f^1$  transition, resulting in parasitic absorption that prevents its use as a tunable blue laser. All of these results suggest that systematic studies of additional host compounds will rapidly lead to a clearer picture of the host's effect on the rare-earth ion's  $4f$  electron binding energies that will motivate fundamental theoretical analysis and accelerate the development of new optical materials.

### References

1. See, for example, G. Blasse and B. C. Grabmeier, *Luminescent Materials* (Springer, Berlin, 1994).
2. C.W.Thiel, et al., *Phys. Rev. B* **64**, 085107-1-13 (2001).
3. C.W.Thiel, et al., *J. Lumin.* **94-95**, in press (2001).
4. J.W.Allen, "Resonant Photoemission of Solids with Strongly Correlated Electrons," in *Synchrotron Radiation Research: Advances in Surface and Interface Science*, edited by R. Z. Bachrach (Plenum Press, New York, 1992), Vol. I, 253-323.

Charles W. Thiel, Herve Cruguel, Huasheng Wu, Yongchen Sun, Gerald J. Lapeyre, and Rufus L. Cone, Department of Physics, Montana State University, Bozeman, MT, Randy W. Equall, Scientific Materials Corporation, Bozeman, MT, Roger M. Macfarlane, IBM Almaden Research Center, San Jose, California.

# Systematics of $4f$ electron energies relative to host bands by resonant photoemission of rare-earth ions in aluminum garnets

C. W. Thiel, H. Cruguel,<sup>\*</sup> H. Wu,<sup>†</sup> Y. Sun, G. J. Lapeyre, and R. L. Cone  
*Department of Physics, Montana State University, Bozeman, Montana 59717*

R. W. Equall  
*Scientific Materials Corporation, 310 Icepond Road, Bozeman, Montana 59715*

R. M. Macfarlane  
*IBM Almaden Research Center, 650 Harry Road, San Jose, California 95120*  
 (Received 9 February 2001; published 7 August 2001)

The energies of trivalent rare-earth ions relative to the host valence band were measured for a series of rare-earth-doped yttrium aluminum garnets  $R_xY_{3-x}Al_5O_{12}$  ( $R=Gd, Tb, Dy, Ho, Er, Tm, Yb$ , and  $Lu$  and  $0 \leq x \leq 3$ ), using ultraviolet photoemission spectroscopy. The  $4f$  photoemission spectra were acquired using synchrotron radiation, exploiting the  $4d$  to  $4f$  “giant resonance” in the  $4f$  electron photoemission cross section to separate the  $4f$  contribution. Theoretical valence band and  $4f$  photoemission spectra were fit to experimental results to accurately determine electron energies. The measured  $4f^n$  ground-state energies of these ions range from 700 meV above the valence band maximum for  $Tb^{3+}$  to 4.7 eV below the valence band maximum for  $Lu^{3+}$ , and all ground-state energies, except for  $Tb^{3+}$ , are degenerate with valence band states. An empirical model is successful in describing the relative energies of the  $4f^n$  ground states for rare-earth ions in these materials. This model is used to estimate the positions of the lighter rare-earth ions, giving good agreement with published excited-state absorption and photoconductivity measurements on  $Ce^{3+}$  in yttrium aluminum garnet. It is shown that the energies of the  $4f$  electrons relative to the valence band can be estimated from the photoemission spectrum of the undoped host, providing a simple method for extending these results to related host crystals. The success of this model suggests that further studies of additional host compounds will rapidly lead to a broader picture of the effect of the host lattice on the  $4f$  electron binding energies.

DOI: 10.1103/PhysRevB.64.085107

PACS number(s): 71.55.-i, 71.20.-b, 68.35.Ja, 73.61.Ng

## I. INTRODUCTION

There is a great body of work on the optical spectra of rare-earth impurities in insulating host crystals, with the vast majority involving the atomiclike intraconfigurational  $4f^n$  to  $4f^n$  transitions. Due to the shielding provided by the outer closed shells of  $5p$  and  $5s$  electrons, the  $4f^n$  electronic states exhibit a strong atomic character that makes them of particular interest for both fundamental research and optical applications that benefit from their unique properties. In contrast to the extensive information available about the  $4f^n$  electronic states, much less is known regarding the relationships between localized  $4f^n$  levels and the electronic band states of the host crystal. Systematic study of the positions of  $4f^n$  levels relative to the host band states for rare-earth ions in a range of materials is necessary to improve the understanding of interactions between these two very different types of electronic states and to allow models with predictive power to be developed and refined. With this goal in mind, we have studied a series of rare-earth ions over a range of concentrations in yttrium aluminum garnet and applied an empirical model for purposes of explanation and prediction.

In this paper, we present the results of resonant photoemission spectroscopy on trivalent rare-earth ions in yttrium aluminum garnet (YAG), the most important host crystal for rare-earth solid-state lasers. Photoemission spectroscopy offers several advantages over other techniques and can pro-

vide information that complements optical measurements. Photoemission allows the energies of both valence and atomic (core) electronic states to be directly determined relative to a common energy reference, whereas interpretation of optical methods such as excited-state absorption and photoconductivity may be complicated by uncertainty regarding the nature of the initial and final states involved. We employed resonant photoemission to measure the binding energies of the  $4f$  and valence band electrons for the series of rare-earth ions from  $Gd^{3+}$  through  $Lu^{3+}$ , which allowed the  $4f$  and valence band spectra to be separated and analyzed independently by exploiting resonances in the  $4f$  photoemission.<sup>1,2</sup> The photoemission spectra of both the valence band and  $4f$  electrons were fit to theoretical models to provide accurate estimates for electron energies and relative positions. Since very little is known about the effect of concentration on the relative energies of the  $4f^n$  levels and band states, measurements were made for materials with rare-earth concentrations ranging from pure YAG to the stoichiometric rare-earth aluminum garnets. Our measurements indicate that the energies of both the rare-earth ions and the valence band maximum (VBM)—the highest-energy valence band state—are insensitive to the doping concentration to within an experimental accuracy of a few hundred meV.

The relative positions of different trivalent rare-earth ions are successfully described by an empirical two-parameter model for the effect of the host crystal. For the heavier rare-earth ions, it is shown that the relative energies are well

described by the difference in free-ion ionization potentials. When extended to the lighter rare-earth ions, which are significantly larger than yttrium, a correction for the change in ionic radius must be included to obtain accurate energies. This model is used to predict the binding energies of the lighter rare-earth ions in YAG and the results agree well with published excited state absorption and photoconductivity measurements, indicating that measurements on as few as two different rare-earth ions in a host are sufficient to predict the energies of the remaining ions. A method derived from an electrostatic model for the effect of the host lattice is also suggested for estimating the binding energies of rare-earth ions that substitute for yttrium through measurement of the binding energies of the yttrium core levels in either doped or undoped samples.

## II. BACKGROUND

Developing a complete picture of the electronic structure of rare-earth-doped insulators is essential for understanding interactions between rare-earth ions and host band states and how they influence basic material properties. In particular, charge transfer between the rare-earth ions and the host can lead to broad absorption bands in the visible or ultraviolet regions of the spectrum, possibly resulting in the generation of color centers in the lattice. Because the charge transfer transition strength depends on the spatial overlap between the initial and final electronic states, intense metal-to-ligand charge transfer bands may appear in an ion's excited-state absorption spectrum even when no corresponding feature is observed in the ground-state absorption spectrum; this is particularly important when the excited state is a mixed configuration such as  $4f^{n-1}5d^1$ . Host band states may also influence the atomic transitions of the ion itself by inducing broadening and an increase in transition probability for forbidden transitions through hybridization, while interactions between the band states and the  $4f$  electrons also provide a mechanism for energy transfer, nonradiative relaxation, and nonlinear optical effects. These processes are all of fundamental physical interest since they represent coupling between the two extremes of highly localized and strongly correlated  $4f$  electrons of the rare-earth ion and delocalized one-electron band states of the host crystal.

The rare-earth ions have found numerous applications in modern technology as optically active impurity ions doped into both insulators and semiconductors. For many of these applications, knowledge of the position of the localized  $4f$  electronic states relative to the band states of the crystalline host lattice is important for understanding the performance of an optical material. For example, in solid-state laser materials, charge transfer transitions from the excited states of rare-earth ions to the conduction band of the host lattice often cause a parasitic absorption that overlaps lasing wavelengths, resulting in crystal heating and a reduction of both gain and tuning range, and may completely inhibit laser action, as for  $\text{Ce}^{3+}$  and  $\text{Pr}^{3+}$  in YAG.<sup>3-5</sup> Excited-state absorption can also create color centers and optical damage and is the dominant reason for the failure of otherwise promising tunable blue and ultraviolet laser materials.<sup>6,7</sup> In contrast,

ionization can be beneficial for applications such as proposed optical memories, optical processors, and frequency standards based on photorefractive effects or photon-gated photoionization hole burning, which may employ controlled ionization of the rare-earth ions for nonvolatile data storage and processing.<sup>8</sup> The one- and two-photon photoionization processes can potentially cause undesirable photodarkening of rare-earth-doped optical fibers and is a mechanism for the generation of optical gratings in these fibers.<sup>9</sup> The radiation hardness of optical materials, which is essential for space-based applications, is strongly influenced by the energy of the rare-earth ions relative to the host bands. In the particular case of YAG, some rare-earth ions resist radiation damage, while others suffer damage through oxidation or reduction.<sup>10</sup> Recent studies suggest that the efficiency of scintillator and phosphor materials is influenced by the position of the  $4f^n$  levels relative to the band states through both ionization of excited rare-earth ions and energy exchange between band states and  $4f^n$  states.<sup>11,12</sup> In new luminescent materials for plasma and flat panel displays, the performance limitations of potential red and blue electroluminescent materials may arise from field-induced or thermal ionization of the rare-earth ions.<sup>13</sup>

Most past experimental and theoretical work to locate  $4f^n$  energies relative to the crystal's electronic states has focused on metals and mixed valence materials, particularly cerium compounds,<sup>14,15</sup> however, there have also been notable efforts to characterize the  $4f^n$  energies of divalent and trivalent rare-earth impurities in insulating host materials. X-ray photoemission spectra of the valence band and  $4f$  electrons have been examined by Wertheim *et al.*<sup>16</sup> for the full series of rare-earth trifluorides, where both the final-state structure of the  $4f$  photoemission and general trends in the  $4f$  binding energies were noted. Much of the work on optical materials has involved optical measurements of transition energies using excited-state absorption or photoconductivity and has arisen from the search for blue and ultraviolet laser materials based on the high-energy transitions of the divalent and trivalent rare earths.<sup>3-5,17,18</sup> The need for more efficient phosphor and scintillator materials has led to measurements of the position of the  $4f^n$  levels relative to band states in oxides containing  $\text{Ce}^{3+}$ ,  $\text{Pr}^{3+}$ ,  $\text{Eu}^{2+}$ ,  $\text{Yb}^{3+}$ , and  $\text{Lu}^{3+}$  as both impurities and host constituents.<sup>12,19</sup> Pedrini *et al.*<sup>20</sup> have also characterized the  $4f^n$  levels relative to band states by studying the photoionization thresholds of the divalent rare-earth ions in several alkaline-earth fluorides and comparing them to thresholds calculated from an electrostatic point-charge model.

## III. APPARATUS AND SAMPLES

The photoemission experiments were performed on the Iowa State/Montana State ERG/Seya beam line at the University of Wisconsin-Madison Synchrotron Radiation Center. The Aladdin electron storage ring was operated at 800 MeV or 1 GeV and the synchrotron radiation was dispersed with a combined ERG/Seya monochromator.<sup>21</sup> The extended range grasshopper (ERG) monochromator was used for these experiments and operated primarily in the energy range of

125–185 eV, with the resolution varying between 125 meV and 275 meV, respectively. The focused spot size at the sample position was 1 mm by 20  $\mu\text{m}$  for these experiments. The measurement end station on the beamline consisted of three chambers. The air interlock allowed for introduction of a sample from atmosphere into the main analysis chamber without breaking its vacuum. The midchamber located between the air interlock and the main chamber was used to outgas the sample and holder before introduction into the main chamber. The main chamber featured a VSW HA50 angle-resolved hemispherical energy analyzer on a double-axis goniometer, a manipulator with three translational and three rotational degrees of freedom, a sample cleaver, a low-energy electron flood gun, an  $\text{Ar}^+$  sputtering gun, and a magnesium evaporator. The analyzer was operated with constant electron pass energy providing a resolution of 250 meV; thus, the total instrumental resolution varied between 275 meV and 375 meV for the photon energies used. The analyzer was aligned to collect electrons emitted normal to the sample surface to maximize the photoemission sampling depth, and the photon beam was typically incident at  $\sim 30^\circ$  from the surface normal.

The materials studied in this work were rare-earth-doped yttrium aluminum garnets ( $R_x\text{Y}_{3-x}\text{Al}_5\text{O}_{12}$ ), which belong to the cubic space group  $Ia3d$  (number 230).<sup>22</sup> Rare-earth concentrations greater than 5% were required to clearly observe the 4f photoemission with the current experimental arrangement. Ions larger than  $\text{Gd}^{3+}$  could not be doped into YAG with sufficient concentration for this series of experiments due to the increasing mismatch of ionic radius with  $\text{Y}^{3+}$ , which limited the materials that could be studied to the heavier rare-earth ions ( $\text{Gd}^{3+}$  to  $\text{Lu}^{3+}$ ). Measurements were made on undoped YAG and rare-earth-doped samples with atomic concentrations ranging from 7% ( $x=0.21$ ) to the stoichiometric rare-earth aluminum garnets ( $x=3$ ). The single-crystal GdAG, TbAG, DyAG, and HoAG samples were grown from flux by S. Mroczkowski at the Department of Applied Physics, Yale University. All other samples were single crystals grown at Scientific Materials Corporation (Bozeman, MT) using the Czochralski method.

Due to the surface sensitivity of the photoemission process, particularly in the 100–200 eV energy range,<sup>23</sup> surface purity was essential. To ensure clean surfaces, all samples were fractured *in situ* using the sample cleaver while the vacuum in the chamber was maintained at  $10^{-9}$  Torr or better at all times. Since YAG has no cleavage planes, fracturing the sample resulted in surfaces with random orientations that were typically uneven across the crystal and of visibly rough texture. No attempt was made to orient the samples. The photon beam was focused onto the smoothest region of each surface to minimize potential depth of field effects. No observable surface contamination was present in any spectra, although a broadening of several meV per minute was observed, possibly due to development of deep differential charging in the sample or relaxation of the fractured surface. To maintain the best possible surface quality for all collected spectra, the samples were refractured whenever spectral broadening became apparent. Each new surface was oriented differently due to the unconstrained nature of the fracture; as

a result, spectra were collected with several surface orientations for each sample. There was no observable dependence on orientation in the experimental spectra, and all results presented here represent an average over several orientations. Both argon ion sputtering and sample heating were tested as alternate preparation methods; however, we found that sputtering significantly broadened the spectral features, while heating tended to produce metallic features in the spectrum, presumably from a depletion of oxygen from the surface.

#### IV. SAMPLE CHARGING CONSIDERATIONS

The process of photoemission ejects electrons from the sample being studied and thus generates a positive charge in the sample. In metals and semiconductors, the conductivity of the sample is sufficient to compensate any removed charge and maintain the sample at a uniform potential. In insulators such as YAG, the resistance of the sample is large enough that a significant positive potential will develop in the region of photoemission. The induced voltage retards ejected photoelectrons, reducing their kinetic energy at the detector and producing an apparent increase in the measured binding energies.<sup>24</sup> Nonuniform charging of the sample can also cause electrons originating from different regions of the sample to experience different retarding potentials. This differential charging effect produces an overall broadening in the observed spectrum and may cause peak shapes to become distorted.<sup>25</sup> Sample charging is highly dependent on crystal purity and experimental conditions, and combinations of electron flooding and spectral calibration to a reference peak are commonly used to compensate for its effects.<sup>26</sup>

For the YAG samples studied, photoemission resulting from the applied ultraviolet light rapidly generated a potential on the sample that was large enough to prevent observation of direct photoemission. To overcome this difficulty, an electron flood gun was used to partially compensate the positive charging from photoemission. We found that flooding electrons with low kinetic energy ( $\sim 10$  eV) minimized distortion and broadening of the spectral features. Residual charging shifts varied from a few eV to tens of eV for the different samples examined and were extremely sensitive to photon energy, surface orientation, and surface quality. Sequences of spectra were recorded independently to monitor time-dependent charging shifts and ensure that there was no drift of the spectrum during the period of data acquisition. To further minimize the effect of time-dependent charging shifts, the maximum acquisition time was restricted to several minutes or less and the spectra were individually calibrated and then averaged together to obtain the final spectrum. The aluminum 2p photoemission peak was used as a reference for removal of relative charging shifts between different spectra of an individual sample. To check for shifts in the binding energy of the Al 2p peak for different samples fractured *in situ*, magnesium was evaporated onto a fractured surface of each sample and the position of the Al 2p peak was measured relative to the metallic Mg 2p peak. The binding energy reference was established using the common method of placing the carbon 1s peak at a binding energy of 290 eV relative to the vacuum level (a value of 285 eV is

often used when binding energies are referenced relative to the Fermi level of the analyzer).<sup>27,28</sup> The calibration was determined by measuring the positions of the core levels in pure YAG relative to the carbon 1s peak, and then using the Mg 2p and Al 2p peaks for subsequent binding energy calibrations. No carbon was observed on any samples fractured *in situ*; therefore, the binding energies were determined using the position of the small carbon 1s signal originating from adventitious carbon contamination on a YAG sample fractured in air. The measured binding energy of the center of the Al 2p peak was 78.8 eV for all samples studied, which agrees well with previous x-ray photoemission studies of core levels in YAG.<sup>29</sup> Since the precise binding energy of carbon 1s depends on the chemical environment (varying between 290 eV and 291 eV for hydrocarbon contaminants) (Ref. 27) and contact potentials present in the electron analyzer, absolute binding energies determined by calibrating to carbon 1s may exhibit a systematic shift relative to their true values; however, any systematic shift in the binding energies does not affect measurements of relative binding energies.

Differential charging was a source of broadening in the spectra and arose from several sources such as the irregular nature of the fractured surfaces, inhomogeneity in the light intensity over the focused spot, reduced probability for electron escape for ions further from the surface, and electric fields originating from regions of the crystal not directly illuminated. The differential charging produced low-binding-energy tails on all of the spectral features as well as an overall broadening. A broadening that varied from 1.5 eV to 2.5 eV was observed in all spectra and was primarily attributed to differential charging, although lifetime broadening could also be a significant contribution.

In addition to simple broadening, spectral distortion due to differential charging was also observed in all spectra. The most obvious distortion was a double-peaked structure present in the spectra of all samples for the photoemission peaks of both lattice constituents and metals evaporated onto the crystals. The double peaks had a relative shift that varied from 2 eV to 8 eV and an intensity ratio of roughly 1:5, with the weaker feature corresponding to regions of lesser charging. The same relative intensity and energy shift was observed for every photoemission peak in each spectrum, although the values could be significantly different for spectra taken at separate times. The relative intensity and energy shift observed in each spectrum was strongly dependent on all aspects of the experiment including sample alignment, electron gun current, source intensity, photon energy, and surface morphology. This effect was clearly due to differential charging and was attributed to a small transverse intensity variation over the source beam.

Since the charging distortion varied significantly between spectra, it was necessary to remove this effect from the data to permit the most accurate comparisons and consistent measurements. The observed peak shapes suggested modeling the measured spectra as resulting from simultaneous photoemission from two separate regions of the sample with different surface potentials. This model viewed the spectrum as composed of two spectra that were identical except for a relative shift, different intensities, and a relative change in

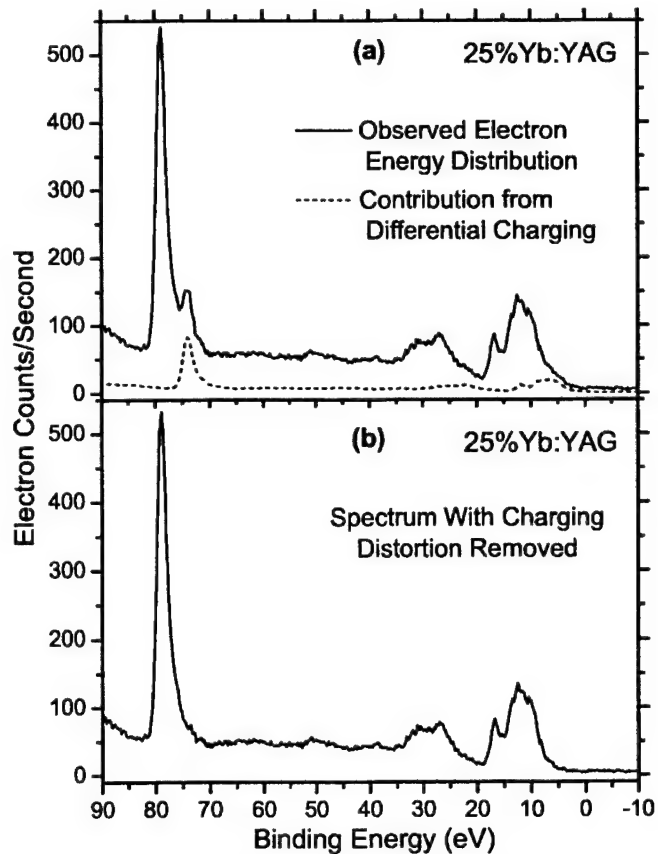


FIG. 1. Example of photoemission spectrum before and after removal of charging distortion (see Sec. IV). (a) The solid line shows the photoemission spectrum of 25% Yb:YAG ( $h\nu = 181.5$  eV) which is composed of two components with a relative charging shift, and the dotted line is the estimate of the smaller component of the spectrum as determined from fitting. (b) The difference of the two spectra in the upper plot. The model used to determine the shape of the subtracted spectrum forces the two components to be identical except for a relative shift, different intensities, and a relative broadening. For this example, the weaker component [dotted line in (a)] corresponds to the stronger component (b) shifted by 4.8 eV, scaled by 0.16, and broadened by 100 meV.

broadening. A relative broadening was included to allow for variations in differential charging between the two regions of the sample, with the weaker feature typically broadened by a few hundred meV relative to the stronger feature. This model was sufficient to separate the two components present in the spectrum without making further assumptions regarding the actual shapes of the photoemission peaks. A nonlinear fitting routine was used on the relatively sharp Al 2p photoemission peak in each spectrum to determine the relative shift, intensity, and broadening of the two components in the model. This model produced excellent results for removal of the charging distortion, and the parameters determined from fitting the Al 2p peak were effective in describing the charging distortion for all features in each spectrum. Figure 1 shows an example of this process for 25% Yb:YAG. The distortion present in the valence band region is relatively small, but must be removed in order to make precise comparisons between spectra.

## V. ANALYSIS OF 4f AND VALENCE BAND PHOTOEMISSION SPECTRA

Photoemission spectroscopy measures the kinetic energy distribution of electrons ejected from a sample exposed to monochromatic light. These energy distribution curves may be used, together with knowledge of the photon energy, to infer the binding energy distribution of the electronic states in the sample. In addition to the features arising from the direct emission of electrons from the sample, a background due to inelastically scattered, or secondary, electrons is also present in the photoemission spectrum. This secondary electron background was removed from each individual photoemission peak when comparing and analyzing spectra. To subtract the background, the well-known Shirley method was employed in which the magnitude of the secondary electron background at any kinetic energy is approximated as proportional to the total direct photoemission at higher kinetic energies.<sup>30</sup> This model was applied iteratively until the estimated background matched the actual background on both sides of the photoemission peak under consideration.

The photoemission spectrum contains information about both the 4f electrons of the rare-earth impurity and the electronic states of the host crystal, allowing the energies of the states to be measured relative to a common reference. In Sec. V A, we outline the use of resonant photoemission to identify and extract the 4f component of the crystal's photoemission spectrum. Sections V B and V C discuss the analysis of the structure of the 4f and valence band photoemission, respectively. In Sec. V D, the binding energy measurements are summarized and discussed.

### A. Separating the 4f and valence band photoemission spectra

One of the difficulties in measuring the position of the 4f<sup>n</sup> levels using photoemission is that they often overlap the host valence band. To extract the 4f component of the spectrum, we employed the technique of resonant photoemission spectroscopy, which exploits resonances in the photoemission cross section through the flexibility provided by synchrotron radiation.<sup>1</sup> For the partially filled 4f shell of rare-earth ions, a "giant resonance" in the 4f photoemission occurs for photon energies that excite the atomic 4d<sup>10</sup>4f<sup>n</sup> to 4d<sup>9</sup>4f<sup>n+1</sup> transition of the ion.<sup>2,15,31</sup> This transition energy lies between 100 eV and 200 eV for the trivalent rare-earth ions,<sup>32</sup> and the technique of constant initial-state-energy spectroscopy (CIS) (Ref. 33) was used to locate the precise position and shape of this resonance for each rare-earth ion studied in YAG. CIS measures the photoemission cross section as a function of photon energy; thus, the 4f resonance can clearly be discerned in the CIS spectrum of the valence band region ( $\sim 5$  eV to  $\sim 20$  eV binding energy) for photon energies from 100 eV to 200 eV. An example CIS spectrum for DyAG is displayed in Fig. 2, as well as photoemission spectra taken at four different photon energies ranging from the minimum of the 4f photoemission to the maximum. The shape of the resonance in the 4f photoemission shows a complex structure due to both the 4f level structure and coupling to the 4d hole, with the individual components exhibiting a distinctive Fano line shape resulting from interfer-

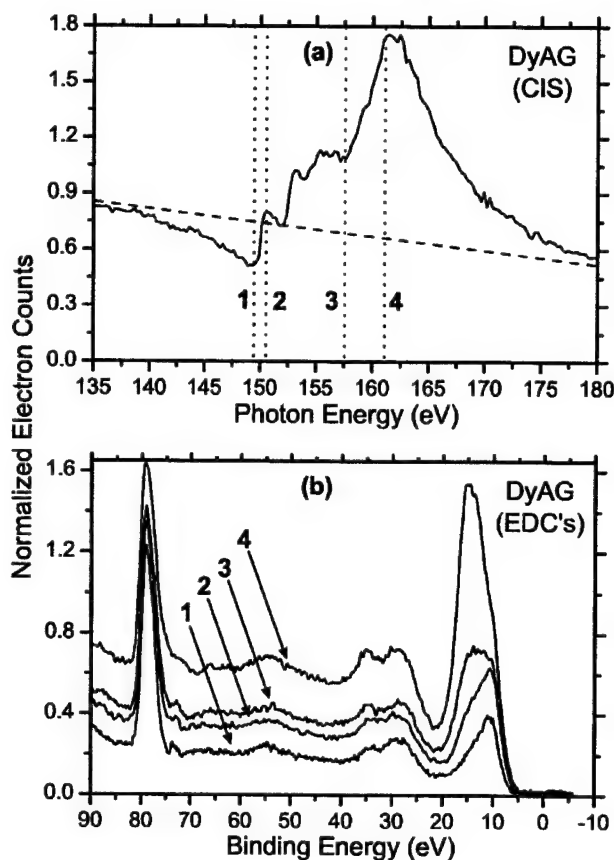


FIG. 2. The 4d to 4f resonance in the 4f photoemission of DyAG. (a) The constant-initial-state energy spectrum (CIS) of the valence band region (5–20 eV binding energy) of DyAG showing the 4d to 4f resonance in the 4f photoemission. The dashed line shows the trend of the combined valence band and 4f cross section outside of the resonance. The four dotted vertical lines indicate the photon energies used in generating the 4f spectra ( $h\nu_1 = 149.5$  eV,  $h\nu_2 = 150.5$  eV,  $h\nu_3 = 157.5$  eV, and  $h\nu_4 = 161.0$  eV). (b) The energy distribution curves (EDC's) corresponding to the four photon energies indicated in the CIS spectrum. The photoemission spectra have all been normalized to the intensity of the Al 2p peak and the charging effects have been removed as discussed in Sec. IV.

ence between the resonant 4d to 4f Auger component and direct 4f component of the photoemission.<sup>1,34</sup> This interference effect causes the total 4f photoemission to be initially suppressed and then enhanced as the photon energy is increased. Because of the relatively large change in the 4f photoemission cross section over this region, the 4f component may be extracted by subtracting a spectrum taken at the minimum of the 4f photoemission from a spectrum taken at the maximum, scaled by a factor to compensate for the small change in the valence band cross section,<sup>35</sup> as shown for 7% Gd:YAG in Fig. 3. The scaling factor, with typical values of 1.0–1.1, is necessary to ensure that the valence band contributions in both spectra are equal and therefore cancel when taking the difference. The precise values of the scaling factors were determined by measuring the CIS spectra of both the valence band and Al 2p peak in undoped YAG and then using the measured photoemission intensity of the Al 2p

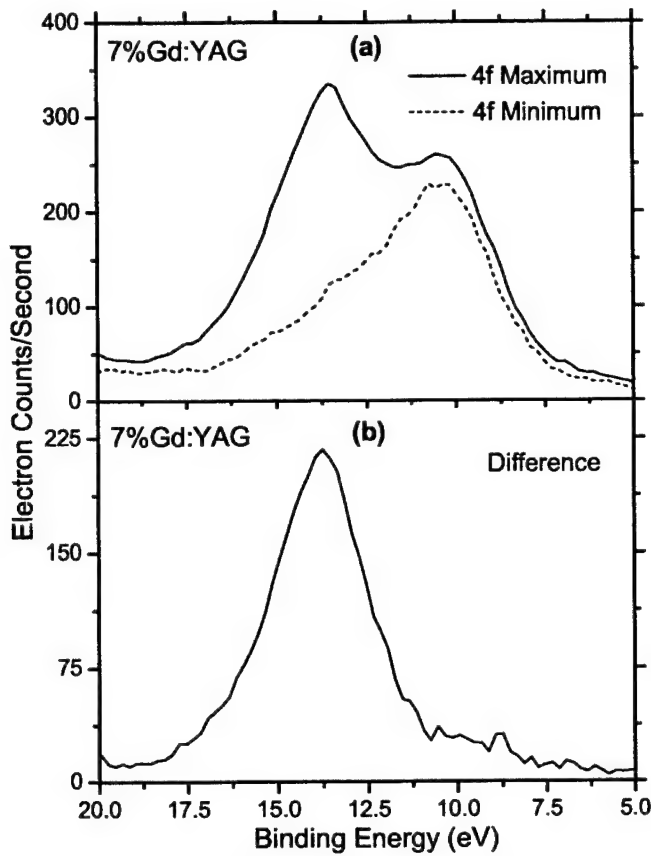


FIG. 3. Example of extracting the  $4f$  component of the photoemission spectrum. (a) Spectra taken at the minimum ( $h\nu = 144.0$  eV) and maximum ( $h\nu = 148.5$  eV) of the  $4f$  photoemission for 7%Gd:YAG. The spectra have been scaled so that the valence band component has the same amplitude in both spectra. (b) The difference of the two curves in (a) gives the  $Gd^{3+}4f$  photoemission.

peak in each spectrum to normalize for both the overall electron yield and changes in the valence band cross section. Because the photon energy dependence of the cross section was determined from undoped YAG, any potential resonance in the valence band resulting from hybridization of the  $4f$  electrons with the valence band was ignored; nevertheless, this effect should be small since mixing of the  $4f^n$  states with the valence band is expected to be negligible. Once the  $4f$  spectrum was obtained, an estimate of the valence band spectrum was acquired by subtracting the small  $4f$  component from the spectrum taken at the minimum of the  $4f$  photoemission.

For  $Lu^{3+}$ , an alternate method was necessary to obtain the  $4f$  spectrum since there is no  $4d$  to  $4f$  transition because of the filled  $4f$  shell. The  $Lu^{3+}$  spectrum was extracted by using the different photon energy dependence of the photoemission cross sections of the rare-earth  $4f$  electrons and valence band electrons, which are primarily of oxygen  $2p$  character in YAG.<sup>36</sup> Over the energy range of 100–200 eV, the  $4f$  cross section remains nearly constant while the oxygen  $2p$  cross section rapidly decreases.<sup>37</sup> As a result, the  $Lu^{3+}$  spectrum may be obtained by subtracting a spectrum taken at low photon energy from a spectrum taken at high

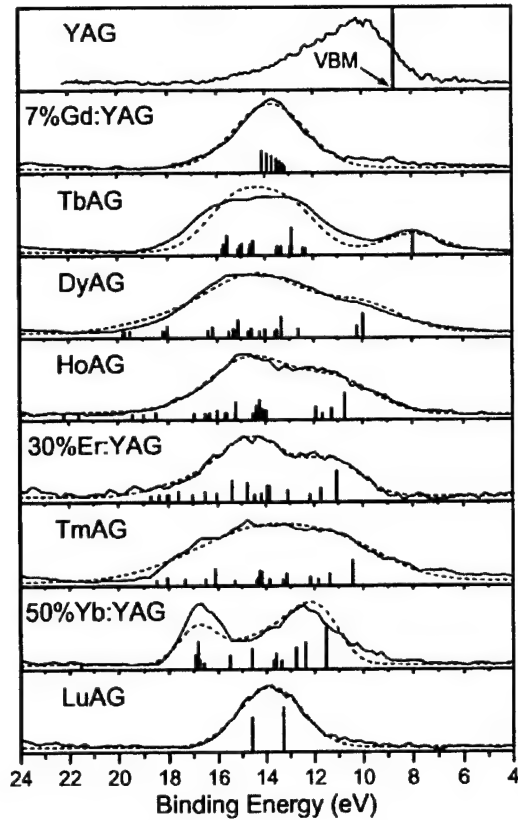


FIG. 4. Representative data for each ion studied. Solid lines represent measured  $4f$  photoemission spectra with the secondary electron background subtracted and dotted lines are fits to the theoretical final state structure (see Sec. V). The vertical lines represent the underlying energy level structure and their height represents their relative contribution to the photoemission (only states that contribute more than 0.1% are shown). The valence band of YAG has been plotted for reference, with the position of the valence band maximum shown as a vertical line.

photon energy, scaled such that the valence band contributions are equal in both spectra.

Once the photon energies corresponding to the minimum and maximum of the  $4f$  photoemission were determined, spectra were taken for several photon energies between these extremes and compared in a pairwise manner to produce a series of  $4f$  spectra. All generated  $4f$  spectra were compared for consistency in both the removal of charging effects and compensation of the different valence band cross sections. Final  $4f$  spectra were generated for each sample by averaging the  $4f$  spectra obtained from each pair of photon energies. Since any peculiarities in the spectra due to charging distortions or calibration errors were usually different for each spectrum, the averaging process tended to reduce distortions to a simple broadening that minimized the possibility of systematic errors. The  $4f$  spectra for a representative concentration of each rare-earth ion studied are given in Fig. 4, along with the spectrum of undoped YAG.

## B. Analysis of $4f$ photoemission final-state structure

The  $4f$  photoemission spectra show structure that extends over a range of up to 10 eV corresponding to excitation of

upper electronic states of the tetravalent rare-earth ions.<sup>38,39</sup> This structure arises because the photoemission process may leave the emitting ion in an excited state, reducing the kinetic energy of the ejected electron, and therefore resulting in an apparent increase in binding energy due to the final state of the system. The contribution to the photoemission spectrum from each final state can be described by the projections of the  $4f^n$  ground-state wave function—with a single electron removed—onto the electronic states of the  $4f^{n-1}$  configuration; thus, the energy levels of the tetravalent ion each contribute to the observed photoemission to a varying degree. The relative magnitude of each level's contribution to the photoemission spectrum was estimated using the fractional parentage method described by Cox.<sup>40</sup> The relative energies of the components present in the photoemission final-state structure are given by the energies of the  $4f^{n-1}$  levels of the tetravalent ion, which may be approximated by the well-known level structure of the isoelectronic trivalent ion,<sup>41</sup> expanded by 5%–15% to account for the enhanced effective nuclear charge of the tetravalent ion.<sup>39</sup> This approximation of the tetravalent energy levels and their relative contributions to the photoemission structure is sufficient for quantitative interpretation of the 4f photoemission spectra and determination of 4f binding energies.

The parameter of greatest interest for this study is the 4f ionization threshold—the energy required to remove one 4f electron and leave the remaining tetravalent rare-earth ion in its ground state. Although the low-binding-energy edge of the 4f photoemission gives a rough estimate for the ionization threshold, broadening obscures the exact location, requiring a method for determining the binding energy of the ground-state component of the final-state structure to facilitate a quantitative analysis of the results. To obtain a precise measurement of the 4f ground-state binding energy, the theoretical final-state structure of the 4f photoemission, including spin-orbit splittings, was fit to the observed 4f photoemission. The fitting process adjusted the energy, intensity, and broadening of the theoretical final-state structure to match the observed spectra. The energy scale factor due to the enhanced effective nuclear charge was also allowed to vary within the expected range of values during the fitting process since the exact values are not known. The fit of the theoretical final state structure to the observed 4f spectrum is displayed in Fig. 4 for each rare-earth ion studied, where the dotted line is the fit and underlying tetravalent energy levels are shown as vertical lines. The height of each vertical line represents its relative contribution to the photoemission and only states that contribute at least 0.1% to the total intensity are shown. By matching the predicted spectra to the measured spectra, particularly for the low-binding-energy region of the 4f photoemission, the binding energy that corresponds to leaving the tetravalent ion in its ground state was estimated and compared to the energy of the VBM. The agreement between the predicted structure and data is not perfect due to approximations in the calculation of the final-state structure, residual valence band contributions, and distortion from differential charging. Using more accurate wave functions in the calculations of the final-state structure would also improve the agreement, particularly for terbium;<sup>39</sup> however,

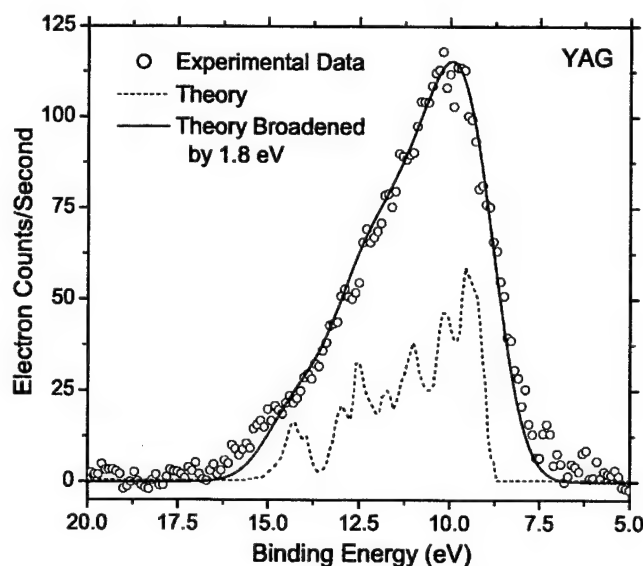


FIG. 5. Circles represent the measured photoemission spectrum of undoped YAG ( $h\nu = 125.0$  eV) with the secondary electron background subtracted. The dotted line is proportional to the theoretical valence band photoemission cross section at this photon energy obtained using the results of Refs. 36 and 37. The solid line is the theoretical shape broadened by 1.8 eV and scaled to match the experimental data. By comparing the theoretical curve to the data, an estimate of 8.7 eV is obtained for the binding energy of the valence band maximum.

this description of the final-state structure is adequate to determine the energy of the ground-state component with an estimated accuracy of several hundred meV. For most samples, the 4f spectra appeared to exhibit an additional broadening of 0.5–1.5 eV relative to the broadening of the valence band and core levels, possibly due to changes in differential charging and calibration between the different spectra used to generate the 4f spectra or lifetime broadening of the 4f photoemission.

### C. Analysis of valence band photoemission

Since we are interested in measuring the energies of the 4f electrons relative to the band states, as well as the effects of the rare-earth doping on the host lattice, an estimate for the binding energy of the VBM is required for each material studied. The photoemission spectrum of undoped YAG is plotted in Fig. 5, with the charging effects and secondary background removed. The VBM corresponds to the low-binding-energy edge of the valence band but experimental broadening obscures the exact location, making a precise measurement difficult. To overcome this difficulty, the observed valence band photoemission was compared to theoretical calculations. The theoretical shape of the valence band photoemission was estimated from the atom-resolved partial density of states calculations of Xu and Ching<sup>36</sup> weighted by the calculated atomic photoemission cross sections from Yeh and Lindau.<sup>37</sup> The theoretical cross section broadened by 1.8 eV gave excellent agreement with the experimental data, allowing an estimate for the underlying VBM to be obtained. Using this method, a value of 8.7 eV

TABLE I. Measured 4f electron ground-state binding energies (BE) relative to the valence band maximum for all samples studied. Following the usual sign convention for binding energies, positive values lie below the valence band maximum and negative values lie within the band gap.

Dopant ion	Concentration	$\Delta$ BE (eV)
Gd	7%	4.8
Gd	100%	4.4
Tb	100%	-0.7
Dy	100%	1.5
Ho	100%	2.1
Er	30%	2.5
Er <sup>a</sup>	30%	2.3
Er	50%	2.5
Er	100%	2.1
Tm	10%	2.1
Tm	100%	1.9
Yb	10%	2.8
Yb	25%	3.0
Yb	50%	3.0
Yb	100%	3.0
Lu	50%	4.7
Lu <sup>a</sup>	70%	4.7
Lu	100%	4.6

<sup>a</sup>Measured in 30% erbium doped lutetium aluminum garnet.

was determined for the binding energy of the VBM. A similar procedure was performed to determine the position of the VBM for each sample studied.

No significant dependence on crystal orientation was observed in the spectra, and the measured results represent an average over several random crystal orientations. This result is expected since the top of the valence band in YAG is very flat, with maximum variations of less than a few hundred meV throughout the Brillouin zone.<sup>36</sup> A flat valence band is characteristic of yttrium and aluminum oxides and implies that the relative energy of the VBM and 4f<sup>n</sup> states has very little orientation dependence in this class of materials.

#### D. Results of measurements and analysis

The measured binding energies of the 4f<sup>n</sup> ground states are given in Table I for all samples studied. Since the VBM exhibited a constant binding energy for all samples to within the experimental accuracy, and energy differences are unaffected by errors in absolute calibration, the position of the 4f<sup>n</sup> ground states are referenced relative to the VBM binding energy of 8.7 eV. Of the ions studied, Tb<sup>3+</sup>, which was 700 meV above the VBM, was the only ion with its 4f<sup>n</sup> ground-state energy within the host band gap. The 4f<sup>n</sup> ground states of all other ions studied were degenerate with valence band states, with Lu<sup>3+</sup> having the lowest ground-state energy at 4.7 eV below the VBM.

To study the effects of concentration on the energy level structure of the samples, rare-earth concentrations varying between pure YAG and the stoichiometric rare-earth aluminum garnets were examined. Although information about the

valence band could be obtained from all samples, the limitations of the experimental arrangement prohibited extraction of useful 4f spectra for samples with concentrations lower than 5%. A comparison of the 4f spectra of each ion for different concentrations revealed that, while the photoemission intensity was roughly proportional to the concentration as expected, the 4f binding energies were unchanged within the experimental accuracy of several hundred meV for the full range of concentrations studied. Additional comparisons of measurements on erbium-doped yttrium aluminum garnet and erbium-doped lutetium aluminum garnet did not reveal any significant shift in the Er<sup>3+</sup> binding energy. This may also be viewed as a lack of concentration dependence where the yttrium has been replaced by lutetium rather than the particular rare-earth ion being studied.

The results discussed above indicate that binding energies obtained for one concentration may be used as an estimate for all concentrations, to within the current experimental accuracy of several hundred meV. Further measurements are required to determine whether there are observable concentration shifts in other materials, with effects more likely to be observed for materials where the rare earths substitute for ions with a significantly different radius or materials in which the rare-earth ions compose a large fraction of the host volume.

Except for slight changes in the overall shape, the valence band remained essentially unchanged by the addition of rare-earth ions, and the valence band maximum maintained a constant binding energy within the experimental accuracy. The dominant oxygen 2p character of the electronic states comprising the valence band, particularly in the low-binding-energy region, might explain the limited effect of the rare-earth ion concentration.<sup>36</sup> In contrast, the strong yttrium and rare-earth character of the low-energy conduction band states might predict a dependence on both rare-earth ion and concentration for the band gaps of the materials.

#### VI. SYSTEMATIC BEHAVIOR OF THE 4f BINDING ENERGIES

There are several approaches to modeling the binding energies of localized electronic levels in a crystalline environment such as density-functional theory,<sup>42</sup> the renormalized atom approach,<sup>43</sup> thermodynamic arguments,<sup>44</sup> and electrostatic methods.<sup>28</sup> One model applicable to localized levels in an ionic host lattice is the electrostatic point-charge model, which was first applied to the estimation of ionization thresholds by Pauling.<sup>45</sup> Various versions of this model have since been used to predict the relative binding energies of core levels, absolute binding energies of electrons, excited-state absorption energies, and photoionization thresholds.<sup>17,18,20,46</sup> The essence of this model is to consider the lattice as consisting of point charges with integer valence, and then to calculate the shift in binding energy resulting from the electrostatic interactions between the ion and host. In this picture, we view the free-ion electron binding energy—which by definition is measured relative to the vacuum level—as being shifted by the electrostatic potential, or Madelung potential, of the lattice site that the ion occupies. Other effects

that must be considered in these calculations include (in order of decreasing importance) polarizability of the lattice, distortion of the lattice site due to the presence of the impurity, interatomic Born repulsive energies, and van der Waal's forces. These terms are generally of significant magnitude compared to the total binding energy, with the final result arising through partial cancellation of relatively large energies with opposite signs, requiring that all effects be calculated precisely. Because of this complexity, calculations of absolute binding energies based on this method are generally of limited accuracy and difficult to extend to more than a few materials because of the amount of information needed for accurate calculations.

### A. Shift of the ionization potential

Regardless of the accuracy in predicting absolute binding energies, one significant consequence of an electrostatic model is that the differences in binding energies for different ions should be approximately equal regardless of the host material. These binding energy differences are most easily found from differences of the known trivalent rare-earth free-ion ionization potentials,<sup>47</sup> which correspond to 4f electron binding energies in the free ions. The shielded nature of the 4f electrons in the trivalent rare-earth ions should provide an ideal case for application of this model, whereas, for most ions, this is an oversimplification due to the electronic mixing with the lattice (covalency) and the changes in the ionic and electronic radii. To test this approximation, we have compared the differences in published values of the free-ion ionization potentials to the measured 4f binding energies in YAG. This is shown in Fig. 6, where our measurements are represented by circles on the plot and the shifted free-ion ionization potentials correspond to the dotted line. The uniform binding energy shift was determined by shifting the average of the free-ion ionization potentials to the average of the measured binding energies, resulting in a shift of 31.6 eV. This simple model gives reasonable agreement with the experimental data to within the combined error bars of the published values for the ionization potentials and the experimental error in determining the binding energies. Due to the phenomenological nature of this model, it has the potential to describe effects not incorporated in an electrostatic model.

The agreement between the simple electrostatic model and the measured binding energies suggests several methods for estimating the 4f electron binding energies for a series of ions from a single measurement. For example, measurements for one rare-earth ion in a material should give an estimate for the energies of all the rare-earth ions by considering the differences in the free-ion ionization potentials. Since this method relies on the similarity in ionic radii, the accuracy of the estimate would decrease for larger changes in the ionic radius. For materials in which the rare-earth ion substitutes for yttrium, which has an ionic radius similar to the rare earths, the electrostatic model suggests the possibility of estimating rare-earth binding energies from the shift in the yttrium ion binding energies. This method would use the intrinsic yttrium ion in a host crystal as a "probe" for determining the effective electrostatic interactions at the lat-

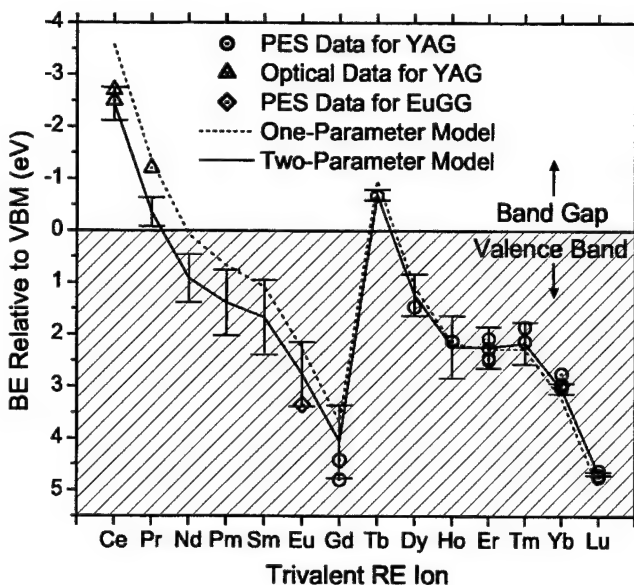


FIG. 6. Systematic behavior of 4f binding energies relative to the valence band maximum. Circles represent our measured binding energies relative to the VBM (at 8.7 eV); negative binding energies are within the band gap of the host and positive energies are below the VBM. The dotted line is the fit of the empirical model to our measured values without considering the effect of ionic radius. The solid line is the fit of the model to our measured values including the effect of ionic radius. The error bars on the model are due to uncertainty in the values of the free-ion ionization potentials and the error bars on the extrapolated values for Eu<sup>3+</sup> through Ce<sup>3+</sup> include the uncertainty due to the accuracy of the fitting parameters. The triangles represent estimated positions from excited-state absorption and photoconductivity measurements in Refs. 4, 5, and 20. The diamond is the estimated position in EuGG from Ref. 52. Note that the bottom of the conduction band lies at about -6.5 eV.

tice site, and then use this information to predict the effect of the lattice on the binding energies of a rare-earth ion placed at that site. For trivalent yttrium, the least bound electrons belong to the filled 4p shell, with a free-ion ionization potential of 61.8 eV.<sup>48</sup> The photoemission spectrum of the yttrium 4p electrons shows the final-state structure due to the spin-orbit splitting of the  $J=3/2$  and  $J=1/2$  levels, where the splitting is 1.2 eV and the  $J=3/2$  level is the ground state of the ionized yttrium.<sup>49</sup> Thus, in a manner similar to the method used for rare-earth ions, the electron energy that corresponds to leaving the tetravalent yttrium ion in its ground state may be determined by measuring the position of the 4p<sub>3/2</sub> level from the photoemission spectrum. In oxides, the oxygen 2s peak lies a few eV below the yttrium 4p peaks, requiring that the oxygen and yttrium peaks be fit simultaneously. The measured position of the 4p<sub>3/2</sub> level is 30.4 eV in YAG, giving a shift of 31.4 eV relative to the free-ion value, which agrees well with the 31.6 eV shift measured from the rare-earth ions. In the simplest approximation, the binding energy shift should be uniform for all core levels, allowing an estimate to be obtained from the shift of one of the well-resolved core levels. For example, the measured 3d<sub>5/2</sub> peak in YAG is at 162.5 eV and should be ~132.7 eV from 4p<sub>3/2</sub>,<sup>49</sup> giving a shift of 32.0 eV. This agreement sug-

gests that analysis of the undoped host's photoemission spectrum may be sufficient to predict the  $4f$  electron energies of the rare-earth ions with an ionic radius similar to yttrium's.

### B. Effect of ionic radius

The electrostatic model may also be used to extrapolate our observed binding energies in YAG to the lighter rare-earth ions, but the effect of the change in ionic radius must be included in the model to obtain accurate estimates for ions with a radius significantly different from yttrium. This effect arises primarily from the distortion of the lattice site caused by the presence of the rare-earth ion and was first considered by Pedrini *et al.*<sup>17</sup> for the case of divalent rare-earth ions in the fluorides, where it was found to be important for describing the observed  $4f$  photoionization thresholds. Any change in the ionic radius affects all of the terms in the electrostatic model through the corresponding changes in bond lengths; as a result, theoretical calculations of this effect would require precise knowledge of the lattice distortions induced by the presence of the impurity ion. Fortunately, the change in ionic radius across the rare earths is small enough to allow the net effect to be modeled as linear in ionic radius. This approximation allows the proportionality constant to be treated as an empirical parameter that can be determined from measurements on two different ions, with comparison of  $\text{Ce}^{3+}$  and  $\text{Lu}^{3+}$  giving the best estimate. Since this approach to the electrostatic model only contains two unknown parameters, measurements on two different rare-earth ions in an ionic host should be sufficient to predict the positions of all the remaining ions in that host, even when substituting for ions with a significantly different radius.

Using the two-parameter model, we extrapolated our measurements for YAG to the lighter rare-earth ions as shown in Fig. 6. This empirical model is given by the following equation:  $E_{4f} = I - E_L + \alpha_R(R - R_0) - E_{VBM}$ , where  $E_{4f}$  is the  $4f$  binding energy relative to the VBM,  $I$  is the free-ion ionization potential,  $E_L$  is the intrinsic electrostatic effect of the lattice ( $E_L = 31.6$  eV),  $\alpha_R$  is the binding energy shift per unit change in ionic radius,  $R$  and  $R_0$  are the effective ionic radii of the trivalent rare-earth and yttrium ions in eightfold coordination ( $R_0 = 1.019$  Å),<sup>50</sup> and  $E_{VBM}$  is the binding energy of the valence band maximum ( $E_{VBM} = 8.7$  eV). The dotted line in Fig. 6 corresponds to this model with a constant binding energy shift ( $\alpha_R = 0$ ), and the solid line corresponds to the full model ( $\alpha_R \neq 0$ ). The error bars in Fig. 6 represent the uncertainty in the free-ion ionization potentials for the ions studied, while the error bars on the extrapolated values for  $\text{Eu}^{3+}$  through  $\text{Ce}^{3+}$  also include the uncertainty in the extrapolation due to the accuracy of the two fit parameters. The effect of the ionic radius was determined by fitting our data to the linear model for the deviation from the free-ion ionization potentials, weighted by the accuracy of the free-ion ionization potentials used in the model. The resulting fit to our measurements indicates an  $\alpha_R = 8.3$  eV/Å effect in YAG arising from the change in ionic radius. This causes the estimated binding energy of  $\text{Ce}^{3+}$  to be increased by 1.0 eV and the estimated binding energy of  $\text{Lu}^{3+}$  to be reduced by 0.35 eV. The origin of this shift can be under-

stood in terms of the effect on the ion's nearest neighbors. An increase in ionic radius increases the distance to the negatively charged neighbors, therefore reducing the negative electrostatic potential at the rare-earth site and increasing the energy required to remove a  $4f$  electron, while the opposite is true for a decrease in radius. A change in radius affects the polarization and repulsive energies as well as the electrostatic potential, but the change in lattice potential should be the dominant contribution to the observed shifts.

It is important to note that although the electrostatic point-charge model provided the motivation for describing the  $4f$  binding energies with a two-parameter model, the limitations of the electrostatic model do not necessarily apply to the empirical model. An empirical treatment avoids weaknesses of the electrostatic point-charge model, such as failure to consider covalency in the lattice, details of the charge distribution, and modifications of the atomic contributions to the binding energy. The two-parameter model allows the effects of these processes to be incorporated into the empirical constants even though they cannot be adequately treated within the theoretical framework of a purely electrostatic model. The success of this empirical picture of the rare-earth binding energies is derived from the well-known chemical similarity of the rare-earth ions and their similar response to the host lattice. Thus, we expect that the empirical two-parameter model will have much wider applicability than a purely electrostatic model, allowing an extension to a wide range of materials, possibly including materials with significant covalency such as semiconductors.

### C. Comparison with optical measurements and extension to related hosts

Excited-state absorption and photoconductivity measurements on Ce:YAG and Pr:YAG allow comparisons to be made with the extrapolation of our measurements using the empirical two-parameter model. Estimates for the energies of  $\text{Ce}^{3+}$  and  $\text{Pr}^{3+}$  relative to the VBM from these published results are included in Fig. 6. Given that both of these techniques involve transitions to the conduction band of the host, knowledge of the band gap is necessary to determine the energies relative to the VBM. The photoconductivity measurements of Pedrini *et al.*<sup>20</sup> on Ce:YAG show that  $\text{Ce}^{3+}$  is 3.8 eV below the conduction band; thus, since the band gap of YAG is 6.5 eV,<sup>51</sup> this places the  $4f^n$  ground state at 2.7 eV above the VBM, which agrees with the value of 2.4 eV  $\pm 0.3$  eV extrapolated from our measurements. Excited-state absorption measurements have been made on both  $\text{Ce}^{3+}$  and  $\text{Pr}^{3+}$  in YAG, although in both cases the absorption thresholds occurred below the measured energy ranges, requiring that the position of the rare-earth ion relative to the conduction band be estimated by extrapolating the low-energy absorption signal back to its onset. In Ce:YAG, Hamilton *et al.*<sup>4</sup> estimated that  $\text{Ce}^{3+}$  was 2.5 eV above the VBM, which is in good agreement with both the photoconductivity measurements and our estimate. Although there has been some uncertainty as to whether the observed excited-state absorption and photoconductivity signals in Ce:YAG corresponded to direct transitions to the conduction band or to higher rare-

earth configurations, such as  $4f^{n-1}6p^1$ , the agreement between the estimated thresholds and the energies extrapolated from our photoemission measurements supports the conclusion that the final state is indeed the conduction band.<sup>6</sup> For Pr:YAG, Cheung and Gayen<sup>5</sup> proposed that  $Pr^{3+}$  was 1.2 eV above the VBM, which is larger than our estimate of  $0.4 \text{ eV} \pm 0.3 \text{ eV}$ . This discrepancy could be attributed to the combined errors in the measurements; however, it may also indicate either that the excited-state absorption threshold in Pr:YAG is due to the upper  $4f^{n-1}5d^1$  levels or crystal defects rather than the conduction band or that the  $Pr^{3+}$  ionization potential used in our model is too large. Further measurements on  $Pr^{3+}$ -doped materials can be used to provide a quantitative analysis of the model's predictions for  $Pr^{3+}$  and the consequences for Pr:YAG.

The  $4f$  binding energy of  $Eu^{3+}$  relative to the VBM in europium gallium garnet (EuGG) as determined from photoemission measurements is also included in Fig. 6 for comparison.<sup>52</sup> Although the binding energies will be shifted relative to YAG, the effects on the VBM and  $4f$  binding energies are expected to be relatively small due to the similar structure of the materials. Since the largest effect on the electrostatic potential should arise from nearest-neighbor ions, we may make a rough estimate for the energy shift of the  $4f$  binding energy by comparing the change in bond lengths between the two materials with the observed effect of ionic radius in YAG. The increase in average yttrium-oxygen bond length in YGG compared to YAG is half of the change in bond length between YAG and GdAG.<sup>53</sup> Given that the estimated shift between YAG and GdAG due to the change in bond length is less than 300 meV to higher binding energy (using  $\alpha_R = 8.3 \text{ eV}/\text{\AA}$ ), we estimate that the  $4f$  binding energy in EuGG might only be 100–200 meV larger than in EuAG. The effect on the VBM is more difficult to estimate, but is probably at most a few hundred meV. The measured value of  $\sim 3.4 \text{ eV}$  below the VBM in EuGG is shifted to higher binding energy as expected but is still within the uncertainty of the predicted value of  $2.8 \text{ eV} \pm 0.6 \text{ eV}$  in EuAG, implying that the difference in relative binding energies between the two crystals is at most several hundred meV.

The extrapolation of our photoemission results using the empirical model offers an opportunity to consider implications for the important solid-state laser material Nd:YAG. The predicted energy of the  $Nd^{3+}$  ground state is 900 meV below the VBM in YAG, which places the  $4f^n$  ground state at 7.4 eV below the bottom of the conduction band. This shows that the single-photon absorption threshold from the  $Nd^{3+}$  ground state to the host conduction band is expected to occur at an energy significantly higher than the fundamental absorption of YAG. Ionization of the  $Nd^{3+}$  through a multi-photon process involving  $1.064 \mu\text{m}$  photons would require a very-low-probability five-photon absorption from the upper laser level, and even the high-energy photons of a flashlamp pump source would lack sufficient energy to ionize a  $4f$  electron. Thus, the large  $4f$  binding energy of  $Nd^{3+}$  in YAG clearly contributes to the well-known efficiency and resistance to optical damage exhibited by high-power Nd:YAG laser systems. Since the measured binding energy of the  $4f^n$

ground state of  $Yb^{3+}$  is even larger than for  $Nd^{3+}$ , ionization would be even less likely to occur in high-power Yb:YAG laser systems.

The success of these comparisons suggests that further studies of additional host compounds will rapidly lead to a clearer picture for the effect of the host lattice on the  $4f$  electron binding energies. That broad picture of the electronic structure of rare-earth-doped optical materials will motivate fundamental theoretical analysis and will be directly useful for designing new optical materials.

## VII. CONCLUSION

Photoemission spectroscopy is a useful tool for locating the energy of localized rare-earth impurity levels relative to host band structure in optical materials. In particular, the ability to measure energies of electronic states relative to a common reference avoids many of the difficulties in interpretation that are present in optical methods and provides information that complements excited-state absorption and photoconductivity measurements. Using synchrotron radiation, resonances in the  $4f$  photoemission cross section, such as the  $4d$  to  $4f$  “giant resonance,” may be exploited to uniquely identify the  $4f$  component of a photoemission spectrum from the often-overlapping host valence band. The ability to separate the  $4f$  spectrum from the host spectrum allows the relative binding energies of the valence band maximum and  $4f$  electrons to be determined. This energy separation is a material parameter that is important for many technological applications of optical materials, such as solid-state lasers, phosphors, scintillators, electroluminescent devices, rare-earth-doped optical fibers, optical memories, and optical processors.

To explore the systematics of the binding energies of the rare-earth  $4f^n$  electronic states relative to the host valence band, we have performed resonant photoemission spectroscopy on a series of rare-earth ions doped into yttrium aluminum garnet. The binding energies of the  $4f$  ground state and the valence band maximum were measured for rare-earth ions from  $Gd^{3+}$  to  $Lu^{3+}$  at atomic concentrations varying from 7% to 100%. No concentration dependence of the  $4f$  or the VBM binding energies was observed, suggesting that measurements for a single concentration are sufficient to locate the binding energies for samples of any concentration; however, we might expect a noticeable effect on the conduction band, which is primarily formed from cation electronic states in an ionic host. To test this, a series of experiments using a technique complementary to photoemission, such as inverse photoemission or photoconductivity, will be required.

To explain the relative binding energies of the different rare-earth ions, we employed an empirical model for the effect of the host lattice on the ion's binding energy. This model describes the differences in binding energies of the rare-earth ions as due to differences in free-ion ionization potentials, modified by a smaller effect due to the variation in ionic radii. Fitting the measured binding energies gave good agreement, with a 31.6 eV shift of the free-ion ionization potentials and an additional  $8.3 \text{ eV}/\text{\AA}$  effect arising from the difference of the rare-earth and yttrium ionic radii. This

model was supported by further comparison with energies obtained from published photoconductivity and excited-state absorption measurements. The empirical model's success in describing the systematic trends in  $4f$  binding energies indicates that measurements on two rare-earth ions in the host may be sufficient to predict the energies of all other rare-earth ions in that host, particularly if the accuracies of the free-ion ionization potentials used in the model are improved by further comparison with measurements.

Another consequence of this model is that, when rare-earth ions substitute for ions of similar radius, it may be possible to obtain preliminary estimates of the rare-earth binding energies through measurement of the binding energy shift of the host crystal's intrinsic ions. This method is motivated by the ionic nature of the rare-earth bonding in insulating optical materials and allows the rare-earth energies to be estimated from examination of the photoemission spectrum of the undoped host crystal, providing a quick and simple technique for surveying potential rare-earth-doped materials.

Additional data with more accurate measurements of electron binding energies will permit a detailed analysis of the empirical two-parameter model and test the range of materials for which it is applicable. Development of improved methods for charge compensation and reducing differential charging while ensuring maximum uniformity in the photon beam intensity will improve the accuracy and sensitivity of the photoemission measurements. By comparing measurements in different materials with the empirical model, improved estimates for the free-ion ionization potentials may be obtained and used in the model to increase the accuracy of its predictions. Study of new materials will undoubtedly reveal lattice-dependent trends that will enhance the predictive power of the empirical model.

Much work is still needed to advance the understanding of relationships between localized  $4f$  electrons and the crystal band states. Measurements over the entire rare-earth series in many different host materials are required to build a more complete picture of rare-earth-doped optical materials. Comparison of experimental results with theoretical predictions will provide insight into the electronic structure of the crystal lattice and provide guidance for calculations of lattice-dependent properties. By supplementing photoemission with complementary techniques such as photoconductivity, excited-state absorption, bremsstrahlung isochromat spectroscopy, and inverse photoemission, the relationships and interactions between rare-earth ions and the occupied and unoccupied electronic states of the host crystal may be thoroughly explored. With sufficient data to guide the theoretical treatment of these processes, it may become possible to better understand the properties of current optical materials as well as direct the development of new materials for specific applications.

#### ACKNOWLEDGMENTS

The authors wish to thank C. G. Olson for advice regarding experimental techniques and apparatus. Samples for this project were supplied by Scientific Materials Corporation, Bozeman, MT, and Stanley Mroczkowski and W. P. Wolf at the Applied Physics Department, Yale University. Funding for this research was provided in part by the Air Force Office of Scientific Research under Grant Nos. F49620-97-1-0411, F49620-98-1-0171, and F49620-00-1-0314. This material was based upon work supported under a National Science Foundation Graduate Research Fellowship. This work is based upon research conducted at the Synchrotron Radiation Center, University of Wisconsin-Madison, which was supported by the NSF under Award No. DMR-0084402.

\*Present address: Département de Recherche sur l'Etat Condensé, CEA/Saclay, F-91191 Gif-sur-Yvette Cedex, France.

<sup>†</sup>Present address: Department of Physics, The University of Hong Kong, Pokfulam Road, Hong Kong, China.

<sup>1</sup>J. W. Allen, in *Synchrotron Radiation Research: Advances in Surface and Interface Science*, edited by R. Z. Bachrach (Plenum Press, New York, 1992), Vol. 1, pp. 253–323.

<sup>2</sup>W. Lenth, F. Lutz, J. Barth, G. Kalkoffen, and C. Kunz, *Phys. Rev. Lett.* **41**, 1185 (1978); J. W. Allen, L. I. Johansson, R. S. Bauer, I. Lindau, and S. B. M. Hagström, *ibid.* **41**, 1499 (1978); W. Gudat, S. F. Alvarado, and M. Campagna, *Solid State Commun.* **28**, 943 (1978); B. Johansson, J. W. Allen, T. Gustafsson, I. Lindau, and S. B. M. Hagström, *ibid.* **28**, 53 (1978).

<sup>3</sup>J. F. Owen, P. B. Dorain, and T. Kobayashi, *J. Appl. Phys.* **52**, 1216 (1981).

<sup>4</sup>D. S. Hamilton, S. K. Gayen, G. J. Pogatshnik, R. D. Ghen, and W. J. Miniscalco, *Phys. Rev. B* **39**, 8807 (1989).

<sup>5</sup>Y. M. Cheung and S. K. Gayen, *Phys. Rev. B* **49**, 14 827 (1994).

<sup>6</sup>R. R. Jacobs, W. F. Krupke, and M. J. Weber, *Appl. Phys. Lett.* **33**, 410 (1978).

<sup>7</sup>K.-S. Lim and D. S. Hamilton, *J. Opt. Soc. Am. B* **6**, 1401 (1989).

<sup>8</sup>R. M. Macfarlane and R. M. Shelby, in *Spectroscopy of Solids Containing Rare Earth Ions*, edited by A. A. Kaplyanski and R.

M. Macfarlane (North-Holland, Amsterdam, 1987), pp. 51–184; R. M. Macfarlane and G. Wittmann, *Opt. Lett.* **21**, 1289 (1996); G. Wittmann and R. M. Macfarlane, *ibid.* **21**, 426 (1996).

<sup>9</sup>M. M. Broer, R. L. Cone, and J. R. Simpson, *Opt. Lett.* **16**, 1391 (1991); G. R. Atkins and A. L. G. Carter, *ibid.* **19**, 874 (1994).

<sup>10</sup>S. Kh. Batygov, Yu. K. Voron'ko, B. I. Denker, A. A. Maier, V. V. Osiko, V. S. Radukhin, and M. I. Timoshechkin, *Fiz. Tverd. Tela* (Leningrad) **14**, 977 (1972) [Sov. Phys. Solid State **14**, 839 (1972)].

<sup>11</sup>G. Blasse and B. C. Grabmeier, *Luminescent Materials* (Springer, Berlin, 1994).

<sup>12</sup>C. Dujardin, C. Pedrini, J. C. Gâcon, A. G. Petrosyan, A. N. Belsky, and A. N. Vasil'ev, *J. Phys.: Condens. Matter* **9**, 5229 (1997); U. Happek, S. A. Basun, J. Choi, J. K. Krebs, and M. Raukas, *J. Alloys Compd.* **303-304**, 198 (2000).

<sup>13</sup>M. Ando and Y. A. Ono, *J. Appl. Phys.* **69**, 7225 (1991); K. Swiatek, M. Godlewski, L. Niinistö, and M. Leskelä, *ibid.* **74**, 3442 (1993).

<sup>14</sup>M. Campagna, G. K. Wertheim, and Y. Baer, in *Topics in Applied Physics*, edited by L. Ley and M. Cardona (Springer-Verlag, Berlin, 1979), Vol. 27, Chap. 4, pp. 217–260.

<sup>15</sup>D. W. Lynch and J. Weaver, in *Handbook on the Physics and Chemistry of Rare Earths*, edited by K. A. Gschneider, L. E-

ring, and S. Hüfner (North-Holland, Amsterdam, 1987), Vol. 10, Chap. 66, p. 231.

<sup>16</sup>G. K. Wertheim, A. Rosencwaig, R. L. Cohen, and H. J. Guggenheim, Phys. Rev. Lett. **27**, 505 (1971).

<sup>17</sup>C. Pedrini, D. S. McClure, and C. H. Anderson, J. Chem. Phys. **70**, 4959 (1979).

<sup>18</sup>J. K. Lawson and S. A. Payne, Phys. Rev. B **47**, 14 003 (1993).

<sup>19</sup>M. Raukas, S. A. Basun, W. van Schaik, W. M. Yen, and U. Happek, Appl. Phys. Lett. **69**, 3300 (1996); W. M. Yen, M. Raukas, S. A. Basun, W. van Schaik, and U. Happek, J. Lumin. **69**, 287 (1996).

<sup>20</sup>C. Pedrini, F. Rogemond, and D. S. McClure, J. Appl. Phys. **59**, 1196 (1986).

<sup>21</sup>C. G. Olson, Nucl. Instrum. Methods Phys. Res. A **266**, 205 (1988).

<sup>22</sup>S. Geller, Z. Kristallogr. **125**, 1 (1967).

<sup>23</sup>C. R. Brundle, J. Vac. Sci. Technol. **11**, 212 (1974).

<sup>24</sup>R. T. Lewis and M. A. Kelly, J. Electron Spectrosc. Relat. Phenom. **20**, 105 (1980).

<sup>25</sup>T. L. Barr, J. Vac. Sci. Technol. A **7**, 1677 (1989).

<sup>26</sup>T. L. Barr, J. Vac. Sci. Technol. A **13**, 1239 (1995); J. B. Metson, Surf. Interface Anal. **27**, 1069 (1999).

<sup>27</sup>T. D. Thomas, J. Chem. Phys. **52**, 1373 (1970).

<sup>28</sup>C. K. Jørgensen, Struct. Bonding (Berlin) **24**, 1 (1975).

<sup>29</sup>D. A. Pawlak, K. Woźniak, Z. Frukacz, T. L. Barr, D. Fiorentino, and S. Seal, J. Phys. Chem. B **103**, 1454 (1999).

<sup>30</sup>D. A. Shirley, Phys. Rev. B **5**, 4709 (1972); P. M. A. Sherwood, in *Practical Surface Analysis*, edited by D. Briggs and M. P. Seah (Wiley, New York, 1983), pp. 445–475.

<sup>31</sup>O. Gunnarsson and T. C. Li, Phys. Rev. B **36**, 9488 (1987).

<sup>32</sup>C. G. Olson and D. W. Lynch, J. Opt. Soc. Am. **72**, 88 (1982).

<sup>33</sup>G. J. Lapeyre, A. D. Baer, J. Hermanson, J. Anderson, J. A. Knapp, and P. L. Gobby, Solid State Commun. **15**, 1601 (1974); G. J. Lapeyre, Nucl. Instrum. Methods Phys. Res. A **347**, 17 (1994).

<sup>34</sup>W. Gudat, S. F. Alvarado, M. Campagna, and Y. Pétroff, J. Phys. (Paris), Colloq. **5**, 1 (1980).

<sup>35</sup>J.-S. Kang, J. H. Hong, J. I. Jeong, S. D. Choi, C. J. Yang, Y. P. Lee, C. G. Olson, B. I. Min, and J. W. Allen, Phys. Rev. B **46**, 15 689 (1992).

<sup>36</sup>Y.-N. Xu and W. Y. Ching, Phys. Rev. B **59**, 10 530 (1999).

<sup>37</sup>J. J. Yeh and I. Lindau, At. Data Nucl. Data Tables **32**, 1 (1985).

<sup>38</sup>P. A. Cox, Y. Baer, and C. K. Jørgensen, Chem. Phys. Lett. **22**, 433 (1973); E. I. Zabolotskii, Y. P. Irkhin, and L. D. Finkel'shtein, Fiz. Tverd. Tela (Leningrad) **16**, 1142 (1974). [Sov. Phys. Solid State **16**, 733 (1974)].

<sup>39</sup>J. K. Lang, Y. Baer, and P. A. Cox, J. Phys. F: Met. Phys. **11**, 121 (1981).

<sup>40</sup>P. A. Cox, Struct. Bonding (Berlin) **24**, 59 (1975).

<sup>41</sup>G. H. Dieke and H. M. Crosswhite, Appl. Opt. **2**, 675 (1963); R. T. Wegh, A. Meijerink, R.-J. Lamminmäki, and J. Hölsä, J. Lumin. **87-89**, 1002 (2000).

<sup>42</sup>W. Y. Ching, Y.-N. Xu, and B. K. Brickeen, Appl. Phys. Lett. **74**, 3755 (1999).

<sup>43</sup>J. F. Herbst, N. D. Lowy, and R. E. Watson, Phys. Rev. B **6**, 1913 (1972).

<sup>44</sup>B. Johansson, J. Phys. F: Met. Phys. **4**, L169 (1974).

<sup>45</sup>L. Pauling, Phys. Rev. **34**, 954 (1929).

<sup>46</sup>C. S. Fadley, S. B. M. Hagström, M. P. Klein, and D. A. Shirley, J. Chem. Phys. **48**, 3779 (1968); P. H. Citrin and T. D. Thomas, *ibid.* **57**, 4446 (1972).

<sup>47</sup>W. C. Martin, R. Zalubas, and L. Hagan, Natl. Stand. Ref. Data Ser. (U.S., Natl. Bur. Stand.) **60**, 1 (1978).

<sup>48</sup>C. E. Moore, Natl. Stand. Ref. Data Ser. (U.S., Natl. Bur. Stand.) **34**, 1 (1970).

<sup>49</sup>M. Cardona and L. Ley, in *Topics in Applied Physics*, edited by M. Cardona and L. Ley (Springer-Verlag, Berlin, 1978), Vol. 26, p. 269.

<sup>50</sup>R. D. Shannon, Acta Crystallogr., Sect. A: Cryst. Phys., Diff., Theor. Gen. Crystallogr. **32**, 751 (1976).

<sup>51</sup>G. A. Slack, D. W. Oliver, R. M. Chrenko, and S. Roberts, Phys. Rev. **177**, 1308 (1969).

<sup>52</sup>C. W. Thiel, H. Cruguel, Y. Sun, G. J. Lapeyre, and R. L. Cone (unpublished).

<sup>53</sup>F. Euler and J. A. Bruce, Acta Crystallogr. **19**, 971 (1965).



ELSEVIER

Journal of Luminescence 94-95 (2001) 1-6

JOURNAL OF  
LUMINESCENCE

[www.elsevier.com/locate/jlumin](http://www.elsevier.com/locate/jlumin)

## Systematics of 4f electron energies relative to host bands by resonant photoemission of rare earth doped optical materials

C.W. Thiel<sup>a,\*</sup>, H. Cruguel<sup>a,1</sup>, Y. Sun<sup>a</sup>, G.J. Lapeyre<sup>a</sup>, R.M. Macfarlane<sup>b</sup>,  
R.W. Equall<sup>c</sup>, R.L. Cone<sup>a</sup>

<sup>a</sup>Department of Physics, Montana State University, Bozeman, MT 59717, USA

<sup>b</sup>IBM Almaden Research Center, 650 Harry Road, San Jose, CA 95120, USA

<sup>c</sup>Scientific Materials Corporation, 310 Icepond Road, Bozeman, MT 59715, USA

### Abstract

Relative energies of  $4f^n$  electronic states and crystal band states are important for a fundamental understanding of rare-earth-doped optical materials and a practical understanding of each material's potential performance in specific applications. With this motivation, the  $4f^n$  ground state binding energies of rare earth ions have been studied in the gallium garnets using resonant photoemission spectroscopy and compared with the aluminum and iron garnets. The 4d-4f photoemission resonance was used to separate and identify the  $4f^n$  and valence band components of the spectra, and theoretical 4f photoemission spectra were fit to experimental results to accurately determine electron binding energies. A two-parameter empirical model was used to successfully describe the relative energies of the  $4f^n$  ground states in these materials. The success of this empirical model indicates that measurements on as few as two different rare earth ions in a host are sufficient to predict the energies of all rare earth ions in that host. This analysis shows that systematic shifts in the relative energies of  $4f^n$  states and crystal band states between different garnets arise entirely from shifts of the band states, while each rare earth ion maintains the same absolute binding energy for all garnets studied. These results suggest that further studies of additional host compounds using both photoemission and optical spectroscopy will rapidly lead to a broader picture of the host crystal's effect on 4f electron binding energies. © 2001 Elsevier Science B.V. All rights reserved.

**Keywords:** 4f binding energies; Resonant photoemission; Rare earth garnets

### 1. Introduction

Interactions between the localized  $4f^n$  electronic states of rare earth ions and the de-localized band states of the crystal lattice can strongly affect the

optical properties of technologically important rare-earth-doped materials. In contrast to the well-developed understanding of the electronic structure of the  $4f^n$  states, relatively little is known about the relationships between these states and the electronic states of the crystal. In recent years, the body of knowledge on this topic has steadily grown due to the strong interest in developing ultraviolet lasers and more efficient phosphor and scintillator materials. The performance of

\*Corresponding author. Fax: +1-406-994-4452.

E-mail address: [thiel@physics.montana.edu](mailto:thiel@physics.montana.edu) (C.W. Thiel).

<sup>1</sup>Present address: Département de Recherche sur l'Etat Condensé, CEA/Saclay, F-91191 Gif-sur-Yvette Cedex, France.

rare-earth-activated optical materials in these applications can be enhanced, reduced, or even entirely inhibited by energy exchange and charge transfer processes between the rare earth ions and the host crystal [1–3]. This has made it increasingly important that the systematic trends and behavior of rare earth energies relative to crystal band states be explored and characterized.

Several experimental techniques have been used to explore the relationships between the  $4f^n$  states and the host electronic states, including vacuum-ultraviolet and excited-state absorption, photoconductivity, and photoelectron spectroscopy. Absorption spectroscopy provides one of the most direct methods for measuring interactions between the rare earth ions and the host crystal and also allows the study of exciton and other localized charge transfer processes that do not directly involve the host band states. However, interpretation is often difficult because of uncertainty in the assignment of initial and final states for observed transitions. Photoconductivity measurements can unambiguously assign the final state of a transition as involving either an electron in the conduction band or a hole in the valence band, although the presence of electron acceptor or donor defects in the lattice can also create ambiguity regarding the origin of observed signals. Photoelectron spectroscopy, or photoemission, measures the energies of occupied electronic states relative to a common energy reference, providing information that can complement optical methods. Combined with the methods of inverse photoemission or Bremsstrahlung isochromat spectroscopy, which measure the energies of unoccupied electronic states, photoemission can be used to provide a clear picture of the electronic states in a material. The primary difficulties in applying photoemission to the study of optical materials are the requirement of ion concentrations of at least a few atomic percent and complications arising from electrical charging due to the highly insulating nature of the materials being studied. However, in the garnets it has been shown that energies determined from measurements on highly concentrated samples accurately reflect the energies in low-concentration samples and that sample charging problems can be over-

come by combinations of experimental techniques and data analysis [4].

This paper briefly reviews the empirical model previously applied in the analysis of 4f electron binding energies in the aluminum garnets and then presents the analysis of new results obtained from resonant photoemission of rare earth gallium garnets (REGG).

## 2. Systematics of the 4f binding energies

A variety of theoretical models have been used to predict and explain the 4f electron binding energies observed in materials ranging from rare-earth-doped insulators to the elemental metals. One model well suited to rare-earth-doped insulators is the electrostatic point charge model [5–8]. In this model, we view the free-ion binding energies of the 4f electrons—which correspond to the free-ion ionization potentials of the rare earth ions—as being shifted through electrostatic interactions with the host lattice. The largest contribution arises from the large negative electrostatic potential, or Madelung potential, at the rare earth's lattice site. This lattice potential raises the energies of the rare earth's electrons, resulting in a corresponding decrease in their binding energies. Other significant contributions must also be considered, such as the lattice polarizability, inter-atomic repulsive energies, and Van der Waal's energies [5,6]. Due to the chemical similarity of the rare earth ions and the non-bonding character of the 4f electrons, the net shift in binding energy is similar for all rare earth ions in a particular material. Deviations from this constant shift are viewed as resulting from changes in the ionic radius and the corresponding changes in bond lengths [7,8]. Although these effects can be calculated for highly ionic materials, in practice the information that is needed is only known for special cases where the precise changes in bond lengths and the lattice relaxation effects can be accurately estimated. Recently, it has been demonstrated that an empirical form of this model can be successfully applied to the description and extrapolation of measured 4f binding energies in optical materials [4]. This empirical model characterizes

the effect of the host lattice on 4f electron binding energies with two empirical parameters, where one parameter describes a constant shift experienced by all rare earth ions and the second parameter describes a smaller dependence on the rare earth's ionic radius. These parameters may be determined from measurements on two different rare earth ions, or, in certain cases, from measurements on the host lattice itself [4].

Another advantage of an empirical treatment is that it may be extended to covalently bonded materials where the ionic picture fails. This is understood by considering the shift in binding energy experienced by 4f electrons in a semiconducting or metallic material. In this case, we again view the free-ion values as being shifted from interactions with the charge distribution inside of the host lattice, with the largest contribution arising from the average Coulomb interaction between the 4f electrons, the charge distributions of the bonding electrons, and the screened nuclear charges of the ligand atoms. Since the lattice may contain mobile charges, particularly in the metals, we must also consider a variety of relaxation effects including screening provided by free electronic charges as well as the dielectric polarizability. The resulting shift is related to the chemical cohesive energy of the lattice site and is similar for all rare earth ions due to their similar chemical properties [9]. However, both the cohesive energy and the screening properties are affected by the increase in effective nuclear charge across the rare earth series that results from the imperfect screening provided by the additional 4f electrons [9]. Thus, we obtain a model in which the binding energies are shifted by a constant value and a smaller effect that varies with the effective nuclear charge. Since the change in effective nuclear charge is directly correlated to the rare earth ion's ionic radius, the empirical two-parameter model for the effect of the host lattice successfully describes the systematic variation of 4f electron binding energies in semiconductors and metals as well as insulators.

As an example of this model's success in describing 4f electron binding energies in covalent solids, Fig. 1 shows the application of this model to the elemental rare earth metals. The data in

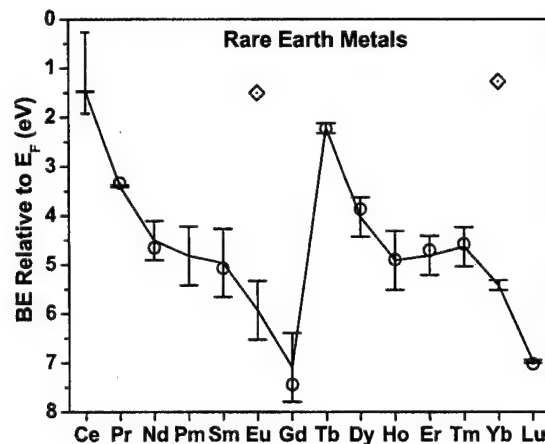


Fig. 1. Systematic behavior of 4f binding energies in rare earth metals. Circles and diamonds represent measured binding energies of 4f electrons relative to the Fermi energy ( $E_F$ ) from Ref. [10]; following the usual convention, states with negative binding energies have absolute energies greater than  $E_F$  while positive binding energies lie below  $E_F$ . The range in which Ce lies is represented by a vertical bar. Circles represent metals with the same number of 4f electrons as trivalent ions; metals with the same number of 4f electrons as divalent ions are represented by diamonds. The solid line is the fit of the model to the measured binding energies (circles), and the error bars represent uncertainty in the free-ion ionization potentials.

Fig. 1 are the 4f electron binding energies relative to the metal's Fermi energy measured by Lang et al. [10]. The number of 4f electrons can be unambiguously determined from the structure of the 4f photoemission spectrum, which provides a unique 'fingerprint' of the electron configuration. These photoemission spectra show that rare earth atoms in the metals have the same number of 4f electrons as trivalent ions, except for Eu and Yb, which have a divalent 4f configuration. The 4f binding energy of Ce was not resolved; however, the range of energies in which it lies is indicated on the graph. The solid line is our fit of the model to the binding energies in the trivalent metals, and the error bars indicate the uncertainty in the values of the free-ion ionization potentials used in the model. This model gives remarkable agreement with the observed binding energies. It is interesting that Sm metal agrees well with the model though its crystal structure is different than the other trivalent metals, indicating that the difference in crystal structure has a small effect on the 4f

electrons in this case or possibly that both the Fermi energy and 4f binding energy experience equal shifts of the same sign.

### 3. The 4f photoemission spectra

The 4f electron photoemission often overlaps photoemission from the host valence band, making interpretation of features and measurement of energies difficult. Resonant photoemission removes this difficulty and allows the 4f component of the spectrum to be unambiguously identified and separated from the host photoemission. This technique relies on the enhancement in 4f photoemission that occurs when employing photon energies resonant with the  $4d^{10}4f^n$  to  $4d^94f^{n+1}$  transition of the rare earth ion [11]. By comparing spectra taken on- and off-resonance, the large change in 4f photoemission cross-section allows the 4f component to be extracted. Since the energy of the resonance is specific to both the ion and its valence, this technique also provides the advantage of being able to separate and identify different rare earth ions or valence states simultaneously present in a single material.

The 4f electron photoemission exhibits structure originating from the excited states of the  $4f^{n-1}$  electronic configuration that results from the removal of an electron during the photoemission process [10,11]. Since the 4f binding energy is the minimum energy required to remove a 4f electron, it corresponds to the component of this photoemission 'final state' structure with the smallest binding energy. To accurately determine the 4f electron binding energies from the observed 4f photoemission, we fit theoretical 4f photoemission spectra to the measured spectra for each sample studied using the method described in Ref. [4].

### 4. Materials and apparatus

This work was carried out on the Iowa State/Montana State ERG/Seya beam line at the University of Wisconsin-Madison Synchrotron Radiation Center using the apparatus and techniques described in Ref. [4]. The absolute binding

energy scale was established by placing the C 1s photoemission peak arising from adventitious carbon contamination at a binding energy of 290 eV relative to the vacuum level.

The single crystal EuGG, TbGG, ErGG, and YbGG samples studied in this work were grown from flux by S. Mroczkowski at the Department of Applied Physics, Yale University.

### 5. Results and analysis

To locate the energies of the 4f electrons relative to the host band states, the precise energy of the valence band must be determined for each sample. The valence bands of the gallium garnets and aluminum garnets have very similar density of states [12], and the technique previously used by Thiel et al. [4] for yttrium aluminum garnet was used to locate the valence band maximum (VBM), which is the highest energy valence band state. A value of 8.3 eV was obtained for the binding energy of the VBM by comparing the observed spectrum to the theoretical photoemission cross-section as estimated using the atom-resolved partial density of states [12]. No shift in the VBM was observed between samples to within the experimental accuracy of several hundred meV. The VBM is significantly shifted to lower binding energy compared to the value of 8.7 eV measured in yttrium aluminum garnet. A shift is expected since the gallium garnets have a band gap of  $\sim 5.5$  eV, while the aluminum garnets have a larger band gap of 6.5 eV.

An example photoemission spectrum for EuGG is shown in Fig. 2(a). To extract the 4f contributions to the photoemission, spectra were taken using photon energies of 137, 139, and 144 eV. By taking the difference of the spectra at 144 and 139 eV, the Eu 4f electron spectrum can be extracted as shown in Fig. 2(b). The calculated contributions to the photoemission cross-section due to final state structure are shown as vertical lines and the dotted line is the fit to the observed spectrum, indicating a 4f electron binding energy of 11.9, or 3.6 eV below the VBM.

A feature unique to EuGG was the presence of a weaker second resonance attributed to the

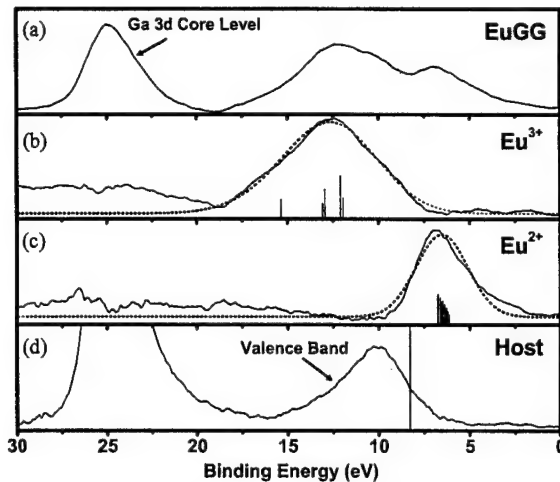


Fig. 2. Extracted  $4f^n$  photoemission spectra for EuGG. (a) Photoemission spectrum taken with a photon energy of  $h\nu = 144$  eV. (b)  $Eu^{3+}$  4f photoemission spectrum obtained from difference of spectra at  $h\nu = 144$  and 139 eV. (c)  $Eu^{2+}$  4f spectrum obtained from difference of spectra at  $h\nu = 139$  and 137 eV. In (b) and (c), vertical lines represent underlying photoemission final state structure and dotted lines are fits to the observed spectrum. (d) Photoemission spectrum with the 4f components in (b) and (c) removed. The estimated VBM energy is shown as a vertical line.

presence of divalent Eu at the surface of the crystal. Sm, Eu, Tm, and Yb are known to sometimes form divalent surface layers that can be clearly distinguished from the trivalent ions in the bulk [9]. By comparing spectra taken at 139 and 137 eV, the divalent component of the spectrum was extracted as shown in Fig. 2(c). The corresponding theoretical final state structure and fit are also shown, giving a binding energy of 6.2 eV. The lower photon energy of the photoemission resonance and the binding energy difference between the two components are both consistent with this second feature arising from a divalent surface component.

Once the 4f components of the spectrum are obtained, they may be subtracted out of the photoemission spectrum at 137 eV to obtain the photoemission due to the host, as shown in Fig. 2(d). The position of the VBM at 8.3 eV is indicated by the vertical line.

By repeating this process for TbGG, ErGG, and YbGG, we obtain 4f binding energies of 7.8, 10.9,

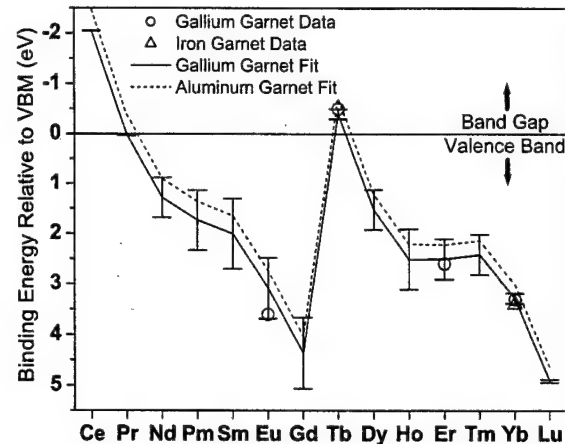


Fig. 3. Systematic behavior of 4f binding energies relative to the VBM in garnets. Circles represent measured binding energies relative to the VBM (at 8.3 eV) for 4f electrons in gallium garnets; negative binding energies are within the band gap and positive binding energies are below the VBM. The solid line is the fit of the model to our measured energies and error bars represent the uncertainty in the values of the free-ion ionization potentials. The dotted line is the fit of the model to 4f binding energies in the aluminum garnets from Ref. [4]. The triangle represents the measured 4f binding energy in Yb iron garnet from Ref. [13].

and 11.6 eV, respectively. The binding energies relative to the VBM are plotted in Fig. 3. The model for the binding energies relative to the VBM is given by  $E_{4f} = I - E_L + \alpha_R(R - R_0) - E_{VBM}$ , where  $E_{4f}$  is the 4f binding energy relative to the VBM,  $I$  is the free-ion ionization potential,  $E_L$  is the uniform shift experienced by the rare earth ions,  $\alpha_R$  is the binding energy shift per unit change in ionic radius,  $R$  and  $R_0$  are the effective ionic radii of the trivalent rare earth ion and the ionic radius reference (the ionic radius of yttrium,  $R_0 = 1.019$  Å, is used to be consistent with the earlier work on yttrium aluminum garnet) [13], and  $E_{VBM}$  is the binding energy of the valence band maximum ( $E_{VBM} = 8.3$  eV). Fitting this model to the observed binding energies in the gallium garnets gives values of  $E_L = 31.65$  eV and  $\alpha_R = 9.2$  eV/Å for the two empirical parameters. The fit of the model is shown in Fig. 3 as the solid line and the error bars represent the uncertainty in the known values of the free-ion ionization potentials used in the model. Note that the relative energy of the bottom of the conduction band for

the gallium garnets would lie at about  $-5.5\text{ eV}$  in Fig. 3. The fit of the binding energies in the aluminum garnets from Ref. [4] is also shown for comparison as the dotted line in Fig. 3.

If we compare the values of the empirical parameters for the gallium garnets to the values of  $E_L = 31.6\text{ eV}$  and  $\alpha_R = 8.3\text{ eV}/\text{\AA}$  measured in the aluminum garnets [4], we see that they are essentially identical. The difference in the  $\alpha_R$  values only represents a relative binding energy shift of  $\sim 70\text{ meV}$  from Yb to Eu, which is within the experimental accuracy of several hundred meV. This shows that the systematic shift in relative energies of the 4f electrons and the host valence band is entirely due to the shift in the gallium garnet valence band, with the 4f electrons having the same absolute binding energies in the gallium and aluminum garnets.

We may also compare these results to the binding energy of the 4f electrons in Yb iron garnet, which has been measured using X-ray photoelectron spectroscopy [14]. These measurements show that the 4f electron binding energy is  $11.5\text{ eV}$  and the VBM is at  $\sim 8\text{ eV}$ . The absolute binding energy of the Yb 4f electrons is essentially the same as for the other garnets while the VBM is shifted to lower binding energy as expected from the smaller band gap of the iron garnets.

In summary, we have used resonant photoemission to study 4f electron binding energies in the garnets and have found that the results are well described by a two-parameter model for the effect of the host lattice. A systematic shift in the relative energies of the 4f electrons and the valence band is observed in the gallium garnets when compared to the results of measurements on the aluminum garnets. This shift was shown to originate entirely from a shift in the valence band while the measured 4f electron binding energies maintained the same values for all the materials studied.

## Acknowledgements

Samples for this project were supplied by S. Mroczkowski and W.P. Wolf of the Applied Physics Department, Yale University. Funding for this research was provided in part by the Air Force Office of Scientific Research under Grant Nos. F49620-97-1-0411, F49620-98-1-0171, and F49620-00-1-0314. This material is based upon work supported under a National Science Foundation Graduate Research Fellowship. This work is based upon research conducted at the Synchrotron Radiation Center, University of Wisconsin-Madison, which is supported by the NSF under Award No. DMR-0084402.

## References

- [1] R.R. Jacobs, W.F. Krupke, M.J. Weber, *Appl. Phys. Lett.* 33 (1978) 410.
- [2] C. Dujardin, C. Pedrini, J.C. Gâcon, A.G. Petrosyan, A.N. Belsky, A.N. Vasil'ev, *J. Phys.: Condens. Matter* 9 (1997) 5229.
- [3] M. Raukas, S.A. Basun, W. van Schaik, W.M. Yen, U. Happek, *Appl. Phys. Lett.* 69 (1996) 3300.
- [4] C.W. Thiel, H. Cruguel, H. Wu, Y. Sun, G.J. Lapeyre, R.L. Cone, R.W. Equall, R.M. Macfarlane, *Phys. Rev. B* 64 (2001) 085107.
- [5] C.S. Fadley, S.B.M. Hagström, M.P. Klein, D.A. Shirley, *J. Chem. Phys.* 48 (1968) 3779.
- [6] P.H. Citrin, T.D. Thomas, *J. Chem. Phys.* 57 (1972) 4446.
- [7] C. Pedrini, D.S. McClure, C.H. Anderson, *J. Chem. Phys.* 70 (1979) 4959.
- [8] C. Pedrini, F. Rogemond, D.S. McClure, *J. Appl. Phys.* 59 (1986) 1196.
- [9] N. Mårtensson, B. Reihl, R.A. Pollak, F. Holtzberg, G. Kaindl, *Phys. Rev. B* 25 (1982) 6522.
- [10] J.K. Lang, Y. Baer, P.A. Cox, *J. Phys. F* 11 (1981) 121.
- [11] J.W. Allen, in: R.Z. Bachrach (Ed.), *Synchrotron Radiation Research: Advances in Surface and Interface Science*, Vol. 1, Plenum Press, New York, 1992, pp. 253–323.
- [12] Y.-N. Xu, W.Y. Ching, B.K. Brickeen, *Phys. Rev. B* 61 (2000) 1817.
- [13] R.D. Shannon, *Acta Crystallogr. Sect. A* 32 (1976) 751.
- [14] C.W. Thiel, Y. Sun, R.L. Cone, unpublished.

## High-resolution photoemission study of acetylene adsorption and reaction with the Si(100)-2×1 surface

S. H. Xu,\* Y. Yang, M. Keefe, and G. J. Lapeyre

Physics Department, Montana State University, Bozeman, Montana 59717

E. Rotenberg

Advanced Light Source, LBNL, Berkeley, California 94720

(Received 9 February 1999)

The adsorption and reaction of acetylene with the Si(100)-2×1 surface has been studied using high-resolution photoemission by monitoring the Si 2p, C 1s, and valence-band (VB) spectra as a function of both acetylene coverage and post-adsorption annealing temperature. After the clean Si(100) surface is exposed to 0.5 monolayer (ML) acetylene, the surface state in the VB is absent. Meanwhile, the curve-fitting results show that there is only one interface component in the Si 2p core level. These results indicate that the asymmetric Si dimers may become symmetric dimers after acetylene adsorption, which can be explained well by the tetra- $\sigma$  model determined from our previous photoelectron holographic results. Significant changes in the electronic structure (Si 2p, C 1s, and VB) are found after subsequent annealing of the saturation overlayer. Annealing at lower temperature can induce some acetylene molecule desorption while most of the molecules decompose into  $C_2H_x$  ( $x = 1, 0$ ) and H species. After annealing above 660 °C, both of the reacted components of the Si 2p and C 1s lines show that the SiC species form clusterlike features. At the same time, the VB and Si 2p spectra indicate a restoration of a Si(100)-2×1 structure, and the asymmetric Si dimers reappear on the surface.

[S0163-1829(99)02040-8]

### I. INTRODUCTION

Since the pioneering works of Yoshinobu and co-workers,<sup>1,2</sup> there has been an increasing interest in the study of acetylene and ethylene on Si surfaces, because it is of practical importance to know the initial stage formation of silicon carbide with the thermal decomposition. A common scenario emerges from the previous studies, including high-resolution electron-energy-loss (HREELS) and low-energy electron diffraction (LEED),<sup>2–4</sup> x-ray photoemission spectroscopy (XPS) and x-ray photoelectron diffraction (XPD),<sup>5</sup> scanning tunneling microscopy (STM),<sup>6</sup> temperature-programmed desorption (TPD),<sup>7</sup> and some theoretical calculations.<sup>8,9</sup> At room temperature (RT), acetylene is predominantly chemisorbed nondissociatively on the Si(100) surface. Above 530 °C, most of the acetylene molecules remain on the surface. Dissociation occurs with increasing annealing temperature. At 660 °C, all of the hydrogen has desorbed and SiC clusters are formed on the Si(100) surface.

Nishijima and co-workers,<sup>2</sup> using HREELS and LEED, suggested that acetylene was di- $\sigma$  bonded to the dangling bonds (DB's) of the first-layer Si dimer (i.e., di- $\sigma$  model<sup>2</sup>) with the C-C rehybridization state of  $sp^3$ . They also found that the adsorbate overlayer still exhibited a 2×1 reconstruction indicating that the Si dimer bonds were not cleaved. On the other hand, Huang *et al.*<sup>3</sup> showed that acetylene had the rehybridization state nearer to  $sp^2$  rather than  $sp^3$ . Taylor and co-workers thought that the substrate Si dimers should be cleaved and the saturation coverage was 1 ML.<sup>7</sup> This is consistent with the latter model proposed by Huang *et al.*<sup>3</sup> However, calculations indicated that the Si dimers were not cleaved, and that the C-C bond was a double bond or be-

tween a single and a double bond.<sup>8,9</sup> Recent STM results suggested that the saturation coverage was 0.5 ML and that the adsorbate overlayer was a 2×2 or a  $c(4\times 2)$  reconstruction.<sup>6</sup> Although these controversies have not been settled, all of these authors thought that acetylene molecules adsorbed across the Si dimer (bridge site). This di- $\sigma$  model is shown in Fig. 1(a). However, in our previous paper,<sup>10</sup> using the photoelectron holographic (PH) technique,<sup>11</sup> we have shown clearly that acetylene adsorbs on the pedestal site rather than on the bridge site. This model is shown in Fig. 1(b). This structure can be termed the tetra- $\sigma$  model, in contrast to the di- $\sigma$  model. In the tetra- $\sigma$  model, each C atom bonds back to two Si atoms of two adjacent dimers. In the di- $\sigma$  model (ethylene case), each C atom bonds back to one Si atom of Si dimer. This gives a natural framework for understanding the observation that ethylene likes to desorb as a molecule while acetylene likes to decompose through the desorption of hydrogen and carbide formation.<sup>7,10,26</sup> In addition, most studies were focused on the SiC formation and atomic structure, few studies exist of the electronic structure, especially in the evolution of the electronic structure as a function of exposure and post-adsorption annealing temperature. To our knowledge there is no high-resolution photoemission spectroscopy (HRPES) study using synchrotron radiation (SR) on the initial adsorption geometry of the acetylene and the fundamental reaction mechanism on the Si(100)-2×1 surface.

In this study, we have exposed a 4° vicinal Si(100) surface to acetylene at RT and then annealed it at a various temperatures in the range 540–700 °C. The adsorption and annealing process was studied *in situ* by HRPES and LEED. In the present work the very early stages of acetylene adsorption and reaction with the silicon surface are studied. The

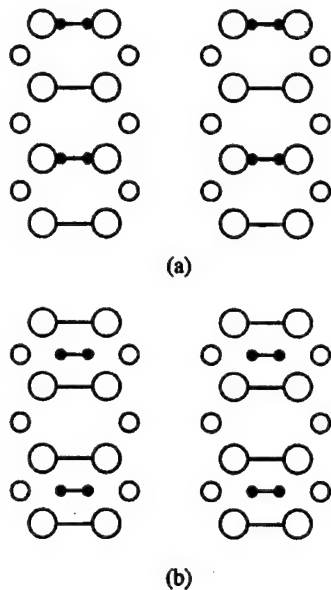


FIG. 1. Top view of the structural models for acetylene saturation (0.5 ML) chemisorbed on Si(100)-2×1 surface proposed by (a) STM (Ref. 6); (b) PH image (Ref. 10). H atoms are not plotted. Large open circle, first-layer Si dimer atoms; small open circle, second-layer Si atoms; filled circle, carbon atom.

results can be directly compared to previous studies,<sup>2–9</sup> especially in the adsorption site and the SiC formation. By itself, HRPES is certainly a very powerful tool to characterize the chemistry of the surface and the interface. The present results support the tetra- $\sigma$  model obtained from the PH data and can help us to elucidate the initial growth mechanism of SiC on the Si surface.

## II. EXPERIMENT

The experimental data were collected at the undulator beam-line station 7 at the Advanced Light Source (ALS) in Berkeley. All of the Si 2p, C 1s core-level, and VB spectra shown in this paper were obtained using a spherical grating monochromator and a large hemispherical electron analyzer. The basic pressure of the analysis chamber is better than  $2 \times 10^{-10}$  Torr. The samples were *n*-type silicon with a 4° miscut relative to the (100). Samples were introduced to the photoemission chamber and outgassed for  $\sim 20$  h at 400 °C. Cyclic annealings at 950 °C produced a clean and well-ordered surface, showing them 2×1 LEED pattern. Research grade acetylene (99.9 mol % purity) was used to dose the sample while the sample was kept at RT. The saturation coverage is 0.5 ML.<sup>6,10</sup> After adsorption of 0.5-ML acetylene, there was no obvious change observed in the LEED pattern. The adsorbate overlayer was then subsequently annealed at different temperatures. After each annealing, Si 2p, C 1s, and VB spectra were collected, and LEED was observed to monitor the surface atomic reconstruction.

HRPES of the Si 2p and C 1s core levels were obtained using photon energies of 150 and 350 eV, respectively, in order to obtain high surface sensitivity as well as high photoelectron signals. The total energy resolutions for the photon energies of 150 and 350 eV were 0.11 and 0.32 eV, respectively. VB spectra were collected using a photon en-

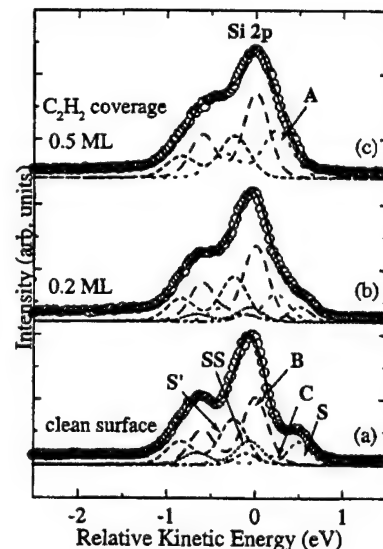


FIG. 2. Decomposition of the Si 2p spectra ( $h\nu = 150$  eV) from (a) the clean surface; (b) the surface exposed 0.2-ML acetylene at RT; (c) the surface exposed 0.5-ML acetylene at RT. The components are also shown: component B (dash line), S (dash dot line), C or A (dot line), SS (short dot line), S' (short dash line), the fitting curve (solid line), and the experimental data (open circles). Details of the fitting are given in the text.

ergy of 150 eV. The Fermi level ( $E_F$ ), corresponding to zero binding energy, was calibrated using the Ta sample clips.

Core-level fitting is a very powerful method of analyzing the interface reaction and often gives quantitative information. In our least-squares fitting procedure, which follows the guidelines outlined by Joyce *et al.*,<sup>12</sup> each Si 2p and C 1s spectrum is fitted into several components consisting of the spin-orbit-split Voigt functions. The parameters used in this program are given below.

## III. EXPERIMENTAL RESULTS

### A. Acetylene adsorption at RT

In Fig. 2 are shown the Si 2p spectra recorded for the clean surface, for the surface exposed to 0.2 ML, and 0.5 ML C<sub>2</sub>H<sub>2</sub> at RT. After adsorption of the acetylene, the Si 2p peak has a rigid shift towards the lower kinetic-energy (KE) side or the higher binding-energy (BE) side. At saturation coverage, this shift is 0.2 eV. There are the same rigid shifts towards the lower KE side both in the C 1s and the VB spectra. It is obvious that this rigid shift is caused by the band bending, which is a very common event in metal-semiconductor interfaces.<sup>13</sup> In Fig. 2, the Si 2p core-level spectra were shifted back (towards the higher KE side) to cancel the effect of the band bending. Also shown in Fig. 2 are the results of the curve fitting. Multiple components were used as well as a Lorentzian width of 0.085 eV, a spin-orbit splitting of 0.602 eV, and a  $p_{1/2}/p_{3/2}$  branching ratio of 0.5.<sup>14,15</sup>

For the Si 2p core level from the clean surface, the number and energy positions of the components as well as their structural assignments are believed to be well understood.<sup>14,16,17</sup> Here, we also decomposed this level into five components (B, S, SS, S', and C). In the original paper

by Landmark *et al.*,<sup>14</sup> the assignments were made for these components as follows: component *B* is due to the bulk Si atoms; components *S* and *SS* correspond to the up and down Si atoms of the asymmetric dimers, respectively; component *S'* is assigned to the second-layer Si atoms; component *C* is probably due to the third-layer Si atoms or defects. The energy shifts relative to the bulk component for the *S*, *C*, *SS* and *S'* components are 0.5, 0.22, -0.062, and -0.245 eV, respectively. The resulting least-squares fit is found to be in excellent agreement with the results of Refs. 14, 16 and 17 except for a very small difference in the energy shifts.

A visual inspection of Fig. 2(c) clearly shows that with exposure to  $C_2H_2$ , the *S*-emission bump disappears while the spin-orbit valley between the two main peaks becomes shallower instead of deeper as observed in the  $Ge/Si(100)-2\times 1$  interface.<sup>15,17</sup> This indicates that the number of components used for fitting may not be the same for these two cases. In fact, in the case of  $C_2H_2$ , we initially tried to decompose the  $Si\ 2p$  level into two components (*B* and *S'*) as used in the  $Ge/Si(100)-2\times 1$  interface,<sup>15,17</sup> which resulted in a poor fit. In contrast to this, three components can give a good fit, as shown in Fig. 2(c). These three components are labeled as *B*, *S'*, and *A*, respectively. The energy shifts for components *A* and *S'* relative to component *B* are 0.239 and -0.245 eV, respectively. The shift of component *S'* relative to component *B* after  $C_2H_2$  adsorption is the same as that before  $C_2H_2$  adsorption. In addition, acetylene is nondissociatively on the  $Si(100)$  surface. Then, component *S'* after acetylene adsorption is still due to the second-layer Si atoms and components *B* is due to the bulk Si atoms. It is interesting that the energy position of component *A* is very close to that of component *C* from the clean surface, but its intensity is even a little stronger than component *S'*. So, most of the contribution to component *A* is not from the third-layer Si atoms or defects as component *C* does on the clean surface. In addition, the intensity of component *A* is roughly equal to the sum of the reduced amount of components *S* and *SS* in intensity. Then we can assign component *A* to the interface component due to the first-layer Si atoms (dimers). Certainly, component *A* should contain a very little contribution from component *C* (i.e., third-layer Si atoms, defects). After 0.2-ML coverage of acetylene, the shoulder at the higher KE side indicates that the surface components are still there. Based on the above consideration, the  $Si\ 2p$  is decomposed into five components (*S*, *SS*, *S'*, *B*, and *A*) in this case. Certainly, component *A* should have a little contribution from component *C*. All these symbols have the same meaning as before. During the fitting process, the energy positions of the components remain constant relative to component *B*, which indicates that our fitting process is reliable.

Another very interesting and important result is that there is only one interface component in the  $Si\ 2p$  core level after acetylene adsorption. The Si dimers are believed to be intact after the adsorption of acetylene at RT.<sup>2,8,10</sup> If the Si dimers bonded to the acetylene molecule were still asymmetric after the acetylene adsorption, two separated components would be presented. Instead, one interface component is observed, showing that the asymmetric dimers may become symmetric dimers after acetylene adsorption. The same behavior has been observed in the  $Si(100)-2\times 1-H$  interface.<sup>18</sup>

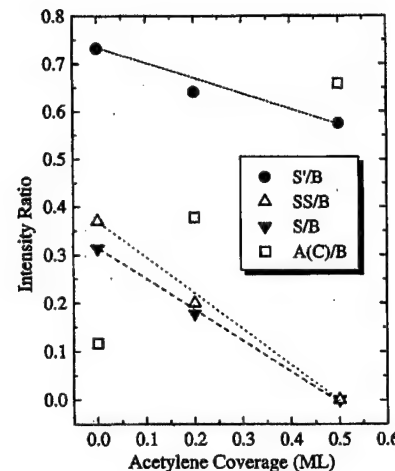


FIG. 3. Intensity ratios of the surface components (*S*, *SS*, and *S'*) to the bulk component (*B*) of the  $Si\ 2p$  core-level spectra for different acetylene coverage. The *S/B* and *SS/B* data points predict an ideal homogeneous adsorption mode.

The ratios of the *S/B*, *SS/B*, *S'/B*, and *A (C)/B* intensity are plotted in Fig. 3 as a function of the  $C_2H_2$  coverage. The ratios of the *S/B* and *SS/B* show an approximate linear decline to zero at the saturation coverage (0.5 ML). At the same time, the *S'/B* data decrease in intensity, too, but they do not decline to zero at 0.5 ML. The intensity of component *A (C)* increases near linearly with increasing the  $C_2H_2$  coverage. At 0.5 ML, its intensity is roughly equal to (a little smaller than) the sum of components *S* and *SS* on the clean surface. This indicates that component *A* mostly comes from components *S* and *SS*.

In Fig. 4 are the  $C\ 1s$  core-level spectra for the 0.5-ML coverage case subsequently heated to different temperatures [Figs. 4(a)-4(g)]. The spectra are normalized to the same height. In Fig. 4, we also shifted the spectra towards the higher KE side to cancel the effect of the band bending.

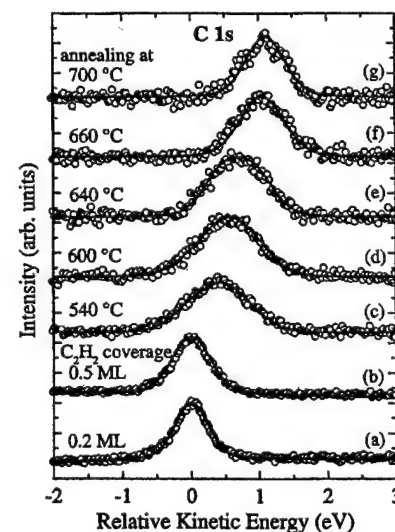


FIG. 4. High-energy-resolution  $C\ 1s$  core-level spectra ( $h\nu = 350$  eV) of (a) the surface exposed 0.2-ML acetylene at RT; (b) the surface exposed 0.5-ML acetylene at RT; (c) annealing at 540 °C; (d) 600 °C; (e) 640 °C; (f) 660 °C; and (g) 700 °C.

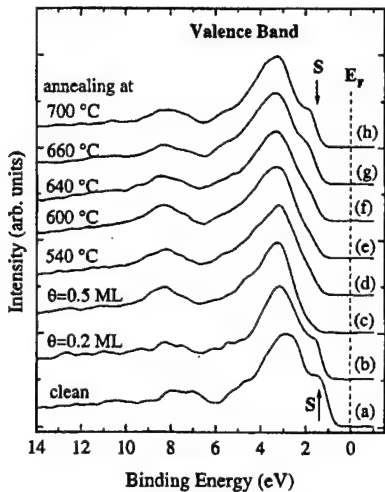


FIG. 5. The VB spectra ( $h\nu=150$  eV) of (a) the clean surface; (b) the surface exposed 0.2-ML acetylene at RT; (c) the surface exposed 0.5-ML acetylene at RT; (d) after annealing at 540 °C; (e) 600 °C; (f) 640 °C; (g) 660 °C; and (h) 700 °C. The surface state is denoted by the symbol  $S$ .

Without annealing, the full width at half maximum intensity (FWHM) of the C 1s core level is only 0.55 eV (0.61 eV) after a coverage of 0.2 ML (0.5 ML) acetylene. The best-fitting results show that the Lorentzian width is 0.138 eV, which is smaller than the 0.3 eV obtained by Dufour *et al.*,<sup>5</sup> but close to the 0.1 eV obtained by Krause *et al.*<sup>19</sup>

More direct proof for the above interpretation can be found in VB spectra. Figure 5 demonstrates the coverage and temperature dependence of VB spectra. The photon energy used here is 150 eV. Although the energy resolution is good, the photon energy is too big for measuring the VB spectra due to the very small cross sections for the valence electrons of C atoms (2s,2p), Si atoms (3s,3p), and the surface state.<sup>20</sup> Fortunately, we can obtain some very useful results from the VB.

For the clean surface, the valence-band maximum (VBM) is measured to be 0.8 eV below the Fermi level. The shoulder (peak  $S$ ) at 1.5 eV below  $E_F$  or at 0.7 eV below the VBM is the surface state, which is caused by the DB's of the Si dimers. The position of the surface state is in agreement with the angle-resolved result.<sup>16</sup> Due to the smaller cross section of the valence electrons, the intensity of this surface state is not strong. After 0.5-ML adsorption of  $C_2H_2$ , the VBM shifts towards higher BE by 0.2 eV. As mentioned before, this shift is caused by the band bending. The surface state decreases when the coverage of acetylene is increased, and it disappears completely after the saturation adsorption (0.5 ML), showing that the Si DB's are quenched by the adsorption of acetylene.

### B. Interface reaction

After the Si surface is exposed to 0.5-ML  $C_2H_2$ , the LEED pattern still exhibits  $2\times 1$  reconstruction. Annealing at 540 °C, the  $2\times 1$  LEED pattern becomes very weak. As the annealing temperature increases, the  $2\times 1$  pattern becomes strong. After annealing at 700 °C, a good  $2\times 1$  LEED pattern is observed. This means that the  $2\times 1$

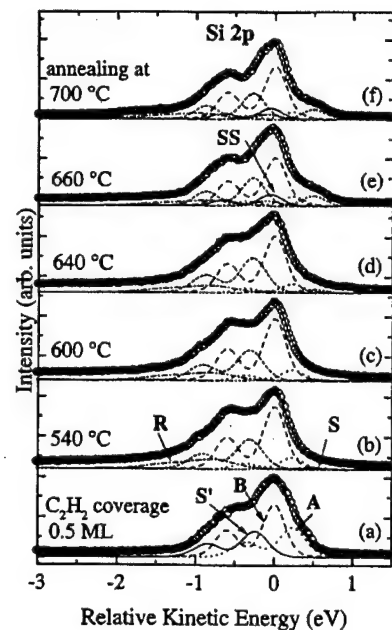


FIG. 6. The temperature dependence of the Si 2p spectra ( $h\nu=150$  eV) after 0.5-ML coverage. (a) The surface exposed 0.5-ML acetylene at RT; (b) annealing at 540 °C; (c) 600 °C; (d) 640 °C; (e) 660 °C; and (f) 700 °C. The components are also shown: component  $B$  (dash line),  $S$  (dash dot dot line),  $C$  or  $A$  (dot line),  $SS$  (short dot line),  $S'$  (short dash line),  $R$  (dash dot line), the fitting curve (solid line), and the experimental data (open circles). Details of the curve fitting are given in the text.

structure is restored. Figure 6 shows the temperature dependence of the Si 2p core-level spectra. Without any data fitting, we find that the Si 2p spectra show broadening at both higher and lower KE sides. After annealing at 700 °C, the line shape of the Si 2p core level looks like that of a clean surface with the exception of a widening at the lower KE side. The development of the shoulder (component  $S$ ) indicates a restoration of the  $2\times 1$  structure, which is in agreement with the LEED observation mentioned above. In the meantime, the widening at the lower KE side shows that interface reaction occurs at the interface.<sup>5</sup>

Based on these observations and assumptions, each Si 2p spectrum should contain all possible components:  $B$ ,  $S$ ,  $A$ ,  $SS$ ,  $S'$ , and  $R$ . Component  $R$  is the reaction Si 2p component. Other symbols have the same meaning as mentioned before. The Gaussian width of the reaction component ( $R$ ) increases to 0.65 eV because the reacted silicon species do not have the same chemical environment. The results show that all of the components change in intensity for increasing temperature, but their energy positions (not including component  $R$ ) remain constant relative to component  $B$  within the tolerances. This shows, again, that our fit is very reliable.

Upon annealing in the 540–640 °C temperature range, component  $S$  grows slowly, then it increases quickly after annealing above 640 °C. Component  $A$  decreases significantly at 540 °C and continues to decrease slowly as the temperature is increased. Meanwhile, component  $R$  appears at 540 °C, and slowly decreases in intensity while shifting slightly towards the lower KE side. Component  $SS$  is too weak to be observed when the annealing temperature is below 640 °C. At 660 °C, it appears in the spectra. The frac-

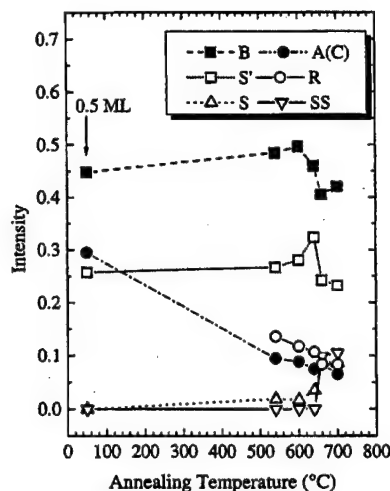


FIG. 7. Variations of the fractional intensities of the components ( $S$ ,  $SS$ ,  $S'$ ,  $A$  or  $C$ ,  $R$  and  $B$ ) of the  $Si\ 2p$  spectra as a function of the annealing temperature. The same component fraction intensities of the surface covered by 0.5-ML acetylene are also shown for the comparison.

tional intensities of components  $S$ ,  $SS$ ,  $S'$ ,  $A$  (or  $C$ ),  $R$ , and  $B$  as a function of temperature are plotted in Fig. 7. Also in Fig. 7 is shown the fractional intensities of the  $Si\ 2p$  for the surface exposed by 0.5-ML acetylene.

After annealing at low temperature (below 660 °C), the appearance of component  $S$  shows the restoration of the  $2\times 1$  structure due to the desorption of acetylene.<sup>2,6</sup> But, its intensity is very weak. That is to say, only some acetylene molecules desorb from the  $Si$  surface. At the same time, no component  $SS$  is observed. These show that the  $Si$  dimer may still be symmetrical. On the other hand, components  $SS$  appears at 660 °C, indicating that the  $Si$  dimers become asymmetric. Annealing above 660 °C, the  $SiC$  is believed to be formed completely,<sup>2</sup> then the large change in components  $S$  and  $SS$  are probably not caused by the desorption of acetylene. Instead, as discussed below, it is induced by the cluster formation of  $SiC$ .

The decrease of component  $A$  indicates that acetylene decomposes into  $C_2H_x$  ( $x=1,0$ ) and  $H$  species and some desorbs from the  $Si$  surface as  $C_2H_2$ . Upon heating to 700 °C, all of the acetylene molecules are decomposed or desorbed.<sup>2</sup> However, component  $A$  is still in  $Si\ 2p$ . As mentioned above, the position of component  $A$  is very close to that of component  $C$  from the third-layer  $Si$  atoms or defects. Thus, now, the contribution to component  $A$  only comes from component  $C$ . Due to the interface reaction, the numbers of defects on the surface must increase. So, the fractional intensity of component  $C$  would be higher than that on the clean surface. It is in agreement with the results shown in Fig. 6. For components  $B$  and  $S'$ , no obvious shifts are found. This shows that the reaction is around the first-layer  $Si$  atoms, which leads to a locally abrupt  $SiC/Si$  interface.<sup>21</sup>

Now, let us look at component  $R$ . As shown in Figs. 6 and 7, even when the annealing temperature is as low as 540 °C, component  $R$  appears in the spectrum. The appearance of component  $R$  is accompanied by the reduction of component  $A$ . Annealing at low temperature (below 600 °C) should not break the C-C bonds, and only causes the acetylene to de-

compose into  $C_2H_x$  ( $x=1,0$ ) and  $H$  species.<sup>2</sup> Thus, we think that component  $R$  is due to these  $Si$  atoms which bond to the  $C$  atoms of  $C_2H_x$  ( $x=1,0$ ) species. With increasing temperature, component  $R$  decreases in intensity slowly and shifts slightly towards the lower KE side. The slow reduction in intensity shows again that most of the acetylene tends to decompose rather than to desorb. When the annealing temperature is higher than 660 °C, the  $SiC$  compound is believed to be formed completely and there are no  $C_2H_x$  ( $x=1,0$ ) species on the  $Si$  surface.<sup>2</sup> Then, component  $R$  is only due to the emission from  $Si$  atoms in the  $SiC$  compound. When the annealing temperature ranges from 600 to 660 °C,  $SiC$  begins to form on the  $Si$  surface, and meanwhile the  $C_2H_x$  ( $x=1,0$ ) species are still on the surface.<sup>2</sup> Thus component  $R$  contains both the contribution of the  $Si-C$  bonds in the  $SiC$  compound and of the  $Si$  atoms which bond to  $C$  atoms of the  $C_2H_x$  ( $x=1,0$ ) species. However, there is not a large shift corresponding in component  $R$  to this reaction process. The reasons will be discussed in detail below.

As shown in Fig. 4, the FWHM of the  $C\ 1s$  peak increases to 1.2 eV at 540–600 °C, and then decreases to 0.72 and 0.67 eV upon annealing at 640 and 700 °C, respectively. Additionally, after annealing at 700 °C, the  $C\ 1s$  peak shifts towards the higher KE side by 1.2 eV. Although they are very wide after annealing,  $C\ 1s$  core-level spectra [Figs. 4(c) to 4(g)] are not well resolved into several peaks yet. According to the results of HREELS (Ref. 2) and the present  $Si\ 2p$  core-level spectra, the wide  $C\ 1s$  spectra are due to the mixture of several different chemical states— $C_2H_x$  ( $x=2,1,0$ ) and  $SiC$  compound. After annealing temperature over 660 °C [Figs. 4(f) and 4(g)], the big reduction of the widths of  $C\ 1s$  core-level spectra implies that all of the  $C$  atoms have almost the same chemical states. That is to say,  $SiC$  is completely formed and the  $C_2H_x$  ( $x=2,1,0$ ) chemical species are totally gone.

After annealing, the surface state develops gradually in VB spectra (Fig. 5). The presence of the surface state shows clearly the restoration of  $2\times 1$  structure, which agrees with the measurement of  $Si\ 2p$  core-level spectra shown in Fig. 6 very well.

#### IV. DISCUSSIONS

Now, let us see which model shown in Figs. 1(a) and 1(b) can fit better with the present HRPES data. In our model proposed by the PH image,<sup>10</sup> one acetylene molecule bonds to the two adjacent  $Si$  dimers on alternate pedestal sites in one row. Since the  $Si$  dimers are not cleaved, each  $Si$  atom has one DB. When it bonds to one  $C$  atom, there is no DB for another  $C$  atom on the adjacent pedestal site. Thus, the saturation coverage is naturally 0.5 ML rather than 1 ML; this is consistent with the STM results.<sup>6</sup> Moreover, after adsorption of 0.5-ML acetylene, we can see that all of the  $Si$  DB's can be destroyed by the adsorption of acetylene, which agrees with the observable disappearance of the surface state in the VB spectra [Fig. 5(c)]. At the same time, all of the first-layer  $Si$  atoms have the same chemical environment (i.e., every  $Si$  atom only bonds to one  $C$  atom) if the  $Si$  dimers are symmetric. This agrees with our observation of only one interface component in the  $Si\ 2p$  spectra.

In our model, of course, the acetylene overlayer also ex-

hibits either a local  $2\times 2$  [Fig. 1(b)] or  $c(2\times 4)$  structure (not shown here), depending on whether acetylene that adsorbs on alternate pedestal sites along the adjacent rows is in phase or out of phase. This  $2\times 2$  or  $c(2\times 4)$  structure, as discussed in Ref. 6, is not in conflict with the observation of a  $2\times 1$  LEED pattern, because the scattering cross section of acetylene may be very small and the  $2\times 2$  reconstruction produces spots which fall at the same position as the original LEED pattern. In addition, another weak  $1\times 2$  domain is observed in the LEED pattern.<sup>10</sup>

Based on STM images, Li *et al.* proposed that acetylene adsorbs on alternate dimers [see Fig. 1(a)].<sup>6</sup> Certainly the acetylene overlayer exhibits either a local  $2\times 2$  or  $c(2\times 4)$  structure, depending on whether acetylene that adsorbs on adjacent rows is in phase or out of phase. However, this model has one shortcoming, i.e., it hardly explains why acetylene likes to adsorb on alternate Si dimers and not on all Si dimers or why the saturation coverage is 0.5 ML rather than 1 ML. Moreover, this model is in disagreement with our present results. As seen in Fig. 1(a), the adjacent Si dimers are not equivalent after saturation adsorption of acetylene. That is to say, one Si dimer is covered by acetylene while the two adjacent Si dimers are "free." Thus their chemical environments are not the same. This may cause the different components in Si  $2p$  spectra. In Fig. 2(c), however, only one interface component is observed. In this model, one-half of the Si dimers are not covered by acetylene at 0.5-ML coverage, which means that one-half of the DB's would not be destroyed by acetylene. Thus the surface state in the VB spectra should decrease in intensity, but never totally disappears. It is in disagreement with the observation of VB spectra. On the other hand, if the saturation coverage is 1 ML,<sup>2,7</sup> this model agrees with our present results because each Si dimer is covered by one acetylene molecule. But, it is not in agreement with our previous PH image.<sup>10</sup>

In our model, each C atom bonds to two Si atoms of two adjacent dimers, another C atom, and H atom. Thus each C atom is naturally the  $sp^3$  rehybridization rather than  $sp^2$  rehybridization. The  $sp^3$  hybridization is observed indeed in Refs. 2, 22, and 23. However, our model does not fit the results observed in Ref. 3. But we think it is better to assign the peak at  $1065\text{ cm}^{-1}$  in their experiments to the single C-C stretch, because it is very close to the stretching energy of the single C-C bond ( $950\text{ cm}^{-1}$ ).<sup>2</sup> Indeed there is no consensus for the interpretation of HREELS data. Unlike other measurements, the PH method is direct and can provide unambiguous three-dimensional atomic geometry for the selected atoms (i.e., carbon).<sup>10,11</sup> Therefore, based on the results from both the PH image<sup>10</sup> and the electronic structure, we can conclude that the model shown in Fig. 1(b) is the correct model.

After annealing, the present results of the electronic structure agree with other works.<sup>2,6</sup> After annealing, wide C  $1s$  core-level spectra [Figs. 1 and 4(c)–4(e)] indicate the mixture of  $\text{C}_2\text{H}_x$  ( $x=2,1,0$ ) and SiC compound. Meanwhile, a weak surface component (peak  $S$ ) appears in the Si  $2p$  and a weak surface state develops in the VB. These show that some chemisorbed acetylene molecules desorb into vacuum as  $\text{C}_2\text{H}_x$  ( $x=2,1,0$ ), while most of them decompose into  $\text{C}_2\text{H}_x$  ( $x=1,0$ ) species. With increasing temperature, more and more acetylene decomposes into  $\text{C}_2\text{H}_x$  ( $x=1,0$ ) species

because component  $A$  in the C  $1s$  spectra decreases. Certainly, some  $\text{C}_2\text{H}_x$  ( $x=2,1,0$ ) species continue to desorb from the surface, which causes component  $R$  to decrease in intensity when the temperature is increased. After annealing  $660\text{ }^\circ\text{C}$ , the reduction of the FWHM of C  $1s$  core levels shows that acetylene is dissociated completely and the SiC forms completely on the Si surface. Meanwhile, component  $SS$  appears in the Si  $2p$  spectrum and the surface state in the VB continues to increase in intensity. These results indicate that the asymmetric Si(100)- $2\times 1$  structure is restored. However, this restoration of the Si(100)- $2\times 1$  structure at this temperature is probably not caused by the desorption of the SiC species because component  $R$  does not decrease too much. Instead, it is mostly caused by the accumulation of SiC clusters.<sup>6</sup> Therefore, we can think that the clusterlike SiC compound is separated by the asymmetric Si(100)- $2\times 1$  structure. This explanation agrees with the results of Refs. 6 and 21.

The shift of the Si  $2p$  core levels between the SiC and the bulk of Si in our experiment (0.85 eV) is smaller than that reported by others [1.7 eV (Ref. 5) and 1.5 eV (Ref. 24)]. From Fig. 4, the total shift of C  $1s$  after annealing between  $540$  and  $700\text{ }^\circ\text{C}$  is about 0.6 eV. It is still smaller than that (1.2 eV) observed in Refs. 5 and 24. That is to say, the differences of the Si  $2p$  and C  $1s$  core levels for the SiC compound between our experiment and others are about 0.85 and  $-0.60$  eV, respectively. This can be explained as follows. In our experiment, the exposure of acetylene is low (0.5 ML). Meanwhile, the clusterlike SiC compound is separately on the Si(100)- $2\times 1$  surface. Moreover, some  $\text{C}_2\text{H}_x$  ( $x=2,1,0$ ) species desorb into the vacuum chamber during annealing. Thus we can think that the SiC compound in our case has not formed the bulk SiC structure. Instead, it is the clusterlike structure.<sup>6</sup> It is well known that there is a core-level shift between the cluster and the bulk, because the electronic structure is not well formed in the cluster and the chemical bonding state in the cluster is not the same with the bulk. It looks like the surface core-level shift (SCLS) in the core-level spectra. In fact, the SCLS of the Si  $2p$  and C  $1s$  core levels is truly observed in the cubic SiC(001) surface.<sup>25</sup> This SCLS is about 0.8 eV (towards the higher KE side) for the Si  $2p$  and  $-1.2$  eV (towards the lower KE side). In normal XPS studies,<sup>5,24</sup> the Si  $2p$  and C  $1s$  core levels are bulk-sensitive due to the great photon energy ( $>1000$  eV). Then the Si  $2p$  and the C  $1s$  signals obtained by XPS mostly come from the bulk. In our experiment, however, both of the Si  $2p$  and C  $1s$  core levels are surface-sensitive. Although the atomic structure of the SiC compound in our experiment is not known and there is a difference in the core-level shifts between the cluster and the surface layer atoms, we can still find that both the direction and the magnitude of the shifts in Si  $2p$  and C  $1s$  between our experiment and Ref. 25 are close. Thus we can attribute these different observed shifts both in the Si  $2p$  and C  $1s$  between the present data and Refs. 5 and 24 to the effect of the SiC cluster. That is the reason why there is no big shift in compound  $R$ (Si  $2p$ ) before and after the SiC formation. Indeed, the cluster model of the initial growth of the SiC on the Si(100) surface was observed.<sup>6,21</sup>

## V. CONCLUSIONS

The HRPES study has been made on the adsorption and interface reaction of acetylene with the Si(100)-2×1 surface. At RT, the experimental results show clearly that acetylene saturates all of the DB's of Si dimers, which cause the disappearance of the surface state in the VB. Meanwhile, the Si 2p spectra indicate that the asymmetric Si dimers may become the symmetric dimers. These results are in agreement with the tetra- $\sigma$  model proposed by our previous PH image. After annealing, C 1s spectra show that acetylene is decomposed into C<sub>2</sub>H<sub>x</sub> ( $x=1,0$ ) species. In addition, some C<sub>2</sub>H<sub>x</sub> ( $x=2,1,0$ ) species desorb from the Si surface. At the

same time, the cluster SiC starts to form on the Si surface. By heating to 660 °C, the Si dimers become asymmetric again from the symmetric Si dimers on the surface exposed by 0.5-ML acetylene, and the SiC compound forms completely. At the same time, the C<sub>2</sub>H<sub>x</sub> ( $x=2,1,0$ ) species are totally gone.

## ACKNOWLEDGMENTS

The authors would like to thank the staff at ALS for their most generous help and support. This work was supported by NSF. The ALS of LBNL is supported by the DOE.

\*Electronic address: shihong@gemini.oscs.montana.edu FAX: 406-994-4452.

- <sup>1</sup>J. Yoshinobu, H. Tsuda, M. Onchi, and M. Nishijima, *Chem. Phys. Lett.* **130**, 170 (1986).
- <sup>2</sup>M. Nishijima, J. Yoshinobu, H. Tsuda, and M. Onchi, *Surf. Sci.* **192**, 383 (1987).
- <sup>3</sup>C. Huang, W. Widdra, X. S. Wang, and W. H. Weinberg, *J. Vac. Sci. Technol. A* **11**, 2250 (1993).
- <sup>4</sup>Yan Chen, Zhaohui Liu, Qingzhe Zhang, Kean Feng, and Zhangda Lin, *Appl. Phys. Lett.* **67**, 2936 (1995).
- <sup>5</sup>G. Dufour, F. Rochet, F. C. Stedile, Ch. Poncey, M. De Crescenzi, R. Gunnella, and M. Froment, *Phys. Rev. B* **56**, 4266 (1997).
- <sup>6</sup>L. Li, C. Tindall, O. Takaoka, Y. Hasegawa, and T. Sakurai, *Phys. Rev. B* **56**, 4848 (1997).
- <sup>7</sup>P. A. Taylor, R. M. Wallace, C. C. Cheng, W. H. Weinberg, M. J. Dresser, W. J. Choyke, and J. T. Yates, Jr., *J. Am. Chem. Soc.* **114**, 6754 (1992).
- <sup>8</sup>R.-H. Zhou, P.-L. Cao, and L.-Q. Lee, *Phys. Rev. B* **47**, 10 601 (1993).
- <sup>9</sup>Y. Imamura, Y. Morkawa, T. Yamasaki, and H. Nakatsuji, *Surf. Sci. Lett.* **341**, L1091 (1995).
- <sup>10</sup>S. H. Xu, M. Keeffe, Y. Yang, E. Rotenberg, and G. J. Lapeyre (unpublished).
- <sup>11</sup>Huasheng Wu and G. J. Lapeyre, *Phys. Rev. B* **51**, 14 549 (1995).
- <sup>12</sup>J. J. Joyce, M. Del Giudice, and J. H. Weaver, *J. Electron Spec-*

trosc. Relat. Phenom.

<sup>13</sup>See, for example, F. Flores, and C. Tejedor, *J. Phys. C* **20**, 145 (1987).

<sup>14</sup>E. Landemark, C. J. Karlsson, Y.-C. Chao, and R. I. G. Uhrberg, *Phys. Rev. Lett.* **69**, 1588 (1992).

<sup>15</sup>D.-S. Lin, T. Miller, and T.-C. Chiang, *Phys. Rev. Lett.* **67**, 2187 (1991).

<sup>16</sup>R. I. G. Uhrberg, E. Landemark, and Y.-C. Chao, *J. Electron Spectrosc. Relat. Phenom.* **75**, 197 (1995).

<sup>17</sup>L. Patthey, E. L. Bullock, T. Abukawa, S. Kono, and L. S. O. Johansson, *Phys. Rev. Lett.* **75**, 2538 (1995).

<sup>18</sup>J. A. Schäfer (private communication).

<sup>19</sup>M. O. Krause and J. H. Oliver, *J. Phys. Chem. Ref. Data* **8**, 329 (1979).

<sup>20</sup>J. J. Yeh and I. Lindau, *At. Data Nucl. Data Tables* **32**, 1 (1985).

<sup>21</sup>M. Kitabatake, M. Deguchi, and T. Hirao, *J. Appl. Phys.* **74**, 4438 (1993).

<sup>22</sup>A. T. S. Wee, Z. C. Feg, H. H. Hng, K. L. Tan, C. C. Tin, R. Hu, and R. Coston, *Appl. Surf. Sci.* **81**, 377 (1994).

<sup>23</sup>R. Kaplan, *Surf. Sci.* **215**, 111 (1989).

<sup>24</sup>S. Juillaguet, L. Kubler, M. Diani, J. L. Bischoff, G. Gewinner, P. Wetzel, and N. Bécourt, *Surf. Sci.* **339**, 363 (1995).

<sup>25</sup>H. W. Yeom, Y.-C. Chao, S. Terada, and R. I. G. Uhrberg, Max-Lab Activity Report 1996 (unpublished).

<sup>26</sup>L. Clemen, R. M. Wallace, P. A. Taylor, M. J. Dresser, W. J. Choyke, and J. T. Yates, *Surf. Sci.* **268**, 205 (1992).

## Defect formation near GaN surfaces and interfaces

L.J. Brillson<sup>a,\*</sup>, T.M. Levin<sup>a</sup>, G.H. Jessen<sup>a</sup>, A.P. Young<sup>a</sup>, C. Tu<sup>b</sup>, Y. Naoi<sup>b</sup>,  
F.A. Ponce<sup>c</sup>, Y. Yang<sup>d</sup>, G.J. Lapeyre<sup>d</sup>, J.D. MacKenzie<sup>e</sup>, C.R. Abernathy<sup>e</sup>

<sup>a</sup>Department of Electrical Engineering, The Ohio State University, 2015 Neil Avenue, Columbus, OH 43210, USA

<sup>b</sup>Department of Electrical Engineering, University of California, San Diego, CA 92093, USA

<sup>c</sup>Department of Physics, Arizona State University, Columbus, OH 432210, USA

<sup>d</sup>Department of Physics, Montana State University, Bozeman, MT 59717, USA

<sup>e</sup>Department Material Science and Engineering, Florida State University, Gainesville, FL 32611, USA

---

### Abstract

We have used low-energy electron-excited nanoscale-luminescence (LEEN) spectroscopy combined with ultrahigh vacuum (UHV) surface science techniques to probe deep level defect states at GaN free surfaces, metal-GaN contacts and GaN/InGaN quantum well interfaces. Employing energies as low as 100 eV and ranging up to 5 keV, we have been able to establish the local nature of these states and their spatial variation normal to the interface plane on an incremental 10-20 nm scale. Coupled with surface science techniques, these measurements show that a variety of discrete deep levels form deep within the GaN band gap due to (a) native defects, (b) metal-induced bonding, (c) reaction products, and (d), in the case of GaN/InGaN heterostructures, local interface phase changes. These results suggest that deep levels are a common feature at GaN interfaces and hence can play an integral role in charge transfer and the formation of local dipoles at GaN heterostructures. © 1999 Elsevier Science B.V. All rights reserved.

**Keywords:** Gallium nitride; Surfaces and interfaces; New experimental techniques

---

### 1. Introduction

Deep electronic states are of central importance in determining the bulk emissive and transport properties of GaN. Theoretical calculations and experimental measurements show that the bulk defect and impurity states have energy levels ranging across the band gap [1-4]. While considerable attention has focused on the trapping and recombination properties of such bulk deep levels, relatively little is known about the electronic states at GaN surfaces and interfaces. The presence of localized states at such boundaries can affect Schottky barrier formation and heterojunction band offsets. The nanometer-scale film thicknesses now being used in nu-

merous GaN heterostructures further amplifies the relative importance of such interface electronic features.

In this paper, we present evidence for a variety of discrete electronic states associated with GaN surfaces and interfaces. Such states are possible to identify and distinguish from bulk features with low-energy electron-excited nanoscale-luminescence (LEEN) spectroscopy. We have used the luminescence associated with optical transitions into or out of gap states in order to characterize electronic features near interfaces. This requires the ability to: (a) excite free electron-hole pairs, (b) produce such excitation near "buried" interfaces, and (c) vary this excitation in depth on a nanometer scale. These criteria are met by LEEN spectroscopy, which has already been applied to a wide variety of semiconductor-semiconductor and semiconductor-metal interfaces [5,6].

Considerable research has shown the strong dependence of bulk deep levels in GaN on the specifics of growth and subsequent processing [7,8]. Additional electronic

---

\* Corresponding author. Fax: (614) 688-4688.

E-mail address: Brillson.1@osu.edu (L.J. Brillson)

states may reside near surfaces and interfaces due to chemical and morphological changes in the crystal. All these extrinsic features can degrade the near band edge (NBE) optical emission as well as transport properties. In this paper, we present evidence for discrete gap states at GaN surfaces, metal-GaN interfaces, and III-V nitride heterojunctions. Furthermore, the use of surface science techniques permits the chemical origin of extrinsic, near-surface states to be investigated.

## 2. Experiment

The LEEN experiment consists of a low-energy (0.1–5 keV) electron beam impinging on a controlled surface in ultrahigh vacuum (UHV). The minority carriers generated recombine either across the band gap (near band edge (NBE) radiation), through deep levels in the band gap, or via (nonradiative) phonon generation. The depth of excitation can be varied as a function of incident electron beam energy from a few nm to a few hundred nm over this energy range [9]. The incident electron beam produces a cascade of secondary electrons and, subsequently free electron-hole pairs. One can calculate the maximum range of penetration  $R_B$  for the Everhart-Hoff relation [10] extending to low energies. The maximum electron-hole pair production of the electron cascade occurs for values approximately one-third of these values. Thus, for example, a 1 keV electron beam produces a cascade of secondaries and generates electron-hole pairs that extend 20 nm below the surface, peaking at  $\sim 6$ –7 nm. Photon emission is collected via IR-UV transmitting optics to photodetectors. This experimental setup is described in previous publications [5,6].

## 3. Results and discussion

Fig. 1 shows LEEN spectra for GaN grown by molecular beam epitaxy (MBE) under different N deposition conditions. A biased electrode provided a means to deflect ionized N atoms from the plasma source away from the growth surface. Fig. 1 shows dramatically different spectral features for GaN grown with different deflection voltages applied to the electrode. The “yellow” luminescence (YL) that dominates the MBE GaN grown without removing N ions decreases with increasing deflection voltage. Likewise, a shallow defect transition at 3.37 eV decreases as well. A deflection voltage of 700 V can achieve almost two orders of magnitude decrease in these peaks. Furthermore, the electron mobility more than doubles from a value of 300–640  $\text{cm}^2/\text{V s}$  from zero to the highest deflection voltage. These results indicate that the presence of N ions gives rise to yellow luminescence, which in turn corresponds to increased electron trapping

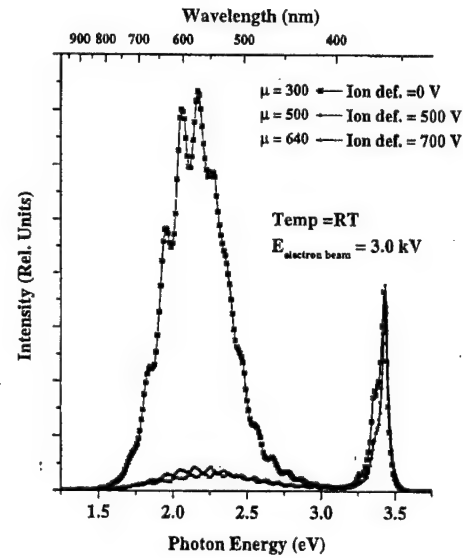


Fig. 1. LEEN spectra with 3.0 keV excitation energy of MBE-grown GaN versus ion deflection voltage. Increasing ion deflection voltage suppresses the midgap and 3.37 eV luminescence.

and reduced mobility. It should also be noted that this yellow luminescence is in fact comprised of at least three overlapping emission peaks centered at 1.75–1.8, 2.15, and 2.4 eV, rather than one broad peak distribution. Similar multiple peak structure in the YL energy range is evident in GaN grown by organometallic chemical vapor deposition (OMCVD) [4]. Finally, it should be noted that the emission spectra in Fig. 1 correspond to a total range of excitation  $R_B$  of 90 nm – well below the free surface. Depth-dependent spectra (not shown) reveal that the yellow luminescence is relatively constant versus depth for the GaN grown without deflection. On the contrary, the GaN grown with N ions deflected shows YL increases by over an order of magnitude for near-surface excitation ( $\leq 1$  keV corresponding to  $R_B \leq 20$  nm). This increased emission suggests either defects formed preferentially near the free GaN surface or the influence of residual N ions associated with the termination of growth.

Fig. 2 illustrates a Ga-related defect at the surface of a GaN specimen grown by metallorganic MBE (MOMBE). The as-grown specimen shows YL with intensity completely dominating the NBE peak for all penetration depths. After annealing at  $T > 1250^\circ\text{C}$ , dramatic new features appear, including a sharp ( $< 0.025$  eV FWHM) peak at 1.81 eV and a broad (0.33 eV FWHM) peak centered at 1.66 eV. Similar emissions have been reported previously as “red luminescence” that appeared when excited via a broad C-excitation band [10]. Auger electron spectroscopy (AES) measurements of surface composition establish a  $> 10\%$  decrease in the Ga/N ratio and a residual C and O concentration of 6% C and  $< 10\%$  O. Depth-dependent spectra reveal that the

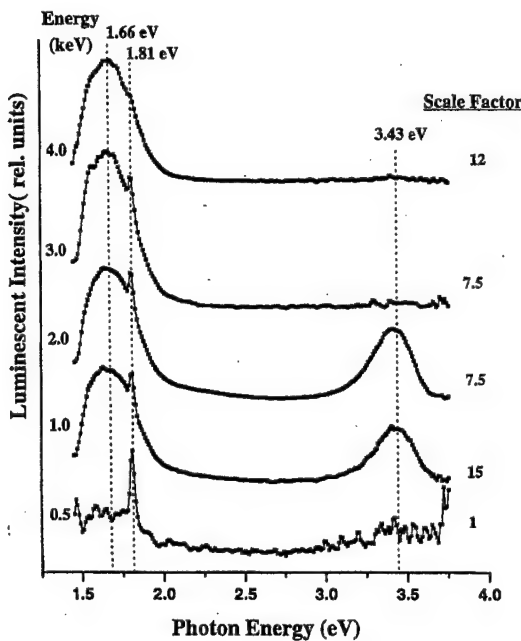


Fig. 2. LEEN spectra as a function of excitation energy and depth showing the near-surface features between 1.5 and 2.0 eV induced by 1250°C annealing.

1.81 eV peak intensity decreases with deeper excitation. The sharpness of this feature, its near-surface location, and the decrease in relative Ga concentration together suggest emission either from a Ga-related nanostructure, e.g., Ga droplets, or a surface segregated impurity, e.g., Al or Cr. The broader feature corresponding to the Ga-deficient surface is at least 120 nm thick. The "bulk" nature of this emission suggests the formation of a defect complex associated with a Ga deficiency. Interestingly, this layer forms under high-temperature conditions usually associated with preferential N desorption. The YL emission does not appear to increase under these conditions. Subsequent UHV deposition of a 1 nm Ga overlayer on this heat-treated surface reduces (but does not eliminate) the 1.66 eV peak and, to a lesser extent, the YL shoulder within the top 6–20 nm, further confirming the Ga-deficient nature of the lower energy feature. The contrast in behavior between these red luminescence features versus the YL indicates that different defects can become dominant recombination sites with different surface treatments near the free GaN surface.

Defect formation also occurs at metal–GaN interfaces. Fig. 3 illustrates LEEN spectra taken at different depths below a bare, MBE-grown GaN surface versus that of a similar crystal coated with 30 monolayers (4.8 nm) of Mg [6]. This metal–GaN interface was formed by evaporation in UHV on a LEED-ordered, MBE-grown surface, then annealed at 1000°C [11]. Fig. 3 shows broad, nearly featureless emission extending from ~3 to below 1.4 eV and relatively uniform at all depths. In contrast

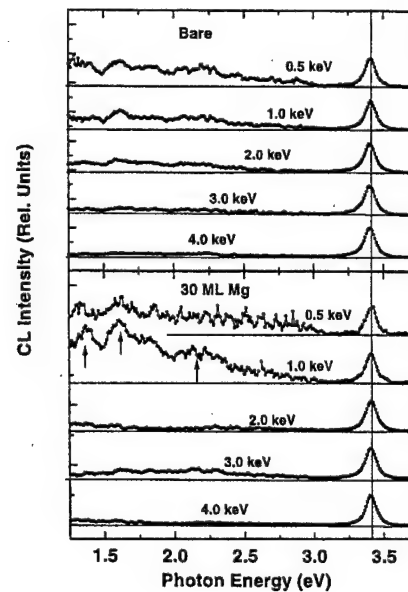


Fig. 3. LEEN spectra as a function of excitation energy and depth for a bare and a Mg-covered GaN single crystal showing the new emissions induced by the metal overlayer plus high-temperature anneal.

the Mg-covered GaN shows a maximum in sub-gap emission at excitation depths of 3–6 nm. Despite the low signal intensities, this emission indicates peak features at 1.4, 1.6, and 2.15 eV. Soft X-ray photoemission spectroscopy (SXPS) measurement of the Fermi level movement for this same sample show that it stabilizes at 2.2 eV above the valence band (1.2 eV below the valence band) [12]. Interestingly, other metals on UHV-prepared n-type GaN surfaces are known to stabilize the Fermi level within a range of 2.0–2.6 eV [13]. This suggests that metal-induced states at the Mg–GaN interface play an active role in the Schottky barrier formation. However, the role of defects may not extend to all metal contacts with GaN. For example, Al–GaN interfaces annealed at 1000°C in UHV result in a reacted interface layer rather than new defect formation [6].

New localized states are also present at GaN heterojunctions. We obtained LEEN depth-dependent spectra from an InGaN quantum well "buried" 30 nm below the free GaN surface. These quantum well structures consisted of an  $In_xGa_{1-x}N$  layer ( $x = 0.14$  or  $0.28$ ) with an average thickness of 2 nm. This layer was confined between a 2  $\mu m$  thick Si-doped ( $n = 3 \times 10^{18} \text{ cm}^{-3}$ ) GaN layer grown at 1050°C over a (0 0 0 1) sapphire substrate and a 30 nm GaN capping layer not intentionally doped and grown at roughly 800°C, the same growth temperature as the  $In_xGa_{1-x}N$  layer [14]. The bowing parameter calculations of In concentration due to McCluskey et al. [15] yield  $x$  values approximately one half of those extracted from a linear extrapolation between the GaN

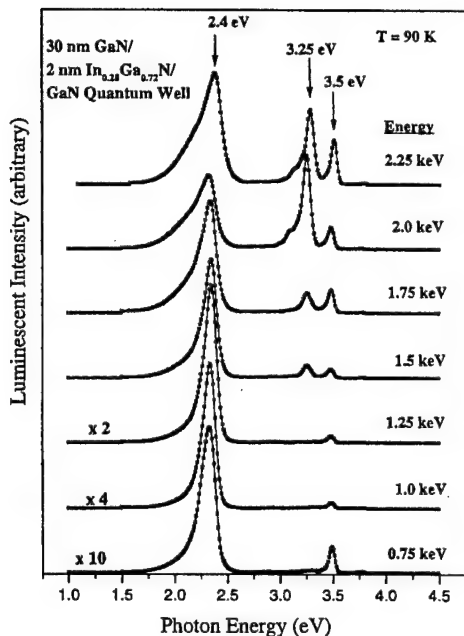


Fig. 4. LEEN spectra versus incident beam energy and depth for a relatively In-rich InGaN quantum well confined buried 30 nm below the GaN surface. At energies corresponding to depths just beyond the quantum well, new emission appears at 3.25 eV, corresponding to a localized electronic state at the deeper of the InGaN-GaN interfaces.

and InN band gaps (Vegard's Law) [14]. Fig. 4 illustrates for beam energies below 1 keV, showing quantum well emission at 2.4 eV that increases relative to the GaN NBE peak. This relative increase corresponds to an increasing penetration of the electron beam and an increase in minority carriers reaching the quantum well region. The quantum well versus NBE ratio reaches a maximum at 1 keV and corresponds to excitation of free electron-hole pairs peaking at depths of  $\sim 6-7$  nm and ranging down to  $\sim 20$  nm, followed by hole diffusion to the quantum well with a diffusion length  $L_D < 25-28$  nm. The latter was extracted from a fit to the onset of quantum well emission in a  $x = 0.14$  In<sub>x</sub>Ga<sub>1-x</sub>N layer that exhibited a similar ratio maximum at 750 eV [16].

In addition to the quantum well and NBE emissions, a new emission feature appears at 3.25 eV at excitation voltages above 1.25 eV. The intensity of this feature rises rapidly with increasing voltage, reaching a maximum relative to both the quantum well and NBE emissions at 2.0 keV. With further voltage increases, LEEN spectra show a decrease and disappearance of this 3.25 eV feature. The appearance of this feature at energies corresponding to the quantum well indicates that its location lies close to that of the quantum well. On the other hand, the 3.25 and 2.7 eV features have different depth dependences, indicating that the former is not a quantum well emission per se, but rather emission from a region localiz-

ed near the quantum well. That it reaches a maximum relative intensity at voltages above the voltage at which the quantum well is maximum suggests that this localization is at or near the deeper quantum well interface. The line shape of the 3.25 eV peak is relatively unchanged with increasing energy. Researchers have found a nearly identical peak feature at 3.26 eV due to the NBE of cubic GaN [5]. Even the lower energy side bands in the LEEN spectra agree with the phonon replicas identified with the cubic phase emission. The formation of cubic GaN in a thin, interfacial region at the deeper quantum well interface is not unexpected, given the low temperature used to begin the InGaN growth and the relatively high In concentration, both of which could induce stacking faults, known to promote nucleation of cubic phase growth [17]. A new quantum well emission is a less likely explanation for this localized feature, given the difference in depth dependence of the quantum well versus 3.25 eV emission intensities. Phase segregation is also a less plausible explanation, given the lack of an even more In-rich peak emission at lower energies lower than 2.4 eV but above the InN band gap (e.g., 1.8 eV) [18]. Finally, transmission electron microscopy (TEM) images of the higher versus lower In concentration quantum well showed more complex lattice structure near the interface. Thus, the most likely origin for the "buried" interface feature is emission from a nanometer - scale layer of cubic GaN near the InGaN/GaN buffer layer interface due to the change in growth temperature and composition.

#### 4. Discussion

The results presented above demonstrate that several types of localized electronic states can occur at GaN surfaces and interfaces. The deep level energies of these states appear at a wide range of energies across the GaN band gap. Incorporation of N ions in an MBE-grown film is shown to induce "yellow" luminescence features at multiple energies and with intensities that increase toward the free surface. The dependence of this intensity on the extent of ionized N incorporation suggests that point defects alone are not sufficient to account for YL emission. Other extrinsic parameters such as H incorporation may be required to account for the ion-dependent results. High-temperature annealing yields Ga-deficient surfaces and new features distinct from the YL emission. The correspondence of this luminescence with features associated with C doping suggests that changes in the near-surface C impurity bonding can alter the electrical activity of surface trap states. C redistribution in GaN is not expected even for higher temperatures (i.e., 1450°C) [19]. The lack of any increase in YL luminescence with a decrease in near-surface Ga suggests that more than Ga vacancies [1,2] are needed to account for this common defect feature. Mg-GaN Schottky barriers induce a set of

"buried" interface features localized at the intimate contact on a nanoscale with energies at and below that of "yellow" luminescence. The correspondence of the defect energies with the range of UHV Fermi level stabilization energies suggests that defects induced by GaN metallization play a significant role in Schottky barrier formation. Finally, we have observed localized states of an entirely different nature at heterojunction interfaces between GaN and InGaN. LEEN spectroscopy clearly highlights the localized nature of these states and provides strong evidence for cubic phase formation on a nanometer scale. The emission from such a cubic "interphase" is quite close to the band offset calculated for a "quantum-like region of zinc-blende material" surrounded by wurtzite GaN [20]. The change in electronic structure at all these "buried" GaN interfaces and free surfaces has until now not been available. Despite the highly localized nature of these states, it is possible to associate their energies with those of defects reported for bulk GaN. The results provided in this paper show that a complete understanding of surface recombination, charge transport across Schottky barriers, and heterojunction barrier confinement involving GaN surfaces and interfaces requires a determination of the extrinsic electronic states present at these junctions.

## 5. Conclusions

Low-energy electron-excited nanoscale-luminescence spectra demonstrate the ability to detect new electronic structure at GaN surfaces and interfaces. These results provide evidence for discrete native defect states across the band gap. Furthermore, both the free surface and heterointerface states display a strong dependence on growth techniques and specific chemical interactions. By feeding back to the growth process, this characterization provides a new approach to monitor and minimize localized deep levels at Schottky barriers and heterojunctions.

## Acknowledgements

This work was supported in part by US Department of Energy grant DE-FG0297ER45666 (Craig Hartley)

(LEEN experiments) and in part by NSF grant DMR-9711851 (LaVerne Hess) (depth calculations).

## References

- [1] J. Neugebauer, C.G. Van de Walle, *Phys. Rev. B* 50 (1994) 8067.
- [2] P. Boguslawski, E.L. Briggs, J. Bernholc, *Phys. Rev. B* 51 (1995) 17255.
- [3] J.I. Pankove, J.A. Hutchby, *J. Appl. Phys.* 47 (1976) 5387.
- [4] W.J. Choyke, I. Linkov, Institute of Physics Conference Series No. 137, IOP Publishing Ltd, London, 1994, pp. 141-146 (Chapter 3).
- [5] J. Schäfer, A.P. Young, L.J. Brillson, H. Niimi, G. Lucovsky, *Appl. Phys. Lett.* 73 (1998) 791.
- [6] A.P. Young, J. Schäfer, L.J. Brillson, Y. Yang, S.H. Xu, H. Curguel, G.J. Lapeyre, M.A.L. Johnson, J.F. Schetzina, *J. Electron. Mater.* 28 (1999) 308.
- [7] T.D. Moustakas, in: *Semiconductors and Semimetals*, Vol. 57, Academic Press, New York, 1999, pp. 33-128.
- [8] E.J. Tarsa, B. Heying, X.H. Wu, P. Fini, S.P. DenBaars, J.S. Speck, *J. Appl. Phys.* 82 (1997) 5472.
- [9] L.J. Brillson, R.E. Viturro, *Scanning Electron Microscopy* 2 (1988) 789.
- [10] T.E. Everhart, P.H. Hoff, *J. Appl. Phys.* 42 (1971) 5837.
- [11] E.E. Reuter, R. Zhang, T.F. Kuech, S.G. Bishop, *MRS Internet J. Nitride Semiconduct. Res.* 4S1 (1999) G3.67.
- [12] Y. Yang, S.H. Xu, G.J. Lapeyre, J.M. van Hove, *J. Vac. Sci. Technol. B*, in press.
- [13] C.I. Wu, A. Kahn, *J. Vac. Sci. Technol. B* 16 (1998) 2218.
- [14] F.A. Ponce, D. Cherns, W. Goetz, R.S. Kern, in: *MRS Symposia Proceedings*, Vol. 482, Materials Research Society, Pittsburgh, 1998, p. 453.
- [15] M.D. McCluskey, C.G. Van de Walle, C.P. Master, L.T. Romano, N.M. Johnson, *Appl. Phys. Lett.* 72 (1998) 2725.
- [16] T.M. Levin, G.H. Jessen, L.J. Brillson, F.A. Ponce, *J. Vac. Sci. Technol.*, submitted for publication.
- [17] A. Munkholm, C. Thompson, C.M. Foster, J.A. Eastman, O. Auciello, G.B. Stephenson, P. Fini, S.P. DenBaars, J.S. Speck, *Appl. Phys. Lett.* 72 (1998) 2972.
- [18] A.F. Wright, J.S. Nelson, *Appl. Phys. Lett.* 66 (1995) 3051.
- [19] X.A. Cao, R.G. Wilson, J.C. Zolper, S.J. Pearton, J. Han, R.J. Shul, D.J. Rieger, R.K. Singh, M. Fu, V. Scarvepalli, J.A. Sekhar, J.M. Zavada, *J. Electron. Mater.* 28 (1999) 261.
- [20] C. Stampfli, C.G. Van deWalle, *Phys. Rev. B* 57 (1998) R15052.

## Defect formation near GaN surfaces and interfaces

L.J. Brillson<sup>a,\*</sup>, T.M. Levin<sup>a</sup>, G.H. Jessen<sup>a</sup>, A.P. Young<sup>a</sup>, C. Tu<sup>b</sup>, Y. Naoi<sup>b</sup>,  
F.A. Ponce<sup>c</sup>, Y. Yang<sup>d</sup>, G.J. Lapeyre<sup>d</sup>, J.D. MacKenzie<sup>e</sup>, C.R. Abernathy<sup>e</sup>

<sup>a</sup>Department of Electrical Engineering, The Ohio State University, 2015 Neil Avenue, Columbus, OH 43210, USA

<sup>b</sup>Department of Electrical Engineering, University of California, San Diego, CA 92093, USA

<sup>c</sup>Department of Physics, Arizona State University, Columbus, OH 432210, USA

<sup>d</sup>Department of Physics, Montana State University, Bozeman, MT59717, USA

<sup>e</sup>Department Material Science and Engineering, Florida State University, Gainesville, FL 32611, USA

### Abstract

We have used low-energy electron-excited nanoscale-luminescence (LEEN) spectroscopy combined with ultrahigh vacuum (UHV) surface science techniques to probe deep level defect states at GaN free surfaces, metal-GaN contacts and GaN/InGaN quantum well interfaces. Employing energies as low as 100 eV and ranging up to 5 keV, we have been able to establish the local nature of these states and their spatial variation normal to the interface plane on an incremental 10-20 nm scale. Coupled with surface science techniques, these measurements show that a variety of discrete deep levels form deep within the GaN band gap due to (a) native defects, (b) metal-induced bonding, (c) reaction products, and (d), in the case of GaN/InGaN heterostructures, local interface phase changes. These results suggest that deep levels are a common feature at GaN interfaces and hence can play an integral role in charge transfer and the formation of local dipoles at GaN heterostructures. © 1999 Elsevier Science B.V. All rights reserved.

**Keywords:** Gallium nitride; Surfaces and interfaces; New experimental techniques

### 1. Introduction

Deep electronic states are of central importance in determining the bulk emissive and transport properties of GaN. Theoretical calculations and experimental measurements show that the bulk defect and impurity states have energy levels ranging across the band gap [1-4]. While considerable attention has focused on the trapping and recombination properties of such bulk deep levels, relatively little is known about the electronic states at GaN surfaces and interfaces. The presence of localized states at such boundaries can affect Schottky barrier formation and heterojunction band offsets. The nanometer-scale film thicknesses now being used in nu-

merous GaN heterostructures further amplifies the relative importance of such interface electronic features.

In this paper, we present evidence for a variety of discrete electronic states associated with GaN surfaces and interfaces. Such states are possible to identify and distinguish from bulk features with low-energy electron-excited nanoscale-luminescence (LEEN) spectroscopy. We have used the luminescence associated with optical transitions into or out of gap states in order to characterize electronic features near interfaces. This requires the ability to: (a) excite free electron-hole pairs, (b) produce such excitation near "buried" interfaces, and (c) vary this excitation in depth on a nanometer scale. These criteria are met by LEEN spectroscopy, which has already been applied to a wide variety of semiconductor-semiconductor and semiconductor-metal interfaces [5,6].

Considerable research has shown the strong dependence of bulk deep levels in GaN on the specifics of growth and subsequent processing [7,8]. Additional electronic

\* Corresponding author. Fax: (614) 688-4688.

E-mail address: Brillson.1@osu.edu (L.J. Brillson)

states may reside near surfaces and interfaces due to chemical and morphological changes in the crystal. All these extrinsic features can degrade the near band edge (NBE) optical emission as well as transport properties. In this paper, we present evidence for discrete gap states at GaN surfaces, metal-GaN interfaces, and III-V nitride heterojunctions. Furthermore, the use of surface science techniques permits the chemical origin of extrinsic, near-surface states to be investigated.

## 2. Experiment

The LEEN experiment consists of a low-energy (0.1–5 keV) electron beam impinging on a controlled surface in ultrahigh vacuum (UHV). The minority carriers generated recombine either across the band gap (near band edge (NBE) radiation), through deep levels in the band gap, or via (nonradiative) phonon generation. The depth of excitation can be varied as a function of incident electron beam energy from a few nm to a few hundred nm over this energy range [9]. The incident electron beam produces a cascade of secondary electrons and, subsequently free electron-hole pairs. One can calculate the maximum range of penetration  $R_B$  for the Everhart-Hoff relation [10] extending to low energies. The maximum electron-hole pair production of the electron cascade occurs for values approximately one-third of these values. Thus, for example, a 1 keV electron beam produces a cascade of secondaries and generates electron-hole pairs that extend 20 nm below the surface, peaking at  $\sim 6$ –7 nm. Photon emission is collected via IR-UV transmitting optics to photodetectors. This experimental setup is described in previous publications [5,6].

## 3. Results and discussion

Fig. 1 shows LEEN spectra for GaN grown by molecular beam epitaxy (MBE) under different N deposition conditions. A biased electrode provided a means to deflect ionized N atoms from the plasma source away from the growth surface. Fig. 1 shows dramatically different spectral features for GaN grown with different deflection voltages applied to the electrode. The “yellow” luminescence (YL) that dominates the MBE GaN grown without removing N ions decreases with increasing deflection voltage. Likewise, a shallow defect transition at 3.37 eV decreases as well. A deflection voltage of 700 V can achieve almost two orders of magnitude decrease in these peaks. Furthermore, the electron mobility more than doubles from a value of 300–640  $\text{cm}^2/\text{V s}$  from zero to the highest deflection voltage. These results indicate that the presence of N ions gives rise to yellow luminescence, which in turn corresponds to increased electron trapping

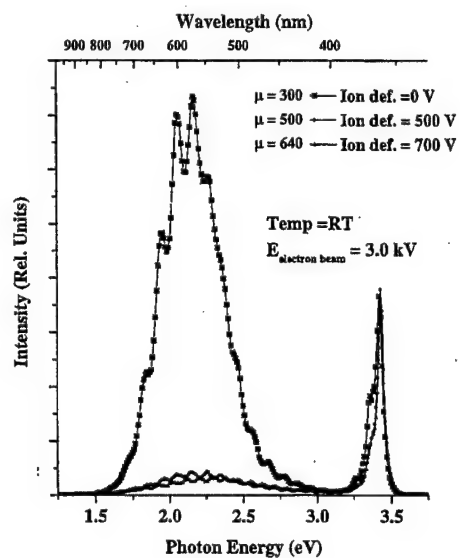


Fig. 1. LEEN spectra with 3.0 keV excitation energy of MBE-grown GaN versus ion deflection voltage. Increasing ion deflection voltage suppresses the midgap and 3.37 eV luminescence.

and reduced mobility. It should also be noted that this yellow luminescence is in fact comprised of at least three overlapping emission peaks centered at 1.75–1.8, 2.15, and 2.4 eV, rather than one broad peak distribution. Similar multiple peak structure in the YL energy range is evident in GaN grown by organometallic chemical vapor deposition (OMCVD) [4]. Finally, it should be noted that the emission spectra in Fig. 1 correspond to a total range of excitation  $R_B$  of 90 nm – well below the free surface. Depth-dependent spectra (not shown) reveal that the yellow luminescence is relatively constant versus depth for the GaN grown without deflection. On the contrary, the GaN grown with N ions deflected shows YL increases by over an order of magnitude for near-surface excitation ( $\leq 1$  keV corresponding to  $R_B \leq 20$  nm). This increased emission suggests either defects formed preferentially near the free GaN surface or the influence of residual N ions associated with the termination of growth.

Fig. 2 illustrates a Ga-related defect at the surface of a GaN specimen grown by metallorganic MBE (MOMBE). The as-grown specimen shows YL with intensity completely dominating the NBE peak for all penetration depths. After annealing at  $T > 1250^\circ\text{C}$ , dramatic new features appear, including a sharp ( $< 0.025$  eV FWHM) peak at 1.81 eV and a broad (0.33 eV FWHM) peak centered at 1.66 eV. Similar emissions have been reported previously as “red luminescence” that appeared when excited via a broad C-excitation band [10]. Auger electron spectroscopy (AES) measurements of surface composition establish a  $> 10\%$  decrease in the Ga/N ratio and a residual C and O concentration of 6% C and  $< 10\%$  O. Depth-dependent spectra reveal that the

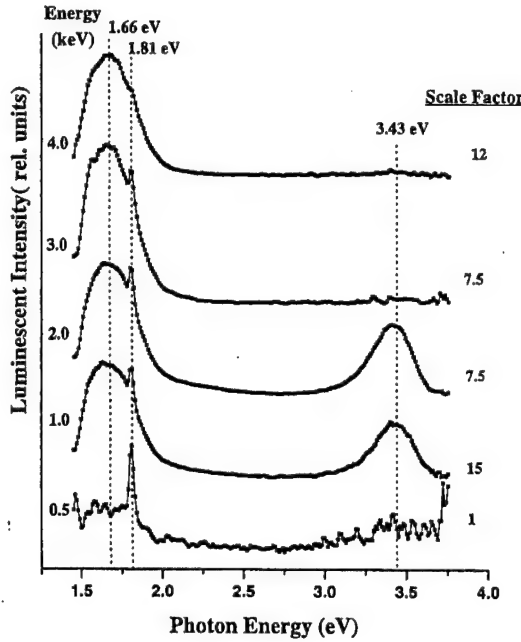


Fig. 2. LEEN spectra as a function of excitation energy and depth showing the near-surface features between 1.5 and 2.0 eV induced by 1250°C annealing.

1.81 eV peak intensity decreases with deeper excitation. The sharpness of this feature, its near-surface location, and the decrease in relative Ga concentration together suggest emission either from a Ga-related nanostructure, e.g., Ga droplets, or a surface segregated impurity, e.g., Al or Cr. The broader feature corresponding to the Ga-deficient surface is at least 120 nm thick. The "bulk" nature of this emission suggests the formation of a defect complex associated with a Ga deficiency. Interestingly, this layer forms under high-temperature conditions usually associated with preferential N desorption. The YL emission does not appear to increase under these conditions. Subsequent UHV deposition of a 1 nm Ga overlayer on this heat-treated surface reduces (but does not eliminate) the 1.66 eV peak and, to a lesser extent, the YL shoulder within the top 6–20 nm, further confirming the Ga-deficient nature of the lower energy feature. The contrast in behavior between these red luminescence features versus the YL indicates that different defects can become dominant recombination sites with different surface treatments near the free GaN surface.

Defect formation also occurs at metal–GaN interfaces. Fig. 3 illustrates LEEN spectra taken at different depths below a bare, MBE-grown GaN surface versus that of a similar crystal coated with 30 monolayers (4.8 nm) of Mg [6]. This metal–GaN interface was formed by evaporation in UHV on a LEED-ordered, MBE-grown surface, then annealed at 1000°C [11]. Fig. 3 shows broad, nearly featureless emission extending from ~3 to below 1.4 eV and relatively uniform at all depths. In contrast

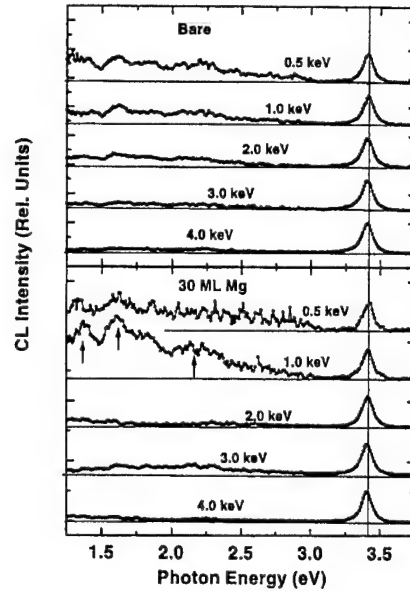


Fig. 3. LEEN spectra as a function of excitation energy and depth for a bare and a Mg-covered GaN single crystal showing the new emissions induced by the metal overlayer plus high-temperature anneal.

the Mg-covered GaN shows a maximum in sub-gap emission at excitation depths of 3–6 nm. Despite the low signal intensities, this emission indicates peak features at 1.4, 1.6, and 2.15 eV. Soft X-ray photoemission spectroscopy (SXPS) measurement of the Fermi level movement for this same sample show that it stabilizes at 2.2 eV above the valence band (1.2 eV below the valence band) [12]. Interestingly, other metals on UHV-prepared n-type GaN surfaces are known to stabilize the Fermi level within a range of 2.0–2.6 eV [13]. This suggests that metal-induced states at the Mg–GaN interface play an active role in the Schottky barrier formation. However, the role of defects may not extend to all metal contacts with GaN. For example, Al–GaN interfaces annealed at 1000°C in UHV result in a reacted interface layer rather than new defect formation [6].

New localized states are also present at GaN heterojunctions. We obtained LEEN depth-dependent spectra from an InGaN quantum well "buried" 30 nm below the free GaN surface. These quantum well structures consisted of an  $In_xGa_{1-x}N$  layer ( $x = 0.14$  or  $0.28$ ) with an average thickness of 2 nm. This layer was confined between a 2  $\mu m$  thick Si-doped ( $n = 3 \times 10^{18} \text{ cm}^{-3}$ ) GaN layer grown at 1050°C over a (0 0 0 1) sapphire substrate and a 30 nm GaN capping layer not intentionally doped and grown at roughly 800°C, the same growth temperature as the  $In_xGa_{1-x}N$  layer [14]. The bowing parameter calculations of In concentration due to McCluskey et al. [15] yield  $x$  values approximately one half of those extracted from a linear extrapolation between the GaN

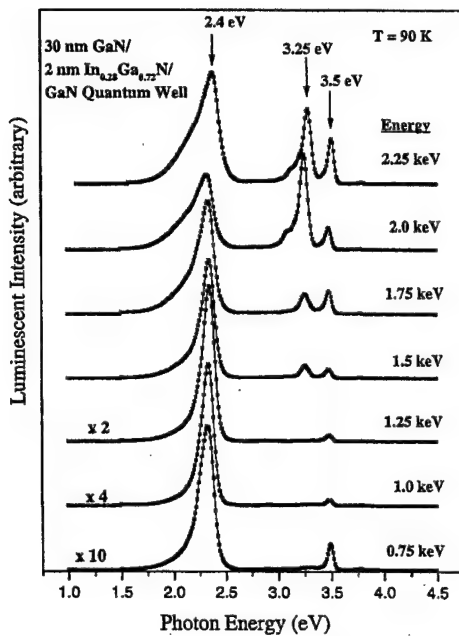


Fig. 4. LEEN spectra versus incident beam energy and depth for a relatively In-rich InGaN quantum well confined buried 30 nm below the GaN surface. At energies corresponding to depths just beyond the quantum well, new emission appears at 3.25 eV, corresponding to a localized electronic state at the deeper of the InGaN-GaN interfaces.

and InN band gaps (Vegard's Law) [14]. Fig. 4 illustrates for beam energies below 1 keV, showing quantum well emission at 2.4 eV that increases relative to the GaN NBE peak. This relative increase corresponds to an increasing penetration of the electron beam and an increase in minority carriers reaching the quantum well region. The quantum well versus NBE ratio reaches a maximum at 1 keV and corresponds to excitation of free electron-hole pairs peaking at depths of  $\sim 6$ –7 nm and ranging down to  $\sim 20$  nm, followed by hole diffusion to the quantum well with a diffusion length  $L_D < 25$ –28 nm. The latter was extracted from a fit to the onset of quantum well emission in a  $x = 0.14$  In<sub>x</sub>Ga<sub>1-x</sub>N layer that exhibited a similar ratio maximum at 750 eV [16].

In addition to the quantum well and NBE emissions, a new emission feature appears at 3.25 eV at excitation voltages above 1.25 eV. The intensity of this feature rises rapidly with increasing voltage, reaching a maximum relative to both the quantum well and NBE emissions at 2.0 keV. With further voltage increases, LEEN spectra show a decrease and disappearance of this 3.25 eV feature. The appearance of this feature at energies corresponding to the quantum well indicates that its location lies close to that of the quantum well. On the other hand, the 3.25 and 2.7 eV features have different depth dependences, indicating that the former is not a quantum well emission per se, but rather emission from a region localiz-

ed near the quantum well. That it reaches a maximum relative intensity at voltages above the voltage at which the quantum well is maximum suggests that this localization is at or near the deeper quantum well interface. The line shape of the 3.25 eV peak is relatively unchanged with increasing energy. Researchers have found a nearly identical peak feature at 3.26 eV due to the NBE of cubic GaN [5]. Even the lower energy side bands in the LEEN spectra agree with the phonon replicas identified with the cubic phase emission. The formation of cubic GaN in a thin, interfacial region at the deeper quantum well interface is not unexpected, given the low temperature used to begin the InGaN growth and the relatively high In concentration, both of which could induce stacking faults, known to promote nucleation of cubic phase growth [17]. A new quantum well emission is a less likely explanation for this localized feature, given the difference in depth dependence of the quantum well versus 3.25 eV emission intensities. Phase segregation is also a less plausible explanation, given the lack of an even more In-rich peak emission at lower energies lower than 2.4 eV but above the InN band gap (e.g., 1.8 eV) [18]. Finally, transmission electron microscopy (TEM) images of the higher versus lower In concentration quantum well showed more complex lattice structure near the interface. Thus, the most likely origin for the "buried" interface feature is emission from a nanometer-scale layer of cubic GaN near the InGaN/GaN buffer layer interface due to the change in growth temperature and composition.

#### 4. Discussion

The results presented above demonstrate that several types of localized electronic states can occur at GaN surfaces and interfaces. The deep level energies of these states appear at a wide range of energies across the GaN band gap. Incorporation of N ions in an MBE-grown film is shown to induce "yellow" luminescence features at multiple energies and with intensities that increase toward the free surface. The dependence of this intensity on the extent of ionized N incorporation suggests that point defects alone are not sufficient to account for YL emission. Other extrinsic parameters such as H incorporation may be required to account for the ion-dependent results. High-temperature annealing yields Ga-deficient surfaces and new features distinct from the YL emission. The correspondence of this luminescence with features associated with C doping suggests that changes in the near-surface C impurity bonding can alter the electrical activity of surface trap states. C redistribution in GaN is not expected even for higher temperatures (i.e., 1450°C) [19]. The lack of any increase in YL luminescence with a decrease in near-surface Ga suggests that more than Ga vacancies [1,2] are needed to account for this common defect feature. Mg-GaN Schottky barriers induce a set of

"buried" interface features localized at the intimate contact on a nanoscale with energies at and below that of "yellow" luminescence. The correspondence of the defect energies with the range of UHV Fermi level stabilization energies suggests that defects induced by GaN metallization play a significant role in Schottky barrier formation. Finally, we have observed localized states of an entirely different nature at heterojunction interfaces between GaN and InGaN. LEEN spectroscopy clearly highlights the localized nature of these states and provides strong evidence for cubic phase formation on a nanometer scale. The emission from such a cubic "interphase" is quite close to the band offset calculated for a "quantum-like region of zinc-blende material" surrounded by wurtzite GaN [20]. The change in electronic structure at all these "buried" GaN interfaces and free surfaces has until now not been available. Despite the highly localized nature of these states, it is possible to associate their energies with those of defects reported for bulk GaN. The results provided in this paper show that a complete understanding of surface recombination, charge transport across Schottky barriers, and heterojunction barrier confinement involving GaN surfaces and interfaces requires a determination of the extrinsic electronic states present at these junctions.

## 5. Conclusions

Low-energy electron-excited nanoscale-luminescence spectra demonstrate the ability to detect new electronic structure at GaN surfaces and interfaces. These results provide evidence for discrete native defect states across the band gap. Furthermore, both the free surface and heterointerface states display a strong dependence on growth techniques and specific chemical interactions. By feeding back to the growth process, this characterization provides a new approach to monitor and minimize localized deep levels at Schottky barriers and heterojunctions.

## Acknowledgements

This work was supported in part by US Department of Energy grant DE-FG0297ER45666 (Craig Hartley)

(LEEN experiments) and in part by NSF grant DMR-9711851 (LaVerne Hess) (depth calculations).

## References

- [1] J. Neugebauer, C.G. Van de Walle, *Phys. Rev. B* 50 (1994) 8067.
- [2] P. Boguslawski, E.L. Briggs, J. Bernholc, *Phys. Rev. B* 51 (1995) 17255.
- [3] J.I. Pankove, J.A. Hutchby, *J. Appl. Phys.* 47 (1976) 5387.
- [4] W.J. Choyke, I. Linkov, Institute of Physics Conference Series No. 137, IOP Publishing Ltd, London, 1994, pp. 141-146 (Chapter 3).
- [5] J. Schäfer, A.P. Young, L.J. Brillson, H. Niimi, G. Lucovsky, *Appl. Phys. Lett.* 73 (1998) 791.
- [6] A.P. Young, J. Schäfer, L.J. Brillson, Y. Yang, S.H. Xu, H. Curguel, G.J. Lapeyre, M.A.L. Johnson, J.F. Schetzina, *J. Electron. Mater.* 28 (1999) 308.
- [7] T.D. Moustakas, in: *Semiconductors and Semimetals*, Vol. 57, Academic Press, New York, 1999, pp. 33-128.
- [8] E.J. Tarsa, B. Heying, X.H. Wu, P. Fini, S.P. DenBaars, J.S. Speck, *J. Appl. Phys.* 82 (1997) 5472.
- [9] L.J. Brillson, R.E. Viturro, *Scanning Electron Microscopy* 2 (1988) 789.
- [10] T.E. Everhart, P.H. Hoff, *J. Appl. Phys.* 42 (1971) 5837.
- [11] E.E. Reuter, R. Zhang, T.F. Kuech, S.G. Bishop, *MRS Internet J. Nitride Semiconduct. Res.* 4S1 (1999) G3.67.
- [12] Y. Yang, S.H. Xu, G.J. Lapeyre, J.M. van Hove, *J. Vac. Sci. Technol. B*, in press.
- [13] C.I. Wu, A. Kahn, *J. Vac. Sci. Technol. B* 16 (1998) 2218.
- [14] F.A. Ponce, D. Cherns, W. Goetz, R.S. Kern, in: *MRS Symposia Proceedings*, Vol. 482, Materials Research Society, Pittsburgh, 1998, p. 453.
- [15] M.D. McCluskey, C.G. Van de Walle, C.P. Master, L.T. Romano, N.M. Johnson, *Appl. Phys. Lett.* 72 (1998) 2725.
- [16] T.M. Levin, G.H. Jessen, L.J. Brillson, F.A. Ponce, *J. Vac. Sci. Technol.*, submitted for publication.
- [17] A. Munkholm, C. Thompson, C.M. Foster, J.A. Eastman, O. Auciello, G.B. Stephenson, P. Fini, S.P. DenBaars, J.S. Speck, *Appl. Phys. Lett.* 72 (1998) 2972.
- [18] A.F. Wright, J.S. Nelson, *Appl. Phys. Lett.* 66 (1995) 3051.
- [19] X.A. Cao, R.G. Wilson, J.C. Zolper, S.J. Pearton, J. Han, R.J. Shul, D.J. Rieger, R.K. Singh, M. Fu, V. Scarveppalli, J.A. Sekhar, J.M. Zavada, *J. Electron. Mater.* 28 (1999) 261.
- [20] C. Stampfl, C.G. Van deWalle, *Phys. Rev. B* 57 (1998) R15052.

# Surface Core level shift on GaN(0001) surface

Y. Yang<sup>a,\*</sup>, S. H. Xu<sup>a</sup>, H. Cruguel<sup>a</sup>, G. J. Lapeyre<sup>a</sup>, H. J. Ho<sup>b</sup> and J. F. Schetzina<sup>c</sup>

<sup>a</sup>*Physics Department, Montana State University, Bozeman, MT 59717*

<sup>b</sup>*TopoMetrix Corporation, Santa Clara, CA 95054*

<sup>c</sup>*Department of Physics, North Carolina State University, Raleigh, NC 27695*

## Abstract

Synchrotron radiation photoelectron spectroscopy (SRPES) has been employed to investigate the electronic structure of clean wurzite GaN(0001) surfaces. The Ga 3d, N 1s and valence band emissions are measured by recording the energy distribution curves (EDC). A surface-shifted core level component is observed in the Ga 3d emission. It is located at 0.6 eV higher binding energy than the bulk component. The surface component is sensitive to atomic H adsorption. The experiment with deposition of the ultra-thin Mg layer strongly supports that it is attributed to the first layer Ga atoms. On the same sample, the surface core level shift of N 1s is identified at 1.0 eV lower binding energy side of the bulk component. The origin of the observed surface core level shifts will be discussed. Atomic-force-microscopy (AFM) image with line profiles is also acquired to determine the surface morphology.

**Key words:** Gallium nitride; Surface electronic phenomena; Photoelectron spectroscopy; Atomic force microscopy

---

Corresponding author.

Mailing address: Lawrence Berkeley National Lab, MS 7-222, 1 Cyclotron Road, Berkeley, CA 94720  
Phone: (510)495-2121; Fax: (510)486-7588; E-mail: yyang@lbl.gov

## 1. Introduction

The wide-band-gap III-V nitrides have attracted much attention because of their great significance in both scientific research and practical applications [1]. Among them, gallium nitride (GaN) is the most interesting material because of its suitable direct energy band gap of 3.4 eV at room temperature, notable chemical inertness, and great physical hardness not far away from diamond. Its fundamental properties are different from other III-V semiconductors (e.g., GaAs). For example the thermal and chemical properties are quite different and it has strong piezoelectric properties particularly in its equilibrium wurtzite structure. These attractive properties make it not only ideally useful for fabricating devices operated near the short wavelength end of the visible range (i.e., blue and ultraviolet light emitting diodes, detectors and laser devices), but also for application in harsh environments, such as high temperature [2,3]. Considerable effort is underway to develop high power electronic devices. Recently, significant progress has been made in the development of GaN-based material technology [4]. High quality GaN films on sapphire or SiC substrates have been grown by metalorganic chemical vapor deposition (MOCVD), molecular beam epitaxy (MBE) and other techniques. Now high performance blue and ultraviolet light emitting diodes (LED) and laser devices are commercially available. This makes it possible to conduct more characterization techniques, such as photoelectron spectroscopy, on GaN-based materials.

Surface electronic structure has always been of great importance for the characterization of semiconductor materials. In the past two decades, with the development of photoelectron

spectroscopy using synchrotron radiation as a light source, a lot of achievements have been made in semiconductor surface electronic structure studies. The observation of surface core level shifts on clean semiconductor surfaces is one of the interesting results. Due to the breaking of atomic configuration at the surface of the crystal, the first layer (even the first two layers) of atoms will show different binding energy for core-level emission compared with the atoms in the bulk in photoelectron spectroscopy. On Si(100) surface, surface-shifted core-level components for the first and second layer Si atoms have been revealed in Si 2p core level emission [5]. On GaAs(100) surface, core level shifts are found for both Ga 3d and As 3d [6]. For GaN, a number of electronic structure studies have been carried out [7-11]. However, surface core-level shift for Ga 3d (or N 1s) has not been reported. This is attributed to the fact that the detection of the surface component of Ga 3d core level for GaN by SRPES is not as straightforward as that for Si(100) or GaAs(100). For Si(100) and GaAs(100) the surface core-level shifts can be singled out in high-resolution energy distribution curve (EDC). Nevertheless, with the same resolution, Ga 3d core level emission from clean GaN(0001) surface is still appearing to be one peak in EDC, even the spin orbit splitting of Ga 3d can not be resolved. This is because that Si and GaAs are high quality bulk single crystal while GaN is a several micron thick film on sapphire or SiC substrate and bulk crystal is still not available. Then the inhomogeneity of the GaN(0001) surface caused by imperfection of the film crystal broadens the Ga 3d emission, making every component in it unresolved. Another reason is that a clean and ordered GaN surface is hard to prepare. A method that will clean the sample and keep the surface crystal structure is needed. In this case, careful experiment and data analysis must be done to identify the surface core-level shifts on the GaN(0001) surface.

In this work, atomic force microscopy (AFM) was used to determine the surface morphology. An effective method was employed to clean the GaN(0001) surface for photoemission measurement in which Ga 3d, N 1s and valence band emissions were investigated. Hydrogen was adsorbed onto the surface to distinguish the surface component in EDC's. With the aid of line fitting, the surface core level was identified at 0.6 eV higher binding energy than the bulk component in the EDC of Ga 3d. Experiments with deposition of ultra thin Mg overlayer strongly supports the surface atom assignment. On the same sample, the surface core level shift for N 1s was located at 1.0 eV lower binding energy side of the bulk component.

The paper is organized as follows. Section II describes the details of the experiment. Section III gives the results and their interpretations. Section IV is to conclude.

## 2. Experimental details

The experiments were performed on the Iowa State/Montana State ERG/Seya beamline at the Synchrotron Radiation Center (SRC) at the University of Wisconsin-Madison. The storage ring-Aladdin is operated at 800 MeV and the synchrotron radiation light is dispersed with an ERG/Seya monochromator [12]. The extended range grasshopper (ERG) monochromator is for higher energies and Seya for lower energies. The two units provide photons from about 4 to 900 eV in which high flux and energy resolution over the photon energy range from 4 eV to 240 eV allows for the measurement of core level and valence band emissions with resolution up to about 130 meV.

The measurement end station on the beam line consists of three chambers. The air interlock allows for introduction of a sample from atmosphere into the main chamber without breaking its vacuum. The mid-chamber located between the air interlock and main chamber accepts the sample, which is transferred from the air inter-lock. The mid-chamber is used to outgas the sample and its holder. The main chamber features a double-pass cylindrical mirror analyzer (CMA) and a VSW HA50 hemispherical energy analyzer on a double-axis goniometer. A low-energy-electron-diffraction (LEED) unit is used to monitor the surface atomic structures.

The GaN film was grown on a SiC substrate by metalorganic vapor phase epitaxy (MOVPE) method at North Carolina State University and is about 1  $\mu\text{m}$  thick. The C plane of the wurzite structure has two orientations, Ga-polarity (0001) face (A type) or N-polarity (000 $\bar{1}$ ) face (B type). The etching test with KOH [13] indicated the A orientation. It is Si-doped n-type. The as-received sample showed both a C and an O signal in the photoelectron spectrum after it was transferred into the main chamber. After heating at about 700°C, C was completely removed while some O was still present. An effective method was employed to eliminate the O contamination. The GaN was held at 700°C while keeping the Ga flux on the surface for about 5 min. After stopping the Ga flux, the sample was left at 700°C for another 10 min. The oxygen was successfully eliminated. The valence band emission showed a strong surface state emission [14]. The LEED pattern demonstrated a 1x1 net. For the sample heating, the sample wafer was mounted on a Si wafer, which is resistively heated. The method is very stable and a given current reproduces the temperature.

When  $H_2$  was dosed into the main chamber, a tungsten filament 5 cm away from the sample surface was turned on. This is for ionizing  $H_2$  to make atomic H that can adsorb on the GaN surface.

The Mg vapor deposition was done on the analysis manipulator in the main chamber. The sample was only moved along the manipulator's principal linear motion for deposition. This allows for the best sample reposition after each deposition. Mg was evaporated from a Ta boat at a pressure of  $(2-3) \times 10^{-10}$  Torr with the GaN sample left at room temperature. The base pressure is in the  $10^{-11}$  Torr range. The deposition rate is 1 ML in about per 40 seconds. The use of a thermocouple spot welded to the Ta boat gave reproducible evaporation rates. The coverage in terms of ML equivalence was determined by Ga 3d core level emission intensity attenuation vs. coverage and the frequency change of a quartz crystal oscillator (QCO). One ML was assigned as the coverage that extinguish the surface state in the valence band emission [14].

Photoelectron energy distribution curves (EDC) were acquired with the CMA on the Ga 3d and the N 1s level using a photon energy of 90 eV and 460 eV. The electron escape depth at 90 eV and 460 eV photon energy are near minimum for the two core levels. A photon energy of 31 eV was used for valence band EDC's. The typical combined resolution of the CMA and monochromator is about 0.2 eV for the valence band and about 0.3 eV for the Ga 3d core level measurement. These were determined by the width of the Fermi level emission from Ta on the sample holder. Every datum point in the EDC's was normalized with the light intensity obtained by measuring the current from a W mesh located in the path of synchrotron radiation light, just ahead of the sample in the main chamber. All measurements were conducted at room temperature.

The AFM picture was taken by near contact mode [15] in air on an Observer scanning probe microscopy (SPM) system at TopoMetrix Co. The sample surface was maintained as-received. A single-crystal silicon AFM probe and a tube scanner with 2  $\mu\text{m}$  scan range were used to acquire the AFM image.

### 3. Results and discussion

#### 3.1. Clean GaN(0001) surface

Figure 1(a) illustrates the AFM image of the as-received sample. The field of view is 1.0X1.0  $\mu\text{m}$ . The flat surface with atomic step edges is demonstrated. Arrow A and B point to the atomic step edges on the surface. From the line profile shown in Fig.1(b), the height of the atomic step edges is determined to be about 15 $\text{\AA}$ . This is the height of three unit cells of wurzite GaN. The solid line in Fig.1(a) shows where the line scan is acquired on the surface.

The etching experiment with KOH [13] showed a Ga-polarity orientation *i.e.* (0001) face. The AFM images (not shown here) showed no difference in surface morphology between the as-received and 3M-KOH-etched GaN samples. This result agrees with the argument that GaN samples grown on SiC substrates by MOVPE are Ga-polarity [16,17].

The EDC's were recorded for the valence band and Ga 3d emission on the GaN(0001) surface cleaned by the method described in Sec. 2. Figure 2(a) depicts the EDC for the valence band taken with a photon energy of 31 eV, and Fig. 2(b) illustrates the Ga 3d core level emission measured with photon energy 90 eV. Both EDC's are plotted in binding energy scale. The zero point of the scale is at the experimentally determined position of Fermi level,  $E_F$ .

In Fig. 2(a), the valence band maximum (VBM) is measured to be 2.5 eV below Fermi level and 17.8 eV above the Ga 3d core level for the clean surface. It is difficult to determine the presence of the VBM, which is obscured by the feature attributed to a surface state. The method used to infer the VBM is to imagine that the surface feature is gone and extrapolate linearly the remaining leading edge of the spectrum to the base line. The intersection is taken as a value for the VBM. The energy position of the Ga 3d line is easier to determine so the energy difference between the Ga 3d and  $E_F$  is determined with a value of 20.3 eV (see the inset). The above results are in agreement with those reported by Bermudez et al [10]. In Fig. 2(a), the region down to about 10 eV below the Fermi level is characterized by three closely spaced peaks (peak A, B, and C) corresponding to the Ga s-p/N p-derived valence bands. The shoulder at 0.2 eV below VBM is associated with Ga dangling bonds of the first layer of Ga atoms and is identified as a surface state. It is present in the EDC when the surface is clean and well ordered.

In Fig. 2(b), the Ga 3d core-level emission from the clean GaN(0001) surface is present. It appears to be a single peak in the EDC with full width at half maximum (FWHM) of 1.0 eV. No component can be singled out in the spectrum. Unlike on GaAs surfaces, the spin-orbit split of  $3d_{3/2}$  and  $3d_{5/2}$  can be clearly seen in the EDC. This broadening effect is not caused by the combined resolution of the spectrometer and the light source (0.3 eV in this experiment). It is attributed to the inhomogeneity of the GaN material introduced by imperfection of the film crystal.

### 3.2. Hydrogen adsorption effects

Adsorbates are widely employed to distinguish the contribution from surface atoms in photoemission spectrum. They either quench the surface components in EDC's or moves them to other energy position due to the changed surface energies. Hydrogen was used in this experiment to investigate the surface components in EDC's of GaN(0001). Atomic H which is able to stick on the GaN surface is made by ionizing H<sub>2</sub> with a 2000°C hot W filament 5 cm away from the sample surface. The dosage of H<sub>2</sub> is 500 Langmuir (L).

Figure 3 shows the valence band EDC collected from clean and hydrogenated GaN(0001) surfaces. The hydrogen-induced band bending moves the surface Fermi level upward by 0.2 eV. As a result, the spectrum shifted to higher-binding-energy side by 0.2 eV. After the EDC's for clean surface (open circles) and 500L-H<sub>2</sub>-exposed surface (open squares) are lined up (i.e., shift the hydrogenated EDC toward low binding energy side by 0.2 eV), a difference curve (solid line) is made between two EDC's. Three features are raised by H adsorption locating at 6.0, 7.0 and 9.5 eV below the Fermi level, respectively. They can be considered as fingerprints of H on GaN(0001) surfaces. Remarkable change is seen at 0.2 eV below the Fermi level. The emission intensity is decreased dramatically by H adsorption. This is attributed to adsorbed H quenches the surface state at 0.2 eV below E<sub>F</sub>. However, a residual of about 1/3 can be found for this surface state after hydrogenation. This is related to strong H-H bonds. When H atoms on the GaN(0001) surface are "close" enough, they will form H<sub>2</sub> and desorb. So H is not able to saturate the surface at the equilibrium condition.

Figure 4 shows EDC's for Ga 3d core level on the clean and the hydrogenated surface. The peak is shifted 0.2 eV to higher binding energy which is in agreement with the valence band data.

Hydrogen exposure changes the line shape of Ga 3d. A narrower line is found on the H-exposed surface. The difference curve shows a feature at 21 eV binding energy. It is attributed to surface Ga atoms and will be discussed in the next subsection.

### *3.3. Surface core level shifts*

Line fitting is used for further investigation on the surface-contributed feature in the Ga 3d EDC that is identified by the H-exposure experiment mentioned in 3.2. The result of the line fitting of the Ga 3d is displayed in Fig. 5. In this line fitting, first, a polynomial background is subtracted from the experimental data (round circles). Then a Gaussian-broadened Lorentzian line (i.e., Voigt line) is used to fit the curve. The Lorentzian width, spin-orbit splitting and branch ration are 0.2 eV, 0.45 eV and 0.6 eV, respectively. These values agree with the line fitting parameters used for Ga 3d on GaAs(110) [18]. The Gaussian width is optimized to be 0.7 eV, which is greater than the energy resolution 0.3 eV in the experiment. The greater Gaussian is assumed to include the effect of broadening caused by inhomogeneity of this GaN film crystal. In Fig. 5, the line fitting of the Ga 3d reveals two components. The intensive one with lower binding energy is from bulk Ga atoms. Another component with binding energy 0.6 eV higher than the bulk component is due to the surface core level shift of the first layer of Ga atoms. Its position of 21 eV below Fermi level agrees with the result of the H-exposure experiment.

The surface-shifted component in Ga 3d on GaN(0001) surfaces is interpreted as follows. For wurzite GaN, Ga and N atoms are in  $sp^3$  bonding configuration. This makes each atom require four electrons, allowing Ga atoms to accept charge from N atoms. For bulk GaN, the tetrahedral bonding configuration dominates the electronic structure. On the Ga-polarity (0001)

surface, tetrahedral bonding for the Ga atom no longer exists. Hence, the hybridization of the s and p orbital is reduced, and the Ga atoms at the surface tend toward their atomic valence with charge transferred from Ga to N. Then the surface Ga atoms have less charge than the bulk Ga atoms, the electrons are bonded more tightly and shifted to higher binding energy. This is in agreement with the experimental data that the surface shifted component is on the higher binding energy side. Likewise, the N atoms at the surface region should have more charge than the bulk N atoms.

Figure 6 illustrates the EDC for N 1s on GaN(0001) and the line fitting. The experimental data (round circles) show a shoulder on the right-hand side. The EDC curve is fitted with Voigt line shape. The Gaussian and Loretzian width are chosen to be 1.4 eV and 0.1 eV, respectively. The main component corresponds to contribution from N atoms in the bulk. The smaller component at lower binding energy is attributed to the emission from surface atoms (i.e., surface-shifted component). The observation of the surface core level shift on lower binding energy side of the bulk component is consistent with the assumption that N atoms at the surface region have more negative charge than bulk atoms.

### *3.4. Effects of the ultra-thin Mg overlayer*

To verify the origin of surface-shifted component in Ga 3d EDC, experiments with deposition of the ultra-thin Mg layer is conducted. Mg is found to grow epitaxially on GaN(0001) surfaces up to 20 Å [19]. Mg is vapor deposited onto clean GaN(0001) in sequential steps up to 1 ML. Figure 7 shows Mg coverage dependence of Ga 3d core level emission with the line fittings. The parameters used in the line fitting are the same as those in 3.3. Two components are observed

for the clean surface, i.e., the surface and the bulk component. With 0.4 ML Mg coverage, compared with clean surface, the intensity ratio of surface to bulk component decreases. A new peak appears at right-hand side of the bulk component. It is attributed to the contribution from surface Ga atoms bonded to Mg adatoms. It is located at 0.9 eV lower binding than bulk component and is assigned as a interface component. As 1.0 monolayer Mg on the surface, the surface component is hardly detected. Meanwhile, the interface component increases, and has about the same intensity (relative to bulk component) as the surface component on the clean surface. This implies that almost all Ga atoms at the surface bond to Mg adatoms, and the charge is transferred from Mg adatoms to first layer Ga atoms. Therefore, the Ga 3d core-level emission from surface Ga atoms is shifted to the lower bind energy side. So this experiment strongly supports the conclusion that the high binding energy side component of Ga 3d on clean GaN(0001) surface is attributed to the surface core level emissions from the first layer Ga atoms.

#### 4. Conclusions

AFM imaging is conducted on as-received MOVPE-grown wurzite GaN(0001) surface. The surface appears to be flat and has atomic step edges. The line profile shows the step edges are about the height of three unit cells.

The electronic structure of the clean wurzite GaN(0001) surface with Ga terminating is investigated by SRPES. Ga 3d, N 1s, and valence band EDC are recorded by high resolution SRPES. With the help of H adsorption and line fitting, the surface core level shift is observed in Ga 3d emission, located 0.6 eV higher binding energy than the bulk component. The surface

component is sensitive to atomic H adsorption. Experiments with deposition of ultra thin Mg overlayer supports that it is from the first layer Ga atoms. On the same surface, the surface core level shift of N 1s is found to be at 1.0 eV lower binding energy side of the bulk component.

In the future, when higher quality film even bulk GaN is available, hopefully, the surface core level shift can be singled out in EDC without line fitting.

### **Acknowledgements**

Research supported by ONR/DEPSCOR grant, SRC supported by NSF and the support of SRC staff is gratefully acknowledged.

### **References**

- [1] S.Srtite and H. Morkoc, J.Vac. Sci. Technol. B 10 (1992) 1237.
- [2] M.A.Khan, J.N.Kuznia, A.R.Bhattarai, and D.T.Olson, Appl. Phys. Lett. 62 (1993) 1786.
- [3] S.Nakamura, T.Mukai, and M.Senoh, Appl. Phys. Lett. 64 (1994) 1687.
- [4] F.A.Ponce and D.P.Bour, Nature 386 (1997) 351.
- [5] Winfried Monch, "Semiconductor Surfaces and Interfaces" 2nd edition, p163, Springer-Verlag.
- [6] D.E.Eastman, T.-C.Chiang, P.Hermann, F.J.Himpsel, Phys. Rev. Lett. 45 (1980) 656.
- [7] R.W.Hunt, L.vanzetti, T.Castro, K.M.Chen, L.Sorba, P.I.cohen, W.Gladfelter, J.M.Van Hove, J.N.Kuznia, M.Asif Khan and A.Franciosi, Physica B 185 (1993) 415.

- [8] S.A.Ding, G.Neuhold, J.H.Weaver, P.Haberle, K.Horn, O.Brandt, H.Yang, and K.Ploog, J.vac.Sci.Technol. A 14 (1996) 819.
- [9] Sarnjeet S.Dhesi, Cristian B.Stagarescu, and Kevin E.Smith, Phys. Rev. B 56 (1997) 10271.
- [10] V. M. Bermudez, J. Appl. Phys. 80 (1996) 15.
- [11] V. M. Bermudez, D. D. Koleske, A. E. Wickenden, Appl. Surf. Sci. 126 (1998) 69.
- [12] C.G.Olson, Nucl. Instrum. Methods Phys. Res. A 266 (1988) 205.
- [13] M.Seelmann-Eggebert, J.L.Weyher, H.Obloh, H.Zimmermann, A.Rar, and S.Porowski, Appl. Phys. Lett. 71 (1997) 2635.
- [14] Y. Yang, S. H. Xu, H. Cruguel, G. J. Lapeyre, J. M. Van Hove, A. M. Wowchak, and P. P. Chow, submitted to Phys. Rev. B.
- [15] H. J. Ho, thesis for Ph.D.
- [16] J. F. Schtezina, private communications.
- [17] Z. Liliental-Weber, private communications.
- [18] T. Miler, T.-C. Chiang, Phys. Rev. B 29 (1994) 7034.
- [19] V. M. Bermudez, Surf. Sci. 417 (1998) 30.

## Figure Captions:

Fig.1 (a) AFM image of n-GaN(0001) surface, the view area is 1.0X1.0  $\mu\text{m}$ . Label A and B indicate the atomic step edges on the surface. (b) The line profile acquired on the surface at the position of the line in the image shown in (a), form the line profile, the atomic step edges is measured to be about 15 $\text{\AA}$ .

Fig.2 EDC's from clean n-GaN(0001) surface. (a) EDC's for valence band emission collected at the photon energy 31 eV. The zero point of binding energy is set at the position of the Fermi level. The inset shows the overview EDC for both the Ga 3d core level and the valence band emissions. (b) EDC for Ga 3d core level emission taken at 90 eV photon energy. The feature shows a single peak.

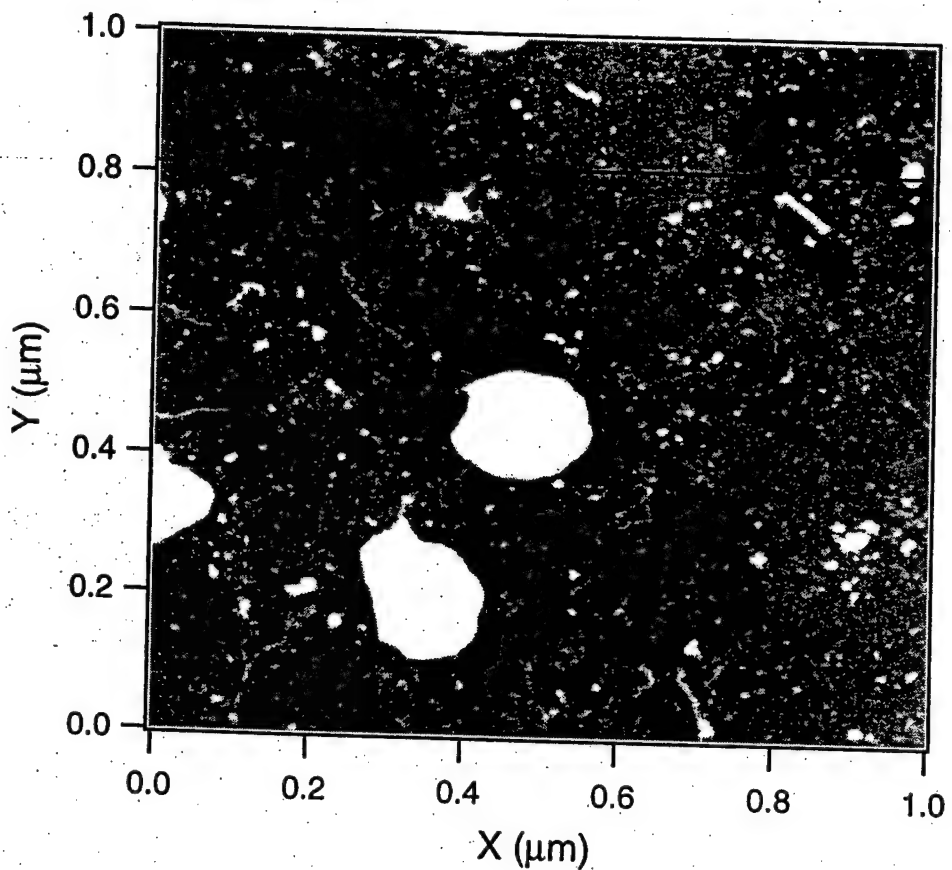
Fig.3 EDC's of valence band emission for clean GaN(0001) surface and the surface exposed to 500 Langmuir hydrogen. The curve with open squares is for clean case, the curve with open circles for the H-exposed surface. The difference curve is illustrated by the solid line.

Fig.4 EDC's of Ga 3d emission for clean GaN(0001) surface and the surface exposed to 500 Langmuir hydrogen. The curve with solid squares is for clean case, the curve with solid circles for the H-exposed surface. The difference curve is illustrated by the solid line.

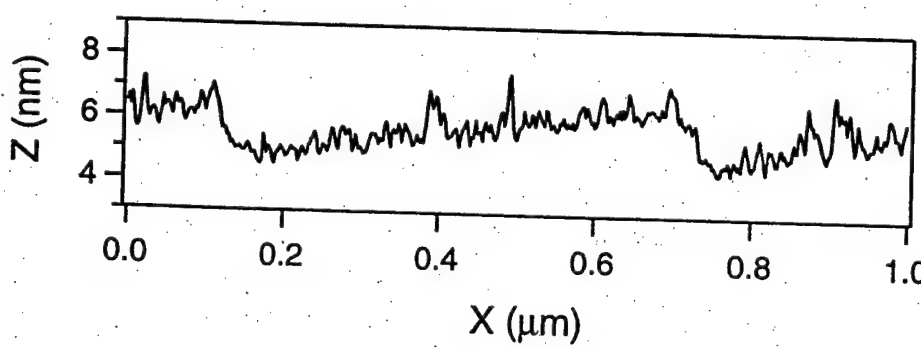
Fig.5. Line fitting of the EDC for Ga 3d on clean n-GaN(0001). The solid circles are experimental data. The solid curve is the fitted curve. The dotted line is for the surface core level shift, and the dash line for the bulk component. The solid line at the bottom shows the residue of the line fitting, i.e. the difference between the experimental and fitted curve.

Fig.6 The line fitting of EDC for N 1s on clean n-GaN(0001). The solid circles are experimental data. The solid curve is the fitted curve. The dotted line is for the surface core level shift, and the dash line for bulk component. The solid line at the bottom shows the residue of the line fitting.

Fig.7 The evolution of EDC's of Ga 3d with increasing Mg coverage. Solid circles represent experimental data. The experimental data are normalized to arbitrary unit. Solid lines, dash lines, dot lines and dot-dash lines are for the fitted curve, the bulk component, surface component and the interface component, respectively.



(a)



(b)

Fig. 1 Y. Yang et al.

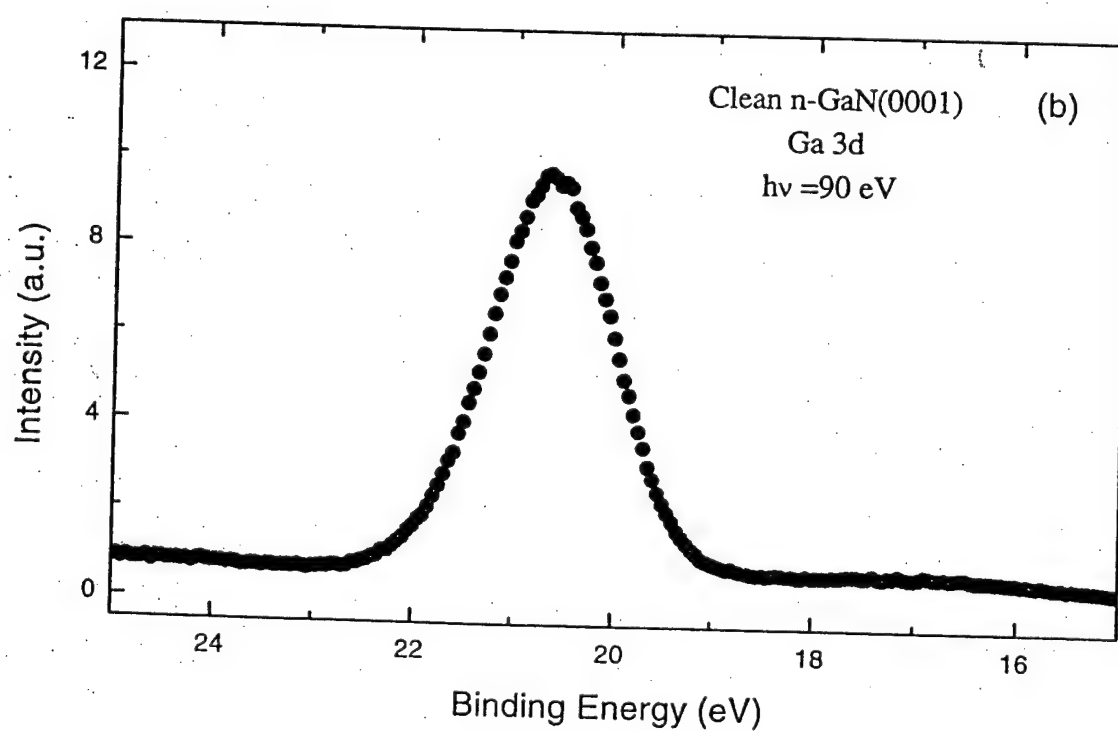
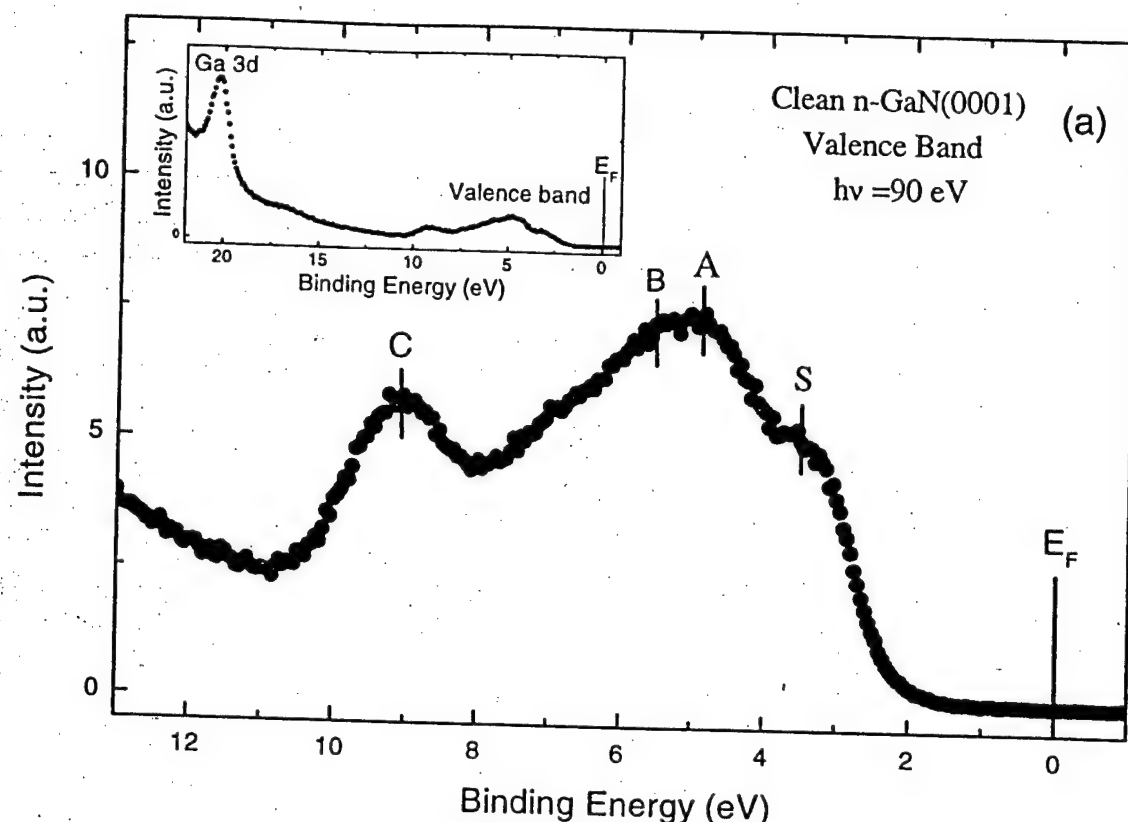


Fig. 2 Y. Yang et al.

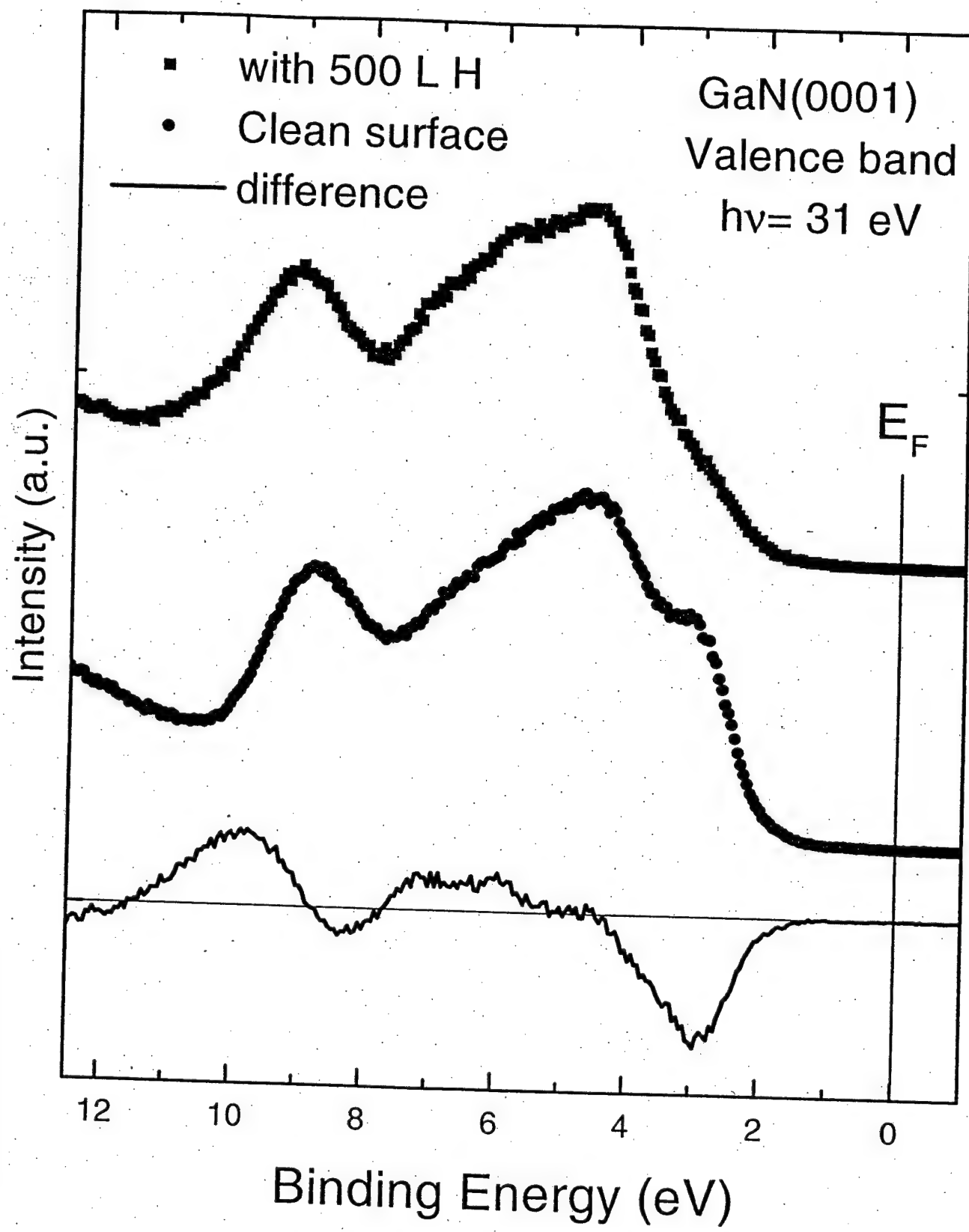


Fig. 3 Y. Yang et al.

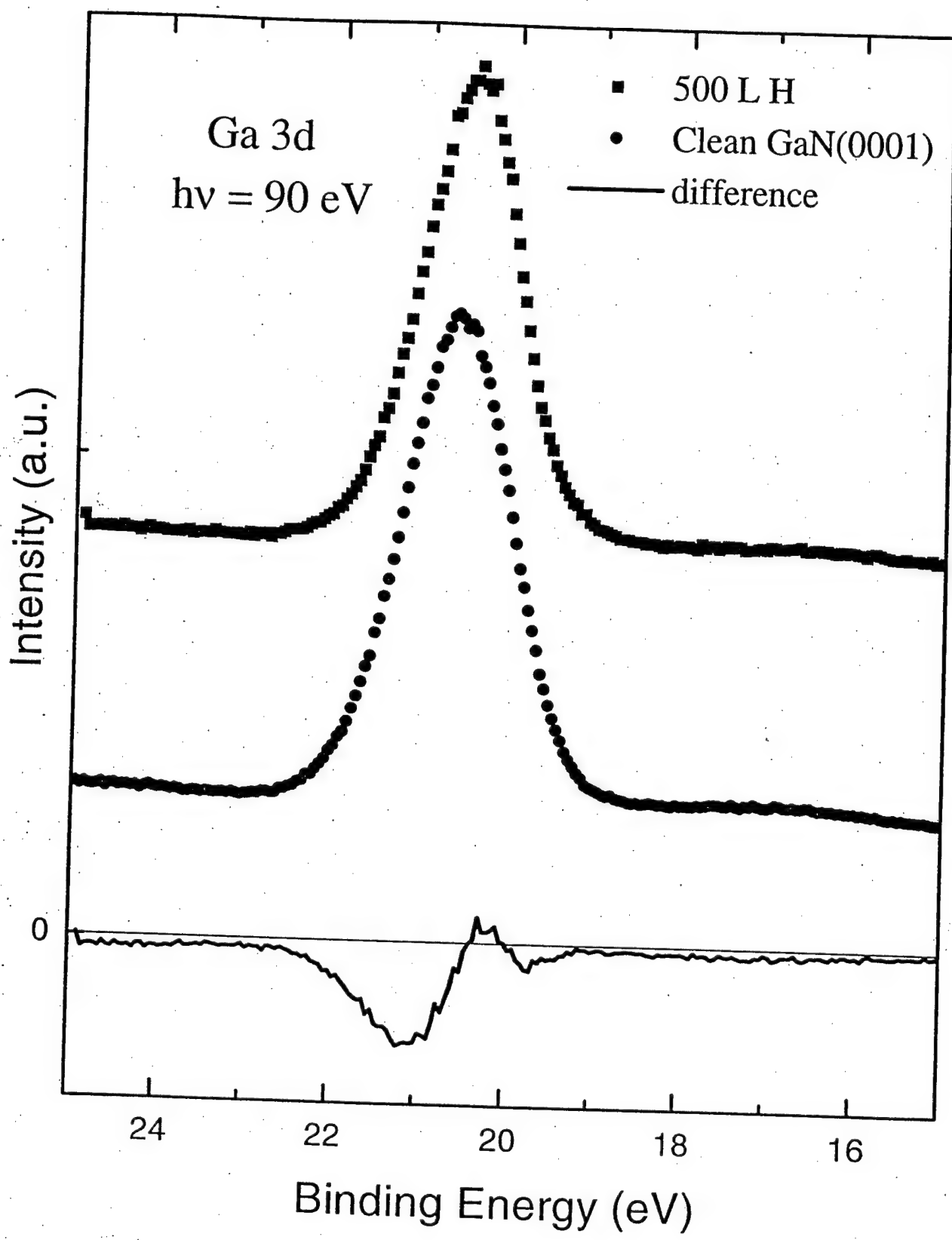


Fig. 4 Y. Yang et al.

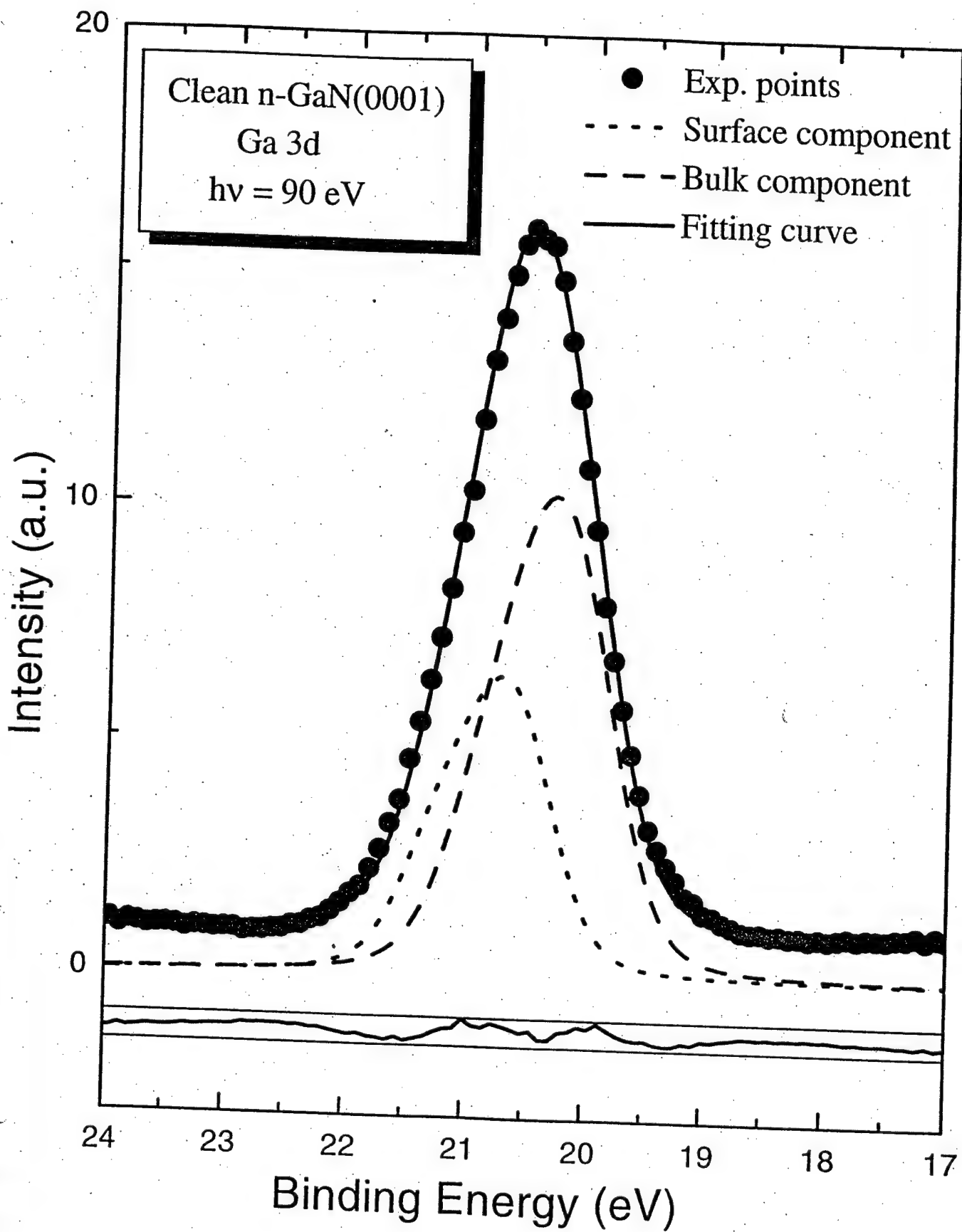


Fig. 5 Y. Yang et al.

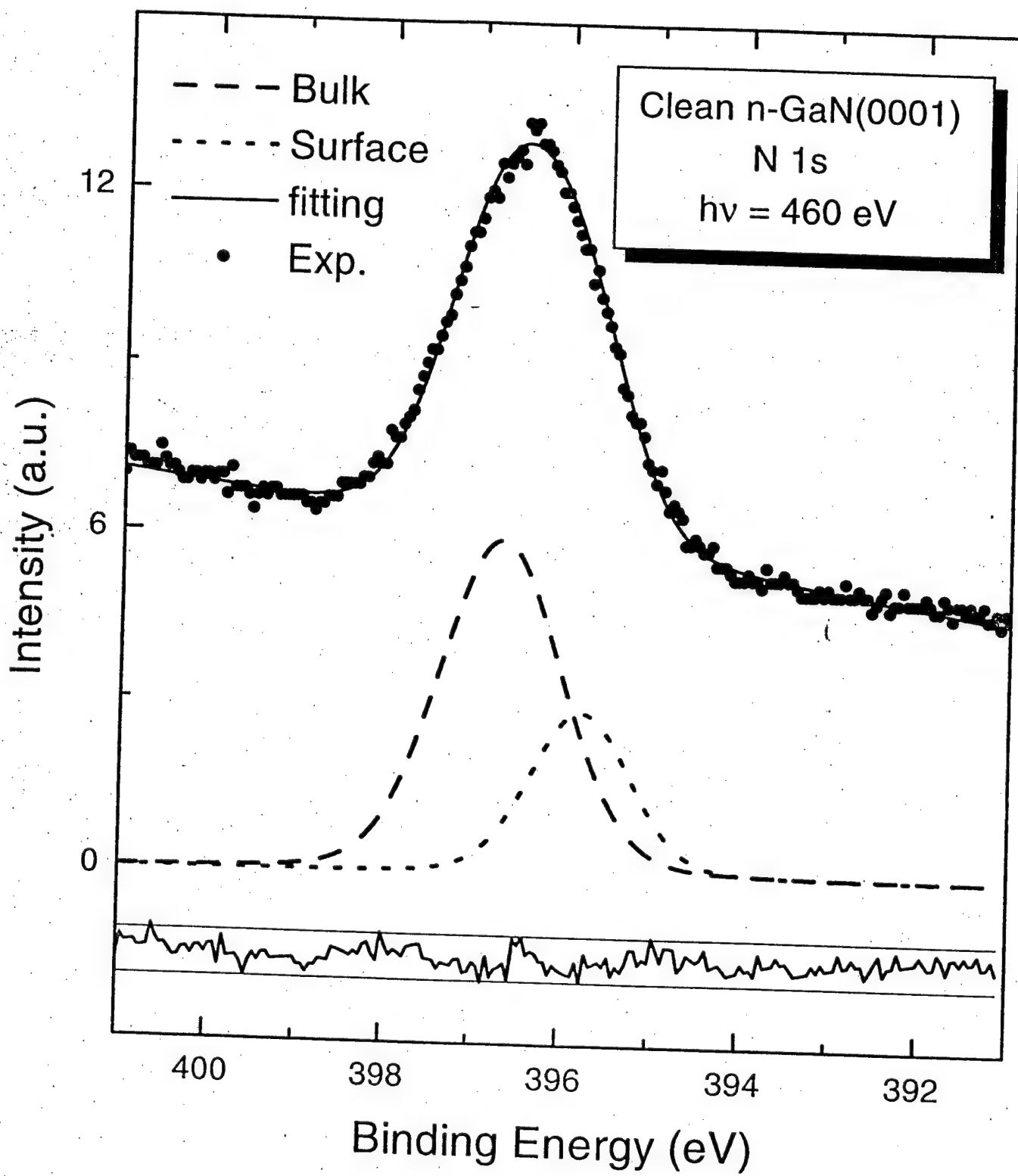


Fig. 6 Y. Yang et al.

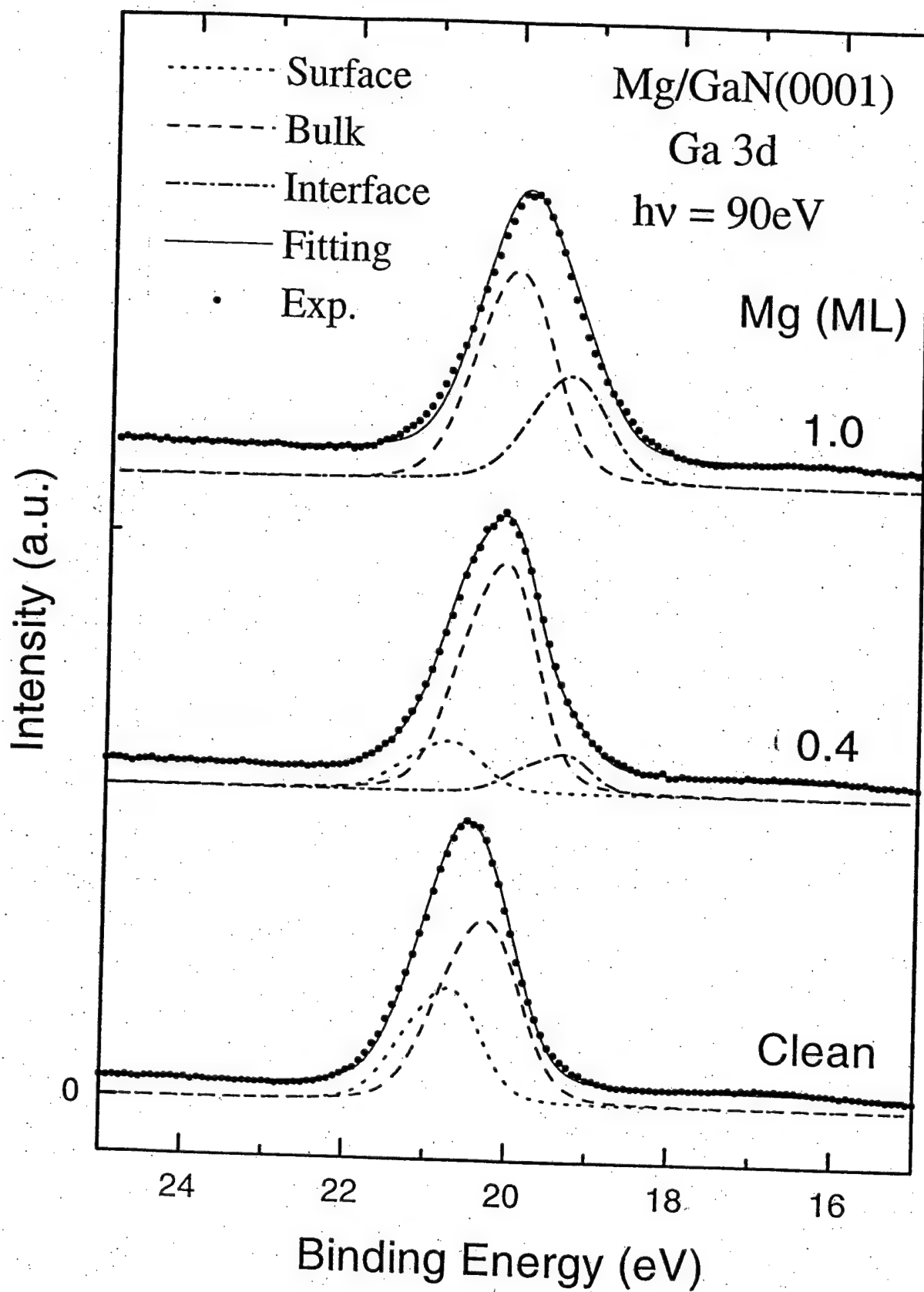


Fig. 7 Y. Yang et al.

## Photoelectron holographic derivative transform for increased range of atomic images

S. H. Xu, H. S. Wu, M. Keeffe, Y. Yang, H. Cruguel, and G. J. Lapeyre

Physics Department, Montana State University, Bozeman, Montana 59717\*

(Received 8 August 2000; revised manuscript received 28 August 2001; published 25 January 2002)

A transform- $k$  derivative spectra (KDS) transform—is introduced for construction of an atomic-structure image from photoelectron diffraction data. A phenomenological theory is used to show that the transform of spectrum derivatives enhances the image peaks by the square of the emitter-scatter distance when used in conjunction with the small cone method. In comparison with the standard transform used in photoelectron holography, the KDS transform allows more distant neighbors (scatterers) to be “seen” by the emitter and suppresses strong forward scattering. The ability to experimentally observe more neighbors of a photoelectron emitter expands the applicability of holographic imaging. The procedure is applied to experimental data obtained from the As/Si(111)-(1×1) and C<sub>2</sub>H<sub>4</sub>/Si(100)-(2×1) surface structures. The latter results show that C<sub>2</sub>H<sub>4</sub> adsorption does not break the Si dimer bond.

DOI: 10.1103/PhysRevB.65.075410

PACS number(s): 61.14.Nm, 61.14.Qp

The determination of the positions of atoms at a surface has been one of the more difficult surface problems to solve. Photoelectron holographic imaging (PHI) using photoelectron diffraction (PHD) data has achieved notable successes in determining adsorbate structures and surface reconstruction structures.<sup>1–12</sup> The technique is appealing, because it directly gives the position of atoms neighboring the electron emitter. The data are inverted to give an atomic image function whose peaks are frequently only very close to the emitter. As a result of the small number, the assignment of atoms to the peaks in the image may be difficult. We present a modification to the inversion which produces more peaks in the image at greater distances from the emitter. In this paper, several examples are presented.

The inversion uses angle-resolved photoemission data for the core level of interest. For each angle the intensity of the emission is measured as a function of wave number  $k$  (the photon energy). The angles used are uniformly distributed over the electron-emission hemisphere. Typically, 70–80 directions are measured with about 25  $k$  points for each direction. Typical spectra are shown in Refs. 2 and 5. The data are first transformed with respect to the wave number, and the second transform is with respect to the angle.<sup>2</sup>

We introduce a transform where the derivative of the data is used in the transform. The wave-number  $k$  derivative-spectrum (KDS) transform successfully yields neighbors at greater distances from the emitter. The PHI images obtained by the KDS transform yield not only the first-nearest-neighbor and the second-nearest-neighbor (SNN) atomic images, but also the third-nearest-neighbor (TNN) images or even more greatly distant images. As a result, this method makes it easier to assign a unique atomic structure to the PHI image.

A short explanation of why the KDS transform works is given, and then two applications to experimental data are described where additional neighbors in the image are shown. The first application is for As on Si(111), where TNN images are found. The second is ethylene on Si(100) which was very recently published in Ref. 5. The Si atoms in the second layer (SNN image) are now seen. Now using bulk Si-Si distances for the second-layer image peaks, a determination of values for the C-C bond and Si-Si dimer lengths are

obtained. The value indicates that the Si dimer bond is not broken by chemisorption, an issue that has received some attention.

The essence of the analysis is to show that the image intensity obtained by transforming the derivative of the spectra is a factor of  $R^2$  larger than the image intensity obtained by transforming the experimental spectra itself;  $R$  is the image-space variable. This behavior is obtained only when the small-cone method is used in the angular transform. If the image obtained by the standard inversion is multiplied by  $R^2$ —a different procedure—no image improvement is found.

According to photoelectron diffraction theory,<sup>2,10</sup> we write a descriptive equation for the object wave,  $\Psi_O$ , and the reference wave,  $\Psi_R$ , in terms of an effective scattering factor  $A(\mathbf{k}, \mathbf{r}_j)$  and the phase factor  $kr_j(1 - \hat{\mathbf{k}} \cdot \hat{\mathbf{r}}_j)$ , where  $\mathbf{k}$  is the photoelectron wave number and  $\mathbf{r}_j$  is the position of the  $j$ th scatterer. The diffraction intensity  $I(k, \hat{\mathbf{k}})$  and its normalization for the interference effect  $\chi(k, \hat{\mathbf{k}})$  obey the relations

$$\chi(k, \hat{\mathbf{k}}) = |\Psi_O|^2 / |\Psi_R|^2 - 1 = I(k, \hat{\mathbf{k}}) / |\Psi_R|^2 - 1$$

$$= \sum_j A(\mathbf{k}, \mathbf{r}_j) e^{ikr_j(1 - \hat{\mathbf{k}} \cdot \hat{\mathbf{r}}_j)} + \text{c.c.}, \quad (1)$$

where c.c. is the complex conjugate of the first term.

Using the Tong-Huang-Wei (THW) inversion,<sup>10</sup>  $\Phi(\hat{\mathbf{k}}, \mathbf{R})$  can be obtained by a Fourier-like transform of each  $\chi(k, \hat{\mathbf{k}})$  function:

$$\Phi(\hat{\mathbf{k}}, \mathbf{R}) = \int_{k_{\min}}^{k_{\max}} \chi(k, \hat{\mathbf{k}}) e^{-ikR(1 - \hat{\mathbf{k}} \cdot \hat{\mathbf{R}})} dk,$$

$$= \int_{k_{\min}}^{k_{\max}} A(\mathbf{k}, \mathbf{r}_j) e^{-ik[R(1 - \hat{\mathbf{k}} \cdot \hat{\mathbf{R}}) - r_j(1 - \hat{\mathbf{k}} \cdot \hat{\mathbf{r}}_j)]} dk. \quad (2)$$

The second line is just the THW inversion of Eq. (1) without the c.c. term.  $\mathbf{R}$  is the real-space variable, and the final and initial points of a measured spectrum interval are  $k_{\max}$  and  $k_{\min}$ . For a finite interval a window function is used to control termination errors. For simplicity, this window function is not shown in the equation, and neither is the sum over the set of the  $j$  scatterers.

The atomic image function  $U(\mathbf{R})$  can be obtained by transforming against the emission angle; this is a sum, since the data are collected for a uniform set of direction  $\hat{k}$ :

$$U(\mathbf{R}) = \left| \sum_{\hat{k} \in \text{Cone}(-\mathbf{R}, w)} \Phi(\hat{k}, \mathbf{R}) \right|^2. \quad (3)$$

As discussed elsewhere<sup>2</sup> the sum uses the small cone method. All the emission directions  $\hat{k}$ , which are uniformly distributed over the emission hemisphere, are grouped into bunches forming small cones of width  $w$ , whose central ray is "swept" over the hemisphere. The parameter  $w$  may range from one spectrum (delta cone) to all spectra on the full hemisphere ( $\pi$ ). Usually a value around  $30^\circ$  yields an image with minimum artifacts.  $U(\mathbf{R})$  has a maximum amplitude when  $\mathbf{R} = \mathbf{r}_j$ , as can be seen in Eqs. (2) and (3).  $U(\mathbf{R})$  does not have a maximum amplitude from the c.c. term in Eq. (1).

Now let us take the derivative of function  $\chi$  [Eq. (1)], with respect to the wave number  $k$ :

$$\begin{aligned} \frac{d\chi(k, \hat{k})}{dk} &= \frac{dA(\mathbf{k}, \hat{r}_j)}{dk} [e^{ikr_j(1-\hat{k} \cdot \hat{r}_j)}] \\ &+ A(\mathbf{k}, \hat{r}_j) (ir_j(1-\hat{k} \cdot \hat{r}_j)) e^{ikr_j(1-\hat{k} \cdot \hat{r}_j)} + \text{c.c.} \end{aligned} \quad (4)$$

Here c.c. is the complex conjugates of the first and second terms. Now, replacing  $\chi(k, \hat{k})$  with  $d\chi(k, \hat{k})/dk$  without the c.c. term in the Tong-Huang-Wei transform [Eq. (2)], the derivative inversion field  $\Phi^d(\hat{k}, \mathbf{R})$  becomes

$$\begin{aligned} \Phi^d(\hat{k}, \mathbf{R}) &= \int_{k_{\min}}^{k_{\max}} \left[ \frac{dA(\mathbf{k}, \hat{r}_j)}{dk} \right] e^{-ik[R(1-\hat{k} \cdot \hat{R}) - r_j(1-\hat{k} \cdot \hat{r}_j)]} dk \\ &+ \int_{k_{\min}}^{k_{\max}} (ir_j(1-\hat{k} \cdot \hat{r}_j)) A(\mathbf{k}, \hat{r}_j) \\ &\times e^{-ik[R(1-\hat{k} \cdot \hat{R}) - r_j(1-\hat{k} \cdot \hat{r}_j)]} dk. \end{aligned} \quad (5)$$

Similar to the behavior of  $\Phi(\hat{k}, \mathbf{R})$ , it is found that  $\Phi^d(\hat{k}, \mathbf{R})$  has a maximum amplitude when the condition  $\mathbf{R} = \mathbf{r}_j$  is satisfied, i.e., the phase factor is zero. The transform described in Eq. (5) is the KDS transform.

In the small-cone method,<sup>2</sup> the  $\hat{k}$  directions are selected in the neighborhood of  $-\hat{R}$ , i.e.,  $\hat{k} \approx -\hat{R}$ . Further, the inversion  $\Phi^d$  has the highest intensity at  $\mathbf{R} = \mathbf{r}_j$ . That is to say, these high-intensity positions are emphasized in the small-cone method, where the backscattering condition  $\hat{k} \approx -\hat{r}_j$  is naturally satisfied. Thus, the second term in Eq. (5) is proportional to the amplitude of  $2\mathbf{r}_j$ , which is essentially  $2\mathbf{R}$ .

In the other parts of space away from the scattering atoms,  $\Phi^d$  has a weak intensity as the condition  $\mathbf{R} = \mathbf{r}_j$  is not satisfied. Then the second term is not proportion to  $R$  and instead depends on the value of  $r_j(1-\hat{k} \cdot \hat{r}_j)$ . The term goes to zero for forward scattering, which would suppress the forward focusing peak which is usually a complication of inversion procedures. In addition, the first term in Eq. (5) for  $\Phi^d$

is obviously not proportional to  $r_j$ . Further, this first term is typically near zero if the scattering function  $A(\mathbf{k}, \hat{r}_j)$  is nearly independent of  $k$ . When the window is  $180^\circ$  for the full hemisphere approach,  $\hat{k}$  is not limited to directions around  $\hat{R}$ , i.e., the condition  $\hat{k} \approx -\hat{R}$  is not generally satisfied. In this case the second term in Eq. (5) depends on the value of  $r_j(1-\hat{k} \cdot \hat{r}_j)$ , and a simple behavior is not found. Therefore, the KDS transform is only effective for surface emitters when used together with the small-cone method, and an increased sensitivity is obtained for more distant neighbors in the atomic image.

After using the small-cone summation of Eq. (3) for the derivative, the image function,  $U^d(\mathbf{R})$ , one sees that is re-

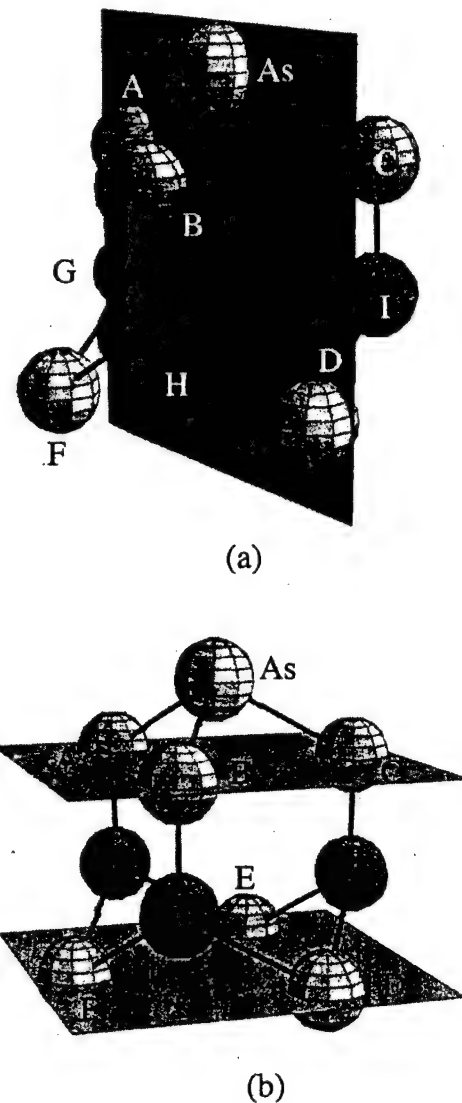


FIG. 1. 3D effective atomic structure for the As/Si(111) system. The arsenic atom replaces the top-layer Si atom, and bonds to Si atoms *A*, *B*, and *C*. Prior to this work, only *A*, *B*, *C*, and *G* were observed in images. (a) The vertical plane represents the *X*-*Z* planar cut shown in Figs. 2 and 3(a). (b) Two horizontal planes represent the *X*-*Y* planar cuts shown in Fig. 2 for *Z* at  $-0.9$  and  $-4.1$  Å.

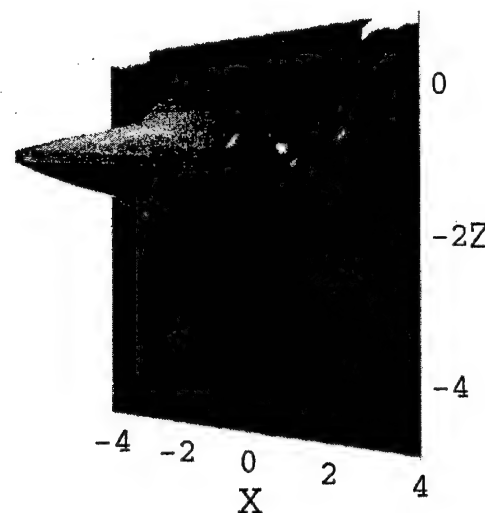


FIG. 2. The vertical  $X$ - $Z$  planar cut of the As/Si(111) system obtained from the standard transform where the "third dimension" is the image intensity. The coordinate unit, Å. The emitter (As) is at the origin.

lated to  $U(\mathbf{R})$  through  $U^d(\mathbf{R}) \sim 4R^2 U(\mathbf{R})$ . This relationship holds if, and only if, there is a scatterer at  $\mathbf{R}$ , that is,  $\mathbf{R} = \mathbf{r}_i$ . The image function  $U(\mathbf{R})$  is obtained with the standard inversion, and  $U^d(\mathbf{R})$  is obtained by the KDS transform. One can clearly see that the intensity is enhanced by  $R^2$  comparing to the standard procedure. High-quality data are needed for a reliable derivative. The atomic image function  $U^d(\mathbf{R})$

allows us to "see" more distant scatterers than the standard inversion function  $U(\mathbf{R})$  for atoms at a surface.

The KDS inversions for several experimental PHD data sets as well as simulated PHD data sets have been examined. The KDS transform always obtains more distant scatterers. Here we present two experimental cases: a single-site emitter in the adsorbate case of As/Si(111), and a double-site emitter in the adsorbate case of  $\text{C}_2\text{H}_4/\text{Si}(100)$ . Note that, due to the phase shift in the electron scattering factor, the distance values may be distorted by  $2/10$ – $3/10$  of an Å.<sup>2</sup>

Arsenic on a Si(111) surface has a well-known structure,<sup>4,13</sup> in which the As atoms replace the Si atoms in the surface layer and bond to three Si atoms. Figure 1 presents this structure using the ball-stick model of atomic structure. In addition to traditional surface science investigations, two holographic imaging experiments have been reported on this system.<sup>4,13</sup> Wu *et al.* obtained images which contained peaks of the first-layer Si atoms (*A*, *B*, and *C*).<sup>13</sup> Luh *et al.* found peaks for the first-layer Si atoms and weak peaks for the second-layer Si atom (*G*) using a method for self-normalizing the constant-initial-energy spectrum data.<sup>4</sup> Figure 2 shows the vertical planar cut obtained from the standard transform.<sup>13</sup>

In the present analysis, using the KDS transform we easily observe an image containing peaks due to the third-layer Si atoms (*D*, *E*, and *F*), as well as first- and second-layer Si atoms. Figure 3 presents the images obtained by the KDS transform. Peaks *A*(*B*, *C*) are due to the first-layer Si atoms, peak *G* to the second-layer Si atom, and peaks *D*(*E*, *F*) to the third-layer Si atoms. Their  $Z$  coordinate values are  $-0.9$ ,

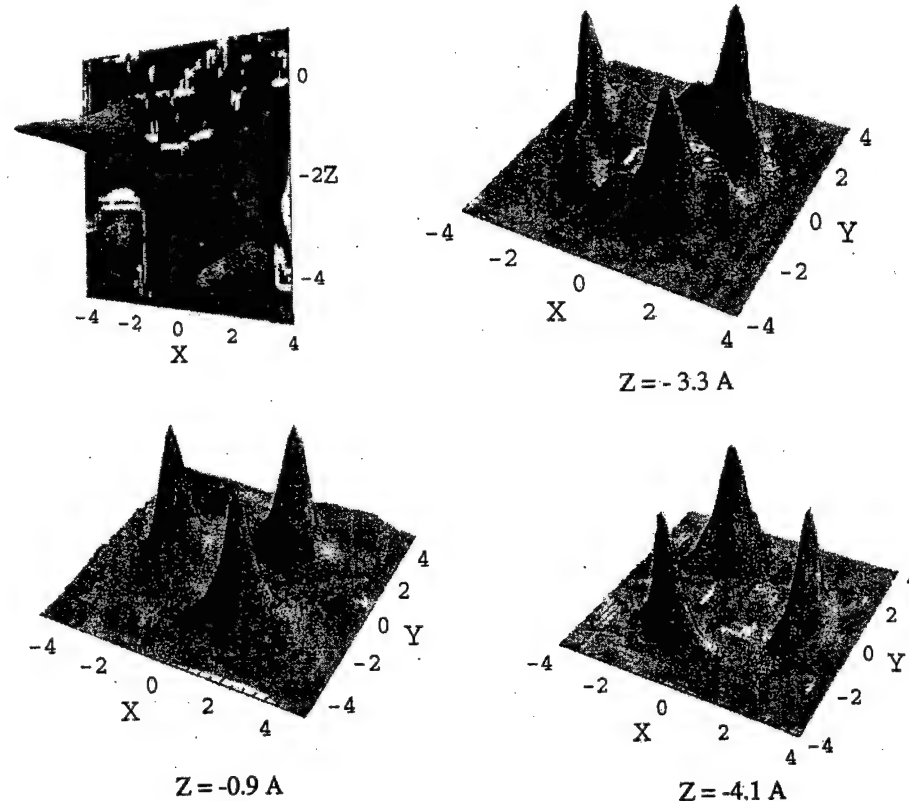


FIG. 3. Planar cuts of the atomic image of the As/Si(111) system obtained from the KDS transform, which show the intensity in the "third dimension." The coordinate unit is Å. The arsenic emitter is at the origin, and the Si labels are from Fig. 1. The vertical ( $X$ - $Z$ ) planar cut appears in the upper left panel. The horizontal ( $X$ - $Y$ ) planar cut is at  $Z = -0.95$  Å passing through Si atoms *A* and *B*. The horizontal ( $X$ - $Y$ ) planar cut is at  $Z = -3.3$  Å passing through Si atoms *G*, *H*, and *I*. The horizontal ( $X$ - $Y$ ) planar cut is at  $Z = -4.1$  Å, passing through Si atoms *D*, *E*, and *F*.

–3.3, and –4.1 Å, respectively. The values of their positions are in reasonable agreement with those known for a bulk Si crystal. The image peak for the third-layer Si atom (*D*) is very strong while the second-layer peak (*G*) is weak. In addition to the three strong peaks (*A*, *B*, and *C*) shown in Fig. 3 ( $Z = -3.3$  Å), there are three weak peaks (*G*, *H*, and *I*) at  $Z = -3.3$  Å in this image. Also, three weak peaks (not shown) are found due to the SNN Si atoms in the first Si layer. The peaks due to the third-layer Si atoms and the SNN Si atoms in the first layer are not observed in the images obtained by either the standard transform or the self-normalization transform.<sup>4,13</sup> To our knowledge, this is the first time a PHI image for a single adsorption site reveals so many of the atoms neighboring the emitter.

In the case of the ethylene on Si(100) system, the two carbon atoms of the ethylene molecule each sit in inequivalent sites. In Ref. 5, reporting experiments, the molecule was found to sit atop a Si-Si dimer. When the standard transform was used, no other Si neighbors were observed. Figure 4 shows the ball-stick model for a PHI image model, where the two carbon atoms *P* and *Q* are placed at the origin. A proper atomic structure construction would have the carbon ball separated. The inversion places *all* emitters at the origin of the image. As discussed in Ref. 5, this makes it more difficult to make atomic assignments for the image peaks. The emitters (two carbon atoms in one ethylene molecule) are labeled *P* and *Q*, and a two-letter label is used for peaks in the image, e.g., *E/P* means Si atom *E* as “seen” by carbon emitter *P*. This work used a single-domain sample with double-high atomic steps. Recently the same site was reported by a “trial and error” comparison of photoelectron diffraction spectra with simulations<sup>14</sup> for a two-domain sample.

Figure 4(b) shows an *X-Y* planar cut which passes through the second-layer Si atoms at  $Z = -2.8$  Å. These atoms are the four strongest spots (*D/Q*, *E/P*, *F/P*, and *G/Q*) in the image. The *X* direction is parallel to the edge of the step, and hence parallel to the dimer bond. The *X* and *Y* coordinates of the spot *D/Q* are 1.2 and 1.9 Å, respectively. The spots form a rectangle. In the bulk crystal structure, however, they should form a square, ignoring any second-layer distortion due to the dimerization. The “double-exposed” rectangular image can be reduced to a square atomic structure by shifting peaks along the *X* direction until a square is formed. A ball-stick atomic structure could be constructed from Fig. 4(a) by imagining the ball *P/Q* to be two superimposed balls which could be separated to form the  $C_2H_4$  “molecule” with concomitant shifts of the Si balls. The shift is 1.4 Å, and represents a carbon-carbon bond length in the ethylene molecule, which agrees with that of the free ethylene molecule (1.34 Å). From this length and the separation (0.6 Å) of the peaks due to the Si-Si dimer given in our paper,<sup>5</sup> we obtain the Si-Si dimer bond length to be 2.0 Å, which is fairly close to the Si-Si dimer length (2.23 Å) of the clean Si(100) surface.<sup>15</sup> This is direct evidence that ethylene adsorption does not break the Si-Si dimer bond, but only modifies the bond. The results essentially resolve one of the questions for ethylene adsorption.

In addition to the two cases mentioned above, the KDS

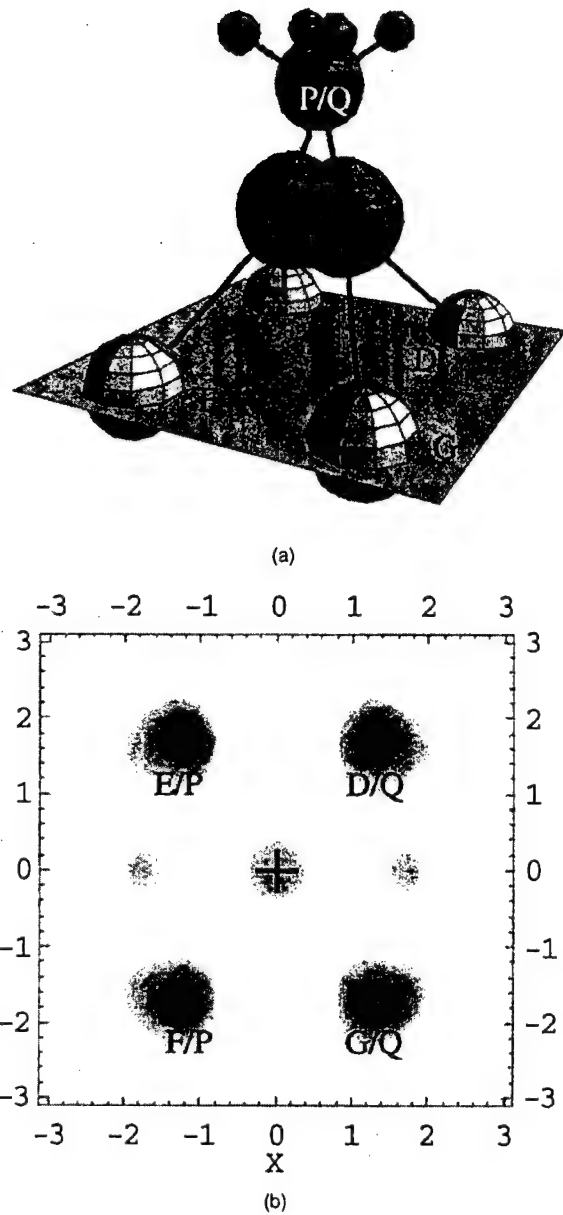


FIG. 4. (a) 3D effective image structure where the two inequivalent carbon emitters are both placed at the origin of the  $C_2H_4/Si(100)-(2\times 1)$  system. Small balls for hydrogen are added in geometrically likely positions based on the expected carbon hybridization. The (*P/Q*) ball represents the carbon atoms. The larger balls below represent the Si dimer atoms. Balls *D*, *E*, *F*, and *G* in the shaded horizontal plane are the Si atoms in second layer. (b) The *X-Y* plane cut at  $Z = -2.8$  Å through the second-layer Si atoms obtained by the KDS transform. The four strong spots (*D/Q*, *E/P*, *F/P*, and *G/Q*) are due to the second-layer Si atoms. The coordinate unit is Å. (The other weak spots are due to the artifacts.) An atomic structure representation would be obtained by expanding the *X* direction (dimer bond direction) to obtain a square mesh for *E*, *D*, *F*, and *G*.

transform has been successfully used for other experimental and simulated PHD data. Thus, we conclude that the KDS transform is a new and very useful method to determine the atomic structure for atoms (adsorbate) at a surface.

In addition, if we take a second- or higher-order derivative of function  $\chi$  with  $k$ , then the atomic image function would be enhanced by a higher power of  $R$ . It would seem that an image with even more distant scatterers would be seen. However, the derivative also "enhances" errors and noise. Hence the "cost" would be an increased precision in the data which would dramatically increase the measuring time.

The KDS transform used here is quite different from the self-normalization method proposed by Luh *et al.*<sup>4</sup> although they sometimes called it the differential or derivative method. Luh *et al.* took the derivative of the PHD data with respect to the photon energy, and then integrated for a  $\chi$  function. In pure mathematics, the derivative-integration cycle would not yield any change to the PHD data. As expected by Luh *et al.*,<sup>4</sup> this process removes the discontinuities that may arise in the PHD data due to the limitations of the experimental condition such as shifts in the photon flux. In our method, however, we only use the derivative of the function  $\chi$  instead of the differentiation-integration cycle. As expected by the theoretical approach, the images obtained by

the KDS transform can truly yield the more distant neighbors (scatterers).

In summary, the KDS transform is successfully used to construct atomic structures for the experimental systems As/Si(100) and C<sub>2</sub>H<sub>4</sub>/Si(100). This illustrates that in the holographic imaging method data are collected and inverted to directly obtain an image which needs to be inspected. No modeling is needed to obtain the adsorption site. In comparison with the standard transform, the images obtained by the KDS transform can yield more distant neighbors (scatterers). The KDS images unequivocally confirm the As adsorption site, and directly show that ethylene adsorption does not break the Si dimer bond. Several investigators suggest the dimer bond is broken. At the same time, no strong artifacts are observed in the images. Therefore, the KDS transform can be widely used for adsorbate systems.

The authors would like to thank the staff at SRC and ALS for their most generous help and support. This work was supported by the DOE and ONR DEPSCoR. The synchrotron facilities are supported by NSF and DoE, respectively.

\*FAX: 406-994-4452. Electronic address: lapeyre@physics.montana.edu

<sup>1</sup>H. Wu, G. J. Lapeyre, H. Huang, and S. Y. Tong, Phys. Rev. Lett. **71**, 251 (1993).

<sup>2</sup>Huasheng Wu and G. J. Lapeyre, Phys. Rev. B **51**, 14 549 (1995), and references therein.

<sup>3</sup>M. A. Mendez *et al.*, Phys. Rev. B **45**, 9402 (1992).

<sup>4</sup>D.-A. Luh *et al.*, Phys. Rev. Lett. **81**, 4160 (1998), and references therein.

<sup>5</sup>S. H. Xu *et al.*, Phys. Rev. Lett. **84**, 939 (2000).

<sup>6</sup>J. G. Tobin *et al.*, Surf. Sci. **334**, 263 (1995).

<sup>7</sup>P. M. Len *et al.*, Phys. Rev. B **59**, 5857 (1999).

<sup>8</sup>J. J. Barton, Phys. Rev. Lett. **67**, 3106 (1991).

<sup>9</sup>L. J. Terminello *et al.*, Phys. Rev. Lett. **70**, 599 (1993).

<sup>10</sup>S. Y. Tong, H. Huang, and C. M. Wei, Phys. Rev. B **46**, 2452 (1992), and references therein.

<sup>11</sup>K.-M. Schindler *et al.*, Phys. Rev. Lett. **71**, 2054 (1993).

<sup>12</sup>The derivative method was presented at the 2000 March APS meeting and the Electron Spectroscopy and Structure Conference in Berkeley, CA (August of 2000). At the latter conference the C.S. Fadly group presented essentially the same derivative method with application for the control of the forward focusing peaks in data analysis for an emitter in the bulk.

<sup>13</sup>H. Wu *et al.* (unpublished); their work about As adsorption on Si(111) and Si(100) surfaces will be submitted; H. Wu, Ph.D. thesis, MSU-Bozeman, 1994.

<sup>14</sup>R. Terborg *et al.*, Phys. Rev. B **61**, 16 697 (2000).

<sup>15</sup>N. Roberts and R. J. Needs, Surf. Sci. **236**, 112 (1990).

# Electronic Near-Surface Defect States of Bare and Metal Covered n-GaN Films Observed by Cathodoluminescence Spectroscopy

A.P. YOUNG,<sup>1</sup> J. SCHÄFER,<sup>2,3</sup> L.J. BRILLSON,<sup>1,2,4</sup> Y. YANG,<sup>5</sup> S.H. XU,<sup>5</sup> H. CRUGUEL,<sup>6</sup> G.J. LAPEYRE,<sup>6</sup> M.A.L. JOHNSON,<sup>6</sup> and J.F. SCHETZINA<sup>6</sup>

1.—Department of Electrical Engineering, The Ohio State University, Columbus, OH 43210-12272. 2.—Present address: Lawrence Berkeley Lab, Advanced Light Source, Mailstop 7-222, 1 Cyclotron Road, Berkeley, CA 94720. 3.—Center for Materials Research, The Ohio State University, Columbus, OH 43210-1272. 4.—Department of Physics, The Ohio State University, Columbus, OH 43210-1272. 5.—Physics Department, Montana State University, Bozeman, MT 59717. 6.—Department of Physics, North Carolina State University, Raleigh, NC 27695-8202

Depth-dependent low energy cathodoluminescence spectroscopy (CLS) has been used to investigate the near-surface optical properties of n-type GaN epilayers grown under various growth conditions. Both bare and reacted-Mg/n-GaN and Al/n-GaN (annealed to 1000°C) surfaces were investigated. We find enhanced emission at ~1.4, 1.6, and 2.2 eV from states within the n-type GaN bandgap near the interface of the reacted Mg with the semiconductor, which correlates with previous measurements of Schottky barrier formation on the same specimens. No clear evidence for p-type doping at the reacted interfacial layer is apparent. For Al on n-type GaN, CLS emission is dominated before and after metallization by "yellow" emission, which correlates only weakly with the Fermi level stabilization. Instead, we observe emission above the GaN band edge emission at 3.85 eV, due either to deep level emission from AlN or to the formation of the alloy  $\text{Al}_x\text{Ga}_{1-x}\text{N}$  ( $x \approx 0.2$ ) in the reacted near-surface region.

**Key words:** Defects states, n-GaN, Schottky barrier

## INTRODUCTION

The electronic states at metal contacts to GaN are of significant concern for a wide range of microelectronic and optoelectronic device applications. Relatively little is known to date about the localized states at GaN junctions and their correlation with chemical interactions and interdiffusion. One metal of particular interest for such interface studies is Mg, because of its low work function and its acceptor nature in GaN.<sup>1-3</sup> Another such metal is Al because of its use as part of the current standard ohmic contact<sup>4-6</sup> to n-GaN, and the existence of a chemical reaction between Al and GaN producing an interfacial AlN layer<sup>7,8</sup> and/or the binary alloy  $\text{Al}_x\text{Ga}_{1-x}\text{N}$ . Possible reactions and diffusion of these metals into the semiconductor may modify the effective doping level and the deep level density, thereby influencing the effective Schottky barrier height. In this work, we investigate the near-surface region of n-type GaN before and after deposition of Al and Mg by cathodoluminescence spectroscopy (CLS) to correlate bulk deep level elec-

tronic properties with the near-surface interfacial chemistry.

## EXPERIMENT

We investigated deep electronic states near the (0001) surface of nominally 1  $\mu\text{m}$  thick n-type GaN doped with silicon to  $n = 1 \times 10^{18} \text{ cm}^{-3}$ . The GaN was obtained from different sources each using a different growth technique: molecular beam epitaxy (MBE) on sapphire (SVT Associates, Inc.), and metalorganic vapor phase epitaxy (MOVPE) on 6H-SiC.

Approximately 30 monolayers (ML) of Mg were evaporated on the (1  $\times$  1) low energy electron diffraction (LEED) (ordered MBE grown surface in ultra high-vacuum (UHV), while  $\approx$  30 ML of Al were evaporated in UHV on the MOVPE grown epilayer, which also displayed a (1  $\times$  1) pattern). The specimens were then characterized by soft x-ray photoemission spectroscopy (SXPS), which provided a measure of the metallic character of the overlayers as well as the Fermi level movement. The Mg/GaN junction was subsequently annealed to 1000°C, aimed at inducing interdiffusion and p-type doping at the interface. Similarly, the Al/GaN junction was also annealed to

(Received August 28, 1998; accepted December 4, 1998)

1000°C to induce an interfacial reaction.<sup>9</sup> The samples were then sent via airmail, where we performed CLS in a UHV chamber with pressures in the low  $10^{-10}$  Torr range. During transit to Ohio State, the samples were exposed to ambient conditions. For the UHV-CLS measurements, an electron gun with an energy range of 0.5–4.5 kV generated the optical emission, with a beam spot size between 0.2–0.5 mm and with emission currents of 0.2–20  $\mu$ A. The angle of the electron beam relative to the sample was 45°. This glancing angle enhances the surface sensitivity relative to normal incidence excitation.

The optical train included an in-situ  $\text{CaF}_2$  lens and an ex-situ prism monochromator with 30–50 meV resolution over the measurement range of the spectra. An S-1 photomultiplier tube (PMT) was used over the spectral range 1.0–4.0 eV to measure both deep level and band edge emission from the GaN. To extend the optical measurement deeper into the ultra violet (UV), an S-20 PMT able to detect luminescence out to the vacuum ultraviolet (~6.2 eV) was also used. The CLS spectra presented have been corrected for the spectral responsivity of the detectors, although not for the full transmission of the optical train.

## RESULTS

In order to establish any changes produced by the metallization/anneal of the n-GaN, we first examined the bulk CLS emission features of similar n-GaN without metal. Furthermore, we examined n-GaN surfaces grown by different methods to better understand the characteristic bulk CLS features since, even if material from one source were entirely reproducible, different growth techniques can easily produce n-GaN with widely differing morphology, dislocation density, and point defect densities. Besides the energies and intensities of the deep level emissions, the CLS experiments also probed these levels as a function of depth below the free surface on a nanometer scale. By increasing the electron beam energy in CLS, one can increase the penetration depth of the hot electrons and hence the depth for the generation of electron-hole pairs.

For electron beam energies of 3 keV, a range of ~30 nm is estimated using the Everhart-Hoff model assuming a simple  $\cos \theta$  angular dependence. Therefore, the generation of electron-hole pairs is shown to occur well into the bulk of the film.<sup>10</sup> As shown in Fig. 1, the deep level and near band edge emission intensities can vary significantly for epilayers made under different growth conditions. By far the most intense emission comes from the MOVPE n-GaN, with the peak emission occurring at 2.15 eV and a full width at half maximum (FWHM) of 0.7 eV. Significantly less intensity at 3.4 eV is evident from the epilayer due to near band edge emission. The n-type GaN grown by MBE, while showing less intensity overall, has almost all luminescence occurring at the band edge. We have also observed a rich spectrum in the bandgap from other GaN specimens prepared by different methods at other energies such as 1.7, 2.3, and 2.7 eV

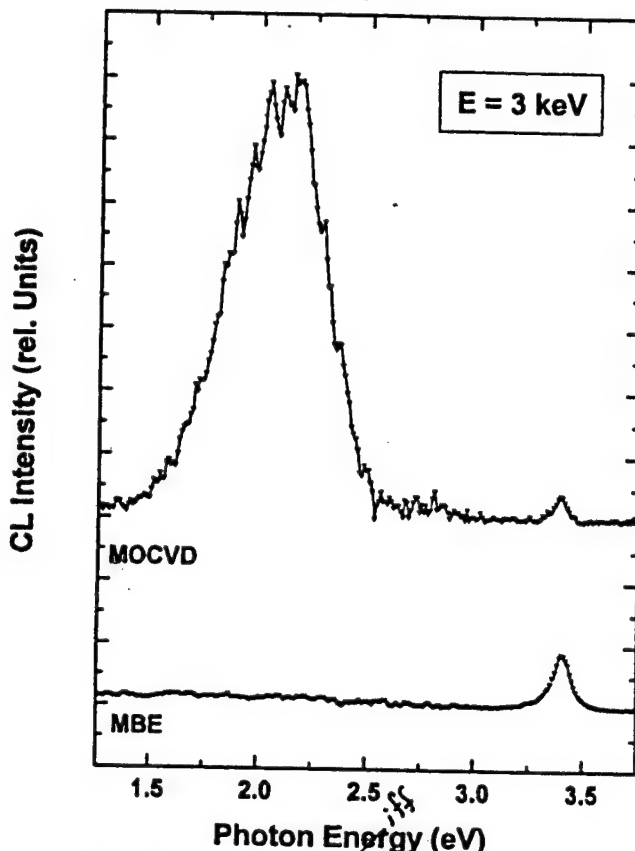


Fig. 1. Comparison of the bulk ( $E = 3.0$  keV) cathodoluminescence properties of the n-GaN grown by different techniques. The measurements were taken at room temperature, and a beam current of 2  $\mu$ A. The spectra are offset for clarity.

of unknown origin in addition to the main broad peak intensity at 2.2 eV.<sup>11</sup>

The near-surface CLS ( $E = 0.5$  keV) measurements shown in Fig. 2 have several differences in comparison with the bulk CLS spectra. As with the bulk measurements, the most intense emission came from the MOVPE epilayer. Near the surface, in addition to the emergence of a new peak at ~2.75 eV and the quenching of the band edge luminescence from the MOVPE n-GaN, the 2.2 eV band is narrower (FWHM = 0.55 eV), and there appears to be a distinct asymmetry to the feature suggesting at least two unresolved peaks.

In the near-surface region, the MBE n-GaN shows the emergence of luminescence over the whole bandgap with the most intensity relative to the band edge emission appearing at midgap energies, including a weak feature at ~1.6 eV. In general, the near-surface regions of these air-exposed specimens all exhibit some mid-gap emissions, with intensities depending on the growth.

## Mg COVERED GaN

The MBE n-GaN specimens before and after the creation of the interdiffused Mg interface were studied in greater detail by depth (dependent CLS over a wide spectral range). As shown in Fig. 3, the dominant feature for both the bare and the metal-covered

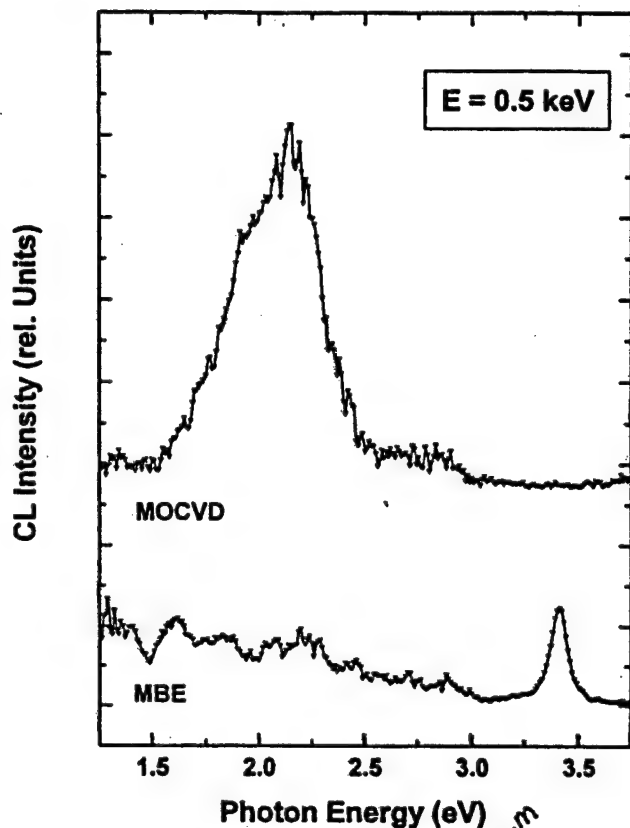


Fig. 2. Near-surface ( $E_{beam} = 0.5$  keV) cathodoluminescence properties of the n-GaN epilayers. Spectra are taken with a electron beam current of 4  $\mu$ A at room temperature. Spectra are offset for clarity.

GaN is the band edge luminescence at 3.4 eV, along with broad features at lower emission energies. The relative intensities of the two main features vary differently as a function of depth. The broad emission features decrease with increasing excitation depth for both metallized and unmetallized surfaces. On the other hand, the near band edge luminescence decreases for both types of surfaces as the excitation depth decreases. The effect of the Mg overlayer is also highlighted by the depth dependence. At higher beam energies (3.0–4.0 keV), the luminescence spectra of the GaN with and without Mg are similar, which is consistent with the bulk nature of the emissions. For lower beam energies, the deep defect band increases dramatically (by up to a factor of 4) relative to the band edge in the Mg/n-GaN case, exhibiting indications of peak structures at 1.4, 1.6 and 2.15–2.2 eV. This characteristic deep level emission reaches its maximum at a probe energy of 1.0 keV. At this probe energy, electrons deposit most of their energy at a depth of only ~5 nm.<sup>13</sup> Subsequently, at 500 eV the deep level emission decreases once again relative to the band edge.

#### Al COVERED GaN

The Al-covered GaN experiment shows a number of significant differences with the Mg-covered GaN results in Fig. 3. Figure 4 shows the depth dependent CLS spectra from a bare MOVPE n-type GaN epilayer

and the Al/n-GaN structure annealed to 1000°C. In contrast with 3, all of the spectra in Fig. 4 are dominated by a broad “yellow” luminescence peak. The shape of this peak shows no dramatic changes as the penetration of the electron beam varies. For the bare surface, the band edge luminescence is observed to be quenched below 2 keV, while in the Al/n-GaN case, there is little or no band edge luminescence observed even for energies up to 4 keV. While the shape of the spectra does not change, the overall intensity does decrease toward the surface.

The “yellow” luminescence intensity centered at 2.15 eV for the bare n-GaN exhibits a maximum below the surface at 1 keV, decreasing by over a factor of three at the lowest electron beam energy. In comparison, for the Al/n-GaN the maximum intensity occurs at the higher beam energy of 2 keV, and by 0.5 keV, the peak intensity has dropped by over an order of magnitude. The appearance of this maximum at deeper excitation energies for the Al-covered surface is consistent with the added thickness of the overlayer. The only other difference between the metallized and air-exposed surfaces is the increase of the surface-related peak at 2.7 eV, which might be due to the reacted interface or due to impurities on the surface. Additional UHV experiments on clean surfaces are planned to address this issue.

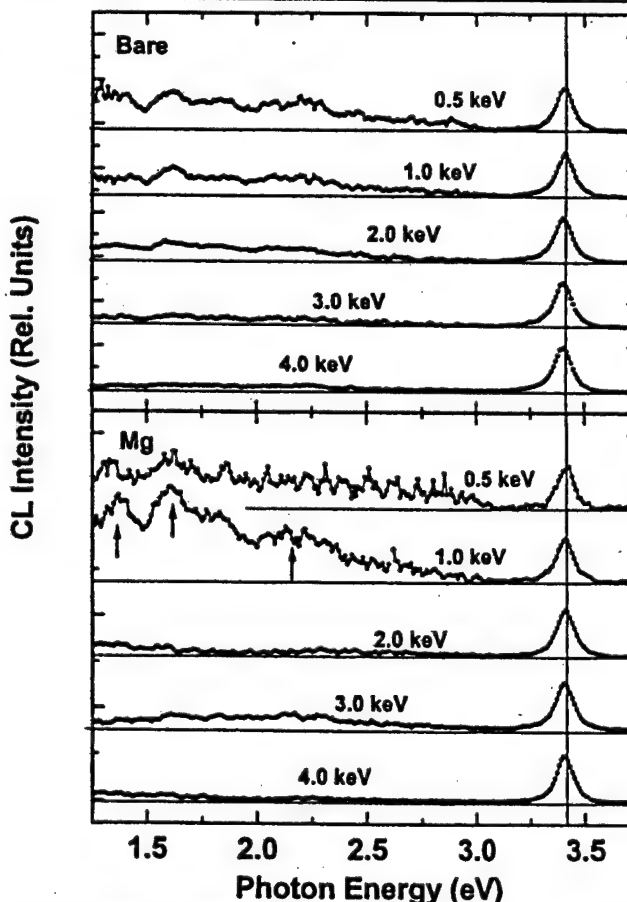


Fig. 3. Depth dependence of the n-GaN bare surface (top panel) and the Mg/GaN interface after annealing to 1000°C (bottom panel).

CLS measurements of the Al/GaN interface using an S-20 PMT, with higher UV sensitivity, provided additional evidence for a reaction between Al and the GaN. Figure 5 shows, in addition to the near-band-edge emission luminescence at 3.4 eV, a high energy shoulder above the bandgap of GaN. This partially resolved peak feature appeared most pronounced at 1 keV, corresponding to approximately the same depth below the free surface as for the features induced by the metal at the Mg/GaN interface. From the inset of Fig. 5, this peak is clearly resolved at 3.85 eV, and cannot be from the GaN.

The SXPS measurements<sup>9</sup> show that the Fermi level of the reacted Mg/n-GaN stabilized 2.2 eV above the valence band edge. For the reacted Al/n-GaN interface, this Fermi level stabilization occurs at 2.4 eV above the valence band edge, reflecting the differences in the electronic and chemical nature of the two metals. For the Mg case, it is unclear from the SXPS measurements whether the Mg diffused beyond a thin  $Mg_3N_2$  layer, or evaporated off the GaN surface before it could diffuse into the semiconductor.<sup>12</sup> In comparison, for the Al/GaN case, there is an indication of the formation of AlN in the SXPS spectra as measured by the observed shift in the Ga 3d core level.<sup>13</sup>

## DISCUSSION

High densities of defects near the surface as well as interfacial chemical bonding are known to be important extrinsic factors in the formation of Schottky barriers between metals and semiconductors. CLS has previously been shown to be sensitive to electronic states capable of trapping charge in the near surface region of semiconductors.<sup>14</sup> Therefore, it is possible that there might be a correlation between the presence of either  $Mg_3N_2$  or AlN, interface states, and the deep levels observed in the respective low energy CLS spectra.

Depth dependent CLS has been performed on GaN previously,<sup>15-17</sup> however, we believe this is the first investigation of GaN by CLS which has looked in detail at emission in the extremely low energy near-surface region below 4 keV. Because the depth of excitation is a strong function of the incident electron beam energy of a few keV or less, this technique provides the capability to probe electronic defect levels localized both within a few nanometers of "buried" interfaces as well as within the junction constituents. Both the Mg/n-GaN and the Al/n-GaN junctions studied here take advantage of this "buried" interface capability. Although both were formed in UHV, transport in air left some adventitious C and O, as measured by Auger electron spectroscopy (AES). Adventitious contaminants act primarily to reduce any optical emission due to surface recombination, not add new features. Our highest energy subsurface spectra allow one to distinguish between optical features related to the local interface vs surface contamination. The subsurface nature of the CLS spectra presented here minimizes effects of such contamination

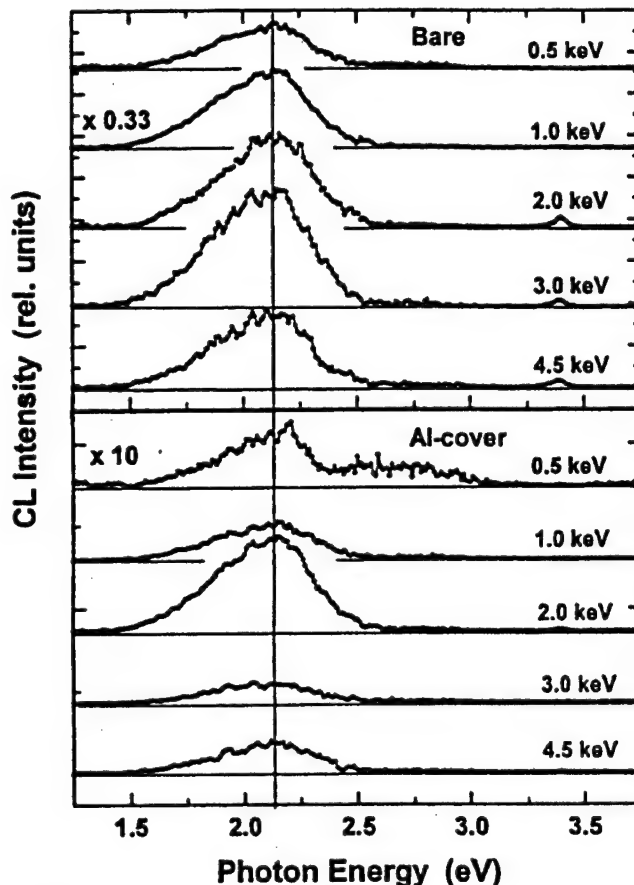


Fig. 4. Depth dependence of the n-GaN bare surface (top panel) and the Al/GaN interface after annealing to 1000°C (bottom panel).

on the optical spectra.

From the results on the free surface shown in Fig. 1, we can already conclude the different growth techniques produce distinctly different luminescence patterns. For the MBE grown n-GaN, the CLS spectra shown in Fig. 3 is dominated by the band edge luminescence, not emission from the deep level at 2.15 eV. Deposition and subsequent annealing to 1000°C of the Mg/n-GaN does not produce enough deep level emission to completely dominate the optical spectrum; instead, enhanced emission is observed at 2.15 eV, along with peaks at 1.6 and 1.4 eV, respectively. Assuming that the Fermi stabilization energy is associated with localized states within the bandgap, one might expect any optical transitions into and out of such a state to occur at 1.2 (outside the detector range) and 2.2 eV, respectively, i.e., complementary transitions adding up to the bandgap of 3.4 eV. Lower energies would result from transitions to or from states separated from the band edges. Thus, the 2.15–2.2 eV spectral feature observed in Fig. 3 does appear to correlate with the 2.2 eV Fermi level stabilization above the valence band.

In addition to producing Fermi level movement and band bending, Mg is also a p-type dopant in GaN. Based on previous measurements of GaN:Mg, the electrically active Mg acceptor level luminescences strongly at 2.9–3.2 eV.<sup>18</sup> Figure 3 shows no clear

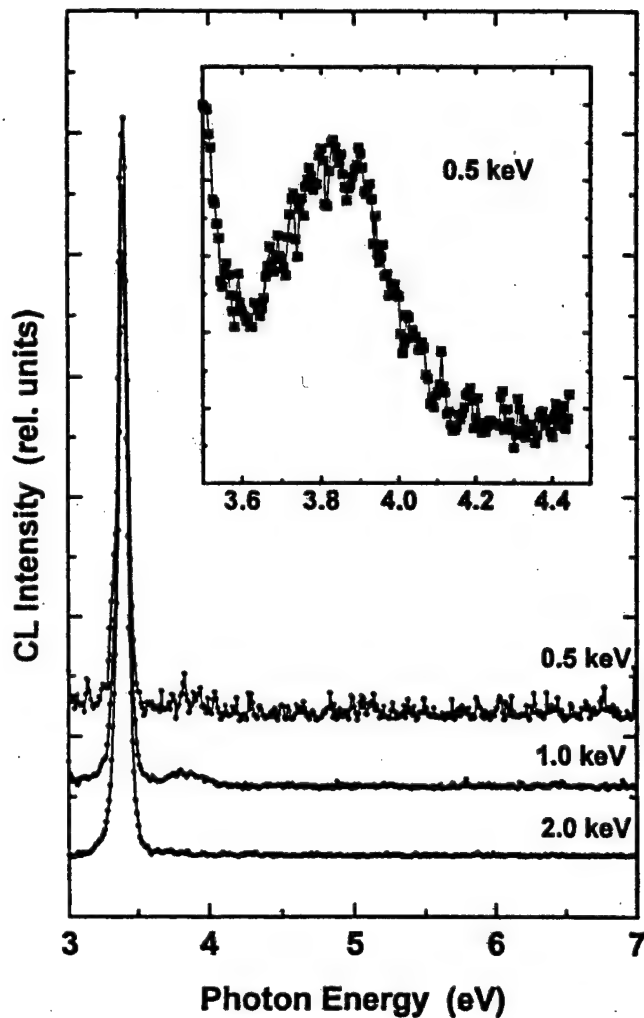


Fig. 5. Depth-dependent CLS spectra of Al/n-GaN above the bandgap of GaN. A long exposure spectrum (inset) shows the emergence of a new peak at 3.85 eV. This emission indicates the presence of either a deep level defect in AlN or an alloy  $\text{Al}_x\text{Ga}_{1-x}\text{N}$  ( $x \approx 0.2$ ) near the surface.

indication of such luminescence. Hence, the "buried" interface CLS measurements provide no evidence to suggest incorporation of Mg within the GaN lattice occurring at the interfacial regime.

For the Al/n-GaN specimen shown in Fig. 4, the CLS spectra at all energies is dominated by the strong "yellow" luminescence centered near 2.15 eV. The deposition and annealing of Al over the n-GaN has not qualitatively changed the spectra of emissions below the band edge, merely enhanced or lowered emission already present in the bare surface case (notwithstanding the new, above-bandgap peak shown in Fig. 5).

For this Al/n-GaN case, SXPS shows that the Fermi level stabilizes at 2.4 eV, an energy 0.2 eV higher in the bandgap than for the Mg case. Although the 2.15 eV luminescence could originate from such a state to final states which lie above the valence band edge, the appearance of new compound formation can account for such differences more directly. The CLS features in Fig. 5 demonstrate emission at the interface from a different material with a higher bandgap.

Such emission may correspond to either a deep level defect from the AlN or the alloy  $\text{Al}_x\text{Ga}_{1-x}\text{N}$  ( $x \approx 0.2$ ).<sup>19,20</sup> Indeed, SXPS core level shift measurements indicate the presence of an Al-N reaction, favoring the formation of AlN over the presence of the alloy. Such an interfacial compound would certainly alter the dependence of Schottky barrier formation on the properties of metallic Al. While the role such a layer plays in altering interfacial charge exchange is not yet evident, the CLS measurements reported here clearly show that a reacted compound with a wider band gap than GaN has formed on a nanometer scale at the Al-GaN junction.

## CONCLUSION

In summary, depth-dependent low energy cathodoluminescence spectroscopy (CLS) has been used to investigate the near-surface luminescence from n-type GaN epilayers grown by various growth techniques. We find enhanced emission from states within the bandgap of the Mg/GaN epilayer *below* the free surface, probably, from the interface of the reacted Mg metal with the semiconductor, but no clear evidence for Mg incorporation into the GaN lattice. The 2.15–2.2 eV emission is in good agreement with the SXPS observation of Fermi level stabilization at 2.2 eV above the valence band maximum. For the Al/n-GaN case, CLS and SXPS data do not correlate as well (the CLS is dominated by luminescence at 2.2 eV, while the SXPS shows a Fermi stabilization energy of 2.4 eV). Above band-gap emission at 3.85 eV provides evidence of a new interfacial compound, either a deep level defect from AlN identified by SXPS or from the alloy  $\text{Al}_x\text{Ga}_{1-x}\text{N}$  ( $x \approx 0.2$ ). CLS has shown the capability of distinguishing the density of deep level states both in the near-surface and sub-surface regions of n-GaN. These results are the first steps toward an understanding of the Schottky barrier formation at free metal-GaN interfaces.

## ACKNOWLEDGMENTS

This work was partially supported by the U.S. Department of Energy under Grant DE-FG02-97ER45666.

## REFERENCES

1. H. Amano, M. Kito, K. Hiramatsu and I. Akasaki, *Jpn. J. Appl. Phys.* **28**, L2112 (1989).
2. S. Nakamura, T. Mukai and M. Senoh, *Appl. Phys. Lett.* **64**, 1687 (1994).
3. C.I. Wu and A. Kahn, *J. Vac. Sci. and Technol. B*, (in press).
4. B.P. Luther, J.M. DeLucca, S.E. Mohney and R.F. Karlicek Jr., *Appl. Phys. Lett.* **71**, 3859 (1997).
5. A.C. Schmitz, A.T. Ping, M. Asif Khan, Q. Chen, J.W. Yang and I. Adesida, *J. Electron. Mater.* **27**, 255 (1998).
6. S. Ruvimov, Z. Lilienthal-Weber, J. Washburn, K.J. Duxstad, E.E. Haller, Z.-F. Fan, S.N. Mohammad, W. Kim, A.E. Rothchko, H. Morkoc, *Appl. Phys. Lett.* **69**, 1556 (1996).
7. Y. Yang, S.H. Xu, G.J. Lapeyre and J.M. van Hove (unpublished).
8. V.M. Bermudez, T.M. Jung, K. Doverspike and A.E. Wickenden, *J. Appl. Phys.* **79**, 110 (1996).
9. Y. Yang, S.H. Xu, G.J. Lapeyre and J.M. van Hove, *J. Vac. Sci. Technol. B* (in press).

10. B.G. Yacobi and D.B. Holt, *Cathodoluminescence Microscopy of Inorganic Solids* (New York: Plenum, 1990), p. 58.
11. A.P. Young, J. Schäfer, and L.J. Brillson (unpublished).
12. C.I. Wu, A. Khan, N. Taskar, D. Dorman and D. Gallagher, *J. Appl. Phys.* 83, 4249 (1998).
13. Y. Yang and G. Lapeyre (unpublished).
14. L.J. Brillson and R.E. Viturro, *Scanning Microscopy* 2, 789 (1988).
15. X. Li and J.J. Coleman, *Appl. Phys. Lett.* 70, 438 (1997).
16. M. Herrera Zaldivar, P. Fernandez and J. Piqueras, *J. Appl. Phys.* 83, 2796 (1998).
17. F.A. Ponce, D.P. Bour, W. Gotz and P.J. Wright, *Appl. Phys. Lett.* 68, 57 (1996).
18. F.J. Sánchez, F. Calle, D. Basak, J.M. G. Tijero, M.A. Sánchez-García, E. Morroy, E. Calleja, E. Muñoz, B. Beaumont, Pierre Gibart, J.J. Serrano and J.M. Blanco, *MRS J. Nitride Semi. Res.* 2, 28 (1997).
19. S. Yoshida, S. Misawa and S. Gonda, *J. Appl. Phys.* 53, 6844 (1982).
20. H. Angerer, D. Brunner, F. Freudenberg, O. Ambacher, M. Stutzmann, R. Höpler, T. Metzger, E. Born, G. Dollinger, A. Bergmaier, S. Karsch and H.-J. Körner, *Appl. Phys. Lett.* 71, 1504 (1997).

# Photoemission spectromicroscopy studies on epitaxial lateral overgrowth GaN surfaces

Y. Yang

Physics Department, Montana State University, Bozeman, Montana 59717

S. Mishra and F. Cerrina

Department of Electrical and Computer Engineering, University of Wisconsin-Madison, Madison, Wisconsin 53706

S. H. Xu, H. Cruguel, and G. J. Lapeyre<sup>a)</sup>

Physics Department, Montana State University, Bozeman, Montana 59717

J. F. Schetzina

Department of Physics, North Carolina State University, Raleigh, North Carolina 27695

(Received 28 April 1999; accepted 10 May 1999)

Photoemission spectromicroscopy is employed to investigate the inhomogeneities of surface electronic structures of epitaxial lateral overgrowth GaN material. The image, acquired on a clean surface, shows the surface morphology and agrees with the atomic force microscopy image. The dominant contrast mechanism is attributed to the angular dependence of the quantum yield for regions at different angles. Energy distribution curves localized to a submicron region for the Ga 3d core level demonstrate that growth-front areas have different Fermi level pinning behavior compared with window areas and overgrowth regions. The sample exposed to atomic hydrogen shows the same Fermi level position for all areas of the surface. Photoemission spectromicroscopy reveals island formation when about 10 monolayers of Mg is deposited on the surface. © 1999 American Vacuum Society. [S0734-211X(99)04404-2]

## I. INTRODUCTION

Wide-band-gap III-V nitrides have attracted much attention because of their scientific significance and for their potential for many practical applications.<sup>1</sup> Among them, gallium nitride (GaN) is the most interesting material because of its suitable direct band gap of 3.4 eV at room temperature, notable chemical inertness, and great physical hardness. These attractive properties make it ideal for fabricating electronic and electro-optic devices. Considerable effort is underway to develop high power electronics. The optical applications include devices operated near the short wavelength end of the visible range [i.e., blue and ultraviolet light emitting diodes (LEDs), detectors, and laser devices].<sup>2,3</sup> However, the development of III-V nitride materials and devices has suffered from the lack of availability of low-dislocation-density, lattice-matched native nitride substrates for device synthesis using metalorganic vapor phase epitaxy (MOVPE) and molecular beam epitaxy (MBE) methods. As a consequence, growth of GaN on mismatched substrates such as sapphire or SiC produces a columnar-like material consisting of many small hexagonal-like grains.<sup>4</sup> When the latter materials are prepared by MOVPE they show high dislocation densities of  $10^9$ – $10^{10}$  per  $\text{cm}^2$ . Recently, there have been demonstrations of defect reduction in the growth of GaN layers on sapphire and SiC using an epitaxial lateral overgrowth (ELO) technique.<sup>5</sup> The technique uses GaN/sapphire (or SiC) layers patterned with  $\text{SiO}_2$  as a substrate, which produces stripes ( $\sim 10 \mu\text{m}$  wide) of GaN and a remarkable reduction in the dislocation density to about  $10^4$  per  $\text{cm}^2$  or less. Laser diodes

with very long continuous wave (cw) lifetimes have been fabricated from these ELO GaN materials.<sup>6</sup>

In this work, the synchrotron-radiation-based photoemission spectromicroscopy technique is employed to study the inhomogeneities of the surface electronic structure of MOVPE-grown ELO GaN materials. Photoemission spectromicroscopy is a combination of classic photoemission techniques and microscopy. The key point in the method is to reduce the size of the light spot on the sample to submicron size while keeping enough photon flux to obtain a good signal-to-noise ratio. In the past several years this technique has been highly developed at high-brightness third-generation synchrotron radiation sources. These experiments used the MAXIMUM microscope in the Advanced Light Source (ALS) in Berkeley.<sup>7</sup> The technique is capable of acquiring chemical and electronic information from a tiny local area so that all investigation of inhomogeneities of sample surfaces can be performed. The measured size of the beam spot is  $0.1 \mu\text{m}$ . Due to a patterned substrate, ELO-grown GaN materials have three different areas, i.e., the window areas between masks (homoepitaxial growth), the areas over the  $\text{SiO}_2$  stripes (lateral overgrowth) and the boundary regions where the growth fronts meet and coalesce. The GaN does not wet the  $\text{SiO}_2$  film. To characterize these materials, photoemission spectromicroscopy with  $\mu\text{m}$  or sub- $\mu\text{m}$  spatial resolution is a suitable technique for mapping these surfaces to obtain their electronic structures. In this article, the experiments have been done on clean surfaces, surfaces exposed to atomic hydrogen, and surfaces covered by about 10 monolayers (ML) of Mg. This article is organized as follows: In Sec. II are details of the experiment. In Sec. III we describe the results and their interpretations. The conclusions are given in Sec. IV.

<sup>a)</sup>Electronic mail: uphg1@gemini.oscs.montana.edu

# MAXIMUM @ ALS

## Beamline 12

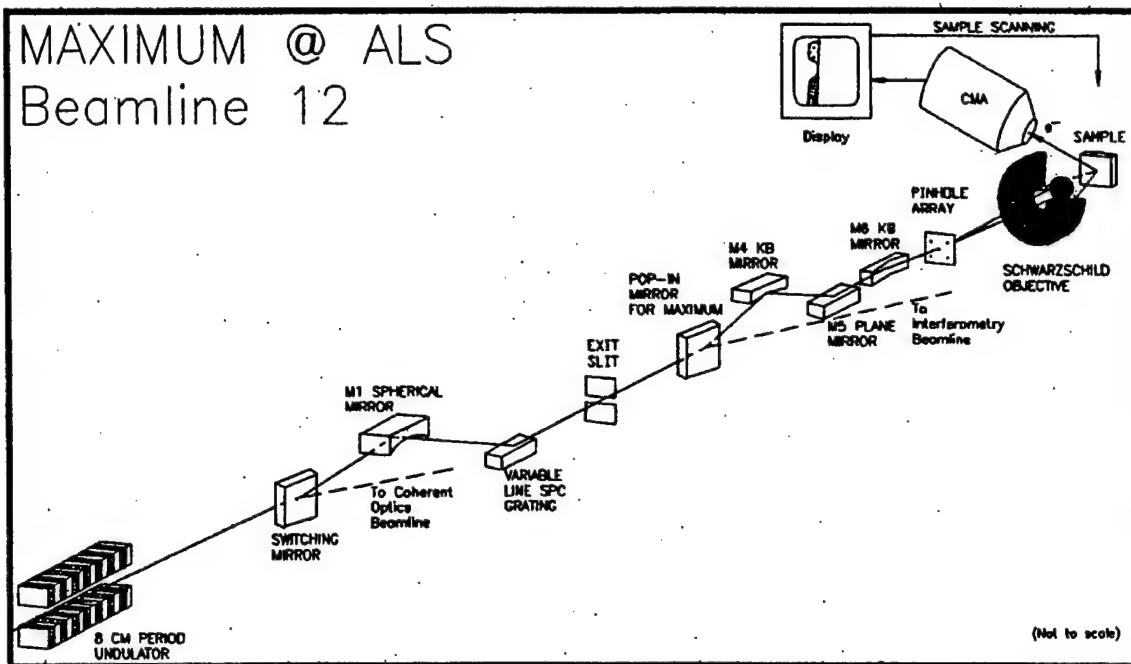


FIG. 1. Schematic layout of the MAXIMUM photoemission microscope and Beamline 12 at the ALS.

## II. EXPERIMENTAL DETAILS

The ELO GaN films used in the experiments were grown on the basal plane of sapphire by MOVPE at North Carolina State University. The first step was to grow a conventional low-temperature ( $\sim 500^\circ\text{C}$ ) buffer layer of GaN on (0001) sapphire followed by the deposition of 1–2  $\mu\text{m}$  of GaN at high temperature ( $\sim 1050^\circ\text{C}$ ). The GaN film contained the typical  $\sim 10^9$ – $10^{10}$  dislocations per  $\text{cm}^2$ . The next step was to make the  $\text{SiO}_2$  pattern by covering the entire wafer with  $\sim 100$  nm of  $\text{SiO}_2$ . Then the window stripes in  $\text{SiO}_2$  were obtained by the conventional photolithography method where etching of the  $\text{SiO}_2$  exposes parallel stripes to clean GaN separated by stripes of  $\text{SiO}_2$ . These stripes were oriented along a {1100} GaN crystal direction. Because of the  $30^\circ$  rotation of the GaN epitaxy on basal-plane sapphire, the GaN stripe length corresponds to the direction of a line drawn from the center of the sapphire wafer that is perpendicular to the {1120} sapphire flat. The window and  $\text{SiO}_2$  stripe widths are 3 and 15  $\mu\text{m}$ , respectively. The resultant substrate was used for final growth of a film of about 7  $\mu\text{m}$ . Homoepitaxy occurs in the window areas with vertical growth. When the slots are filled the film also grows laterally.

The surface morphology of ELO GaN films was characterized by the atomic force microscopy (AFM) technique. The AFM image was taken in contact mode with a TopoMetrix Explore spectroscopic phase modulated scanning probe microscopy (SPM) system.

The photoemission spectromicroscopy investigations were conducted with MAXIMUM on the undulator Beamline 12 at ALS, Berkeley.<sup>8</sup> Figure 1 is a schematic layout of the MAXIMUM microscope. The monochromatic beam is

focused onto a 2  $\mu\text{m}$  pinhole, which is demagnified with a Schwarzschild lens. The 2  $\mu\text{m}$  pinhole gives a sample surface spot size of 0.1  $\mu\text{m}$ . To obtain high reflectivity the surfaces are coated with a multilayer film designed for  $h\nu = 130$  eV. The band pass is quite narrow, so the photon energy is not tunable. Scanning of the sample surface to obtain an image is realized by rastering the sample in a plane (X-Y) perpendicular to the beam. Photoelectrons are detected by a cylindrical mirror analyzer (CMA). The symmetry axis of the CMA is in the plane defined by the sample surface. The polar angle,  $\theta$ , of the emitted electrons varies from  $60^\circ$  to  $90^\circ$ . The sample is oriented so that the CMA “looks” across the stripes resulting in images of the groove with some asymmetry. Data are collected in two modes: (a) the scanning mode where two-dimensional (2D) image is acquired by measuring the photoelectrons at a given kinetic energy, and (b) the microprobe mode where an energy distribution curve (EDC) is acquired at the position of interest. Independent tests show that the beam spot is 0.1  $\mu\text{m}$ .

The samples were cleaned by heating them in an ultrahigh vacuum (UHV) chamber with a recipe used in other studies.<sup>9</sup> The samples were exposed to atomic hydrogen with a typical hot W filament near the sample surface. Magnesium was evaporated from a Ta boat.<sup>9</sup>

## III. RESULTS

### A. Clean surface

The AFM image of the ELO GaN surface (sample M287) is depicted in the  $100 \times 100 \mu\text{m}^2$  image of Fig. 2(a). The lateral growth fronts meet and leave grooves as clearly seen

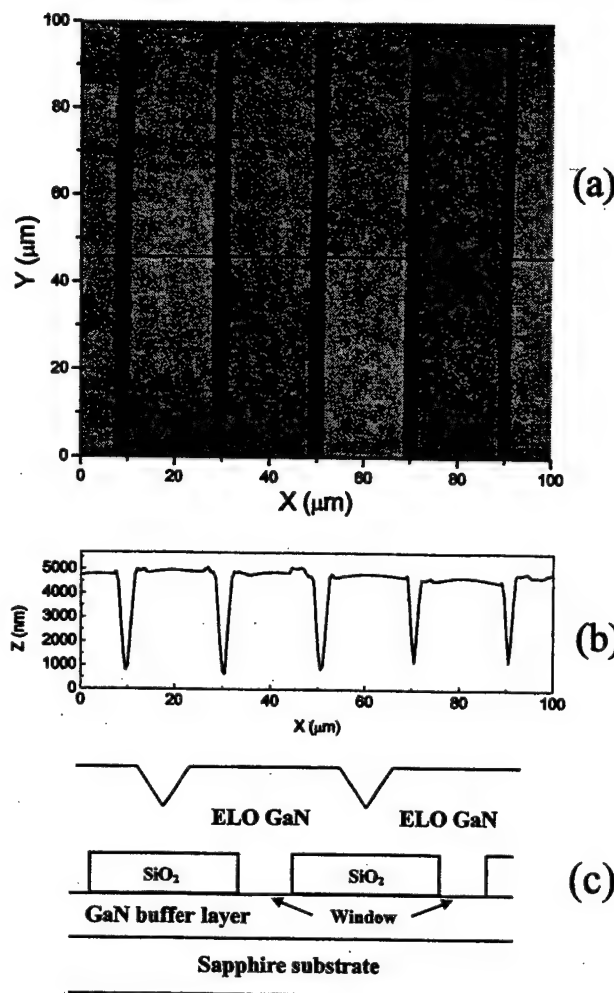


FIG. 2. (a) AFM image of a  $100 \times 100 \mu\text{m}^2$  area of the ELO GaN surface (sample M287). The bright areas represent the flat growth stripes and the dark areas are the fronts where the growth stripes meet. (b) Line profile obtained from the above image at the position marked by the horizontal line across the image. (c) Schematic drawing of the structure of the ELO GaN material.

in the image (dark stripes). The growth fronts have a partial coalescence. Figure 2(b) shows a line profile made across the sample at the location indicated by the horizontal line. Figure 2(c) shows a sketch of the cross section of the ELO GaN. The (0001) surfaces of the GaN stripes are very flat but differ in height from each other. The front-meeting grooves are 4  $\mu\text{m}$  wide and about 4.3  $\mu\text{m}$  deep. The angle between the walls of the fronts that meet and the sample's surface [i.e., the (0001) face] in the line profile is about 65°, which suggests that it is the {1101} plane. The AFM tip used in this measurement is 20°. The growth side wall is {1120} and depends on the growth conditions (the III–V ratio). The inclined walls at the growth-front areas are either in the {1122} or the {1101} facet, which is 50° or 62°, respectively, to the sample's surface. The measured face is attributed to the latter.

The scanning-mode measurement of the photoemission signal with the spectromicroscope is used to obtain an overview of the above sample. Figure 3(a) is the image and Fig.

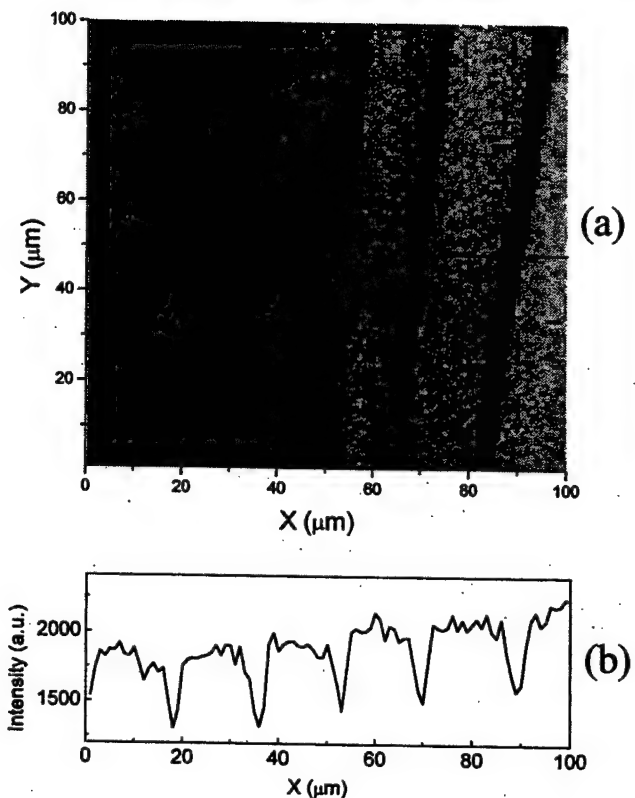


FIG. 3. (a) Photoemission spectromicroscopy image of a  $100 \times 100 \mu\text{m}^2$  area of the ELO GaN surface (sample M287) formed by the signal at the peak of the Ga 3d core-level emission at a kinetic energy of 104.6 eV. In the 2D map, the bright areas represent growth stripes and the dark areas represent the stripes where the growth fronts meet. The CMA detects the electron emission directed to the left. (b) Line profile obtained from the above image at the position of the straight line across the image.

3(b) the line profile. The  $100 \times 100 \mu\text{m}^2$  image is acquired with a step size of 1  $\mu\text{m}$  by recording the signal from Ga 3d core-level emission peak at a kinetic energy of 104.6 eV. In the image, bright areas correspond to stripes of GaN and dark areas are stripes due to the front-meeting grooves. The photoemission signal (PESS) line profile shows the same general features as the AFM results shown in Fig. 2. The PESS has a slightly wider "V" groove than that in the AFM micrograph; they are about 4.2 and 3.6  $\mu\text{m}$ , respectively.

The contrast mechanism producing the spectromicroscopy image is largely due to the angular dependence of the yield and the different orientations of the plateau areas and the valley areas. So the CMA analyzer "looks" at plateau and valley areas from different angles. The photoemission intensity falls off as the horizon is approached and is nominally proportional to  $\cos^2 \theta$  where  $\theta$  is the photoelectrons' takeoff angle. Thus, the CMA will measure different emission intensity from surfaces at different angles. Other contrast mechanisms can be the inhomogeneity of the chemical environment, the electronic structures, etc. In addition to these properties that modulate the emission signal strength, they may also cause kinetic energy shifts that can be monitored.

For better understanding of inhomogeneities of the sample's surface electronic structure, high-spatial-resolution im-

ages are acquired. Then, based on this image, localized EDCs of the Ga 3d core-level emission are obtained by the microprobe mode from different locations on the surface. Figure 4(a) shows a  $30 \times 30 \mu\text{m}^2$  image with a step size of  $0.3 \mu\text{m}$  made with the Ga 3d peak emission at an electron kinetic energy of 104.6 eV. Figure 4(b) is a line profile across the sample surface at the position marked by the arrow where the CMA electron detector is on the left side. The PESS is shown by a gray scale and one can note that the average intensity decreases as the ALS storage ring's stored current decreases, i.e., the scan is from right to left. The curvature in the image is due to drift in the microscope. Localized EDCs for the Ga 3d core level are obtained from the sample at positions labeled (a), (b), and (c) in the image with about a  $0.1 \mu\text{m}$  spot size located at the front-meeting area, lateral overgrowth area, and vertical-growth window area, respectively. The spectra are shown in Fig. 4(c) where the three EDCs are normalized to the same peak intensity. The difference curve "(c)-(b)" is a flat featureless line, which demonstrates the uniformity in surface electronic structures for the vertical-growth window areas and the lateral overgrowth areas. However, curve (a), which is from a front-meeting area shows a shift of 0.15 eV. However, the difference curve "(b)-(a)" is also flat after curves (a) and (b) are lined up. These observations suggest no line shape changes and the shift is attributed to a change in the surface Fermi level position. The surface Fermi level pinning position for the GaN stripes (including the window and overgrowth areas) is about 0.15 eV lower than that for the region where the growth fronts meet.

Photoemission data from another sample (M273) are shown in Fig. 5, which has narrower growth-front grooves. The former sample is used for atomic H adsorption and the latter for Mg adsorption experiments. The Ga 3d EDC set shows the same Fermi level pinning behavior for the front-meeting regions versus the flat stripes. The only difference is that the front-meeting grooves are about  $2 \mu\text{m}$  wide. Note that the flat region near the groove, particularly the right side, has a slightly larger PESS (the white stripe). There is no present explanation for this unless the film "pushes" up a bit next to the coalescence line.

## B. Atomic hydrogen adsorption

The clean ELO GaN surface is exposed to atomic H by the use of a 2000 °C W filament very close (5 cm) to the sample surface. The molecular H<sub>2</sub> dose was about 1000 langmuir. Figure 6(a) illustrates the photoemission spectromicroscopy formed from the peak emission of the Ga 3d level, where the image is  $30 \times 30 \mu\text{m}^2$  with a  $0.5 \mu\text{m}$  step size. The same Ga 3d peak position of kinetic energy, 104.6 eV, is used. Figure 6(b) depicts the line profile taken across the sample at the position marked by the arrow. The sample had to be moved to the preparation chamber for dosing, so the exact sample position is not reproducible. Furthermore, the sample stage in the microscope permits some variation of the angle between the light beam and the sample normal, which is the reason why the signal in Fig. 6(b) has a slope. Com-

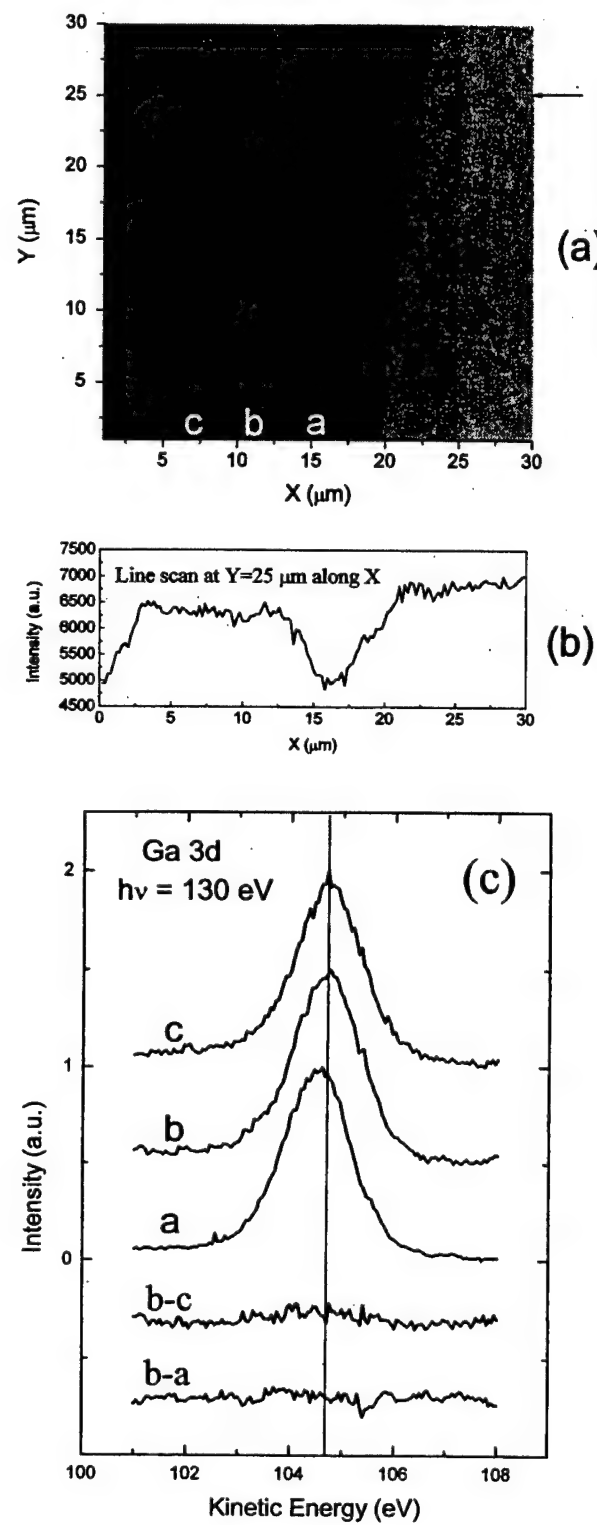


FIG. 4. (a) Photoemission spectromicroscopy image of a  $30 \times 30 \mu\text{m}^2$  area of the ELO GaN surface (sample M287) formed by the signal at the peak position of the Ga 3d core-level emission at a kinetic energy of 104.6 eV. (b) Line profile obtained from the above image at the position marked by the arrow. (c) Ga 3d core-level EDCs collected by the microprobe mode with a  $0.1 \mu\text{m}$  beam spot at positions (a), (b), and (c) shown in the image. The curve "(b)-(c)" is the difference between curves (b) and (c), where one is from vertical growth in the window and the other is from the lateral overgrowth area, respectively. The curve "(b)-(a)" is the difference between curves (b) and (a), which is from a front-meeting region after they are shifted to line up.

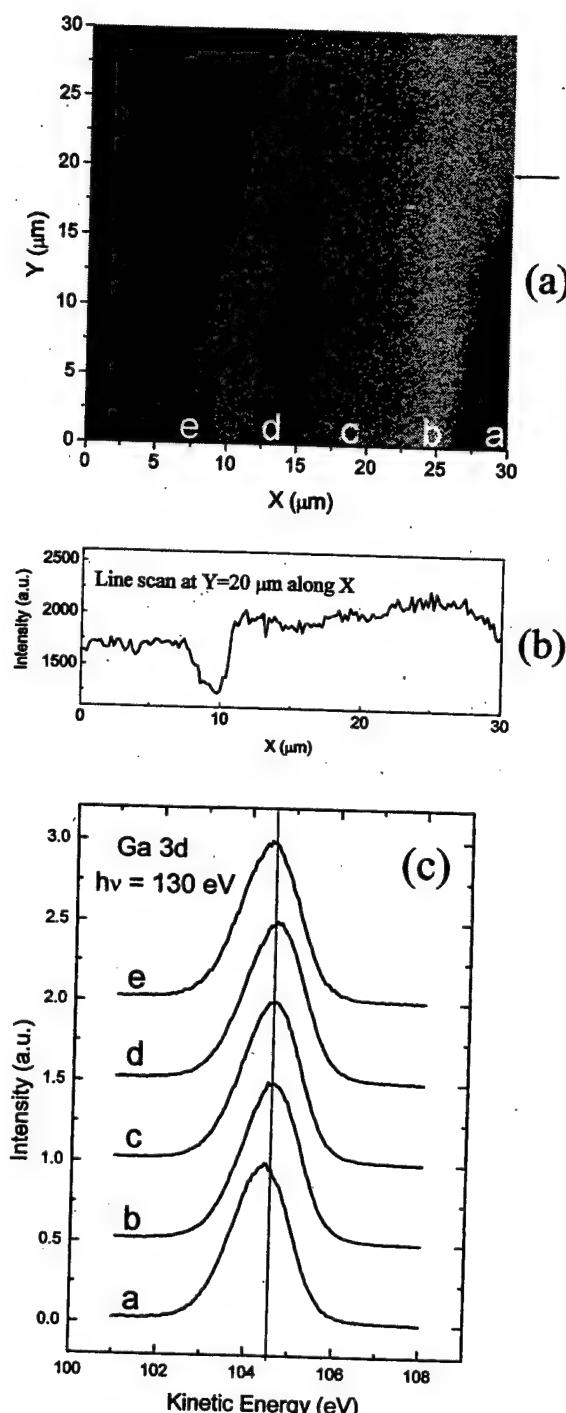


FIG. 5. Scanning mode image (a) with line profile (b) and microprobe Ga 3d EDCs (c) obtained from sample M273. The results are basically the same as those in Figs. 3 and 4 (sample M287) except for the width of the front-meeting stripes which are 2  $\mu\text{m}$  according to the AFM data.

pared with the image and line profile from the clean surface in Fig. 4, the atomic hydrogen exposure causes dramatic changes for the ELO GaN surface. On clean surfaces, the window and overgrowth areas have uniform intensity, and the front-meeting signal looks like a V-shaped groove, which is analogous to the AFM "true" morphology. The ratio of the photoemission signal for the uniform area to the center of the front-meeting minimum is about 3/2. On the H-exposed

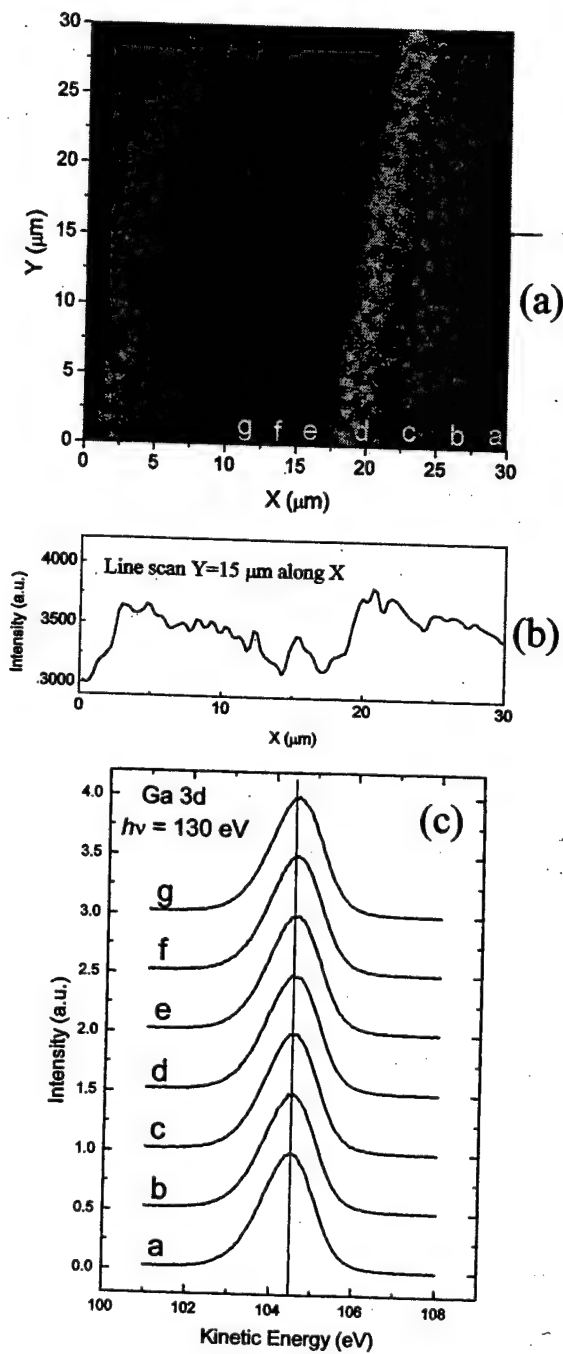


FIG. 6. (a) Photoemission spectromicroscopy image of a 30x30  $\mu\text{m}^2$  area of the ELO GaN surface (sample M287) exposed to atomic hydrogen. It is acquired by collecting the photoelectron signal from the peak of the Ga 3d core-level emission at a kinetic energy of 104.6 eV. (b) Line profile obtained from the above image at the position marked by the arrow. The weakest emission (darkest) stripe is attributed to the bottom of the "V" in the front-meeting region. (c) Microprobe Ga 3d EDCs collected at the position noted by (a)-(g) in the image. All the EDCs are essentially equivalent.

surfaces, the window and overgrowth areas are still rather uniform, but the front-meeting region has a "W" shape. The darkest lines in the image are attributed to the darkest line in the image of the clean surface. The CMA is collecting photoelectrons going to the "left." The ratio of the signal between the "groove" and the uniform region appears to be

close to 1. The photoemission image of the growth-front region has a width of about  $6.5 \mu\text{m}$ . The H appears to increase the emission signal at the groove centers, which face the CMA detector. An interpretation of this is not straightforward, but we suggest that H at the corner portions of the growth-front area increases the emission normal to the emitting surface which is off normal towards the groove with respect to the overall surface normal. This would increase the emission at the right corner and decrease it at the left corner, as observed in the data. If the corner has a weaker slope angle than the groove side wall, one could say that the H peaks the emission in the forward direction and the detector's orientation is such that we see a bigger signal on one side and a smaller one on the other. Another mechanism could be different H adsorption properties for the different crystalline surface and it would not be expected that one side wall would be different from the other side wall.

A set of localized Ga 3d EDC data was taken on a line with a uniform distribution of positions, as shown by the letters in the image shown in Fig. 6(c). Some are from the flat region and some are from the groove. The spectra are essentially all the same shape and at the same energy position, as shown in Fig. 6(c). The peaks are at a kinetic energy of 104.45 eV, which is the same position as the Ga 3d peak from the front-meeting regions for the clean surfaces. The H adsorption shifted peaks from the vertical and lateral growth areas from 104.6 to 104.45 eV (i.e., 0.15 eV). The uniform Fermi level is a bit of a surprise.

### C. Magnesium films

Magnesium was vapor deposited onto a clean ELO GaN surface. About 10 ML on sample M273 gives an image that is quite similar to the one observed for the clean surface; see Figs. 7(a) and 5(a), respectively. As is seen in the line scan of Fig. 7(b) the signal strength ratio for the flat region versus the groove is about 3/2, the value for the clean surface. The result is quite different from the behavior for atomic H exposures. Figure 7(c) shows localized EDCs for the Ga 3d level from the Mg-covered ELO GaN surface taken by the microprobe mode. The curves from points located at positions labeled (a)–(f) show different line shapes and kinetic energy positions. The differences show no obvious relationship with the sample's structure. The differences are attributed to the inhomogeneities in the Mg overlayer thickness on the ELO GaN material. Based on the previous data we have measured for Mg/GaN contacts<sup>9</sup> (done on conventional GaN samples). We found that Mg grows on the GaN surface by Stranski-Krastanov (SK) mode with one or two layers for wetting layer followed by island growth. The EDCs for positions (a) and (e) should be viewed differently than those for other positions since the absorption on crystalline faces in the groove can be different. Notice that the groove images are not uniform, which is again attributed to Mg island formation. If it is also the case for this ELO GaN material, then the photoemission spectromicroscope can "see" either island areas or the between-island areas. These two areas have different Mg coverages and this causes the differences in Ga

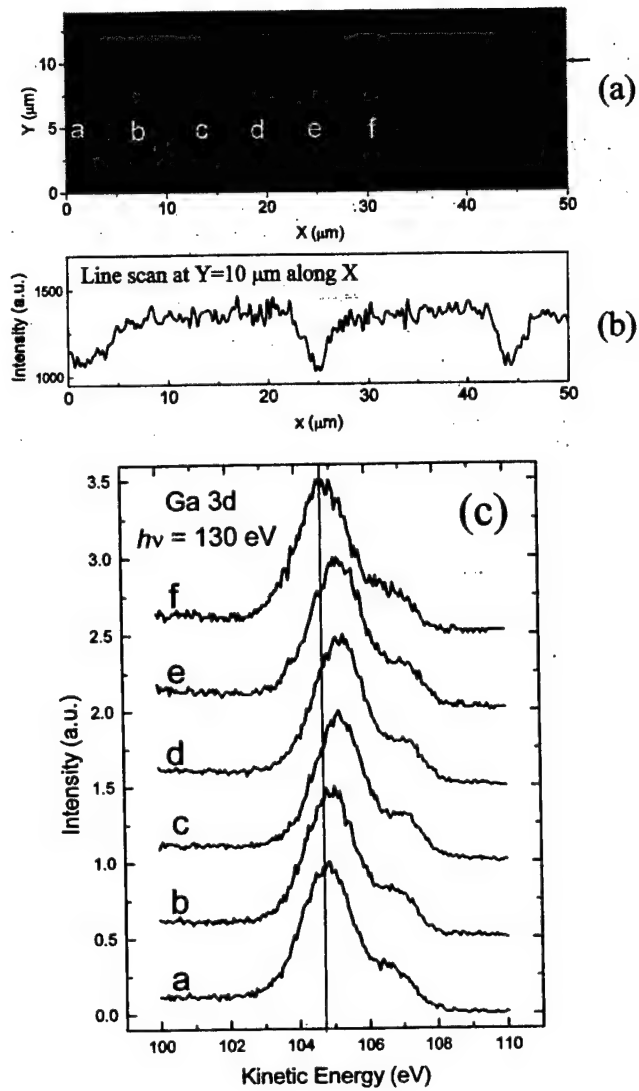


Fig. 7. (a) Photoemission spectromicroscopy image of a  $50 \times 15 \mu\text{m}^2$  area of the ELO GaN surface (sample M287) with a 10 ML equivalent Mg deposition. (b) Line profile obtained from the above image at the position marked by the arrow. (c) Microprobe Ga 3d EDCs collected at the positions from (a)–(f) noted in the image. All the curves have different energy positions that have no apparent relationship to the growth stripes on the film.

3d core-level emission lines. The island areas have a thicker Mg film so Mg-induced band bending can be larger and the Mg/GaN reaction can be more prevalent. As a result, the Ga 3d core level peak shifts to the higher kinetic energy side. For the same reason, if the probe beam spot is on the areas between islands, which have less Mg coverage compared with the islands, the Ga 3d core level will show a smaller energy shift. The small shoulder on the right-hand side of the main peak is attributed to metallic Ga atoms. It forms due to the reaction between GaN and Mg, where Mg atoms replace Ga atoms. The intensity of this shoulder also shows some weak variations in the EDCs from different positions.

### IV. CONCLUSIONS

Photoemission spectromicroscopy has been employed to investigate the inhomogeneities of the surface electronic

structure of ELO GaN films. The PESS image acquired by the scanning mode on the clean surface shows a surface morphology which is similar to that of the AMF image. The contrast mechanism is attributed to the angular dependence of the photoemission yield. While Mg deposition has little effect on the mechanism, atomic H adsorption modifies it. Contrast changes due to the presence of adatoms appear to be quite weak. The relative orientation of the grooves and the CMA shows some differences in the groove areas. Nominally the emission is greater when the groove face is oriented towards the CMA. Localized EDCs for Ga 3d core-level emission taken with the microprobe mode show morphological differences. On the clean surface, the Fermi level pinning position for the front-meeting regions shifts 150 meV compared with the window areas and overgrowth areas. However, the position dependent EDCs showed no difference for vertical growth from the windows and the lateral growth areas.

Hydrogen adsorption induced changes in the image and the EDCs energy position. The front-meeting area showed an increased signal strength for the corner facing the CMA and a decrease of emission from the corner on the other side. This is attributed to H changing the emission direction more toward the local-face normal. Effects due to crystalline face orientation or defect densities, if they exist, were not strong enough to be observed. All the EDCs for the hydrogenated

surface have the same energy position, which is the one measured from the grooves on the clean surface.

The Mg-covered sample has an image quite similar to the clean case, indicating that the crystal orientation effects are weak. The energy dependence of the Ga or Mg EDC peak positions varies a good bit, but with no correlation to the GaN film's striped character. The variation is attributed to island formation in the SK growth mode.

## ACKNOWLEDGMENTS

The help from ALS staff is gratefully acknowledged. This work is supported by ONR DESPCoR. ALS is supported by the DOE.

<sup>1</sup>S. Srtite and H. Morkoç, *J. Vac. Sci. Technol. B* **10**, 1237 (1992).

<sup>2</sup>M. A. Khan, J. N. Kuznia, A. R. Bhattachari, and D. T. Olson, *Appl. Phys. Lett.* **62**, 1786 (1993).

<sup>3</sup>S. Nakamura, T. Mukai, and M. Senoh, *Appl. Phys. Lett.* **64**, 1687 (1994).

<sup>4</sup>F. A. Ponce, *MRS Bull.* **22**, 51 (1997).

<sup>5</sup>Z. Yu, M. A. L. Johnson, T. McNulty, J. D. Brown, J. W. Cook, Jr., and J. F. Schetzina, *Internat J. Nitride Semicond. Res.* **3** (1998).

<sup>6</sup>S. Nakamura *et al.*, *Appl. Phys. Lett.* **72**, 211 (1998).

<sup>7</sup>H. H. Solak, G. G. Loursso, S. Singh-Gasson, and F. Cerrina, *Appl. Phys. Lett.* **74**, 22 (1999).

<sup>8</sup>A. K. Ray-Chaudhuri *et al.*, *J. Vac. Sci. Technol. A* **11**, 2324 (1993).

<sup>9</sup>Y. Yang, S. H. Xu, H. Cruguel, G. J. Lapeyre, J. M. Van Hove, A. M. Wowchak, and P. P. Chow, *Phys. Rev. B* (submitted).

## A KINETIC MODEL FOR THE REMOVAL OF SULFUR FROM POLYCRYSTALLINE TITANIUM SURFACES EXPOSED TO OXYGEN

R. REIBEL, S. SCHNEIDER, H. CRUGUEL, J. LAPEYRE and R. J. SMITH\*  
*Montana State University, Bozeman, MT, USA*

Received 12 September 1999

Recent studies using Auger Electron Spectroscopy (AES) on polycrystalline titanium surfaces led to the discovery of a temperature-dependent phenomenon for the removal of sulfur using oxygen exposures. It was seen that at temperatures greater than 200°C and pressures lower than  $10^{-7}$  Torr O<sub>2</sub> the rate of sulfur removal from the surface was decreased significantly. The decrease in this rate of sulfur removal can be linked to several factors, including the temperature-enhanced diffusion of sulfur to the surface and the temperature-enhanced diffusion of oxygen into the bulk. By varying the pressure of oxygen and the temperature of the substrate and by monitoring the surface with AES we were able to identify the significant factors. A kinetic model for the two surface species is discussed and fit to the experimental results. This kinetic model includes physical parameters for such things as the activation energy for the sulfur diffusion to the surface as well as sticking coefficients for oxygen on the surface. Through this model the relevant factors for the decrease in the rate of sulfur removal are examined.

### 1. Introduction

There has been much interest in polycrystalline titanium films and their abilities to adsorb gasses over the years. Several studies on adsorption,<sup>1,2</sup> especially oxygen adsorption,<sup>3-6</sup> have been done on this surface. In these studies little attention has been paid to the role of contaminants, such as sulfur, in titanium and their effects upon the adsorption of these gasses. In fact contaminants can play a significant role in the sorption of these gasses, as shown in a hydrogen and oxygen adsorption study.<sup>7</sup> Teter showed that sulfur, the major contaminant in titanium, had a significant impact upon the oxidation of polycrystalline titanium at temperatures above 400°C. It was seen that at high temperatures and pressures below  $10^{-7}$  Torr the sulfur played a significant role in reducing the rate of oxidation on titanium. This result could be explained by the segregation of sulfur to the surface at these higher temperatures. It was our intent to expand on the previous experiments and to

show the mechanisms for the reduction of the rate of oxidation when sulfur is segregating to the surface.

### 2. Experimental Setup

The experiments were carried out in the Ion Beams Laboratory at Montana State University in a stainless steel vacuum chamber designed for gas adsorption studies. The chamber is equipped with an Auger Electron Spectrometer with a cylindrical mirror analyzer acquiring in the  $N(E)$  mode. It is also equipped with a UTI quadrupole mass spectrometer, a flood sputter gun, and a system of Varian leak valves. The pressure in the chamber was monitored with an uncalibrated nude ion gauge with an Inficon controller. The base pressure after bakeout was  $10^{-10}$  Torr.

The polycrystalline titanium sample was purchased from Alfa AESAR. The manufacturer claimed a purity of 99.99+. The sample thickness was 0.25 mm. It was spot-welded to a thicker piece of manufacturing quality titanium to keep the sample

\*Corresponding author. Address: Department of Physics, Montana State University, Bozeman, MT 59717, USA.  
E-mail: smith@physics.montana.edu

from deforming during heating. Heating was accomplished with a hot W filament behind the sample to temperatures of 450°C and to higher temperatures by electron beam heating. Temperature measurements were made with a chromel-alumel thermocouple spot-welded to the back of the sample.

The sample was annealed by electron beam heating to 750°C on entry into the vacuum system in order to remove the buildup of carbon and oxygen. The sample was maintained at 750°C for two minutes before each oxygen exposure, allowing the sulfur to segregate to the surface until saturation occurred. Two sets of exposures to O<sub>2</sub> were done at temperatures of 20°C, 200°C, 300°C, 350°C and 400°C. The first set of exposures was with pressures at or below 10<sup>-7</sup> Torr O<sub>2</sub>. The same temperatures were used in the second set. The second set of exposures started with a pressure at or below 10<sup>-7</sup> Torr O<sub>2</sub> for approximately the first 40 langmuirs (1 L = 10<sup>-6</sup> Torr sec). The pressure was then increased to 10<sup>-6</sup> Torr O<sub>2</sub> until saturation of the oxygen signal. This set was done in order to provide a comparison to the lower pressure exposures. In both sets of exposures AES was used to monitor the surface composition. The relative concentrations of species on the surface was then determined using the derivative peak to peak

amplitudes and proper sensitivity factors for the AES spectra. Figure 1 shows typical AES derivative spectra (a) before oxygen exposure and (b) after 387 L of O<sub>2</sub>.

A room temperature exposure of 5 × 10<sup>-8</sup> Torr O<sub>2</sub> was also done in a chamber equipped with X-ray Photoelectron Spectroscopy (XPS) and a hemispherical energy analyzer with normal angle of emission. The sample was prepared and annealed in the same way as the previous experiments. The base pressure in this chamber was 7 × 10<sup>-11</sup> Torr after bakeout. The titanium 2p (BE 2p<sub>1/2</sub> = 460.2 eV, 2p<sub>3/2</sub> = 453.8 eV), the oxygen 1s (BE = 532 eV), and the sulfur LVV (KE = 152 eV), 2s (BE = 230.9 eV) and 2p (BE 2p<sub>1/2</sub> = 163.6 eV, 2p<sub>3/2</sub> = 162.5 eV) transitions were monitored during exposure.<sup>4,8,9</sup> By evaluating the differences in the peak areas of the S LVV Auger transition and S 2p emission we hoped to confirm the desorption of sulfur from the sample surface by oxygen exposures.

### 3. Results and Discussion

In Fig. 2, the relative concentrations of sulfur and oxygen for the room temperature exposures are plotted as a function of exposure (L). Figure 2(a) shows

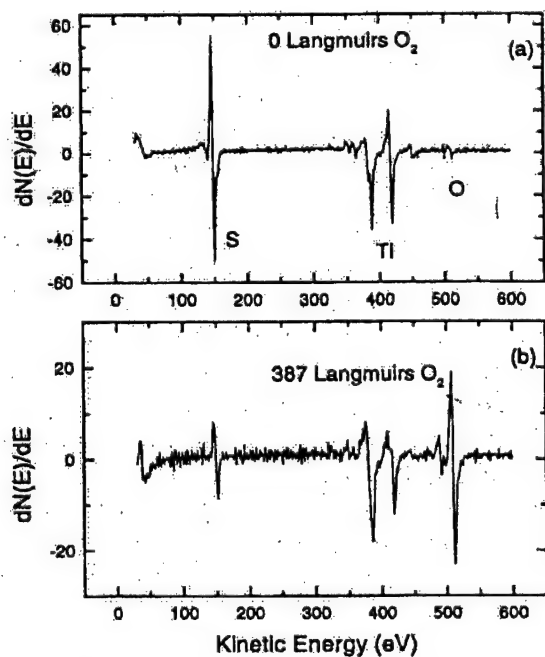


Fig. 1. Typical AES derivative spectra (a) before oxygen exposure and (b) after 387 L of O<sub>2</sub>.

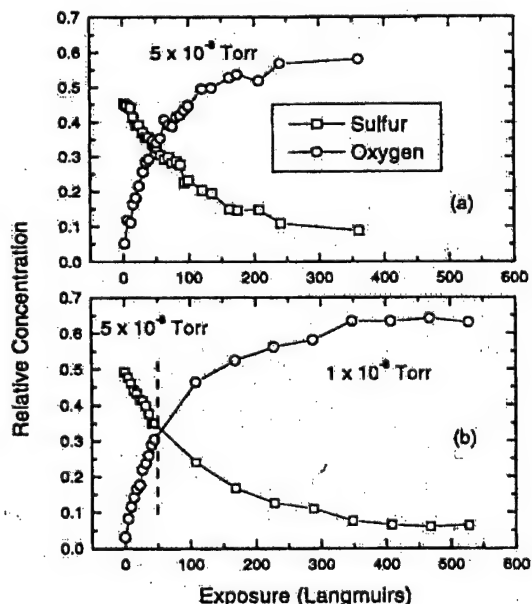


Fig. 2. Oxygen and sulfur concentration vs. exposure (L) of O<sub>2</sub> at 20°C. (a) 5 × 10<sup>-8</sup> Torr O<sub>2</sub>, (b) 5 × 10<sup>-8</sup> Torr O<sub>2</sub> for first 50 L, then 10<sup>-6</sup> Torr O<sub>2</sub> until saturation of oxygen.

the  $5 \times 10^{-8}$  Torr O<sub>2</sub> exposure, and Fig. 2(b) shows the combination exposure, starting at  $5 \times 10^{-8}$  Torr and then switching to  $10^{-6}$  Torr O<sub>2</sub>. Both plots exhibit the removal of sulfur during the exposure and the rapid and complete saturation of oxygen on the surface. By comparing (a) and (b) we see that there is no pressure dependence in the room temperature exposures.

At the higher temperature exposures a dramatic reduction in the rate of sulfur removal and the rate of oxidation occurs. In Fig. 3, the relative concentration of sulfur and oxygen for the 350°C exposures are plotted as a function of exposure (L). Figure 3(a) shows the  $10^{-7}$  Torr O<sub>2</sub> exposure, and Fig. 3(b) shows the combination exposure starting at  $10^{-7}$  Torr and then increasing to  $10^{-6}$  Torr O<sub>2</sub>. By comparing the low pressure plot at 350°C, Fig. 3(a), to the room temperature low pressure plot, Fig. 2(a), we notice that the sulfur concentration drops much slower, and the oxygen concentration increases much slower. This effect can be attributed to the increase in sulfur segregation to the surface at 350°C, or to the well-documented reduction in the sticking coefficient of oxygen at higher temperature.<sup>2</sup> But by comparing the low and high-pressure exposures

at 350°C, Figs. 3(a) and 3(b), we notice a definite pressure dependence to the exposures.

This pressure dependence at higher temperatures can be accounted for by postulating that the sulfur and oxygen are competing surface species. At low pressures of O<sub>2</sub> the rate of sulfur segregating to the surface from the bulk, and the rate of impingement of oxygen from vacuum are similar. However, at higher pressures of O<sub>2</sub>, the rate of oxygen impingement has increased to the point where it greatly wins out in the competition for surface sites. In Fig. 4, the 350°C concentrations are again plotted, this time as a function of exposure time (seconds) to show this increased rate of oxygen impingement upon the surface. Figure 4(a) shows the low-pressure plot, again demonstrating the slow removal of sulfur and slow oxygen increase. In Fig. 4(b) the combination exposure is plotted. Once the exposure is increased to  $10^{-6}$  Torr it is obvious that the rate of oxygen impingement has increased on the surface, thus quickly dominating the slower sulfur segregation to the surface.

Finally, the question arose as to whether the sulfur was really being removed by the oxygen exposures

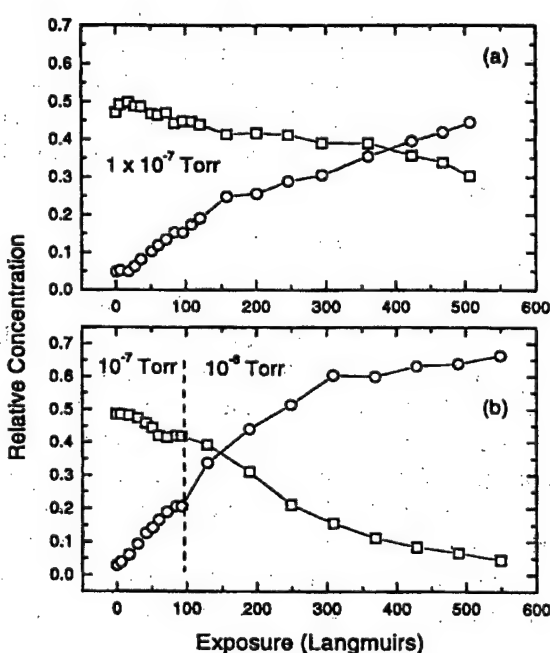


Fig. 3. Oxygen and sulfur concentration vs. exposure (L) of O<sub>2</sub> at 350°C. (a)  $10^{-7}$  Torr O<sub>2</sub>, (b)  $10^{-7}$  Torr O<sub>2</sub> for first 100 L, then  $10^{-6}$  Torr O<sub>2</sub> until saturation of oxygen.

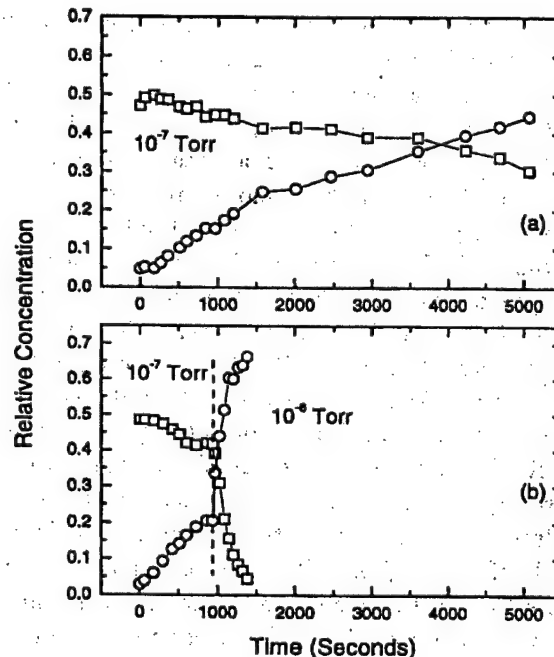


Fig. 4. Oxygen and sulfur concentration vs. time (seconds) at 350°C. (a)  $10^{-7}$  Torr O<sub>2</sub>, (b)  $10^{-7}$  Torr O<sub>2</sub> for first 100 L, then  $10^{-6}$  Torr O<sub>2</sub> until saturation of oxygen.

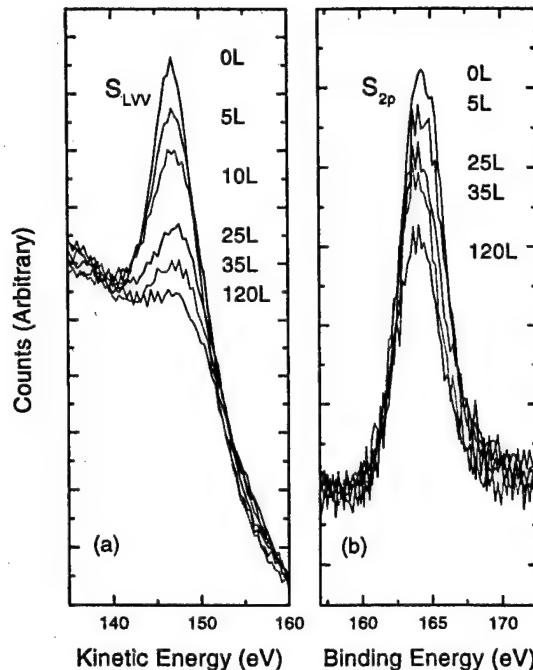


Fig. 5. (a) The S LVV Auger transition and (b) S 2p XPS peak at various stages during a  $5 \times 10^{-8}$  Torr  $O_2$  exposure monitored with XPS.

or was being covered by the oxide layer forming over the sulfur on the surface. Since the kinetic energies of the outgoing electrons in the XPS experiment are different for the S LVV and S 2p transitions, 152 eV and 1323 eV respectively, the S LVV transition is certainly more surface-sensitive. In Fig. 5, (a) the S LVV Auger transition and (b) the S 2p emission are plotted for various oxygen exposures. It is apparent that the S LVV peak drops more rapidly than the S 2p peak. Figure 6 details the normalized peak areas for the S LVV peak and the S 2p peak as a function of exposure ( $L$ ). Notice that the overall drop for the S 2p peak is 35% compared to 50% for the S LVV Auger transition. One interpretation of this data is that since both peaks drop, and since the S LVV Auger peak drops more quickly, the sulfur is being removed from the sample by the oxygen. However, it is important to note that quantitative analysis cannot be done without knowing the depth profile of the original sulfur concentration. Experiments to gain this depth profile are being planned and will appear in a future publication. The other XPS peaks that were monitored during the exposure followed the same trends as in other oxidation experiments in the literature (see for instance Azoulay et al.<sup>4</sup>).

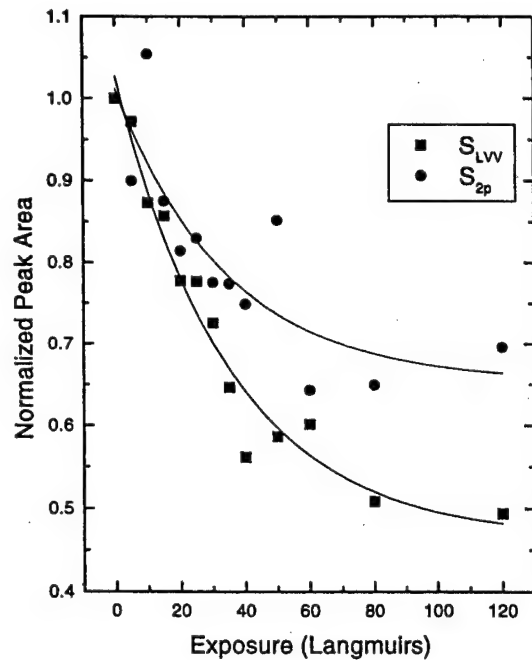


Fig. 6. Normalized S LVV and S 2p peak areas as a function of exposure ( $L$ ).

#### 4. Kinetic Modeling

A model was developed and fit to the AES data to help clarify the mechanisms for the reduction in the rate of sulfur removal and oxidation at the higher temperatures. First it was noted that the oxygen intensity appeared to be following a standard two-site Langmuir adsorption model.<sup>10</sup> So the kinetics for the oxygen were fit fairly well with a Langmuir kinetic model given in Eq. (1).

$$d\theta_o/dt = (2\Gamma S_o/N_o) \cdot (1 - \theta_o)^2. \quad (1)$$

Here  $\theta_o$  is defined to be the normalized surface concentration of oxygen as seen by AES,  $S_o$  is the sticking coefficient of adsorption,  $\Gamma$  is the flux given by  $p/(2\pi m k_B T)^{1/2}$ , where  $p$  is the pressure, and  $N_o$  is the maximum number of surface sites available to the oxygen. If sulfur in any way affected the oxygen adsorption it would show up in the  $S_o$  term in essentially the same way as temperature is known to affect this term. The rate for sulfur removal from the surface was fit with two terms defined in Eq. (2).

$$d\theta_s/dt = v(1 - \theta_s)(1 - \theta_o)^2 - k\theta_s. \quad (2)$$

Here  $\theta_s$  is the normalized surface concentration of sulfur as seen by AES. The first term is a growth

term for sulfur at the surface and suggests that in order for sulfur to segregate to the surface it requires an empty site surrounded by two empty oxygen sites. The second term in (2) is a typical first order desorption term. It could be argued that the desorption term should not appear as a first order term since the desorption should be in the form of  $\text{SO}_2$ . However, non-first-order terms did not fit the data well whereas the linear term seemed to fit well. From first principles, it might be expected that  $v$  and  $k$  both follow Boltzmann factors (3) and (4) due to the thermally enhanced diffusion and desorption respectively. However,  $k$  might also have an oxygen pressure dependence as well as a temperature-dependent reaction rate for the production of  $\text{SO}_2$ .

$$v = v_0 \exp(-E_v/k_B T), \quad (3)$$

$$k = k_0 \exp(-E_k/k_B T). \quad (4)$$

Figure 7 shows the fit for the  $300^\circ\text{C}$   $10^{-7}$  Torr  $\text{O}_2$  exposure. Good agreement was found with the model for the  $300$ ,  $350$  and  $400^\circ\text{C}$  temperatures. The room temperature and  $200^\circ\text{C}$  exposures fit well to the model but the coefficients did not compare well

with the higher temperature data. This could be associated with the differences in pressures between the low temperature and high temperature data ( $5 \times 10^{-8}$  Torr for  $20$  and  $200^\circ\text{C}$  and  $10^{-7}$  Torr for  $300$ ,  $350$  and  $400^\circ\text{C}$ ).

Table 1 details the results of the fits for  $S_o$ ,  $v$  and  $k$  for  $300$ ,  $350$  and  $400^\circ\text{C}$ . It can be seen that the coefficient for the oxygen term defined in (1) decreases as the temperature is raised. Using a value for the maximum number of sites ( $N_o = 1.17 \times 10^{15}$  sites  $\cdot \text{cm}^{-2}$ ) taken as an average from Azoulay *et al.*,<sup>4</sup> we find the dependence of  $S_o$  as a function of temperature also given in Table 1. The result for  $S_o$  of  $2.19 \times 10^{-2}$  at  $300^\circ\text{C}$  is significantly lower than that

Table 1. Results for the terms in the kinetic model for the high temperature  $10^{-7}$  Torr  $\text{O}_2$  exposures. The  $S_o$  column was calculated using a fixed value for  $N_o = 1.17 \times 10^{15}$  sites  $\cdot \text{cm}^{-2}$ .

Temperature ( $^\circ\text{C}$ )	$2\Gamma S_o/N_o \times 10^{-4}$	$S_o \times 10^{-3}$	$v \times 10^{-4}$	$k \times 10^{-4}$
300	14	21.9	5.5	3.0
350	3.4	5.3	8.0	1.5
400	0.8	1.2	9.1	1.7

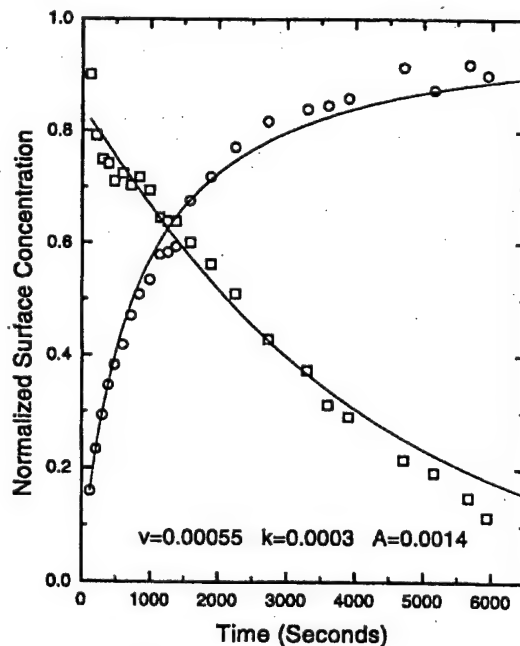


Fig. 7. Normalized oxygen and sulfur surface concentrations for the  $300^\circ\text{C}$   $10^{-7}$  Torr  $\text{O}_2$  exposure. The lines indicate the best fits to the experimental data according to the kinetic models given by Eqs. (1) and (2).

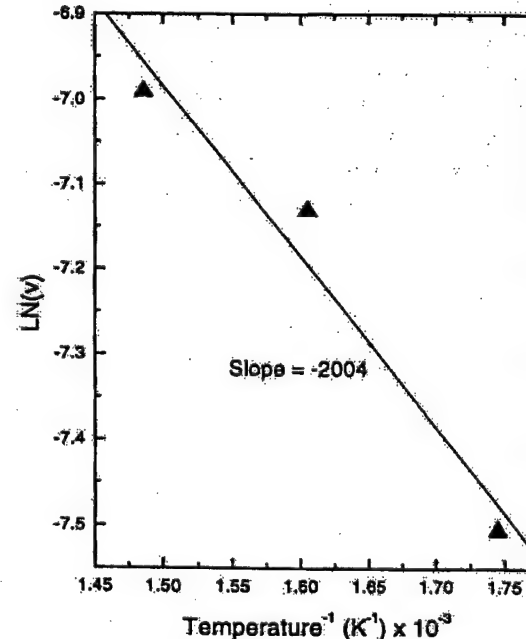


Fig. 8. Arrhenius plot of the sulfur growth parameter  $v$ . The slope is  $-2004$ , giving a value for  $E_v$  of  $4.0$  kcal/mole.

found by Biryukova ( $S_o = 0.67$ ).<sup>2</sup> This suggests that the sulfur is significantly impacting the sticking of the oxygen to the surface. This indicates that the sulfur segregation is playing a strong role in the kinetics at low pressures in the oxidation of titanium.

Figure 8 is an Arrhenius plot of the sulfur growth parameter  $v$ . The slope gives a value for  $E_v$  of 4.0 kcal/mole. This value is down by a factor of 4 from others in the literature.<sup>11</sup> The initial saturated surface condition and the higher concentrations of sulfur near the surface due to this initial state could contribute to this lower value. Finally, the values for  $k$  do not follow a Boltzmann factor and instead decrease as temperature increases. This suggests that the rate of sulfur removal by oxygen decreases as temperature is increased. The enhanced diffusion of oxygen into the bulk at high temperatures<sup>1</sup> could easily explain this result.

## 5. Conclusions

The presence of sulfur on the surface of polycrystalline titanium has a significant impact upon the oxidation. It was shown that at high temperatures and pressures below  $10^{-7}$  Torr O<sub>2</sub> the sulfur segregation to the surface greatly reduces the sticking coefficient of oxygen on the surface. The pressure dependence of the rate of oxidation detailed in Fig. 3 proves that it is this segregation of sulfur to the surface that is reducing the rate of oxidation. A kinetic model fit to the data gave an activation energy for sulfur diffusion of 4.0 kcal/mole. Even though this value is low compared to other values in the literature, it again shows the increased sulfur segregation to the surface at higher temperatures. XPS data shows a

rapid decrease in the S LVV peak as compared to the S 2p peaks. This result seems to indicate that the oxygen removes some sulfur from the surface instead of growing an oxide layer over the top of the initial sulfur concentration.

## Acknowledgments

The authors are pleased to acknowledge the technical support of Erik Andersen and Norm Williams. Special thanks to Yong-Wook Kim for his wisdom and guidance and to S. L. Smith for her encouragement and patience. Work supported by the National Science Foundation under Grant DMR-9710092, and by NASA EPSCoR Grant NCCW-0058.

## References

1. Y. Fukuda, G. M. Lancaster, F. Honda and J. W. Rabalais, *J. Chem. Phys.* **69** (8), 3447 (1978).
2. D. J. Harra, *J. Vac. Sci. Technol.* **13**, 471 (1976).
3. Z. Tass, G. Horvath and V. K. Josepovits, *Surf. Sci.* **331-333**, 272 (1995).
4. A. Azoulay, N. Shamir, E. Fromm and M. H. Mintz, *Surf. Sci.* **370**, 1 (1997).
5. I. Vaquila, M. C. G. Passeggi Jr. and J. Ferrón, *Surf. Sci. Lett.* **292**, L795 (1993).
6. I. Vaquila, M. C. G. Passeggi Jr. and J. Ferrón, *Appl. Surf. Sci.* **93**, 247 (1996).
7. M. Teter, thesis (Montana State University, 1997).
8. J. A. Bearden and A. F. Burr, *Rev. Mod. Phys.* **39**, 125 (1967).
9. M. Cardona and L. Ley, *Photoemission in Solids I: General Principles* (Springer-Verlag, Berlin, 1978).
10. J. W. Davenport, G. J. Dienes and R. A. Johnson, *Phys. Rev.* **B25**, 2165 (1982).
11. R. A. Outlaw, W. S. Lee, S. J. Hoekje and S. N. Sankaran, *Appl. Surf. Sci.* **81**, 143 (1994).

## Photoelectron Diffraction Imaging for $C_2H_2$ and $C_2H_4$ Chemisorbed on Si(100) Reveals a New Bonding Configuration

S. H. Xu,<sup>1</sup> M. Keeffe,<sup>1,\*</sup> Y. Yang,<sup>1</sup> C. Chen,<sup>1,†</sup> M. Yu,<sup>1,‡</sup> G. J. Lapeyre,<sup>1</sup> E. Rotenberg,<sup>2</sup> J. Denlinger,<sup>2,§</sup> and J. T. Yates, Jr.<sup>3</sup>

<sup>1</sup>Department of Physics, Montana State University, Bozeman, Montana 59717-3840

<sup>2</sup>Advanced Light Source, LBNL, Berkeley, California 94720

<sup>3</sup>Surface Science Center, Departments of Chemistry and Physics, University of Pittsburgh, Pittsburgh, Pennsylvania 15260  
(Received 9 February 1999; revised manuscript received 1 October 1999)

A new adsorption site for adsorbed acetylene on Si(100) is observed by photoelectron imaging based on the holographic principle. The diffraction effects in the carbon 1s angle-resolved photoemission are inverted (including the small-cone method) to obtain an image of the atom's neighboring carbon. The chemisorbed acetylene molecule is bonded to four silicon surface atoms. In contrast to the  $C_2H_2$  case, the image for adsorbed  $C_2H_4$  shows it bonded to two Si surface atoms.

PACS numbers: 68.35.Bs, 42.40.-i, 61.14.-x

In a surprising contradiction to the existing literature, the adsorption site for acetylene at saturation coverage was observed to be different from that of ethylene. The adsorption sites for chemisorbed ethylene,  $C_2H_4$ , and chemisorbed acetylene,  $C_2H_2$ , on the (100) face of silicon have been directly observed using photoelectron holographic imaging. In this recently developed technique, photoelectron diffraction intensities are measured and then inverted, to directly obtain the local three-dimensional environment of the emitting atoms [1,2]. The small-cone inversion technique is used [1]. This study is believed to be the first photoelectron holographic study of a multiatomic adsorbate. No model calculations were used in the adsorption site determination. An understanding of the bonding of the ethylene and acetylene molecules provide a foundation for understanding the adsorption behavior of complex unsaturated organic molecules. The carbon-carbon double bond or triple bond in a hydrocarbon molecule may be used to "fasten" the molecule to the Si(100) surface. Such molecules could have a broad range of functions, which have interesting and important applications [3]. Such species are also important in the science of carbide formation.

The ethylene adsorption site found here agrees with the previously reported site, but the acetylene adsorption site was determined to be different. Identical adsorption sites for the two molecules have been reported based on the results of high-resolution electron-energy-loss spectroscopy [4], photoemission spectroscopy [5], scanning tunneling microscopy [6], and near-edge x-ray-adsorption fine structure (NEXAFS) [7], and also in theoretical studies [8]. The experimentally determined image for adsorbed  $C_2H_4$  shows it bonded to the dangling bond of two silicon surface atoms. In contrast, the image for adsorbed  $C_2H_2$  shows bonding to four silicon surface atoms, while retaining one C-C type bond as does chemisorbed  $C_2H_4$ .

Photoelectron diffraction occurs when the direct wave from an emitter (carbon) interferes in the far field with a wave from the scatterers (silicon). The method of obtaining an image from the data has been published [1]. The

angle-resolved emission strength for the emitter's core level of interest is measured for a range of incident photon energies. Since the initial energy for the core level is a constant, the resultant spectrum is a constant-initial-energy spectrum (CIS) [9]. Representative CIS spectra are shown in Fig. 1. The first step is the separation in the CIS spectrum,  $I_k(k)$ , of the diffractive portion from the background,  $I_{k0}(k)$ , and an example background (dotted line) is shown. The diffractive portion of the experimental spectrum is extracted using  $\chi_k(k) = I_k(k)/I_{k0}(k) - 1$ . EXAFS uses a similar  $\chi$  function and the present method may be called vectorized EXAFS. The data are inverted to obtain an image function [10]:

$$U(\mathbf{R}) = \left| \sum_{\mathbf{k}} \int_{k_{\min}}^{k_{\max}} \chi_{\mathbf{k}}(k) e^{-ik\mathbf{R}(1-\mathbf{k}\cdot\mathbf{R})} dk \right|. \quad (1)$$

The inversion is based on the holographic principle and  $\mathbf{R}$  denotes a direct-space position vector with its origin at the emitter. It is important to first do the transform against wave numbers. The small-cone method is used in the sum over the angles which minimizes artifacts [1]. The position of a given atom is given by the local maximum in  $U(\mathbf{R})$  and its centroid is used in the determination of interatomic distances. The precision of the numerical results may be distorted by as much as one- or two-tenths of an angstrom [1,2,10].

Strictly speaking, the wave from each of the numerous emitters on the surface forms an internal-source holographic image. The atomic image obtained comes from many reference waves. Each emitter's signal is incoherent with respect to the other emitters, so the image intensities from each emitter are summed by simple addition. The image resulting from each individual emitter, however, has the same origin in the inverted aggregate image, so the expression "holographic image" is a more liberal usage of the term. In the case of a single site adsorbate, where each adsorbate emitter atom has an identical local geometry, the assignment of peaks in the image is straightforward. When

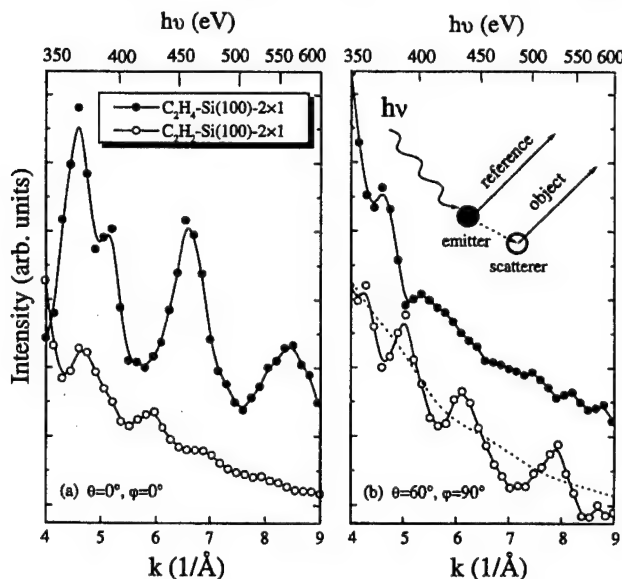


FIG. 1. Photon-energy dependent CIS of the C 1s emission strength from  $\text{C}_2\text{H}_4$  and  $\text{C}_2\text{H}_2$  adsorbed on Si(100) where the lower axis is the electron's wave number and the upper is photon energy proportional to the wave number squared. The emission directions are in polar coordinates;  $\theta = 0$  is normal emission. The interference effects are different for the two species with the immediate implication that each is in a different adsorption site.

there are two emitters in inequivalent adsorption sites, the resultant image for the pair of atoms is akin to a double-exposed photograph. The atomic structure may be obtained through reduction of the image by examination of the image in light of other information regarding the molecular structure of the adsorbate, the bulk crystal structure of the substrate, etc. This is important for the present study since both of the chemisorbed species have two carbon-atom emitters with the carbon atoms in inequivalent locations in the surface unit cell. If some of the adsorbed molecules were in different adsorption sites, they also would make their additive contribution to the experimental image. If the concentration of these molecules were small, it would be difficult to differentiate their image features from artifacts associated with the image of the molecule in the dominant adsorption site.

The Si(100) surface is reconstructed and composed of rehybridized silicon atoms referred to as dimers. Each atom of the dimer pair also has a dangling bond which is very reactive. The surface structure is  $2 \times 1$  and a single domain stepped surface is obtained when the Si substrates are miscut by  $\sim 3.5^\circ$ . The adsorbate coverage was near saturation for both cases. Low-energy electron diffraction was used to determine the direction of the step edge and the direction of the dimer bond.

The data were collected at beam line 7 at the Advanced Light Source at the Lawrence Berkeley Laboratory, one of only a couple of beam lines that can do this imaging. Incident photon energies of  $\sim 350$ – $600$  eV were used to probe the C 1s core level corresponding to a range in wave number  $k$  of  $\sim 4$ – $9 \text{ \AA}^{-1}$ . About 80 CIS were collected

on a grid covering one-fourth of the emission hemisphere, which is an irreducible symmetry element of the surface.

To facilitate the presentation of the experimental images, three-dimensional ball-and-stick models of the determined adsorption sites for  $\text{C}_2\text{H}_4$  and  $\text{C}_2\text{H}_2$  are shown in Fig. 2. The balls are arranged according to the directly determined atomic locations, except for H which is not detected. In the case of ethylene, carbon atoms in the molecule sit above the surface silicon dimer so that the C-C bond and the Si-Si bond axes are parallel; the bar represents the dimer bond. In the case of acetylene, the carbon atoms in the molecule sit between two silicon dimer pairs, above the dimer plane.

A planar vertical cut from the experimental image function  $U(X, Y, Z)$  obtained for the chemisorbed ethylene species is shown in Fig. 3. To aid in recognizing the individual atoms, the cut is accompanied by a ball-and-stick construction for the image. When viewing the experimental image function, it is important to realize that the emitter does not see itself but is always located at the origin (0, 0, 0) of the three-dimensional image. The double peak, Si(1), is observed and corresponds to the first layer silicon atoms. The lower-intensity features located between the origin and the first layer Si peaks are attributed to artifacts.

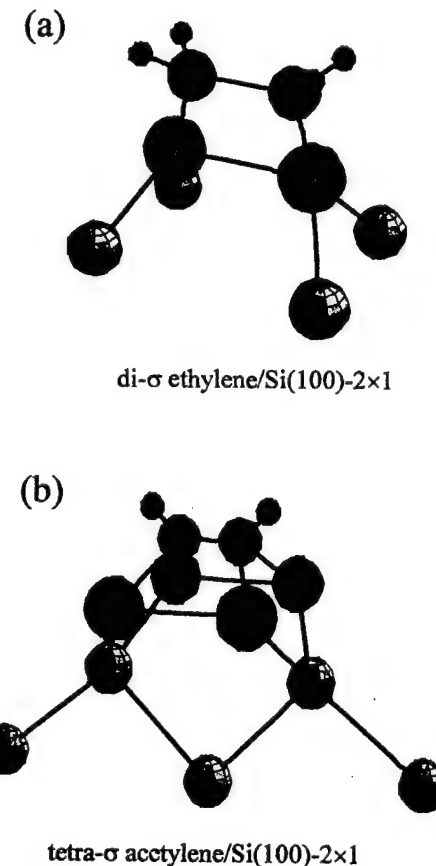
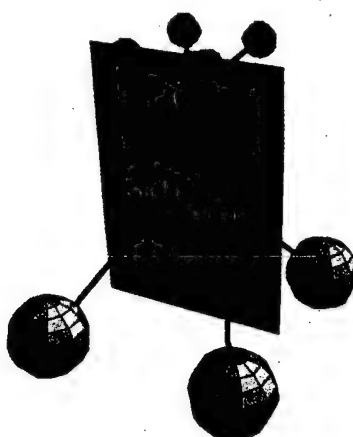
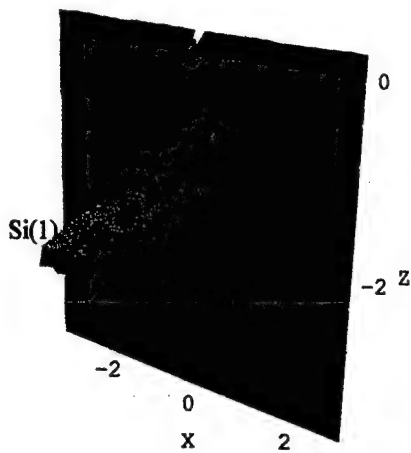


FIG. 2 (color). Ball-and-stick sketches of the Si(100) adsorption sites for (a)  $\text{C}_2\text{H}_4$  and (b)  $\text{C}_2\text{H}_2$  showing two and four Si neighbors, respectively. The big green balls: C; the orange balls: first layer Si; the pink balls: second and third layer Si. The small green balls added in the likely positions for the H atoms.



To relate to the earlier ball-and-stick model of the atomic structure in Fig. 2(a), consider that the ball representing the carbon emitters is not one atom but two superimposed carbon atoms. Now imagine shifting the carbon balls in Fig. 2(a), representing the emitting carbon atoms of the atomic-model sketch, towards each other along the line joining them, until they coincide. The resulting ball-and-stick construction is that shown with the image in Fig. 3. This shift represents the C-C bond length. Note that the separation (0.6 Å) in the double peak is not an interatomic distance but is the difference between the C-C bond length and the Si-Si dimer bond length [11].

A preview of the chemisorbed acetylene result is given before the image is discussed. Its interpretation is more involved since  $U(\mathbf{R})$  shows peaks for atoms in the second and third layers. First, it is shown that the  $\text{C}_2\text{H}_2$  chemisorption site is such that the molecule does not sit directly over the first layer Si atoms. Instead the molecule is over the second and third layer Si atoms which by virtue of the crystal structure means that the  $\text{C}_2\text{H}_2$  adsorbed molecule has four Si atoms for neighbors in the first layer. Second, the image contains a third layer Si(3) atom signal that allows one to reduce the double image and to obtain a value for

FIG. 3 (color). Vertical  $X$ - $Z$  cut at  $Y = 0$  through the chemisorbed  $\text{C}_2\text{H}_4$  image function whose intensity is in the third dimension. Both carbon emitters are at the origin, marked with a "+" sign.  $X$  is the Si-Si dimer direction. The image has to be reduced to get the atomic structure in Fig. 2(a). The image shows a strong doublet for two first-layer silicon atoms (depth 1.8 Å and horizontal separation 0.6 Å) whose actual separation is that observed in the image plus the C-C separation (see text).

the C-C bond length as well as the first layer Si-Si distance [11].

Figure 4 shows a vertical cut from the chemisorbed acetylene image. The strongest features in  $U(\mathbf{R})$  are the two peaks located under the emitters at  $Z = -1.6$  Å which are due to the second layer Si(2) atoms. The third layer silicon atoms Si(3) at  $Z = -3.0$  Å also have quite evident peaks. The image clearly shows that the carbon emitters are in the vertical plane containing the second and third layer atoms, which means they are not "directly" above the first layer Si atoms. Presumably, this is why the carbon emission is strongly scattered by the deeper Si atoms. In a manner analogous to the above  $\text{C}_2\text{H}_4$  image discussion, separation of the carbon atom in the ball-and-stick *image* construction shown in Fig. 4 will give the ball-and-stick atomic structure *model* shown in Fig. 2(b). The most important finding is that the acetylene molecule has four first layer Si atoms as nearest neighbors (two Si dimers).

A curious and significant feature due to the "double exposed" nature of the image allows a determination of the C-C distance for adsorbed  $\text{C}_2\text{H}_2$ . The twin peak at  $Z = -3.0$  Å is actually due to a SINGLE silicon atom Si(3) in the third layer of Si atoms. In the image, this atom

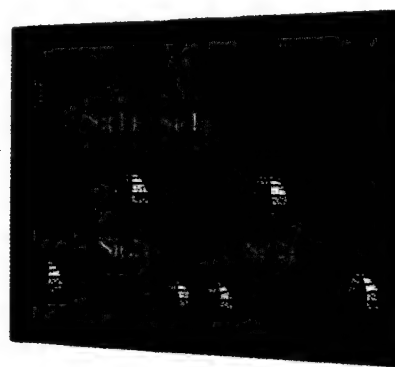
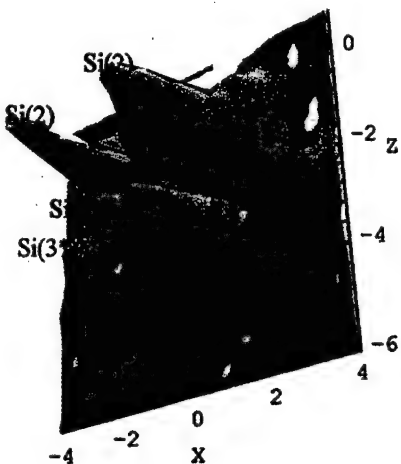


FIG. 4 (color). Vertical planar  $X$ - $Z$  cut at  $Y = 0$  through the chemisorbed  $\text{C}_2\text{H}_2$  image function whose intensity is in third dimension. The carbon emitters (origin) are in the plane. The two strong peaks in the image are second-layer Si(2) atoms and just below them are the peaks for third-layer Si(3), where Si(2) and Si(3) have vertical depths of 1.6 Å and 2.8 Å, and horizontal separations of 3.0 Å and 1.1 Å, respectively.  $X$  is the dimer direction.

is being "seen" by both of the inequivalent carbon emitters in the molecule but each emitter's image has the same origin so Si(3) appears twice in the image. As discussed above for the relationship between the ball-and-stick constructions for the image and for the atomic-structure model, one can imagine collapsing the carbon atoms in Fig. 2(b) along their bond direction until the carbon atoms are superimposed. This manipulation makes two balls from the single ball that represents the third layer Si atom Si(3) in Fig. 2(a). The image shows two such peaks and their distance of separation of 1.2 Å gives the interatomic distance between the two carbon emitters in the adsorbed C<sub>2</sub>H<sub>2</sub> molecule. That is, the image itself (Fig. 4) contains the numerical information needed to reduce the double exposed image to the atomic structure [Fig. 2(b)] [12].

Now, examine the strongest image peaks in Fig. 4 due to the second layer Si atoms. The true interatomic distance (reduced image) between the second layer Si atoms is the sum of the distance between the peaks, Si(2), in the image, 2.8 Å, plus the 1.2 Å needed to reduce the double exposed image. The sum of 4.0 Å is close to bulk the Si-Si distance of 3.84 Å and forms a consistency check.

Having experimentally determined the adsorption site, the bonding models are considered. For C<sub>2</sub>H<sub>4</sub> and C<sub>2</sub>H<sub>2</sub>, *sp*<sup>2</sup> and *sp* hybridization of carbon exists. The remaining *p*-like states form  $\pi$  bonds that do not lie on the molecular axis. The chemisorption is then viewed as the severing of a  $\pi$  orbital allowing for bonding to the dangling bonds of the dimer atoms. The new bonds have sigma character. Pauling presents an equivalent description, the bent bond picture, in which each carbon atom tends to form tetrahedral *sp*<sup>3</sup>-like orbitals [13]. In the free ethylene and acetylene molecules, bent (and strained) bonds form between the two carbons giving the ethylene a C-C double bond and the acetylene a C-C triple bond. Hence, on chemisorption the "bent bonds" simply open up and attach to the dangling bonds on the silicon surface atoms, which leaves just a single bond between the carbon atoms in each case. Thus from the initial hybridization states in each molecule, the chemisorbed form adopts a *sp*<sup>3</sup> carbon hybridization and a surface "alkane" species forms in each case. There is an interesting comparison between the C<sub>2</sub>H<sub>4</sub> and C<sub>2</sub>H<sub>2</sub> surface complexes since they can be viewed as surface molecules C<sub>2</sub>H<sub>4</sub>Si<sub>2</sub> and C<sub>2</sub>H<sub>2</sub>Si<sub>4</sub> suggesting a similarity between the C-H and C-Si bonds. In thermal breakdown, it is known that C<sub>2</sub>H<sub>4</sub> is liberated in the one case, and for the other C<sub>2</sub>H<sub>2</sub> decomposes forming a carbide [14]. The latter complex stays on the surface, probably because it has two bonds for each carbon while the C<sub>2</sub>H<sub>4</sub> case forms only one bond. The analysis of the line shape for the high-resolution core-level-photoemission peaks supports the assignments made here [15], as does the observed vibrational frequency [16].

Research support at Montana State University by NSF Grant No. DMR 9505618 is gratefully acknowledged and

the support by ONR/DEPSCOR is gratefully acknowledged. DOE research support at the University of Pittsburgh is acknowledged with thanks. The Advanced Light Source is supported by DOE. We thank the staff at ALS for their support. Discussions with David Single of MSU are gratefully acknowledged.

\*Present address: Carroll College, Helena, MT 59625.

<sup>†</sup>Present address: Davicom Semicon., San Jose, CA.

<sup>‡</sup>Present address: IBM, Burlington, NY.

<sup>§</sup>Present address: Univ. of Michigan, Ann Arbor, MI.

- [1] Huasheng Wu and G. J. Lapeyre, Phys. Rev. B **51**, 14549 (1995); a discussion of the method's foundation is submitted.
- [2] H. Wu, G. J. Lapeyre, H. Huang, and S. Y. Tong, Phys. Rev. Lett. **71**, 251 (1993).
- [3] J. T. Yates, Jr., Science **229**, 335 (1998); J. S. Howisard and R. J. Hamers, J. Phys. Chem. B **101**, 9581 (1997).
- [4] M. Nishijima *et al.*, Surf. Sci. **192**, 383 (1987).
- [5] G. Dufour *et al.*, Phys. Rev. B **56**, 4266 (1997).
- [6] L. Li, C. Tindall, O. Takaoka, Y. Hasegawa, and T. Sakurai, Phys. Rev. B **56**, 4648 (1997).
- [7] F. Matsui *et al.*, Surf. Sci. **401**, L413 (1998).
- [8] R. H. Zhou *et al.*, Phys. Rev. B **47**, 10601 (1993); Y. Imamura *et al.*, Surf. Sci. **341**, L1091 (1995).
- [9] G. J. Lapeyre, Nucl. Instrum. Methods Phys. Res., Sect. A **347**, 17 (1994).
- [10] S. Y. Tong, H. Huang, and C. M. Wei, Phys. Rev. B **46**, 2452 (1992).
- [11] The images that show weak spots due to one carbon atom's emission scattering from the other carbon atom of the molecule will be presented elsewhere. For C<sub>2</sub>H<sub>2</sub> the separation of these spots is 1.1 Å in agreement with the 1.2 Å value observed for the third layer silicon. For C<sub>2</sub>H<sub>4</sub> the separation is 1.6 Å. These values give, respectively, 2.2 and 2.3 Å for the Si-Si dimer bond length in the surface complex which compares to 2.23 Å for the clean surface. Apparently, the adsorption does not break the dimer bond.
- [12] The first layer results from the acetylene image, to be presented elsewhere, give an interplanar separation between the adsorbed C and first layer Si of 0.8 Å and a Si-Si dimer length of 2.3 Å. The C-Si distance is 1.8 Å and for C<sub>2</sub>H<sub>4</sub> the observed value is 2.2 Å which compares to the 1.89 Å. For bulk SiC the bond length is 1.89 Å.
- [13] L. Pauling, *Nature of the Chemical Bond* (Cornell University Press, Ithaca, NY, 1963), 3rd ed., p. 137.
- [14] P. A. Taylor, R. M. Wallace, C. C. Cheng, W. H. Weinberg, M. J. Dresser, W. J. Choyke, and J. T. Yates, Jr., J. Am. Chem. Soc. **114**, 6754 (1992), and references therein.
- [15] S. H. Xu, Y. Yang, M. Keefe, G. J. Lapeyre, and E. Rosenberg, Phys. Rev. B **60**, 11586 (1999).
- [16] The vibrational spectrum for chemisorbed C<sub>2</sub>H<sub>2</sub> is in agreement since it shows a C-C frequency, 1040 cm<sup>-1</sup>, very near to that known for single C-C bonds, 950 cm<sup>-1</sup>. See Ref. [4].

S.H. Xu, M. Keeffe, Y. Yang, C. Chen, M. Yu,

and G.J. Lapeyre (Montana State University);

**Photoelectron Diffraction Imaging Reveals  
a New Bonding Configuration for  $C_2H_2$   
and  $C_2H_4$  Chemisorbed on Si(100)**

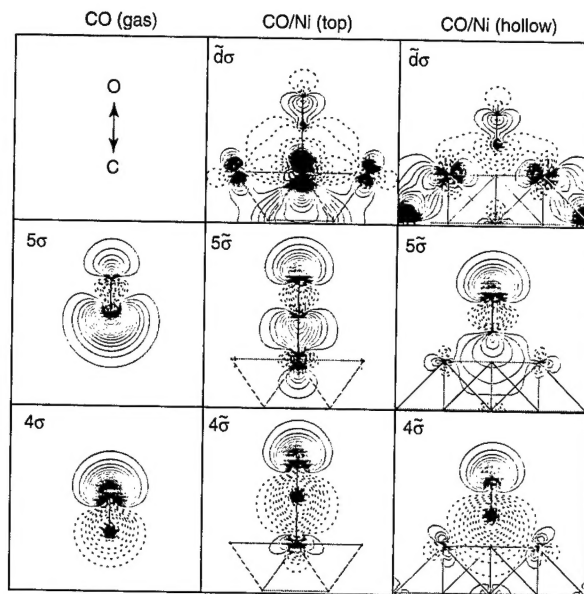


**Figure 6** Contour plots of  $\sigma$  orbitals for CO in the gas phase and adsorbed on Ni(100) in the top and hollow sites, again showing strong modifications to the CO orbital structure for different adsorption sites, in line with the experimental observations.

to the substrate. Based on the findings reported here, such phenomena can be understood in terms of the interplay between the  $\pi$  and  $\sigma$  interactions. The  $\pi$  interaction weakens the internal CO bond, decreasing the CO stretch frequency as coordination increases, and the balance between  $\pi$  bonding and  $\sigma$  repulsion leads to small differences in adsorption energies despite very large differences in electronic structure.

#### INVESTIGATORS

A. Föhlisch, J. Hasselström, O. Karis, P. Bennich, and A. Nilsson (Uppsala University, Sweden) and M. Nyberg, L. Triguero, and L.G.M. Pettersson (University of Stockholm, Sweden).

#### FUNDING

Swedish Natural Science Research Council (NFR) and the Göran Gustafsson Foundation for Research in Natural Sciences and Medicine.

#### PUBLICATIONS

1. A. Föhlisch et al., "How carbon monoxide adsorbs in different sites," *Phys. Rev. Lett.* **85**, 3309 (2000).
2. A. Föhlisch et al., "The bonding of CO to metal surfaces," *J. Chem. Phys.* **112**, 1946 (2000).

*Determining the atomic structure (where the atoms are) of crystalline solids (metals, semiconductors, ceramics, and so on) is comparatively easy with the technique of x-ray diffraction. Solving the same problem for the atoms at a surface is not so easy, in part because the surface structure is only one or a few atomic layers thick, so that the x-ray diffraction signal is weak compared to that from the rest of the sample. Electron techniques have the advantage of being surface sensitive, but interpreting experimental data in terms of atomic positions is extremely challenging. Photoelectron holography is a new method based on the use of electron rather than light waves for directly imaging surface atomic structure. Researchers from Montana State University and their colleagues have used this technique to image the local structure of ethylene and acetylene molecules on a silicon surface and found some surprising results that contradicted the prevailing thinking.*

The adsorption of small hydrocarbons on silicon surfaces is of particular interest because of the role that silicon plays in technology. For example, ethylene ( $C_2H_4$ ) and acetylene ( $C_2H_2$ ) groups are commonly used to attach larger molecules with specialized functional groups to a silicon surface. It has long been believed that both ethylene and acetylene bond with the same site symmetry to a pair of silicon atoms on the silicon(100) surface via the silicon dangling bonds. The pair of silicon atoms is that formed when the clean silicon (100) surface reconstructs by forming dimer pairs (2×1 reconstruction). Our photoelectron diffraction experiments, however, show that acetylene unexpectedly can bond to four silicon surface atoms, while ethylene, as expected, bonds to two silicon surface atoms.

To image the molecule's site position (symmetry), we inverted carbon 1s photoelectron diffraction oscillations to generate direct real-space images of silicon atoms neighboring the carbon emitters. Ball-and-stick representations of the local atomic structures obtained in this way are shown in Figure 7. We used the photon-energy-scanned, constant-initial-energy spectra (CIS) technique. Representative CIS are shown in Figure 8. The oscillations in the

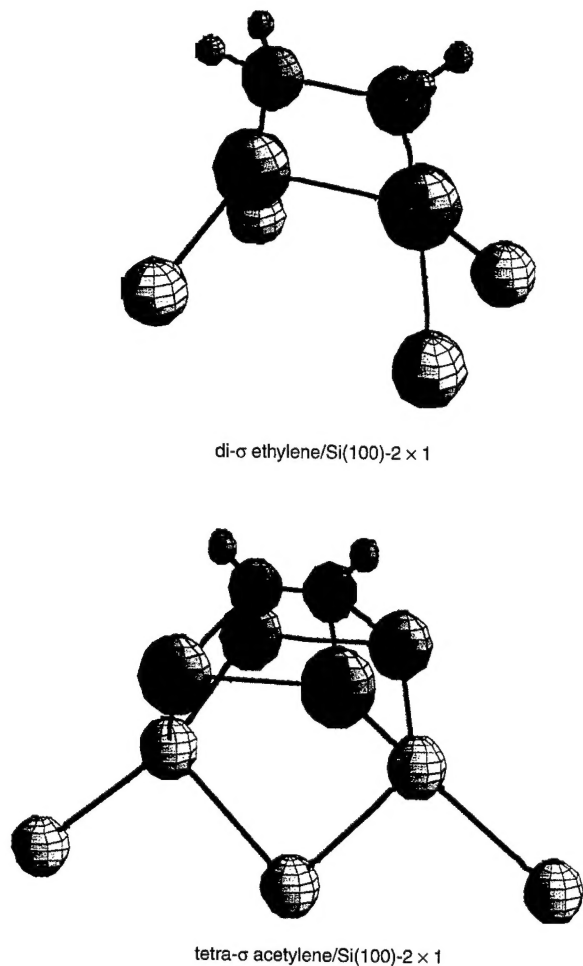


**Figure 7** Ball-and-stick sketches of the silicon (100) adsorption sites for (top) ethylene ( $C_2H_4$ ) and (bottom) acetylene ( $C_2H_2$ ) obtained by holographically inverting carbon 1s photoelectron diffraction oscillations. Ethylene bonds to two silicon atoms, whereas acetylene unexpectedly bonds to four. The large green balls are carbon atoms, the orange balls are first-layer silicon atoms, and the pink balls are second- and third-layer silicon atoms. The small blue balls represent likely positions for hydrogen atoms.

photoelectron diffraction spectra for ethylene and acetylene have different frequencies in Figure 8, already indicating that the sites are different.

The inversion is based on the internal-reference-beam holographic principal, where the reference wave and the scattered wave come from the same source, namely, the photoelectron-emitting carbon atoms. Inversion involves a transform first against the set of wave numbers (photon energies) and then the set of directions. The latter organizes the measured beam directions into collections of small cones, which span all directions (small cone method). The holographic-based inversion generates

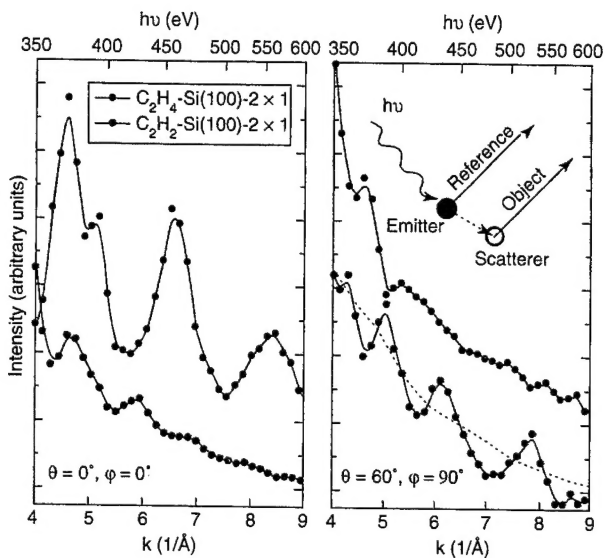


**Figure 8** Constant-initial-energy photoelectron diffraction spectra for ethylene and acetylene in two different photoelectron emission directions. The oscillations in the spectra for ethylene and acetylene have different frequencies, already indicating that the adsorption sites are different. The inset illustrates the internal-reference holographic principle in which a photoelectron wave from a carbon emitter atom serves as both the reference wave and, when scattered from a neighboring silicon, the object wave.

an "image function" represented by an intensity value for every point in space.

The image can be displayed in a number of ways. Choosing gray-scale, horizontal planar cuts through the second layer of silicon atoms, we see immediately that the images are quite different in that ethylene (Figure 9) shows four intense spots centered at a depth 2.8 Å below the carbon emitters, while acetylene (Figure 10) shows only two spots at a depth of 1.6 Å. The distance values may be in error by several tenths of an angstrom. The second-layer spots together with first- and third-layer spots contained in the image function establish the local atomic structure shown in Figure 7.

The image structure and the local atomic structure are not the same. Since each emitting atom sends out its own reference beam, the inversion places all emitters at the same place in the image (the origin). If every emitter has the same site symmetry, the image and the atomic structure are the same, but in these molecules, the two carbon atoms are in inequivalent sites. As a result, both emitters appear at the origin of the composite image, giving the image a kinship to a double-exposed photo. To extract the local structure from the image, one looks

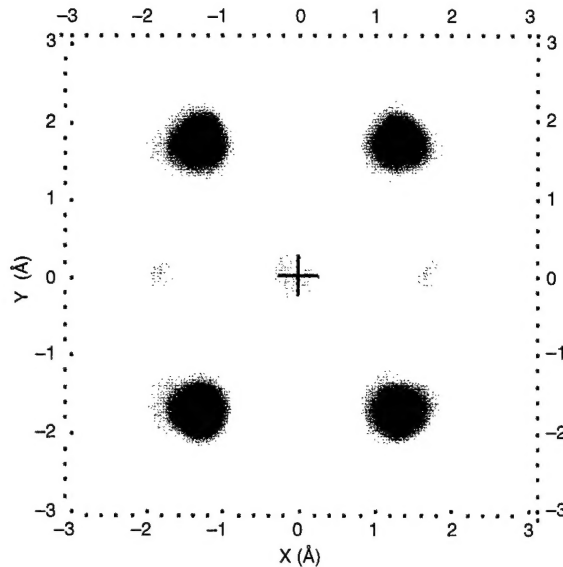


**Figure 9** Horizontal, planar cut of the ethylene image function through the second layer of silicon atoms (pink balls in top structure in Figure 7). The image intensity is indicated by the gray scale. The positions of the two carbon emitter atoms are the same in the image, directly above the center of the cut. The value of the stretch in the *X* (dimer) direction needed to make the rectangular into a square pattern is the value for the C-C separation in the actual molecule.

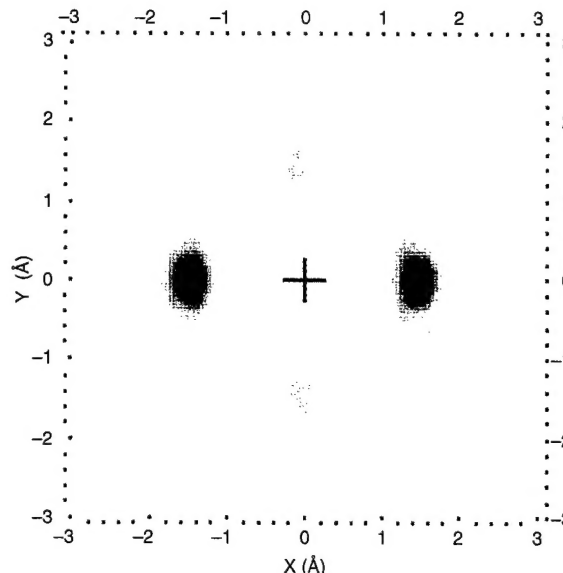


**Figure 10** Horizontal, planar cut of the acetylene image function through the second layer of silicon atoms (pink balls in bottom panel of Figure 7). The positions of the carbon emitter atoms in the image are again identical, directly above the center of the cut. To obtain a value for the C-C separation in the actual molecule, it is necessary to examine a planar cut for the third layer of silicon atoms.

for features in the image that can be used to determine the C-C separation.

The square unit cell of a bulk (100) plane is taken to be a reasonable description for the second and third silicon layers after adsorption. For ethylene, notice that the spots in the horizontal cut containing the second-layer silicon atoms form a rectangular pattern (Figure 9). To make the spots into a square, the pattern has to be extended in the *X* direction by a distance 1.4 Å that represents the value of the C-C separation. The value also be used to infer a first-layer Si-Si (dimer) separation of 2.0 Å. For acetylene, a C-C separation of 1.2 Å is found when the third-layer image spots are used for the determination. In neither case does the value of the Si-Si distance suggest that the dimer bond has been severed but rather only modified.

#### INVESTIGATORS

S.H. Xu, M. Keeffe, Y. Yang, C. Chen, M. Yu, and G.J. Lapeyre (Montana State University); E. Rotenberg and J. Denlinger (ALS); and J.T. Yates, Jr. (University of Pittsburgh).

#### FUNDING

U.S. Department of Energy, Office of Basic Energy Sciences; Office of Naval Research (DEPSCoR), and National Science Foundation.

#### PUBLICATION

1. S.H. Xu, et al., "Photoelectron diffraction imaging for  $C_2H_2$  and  $C_2H_4$  chemisorbed on Si(100) reveals a new bonding configuration," *Phys. Rev. Lett.* **84**, 939 (2000).